UNIVERSITÀ DEGLI STUDI DELL'AQUILA
DIPARTIMENTO DI INGEGNERIA INDUSTRIALE E DELL'INFORMAZIONE E DI ECONOMIA

Dottorato di Ricerca in Ingegneria Industriale e dell'Informazione e di Economia

Curriculum in Ingegneria Elettrica, Elettronica e dell'Informazione

XXXIII ciclo

Titolo della tesi

Modeling and Experimentation of short range communications for sensing and IoT

SSD ING-INF/02

Dottorando

Antonio DI NATALE

Coordinatore del corso

Prof. Giuseppe FERRI

Tutor

Prof. Emidio DI GIAMPAOLO

A.A. 2019/2020

Contents

A chi quest'anno
ci ha lasciato e
a chi lo ha quasi
fatto e fortunatamente
è rimasto.
A mio fratello Christian e
ai miei genitori
Maurizio e Maria Cristina.
A voi grazie per esserci
stati sempre.

Abstract

The thesis reports the mathematical models, experimental results and related activities for the development of wireless devices in short-range communication systems aimed at sensing and the Internet of Things. The work originates from the idea of Wireless Body Area Network where low-cost sensors and communication systems can be worn or integrated into clothes. Subsequently, the investigation was extended to devices external to the body to be used as laboratory sensors or as a communication device.

The first part of the work dealt with the design and construction of wearable, fully textile and reconfigurable Ultra Wide Band (UWB) antennas for Wireless Body Area Network (WBAN) applications. These antennas have the ability to be used in two different configurations (monopole, microstrip), in order to change the topology of the short-range network and the type of communication (on-body communication and off-body communication). The obtained antennas are then used in the realization of a wearable radio-localization system based on the principle of harmonic RADAR. A completely passive device, which allows to replicate the received signal in second harmonic, has been designed and built in order to be integrated into wearable UWB antennas. One envisaged use concerns the radio-localization of people within post-disaster scenarios or by connecting it to a transducer (for example of temperature) it can be used as a sensor.

For the development of textile antennas, it has been envisaged the use of non-conventional dielectric materials, such as fabrics, paper, plastic and organic materials with the aim to use them in the design and construction of low cost and low environmental impact sensors and antennas in the microwave band. For that purpose, their dielectric characterization has been necessary. A permittivity measurement system has been designed based on the ring resonator principle which has elements of versatility and can also be used for the characterization of some types of liquid material. In this context, the research has been extended to the design and construction of low-cost microwave microfluidic sensors for the characterization of aqueous solutions and liquids in general.

For what concerns the development of sensors to be used in laboratory, a completely passive RFId (Radio Frequency Identification) tag at 867 MHz has been designed and realized, in order to use it as a sensor in breaking test activities in the laboratory. The designed sensor exploits the variation of the input impedance of a twin line with variable parameters (tapered). Finally, in the context of reconfigurable beam antennas, a Low Noise Amplifier was designed and built to be replicated on the branches of the beam forming network of an antenna array operating at 5 GHz for Wi-Fi (Wi-Fi5) applications. The developed LNA has the peculiarity to work not only as a low-noise amplifier but also as a microwave switch which, when properly piloted, allows the reconfiguration of the antenna beam. This solution avoids the use of microwave switches or circulators and thus reduces the noise of the receiving chain and the overall dimensions.

Key words: Ultra Wide Band, Wireless Body Area Network, All-Textile Antenna, metamaterials, Harmonic RADAR, microwave characterization of materials, microwave microfluidic analysis, microwave passive sensors, RFId passive tag, microwave Low Noise Amplifiers

List of pubblications

Published articles

1. A. Di Natale, E. Di Giampaolo. *A reconfigurable All-Textile Wearable UWB Antenna*, Progress In Electromagnetics Research C, Vol. 103, pp. 31-43, 2020.

2. A. Di Natale, E. Di Giampaolo. *UWB Reversible Structure All-Textile Antenna for Wireless Body Area Networks Applications*, 2019 Photonics & Electromagnetics Research Symposium - Spring (PIERS – Spring), 17-20, June, 2019, Rome, Italy.

3. E. Di Giampaolo, A. Di Natale. *A Configurable Microwave Microfluidic Sensor for Medical Diagnosis and Chemical Analysis*, 2019 Photonics & Electromagnetics Research Symposium - Spring (PIERS - Spring), 17-20, June, 2019, Rome, Italy.

Articles under submission

1. A. Di Natale, A. Di Carlofelice, and E. Di Giampaolo. *A rescue tag based on harmonic radar principle.*

2. A. Di Natale, A. Di Carlofelice, and E. Di Giampaolo. *An RFID-based breaking test sensor.*

Acknowledgements

Before proceeding with the presentation of the thesis, I would like to thanks my tutor, Professor Emidio Di Giampaolo for having coordinated and shared impressions and reasonings regarding all the activities concerning the design of antennas and passive radiofrequency sensors collected in this work, and treated in the three-years research doctorate. Thanks to his knowledge, I was able to deal with very heterogeneous themes in the design of telecommunications devices.

To his thanks are added my thanks to Professor Piero Tognolatti and to Doctor Alessandro Di Carlofelice for their valuable advice due to their great experience in the field of electromagnetic design.

Special thanks go to Professor Giorgio Leuzzi and Doctor Leonardo Pantoli who guided me in the design of active microwave devices described in the last part of this thesis.

Chapter 1

WSNs and IoT: opportunities and challenges

1.1 Introduction

The strong development of wireless communications that has been underway for several decades has allowed the increasingly widespread and intelligent interconnection of users and people. The goal has always been to reduce geographical distances and make efficient services usable with positive impacts on the quality of life. The evolution of this world has occurred through numerous studies carried out in the field of electronic and information engineering which have led, over time, to the birth of the World Wide Web as it is known today. Technological standards such as Wi-Fi (IEEE 802.11), Bluetooth (IEEE 802.15.1), ZigBee (IEEE 802.15.4), and technologies such as Near Field Communication (NFC) and Radio Frequency Identification (RFId), are used in the development of Wireless Sensor Networks (WSNs), with the aim of making some of the activities carried out, for example, in homes and in some industrial production processes, stating the future of sectors such as home automation [1] and industry 4.0 [2].

A sensor network is usually designed to detect events or phenomena, collect and process data, and transmit sended information to interested users. Basic features of sensors neworks are:

- self-organizing capabilities;

- short-range broadcast communication and multihop routing;

- dense deployement and cooperative effort of sensor nodes;

- frequently changing topology due to fading and node failures;
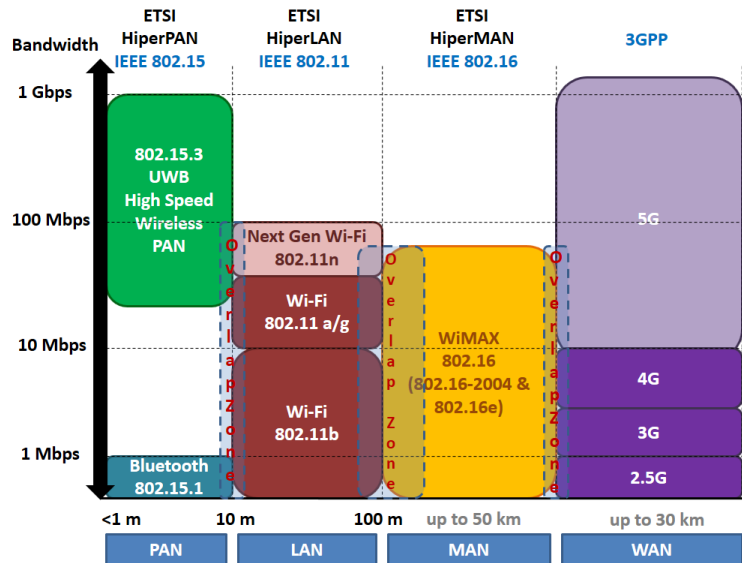
Figure 1.1.1: Overview of the various wireless networking technologies used in this period.

- limitations in energy, transmit power, memory, and computing power.

These characteristics make sensor networks different from other wireless ad hoc or mesh networks. Clearly, the idea of mesh networking is not new; it has been suggested for some time for wireless Internet access or voice communication. Similarly, small computers and sensors are not innovative per se. However, combining small sensors, low-power computers, and radios makes for a new technological platform that has numerous important uses and applications [3].

For this reason reasearch and commercial interest in the area of wireless sensor networks are currently growing exponentially. The use of this type of network, in fact, is the basis of the concept of the Internet of Things (IoT), in which any object ("thing") manages to make itself recognizable, acquiring intelligence thanks to the fact that it can communicate data about itself, and to be able to access aggregate information by others. The term "Internet of Things" was conied by Kevin Ashton in 1999 [4]. At that point, he viewed Radio Frequency Identification (RFId) as essential to the Internet of Things [5], which would allow computers to manage all individual things [6]-[8]. Over the years, however, other wireless communication standards have also been used such as Wi-Fi, Bluetooth, Zigbee, etc., allowing the integration of data collection networks based on WSNs to the data networks already present and used to access the Internet.
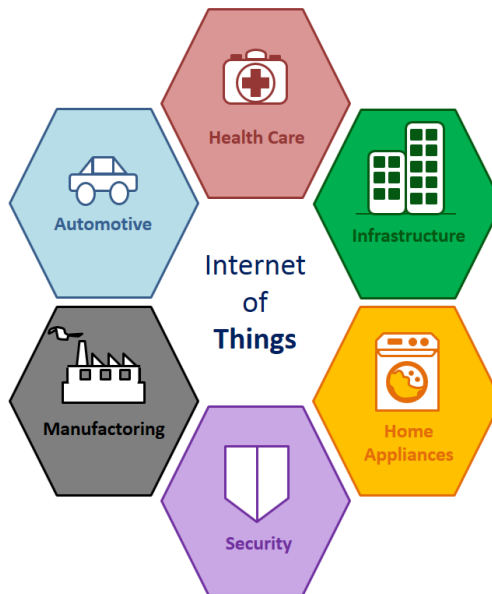
Figure 1.1.2: Wireless Sensor Networks and Internet of Things application fields.

Also in recent years mobile radio communications have had a strong push from the point of view of pervasiveness, leading to the birth of the fifth mobile radio generation (5G), with a view to making optimum access to Internet services even in high-density users environments. In literature there are many recent studies in which the communication concepts envisaged for 5G mobile systems are applied in IoT fields [9]. An overview of the actual standards for wireless communications are reported in Fig. 1.1.1

Wireless Sensor Networks (WSNs), and the IoT concept in general, are used in many fields and for different uses [3] (see Fig. 1.1.2):

- **General Engineering**

  - *Automotive telematics*: cars, which comprise a network of dozens of sensors and actuators, are networked into a system to improve the safety and efficiency of traffic;
  - *Sensing and maintenance in industrial plants*: complex industrial robots are equipped with up to 200 sensors that are usually connected by cables to a main computer. Thanks to wireless sensors nodes it is possible to remove wired connections in order to reduce costs and robot's movments reduction;
  - *Aircraft drag reduction*: achieved by combining flow sensors and blowing/sucking actuators mounted on the wings of an airplane;

- *Smart office spaces*: areas equipped with light, temperature, and movement sensors, microphones for voice activation, and pressure sensors in chairs. Air flow and temperature can be regulated locally for a specific room rather than centrally;
- *Tracking of goods in retail stores*: tagging facilitates the store and warehouse management;
- *Tracking of containers and boxes*: shipping companies are assisted in keeping track of their goods, at least until they move out of range of other goods;
- *Social studies*: equipping human beings with sensor nodes permits interesting studies of human interaction and social behavior;
- *Commercial* and *residential security*.

- **Agricolture and Environmental Monitoring**

  - *Precision agricolture*: crop and livestock management and precise control of fertilizer concentrations are possible;
  - *Planetary exploration*: exploration and surveillance in inhospitable environments such as remote geographic regions or toxic locations can take place;
  - *Geophysical monitoring*: seismic activity can be detected at a much finer scale using a network of sensors equipped with accelerometers;
  - *Monitoring of freshwater quality*: the field of hydrochemistry has compelling need for sensor networks because of the complex spatiotemporal variability in hydrologic, chemical, and ecological paramenters and the difficulty of labor-intensive sampling, particularly in remote locations or under adverse conditions. In addition, buoys along the coast could allert surfers, swimmers, and fishermen to dangerous levels of bacteria;
  - *Habitat and fauna monitoring*: scientists could measure humidity, pressure, temperature, infrared radiation, total solar radiation, and photosyntetically active radiation. Animals and fauna movement tracking systems are also used in scientific research for understand the movements of some specimens of a given species whitin a specific area;
  - *Disaster detection*: forest fire and floods can be detected early and causes can be localized precisely by densely deployed sensor networks;

- *Contaminant transport*: the assessment of exposure levels requires high spatial and temporal sampling rates, which can be provided by WSNs.

- **Civil Engineering**

  - *Monitoring of structures*: sensors will be placed in bridges to detect and warn of structural weakness and in water resevoirs to spot hazardous materials. The reaction of tall buildings to wind and earthquakes can be studied and material fatigue can be monitored closely;

  - *Urban planning*: urban planners will track groundwater patterns and how much carbon dioxide cieties are expelling, enabling them to make better land-use decisions;

  - *Disater recovery*: buildings razed by an earthquake may be infiltrated with sensor robots to locate signs of life.

- **Military Applications**

  - *Asset monitoring and management*: commanders can monitor the status and locations of troops, weapons, and supplies to improve military command, control, communications, and computing;

  - *Surveillance and battle-space monitoring*: vibration and magnetic sensors can report vehicle and personnel movement, permitting close surveillance of opposing forces;

  - *Protection*: sensitive objects such as atomic plants, bridges, retaining walls, oil and gas pipelines, communication towers, ammunition depots, and military headquarters can be protected by intelligent sensor fields able to discriminate between different classes of intruders. Biological and chemical attacks can be detected early or even prevented by a sensor network acting as a warning system;

  - *Self-healing minefields*: this system is designed to achieve an increased resistance to dismounted and mounted breaching by adding a novel dimension to the minefield. Instead of a static complex obstacle, the self-healing minefield is an intelligent, dynamic obstacle that senses relative positions and responds to an enemy's branching attempt by physical reorganization.

- **Health Monitoring and Surgery**

5
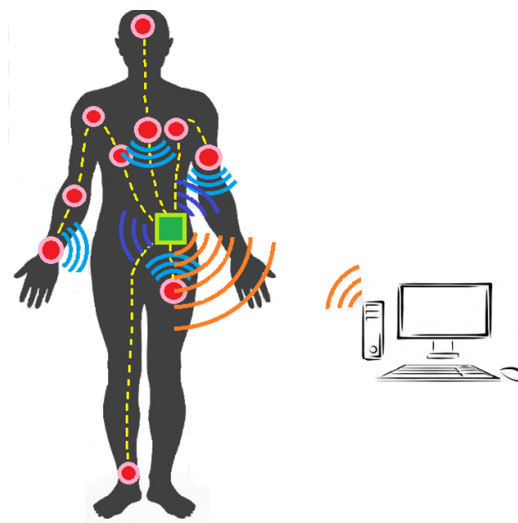
Figure 1.1.3: Example of Wireless Body Area Network in bio-medical application.

- *Medical sensing*: physiological data such as body temperature, blood pressure, and pulse are sensed and automatically transmitted to a computer or physician, where it can be used for health status monitoring and medical exploration. Wireless sensing bandages may warn of infection. Tiny sensors in the blood stream, possibly powered by a weak external electromagnetic field, can continuously analyze the blood and prevent coagulation and thrombosis;

- *Micro-surgery*: a swarm of MEMS[1]-based robots may collaborate to perform microscopic and minimally invasive surgery.

From the application fields just described, it can be seen how, in some cases, WSNs and the IoT in general, are increasingly used in areas where the various communicating nodes (sensors) are arranged very close to each other (tens of meters, or tens of centimeters). In particular, it refers to the biomedical, rescue and military fields. An example of a hypotetical scenario in biomedical applications is shown in Fig. 1.1.3.

In biomedical fields, medical staff could find information on the vital signs and the state of health of patients through non-invasive and real-time surveys; in the other fields, instead, technologies based on the RADAR principle could be exploited, in order to identify people to be rescued in environments

---

[1]MEMS: Micro Electro-Mechanical Systems.
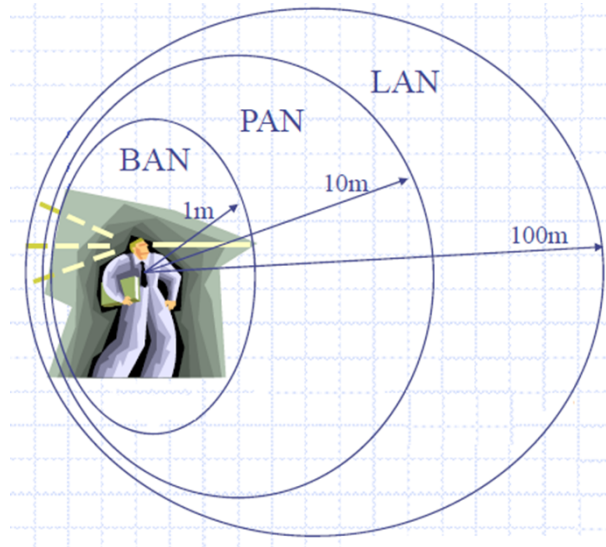
Figura 1.1.4: Typical ranges of action of Body Area Network, Personal Area Network, and Local Area Network.

affected by natural (or man-made) disasters, or to determine whether hostile situations, or the presence of allied units and supplies. For these applications, given the reduced range of action required, we can speak of Wireless Personal Area Network (WPAN) [10]-[11] and Wireless Body Area Network (WBAN) [12]-[14] (see Fig. 1.1.4).

The implementation of a Wireless Body Area Network (WBAN), for example, can be made possible thanks to the use of Ultra Wide Band (UWB) [15]-[16] technology, which allows to process information on very wide frequency bands ($\geqslant 500$ MHz), thanks to very short pulses (nanoseconds), making it possible to exchange data in a robust way against the multipath that could occur in environments where there are many obstacles between the transmitting and receiving units.

The widespread access to the various technologies that exploit wireless communications has therefore contributed to the spread of a large number of communicationg devices. It was therefore realized the need to reduce their number through the development of equipment operating on several frequency bands or on very wide bands. Also from technological point of view, this new generation of devices opens up many research fronts, especially in terms of low energy and environmental impact (green technology). In fact, in many systems, such as RFId ones, there is a tendency to design and use passive or semi-passive devices with low energy consumption, in order to eliminate or reduce as much as possible the use of batteries necessary for the
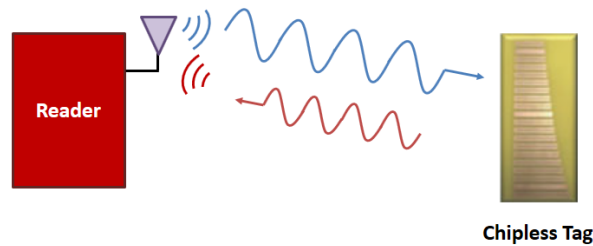
Figura 1.1.5: Chipless RFId System.

operation of the transponders (tags) affixed to a specific object belonging to a given network. The tendency is therefore to be able to transmit and exchange information thanks to devices called "chipless", which do not need electronic circuitry (especially active) on board [17]. An example of a chipless RFId system is shown in Fig. 1.1.5.

Given the numerous fields of application, the world of research is not only aimed at what is related to the aspect of communications itself, such as:

- *Energy efficiency/system lifetime.* The sensors are battery operated, rendering energy a very scarce resource that must be wisely managed in order to extend the lifetime of the network [18].

- *Latency.* Many sensor applications require delay-guaranteed service. Protocols must ensure that sensed data will be delivered to the user within a certain delay. Prominent examples in this class of networks are certainly the sensor-actuator networks.

- *Accuracy.* Obtaining accurate information is the primary objective; accuracy can be improved through joint detection and estimation. Rate distortion theory is a possible tool to assess accuracy.

- *Fault tolerance.* Robustness to sensor and link failures must be achieved through redundancy and collaborative processing and communication.

- *Scalability.* Because a sensor network may contain thousands of nodes, scalability is a critical factor that guarantees that the network performance does not significantly degrade as the network size (or node density) increases.

- *Transport capacity/throughput.* Because most sensor data must be delivered to a single base station or fusion center, a critical area in the sensor network exists (the green area in Fig. 1.1.6.), whose sensor nodes must relay the data generated by virtually all nodes in the network.
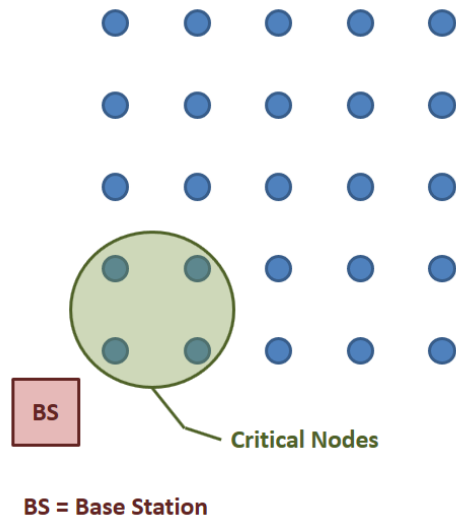
Figure 1.1.6: Sensor network with base station (or fusion center). The green-shaded area indicates the critical area whose nodes must relay all the packets.

> Thus, the traffic load at those critical nodes is heavy, even when the average traffic rate is low. Apparently, this area has a paramount influence on system lifetime, packet end-to-end delay, and scalability.

Even the technological aspects related to the hardware is a real breeding ground in which experts are turning their attention. In fact, there are numerous studies also in the materials to be used for the manufacture of these new telecommunication devices. The idea is to be able to use commonly used materials in the realization of sensors such as paper, plastic films, wood, plexiglass, etc., trying to minimize the costs for their construction and the environmental impact. The choice of new materials could allow, for example, to make telecommunication devices wearable and "transparent" for the user. As part of the materials, there are many studies in which the dielectric substrates that usually make up the various sensors, antennas, circuits, etc., are applied innovative materials such as graphene, in order to modify the physical and dielectric properties. Thanks to them, in fact, it is possible to modify the dielectric properties of the substrate to the point of obtaining a very strong miniaturization of the device. It is no coincidence that substances such as graphene have found wide use in applications operating in the terahertz [THz] band [19]-[20]. The use of these substances are, in most cases, made possible thanks to the use of specific and innovative 3D printing techniques, or through chemical procedures with which the substrates are impregnated. Other studies, on the other hand, especially in the design of

antennas and microwave sensors, have focused on the use of Artificial Magnetic Conductors (AMC), in order to create periodic metallic structures, having particular geometries (metamaterials), which are able to modify the intrinsic properties of the substrate on which it is affixed [21]-[23]. Interesting fields of research also fall into the development of conductive inks, such as, for example, those consisting of carbon nanotubes [24]-[26], and in the automated printing techniques of the various metal parts that make up the sensors (cutting plotter, conductive ink plotter, etc.) [27]-[29].

1.2   Research Objectives

The general objective of the work is the development of battery-free short range communications and sensing devices designed to be used pervasively in the context of IoT. For these reasons, devices must have low cost, simplicity of construction and use and suitability often specialized to the specific application. For these reasons they are heterogeneous both from the point of view of the frequencies used and from the point of view of technologies. In fact, in the thesis work I explored different technologies and application areas both for personal interest and for contingent needs, while maintaining the set goal. The above mentioned objective includes: the development of wearable UWB antennas for sensing in the context of the Wireless Body Area Network, a scattering tag based on the principle of harmonic radar that is integrated in the UWB antenna, the model of microfluidic sensor which, despite having remained at a preliminary stage development, shows the potential and methods for integration in the context of sensors for IoT. The breaking test tag using RFID technology was developed for specific laboratory applications and falls into the broad category of RFID short-range sensing tags. Alongside these main topics, additional ancillary topics have been addressed. I define them ancillary not because they are of minor importance but because they are helpful or enabling for those defined as main. This is the case of techniques and development of devices for the measurement of the dielectric constant, they have been necessary to identify and characterize alternative materials for the construction of wearable antennas. Similarly, was the development of the LNA switchable system. Although this last topic has remained limited to the design and construction of the specific device, it is thought to be an enabling block of a more complex IoT system in which the designed block allows the switching on and off of the antenna elements of an array (over time) in order to realize the so-called Time Modulated Array (TMA). TMA permits the development of systems for intelligent beam steering, field focusing, estimation of the direction of arrival of signals, all applications that are of

interest in the context of short range communication and sensing. For what concerns the innovative aspects of the research, the UWB antennas have introduced models and methods to reconfigure the antennas by alternating two different topologies: the monopole and the planar one that is not proposed before in the literature. The tag for the harmonic radar has the innovation, not found in literature, of using a single port to perform the matching to the non-linear device. So that, it needs only one antenna, but also performs the matching for both the fundamental and the first harmonic at the same time and manages the translation of the matching bandwidth in agreement with the variation of capacitive loads that can be used as additional sensors. The UHF RFID tag proposes a new sensor model for applications widely studied in the literature. Regarding the specific objectives of the individual research topics they concern the development of mathematical and electromagnetic models aimed at the development of innovative low-cost antennas, and low power consumption sensors and radio frequency devices that can be used in wireless sensors networks and in IoT applications.

In particular, we wanted to identify Ultra Wide Band (UWB) impedance matching techniques in order to obtain reconfigurable all-textile wearable antennas. By reconfigurability we mean the ability of the device to function in at least two different modes while maintaining the same basic structure. To obtain this type of device, it was decided to appropriately modify the geometry of the conductive parts of the antennas, or through the application of frequency selective structures (metamaterials) appropriately designed.

The development of wearable antenna requires the use of non-conventional materials like fabrics and rubbers for that reason another important research goal is to be able to characterize unconventional dielectric materials in the microwave band, through the use of numerical algorithms and the development of an appropriate sensor. In fact, in the context of the design of microwave devices, canonical materials such as Rogers, Taconic, Duroid, etc., are indeed performing, but they are also very expensive and not so easy to find. Through the characterization of commonly used materials such as paper, plastics, fabrics, etc., we want to try to use them in the design and construction of laboratory antennas and sensors, possibly passive, for short range networks.

A further research objective concerns the study of active electronic / electromagnetic design techniques in the context of intelligent reconfigurable-beam receiving systems. By intelligent we mean system with low energy consumption, controllable by appropriate control signals, whose dimensions in terms of layout, and performance in term of noise (noise figure) must be reduced to a minimum. For that purpose, the architecture of Time Modulated Array (TMA) permits to realize a kind of 4-D antenna array since

it introduces time as an additional dimension for the generation, detection, and modulation of electromagnetic beams. That architecture is suitable for short-range communications and sensing because enables novel characteristics of the antenna array including ultra-low side-lobes at the fundamental component and realizing real-time beam scanning by harmonic components. Different applications are possible: space-division multiple access, direction finding, multiple input multiple out radar, near-field focusing. From the theoretical point of view there is a rich literature, nevertheless the practical application feels the limits of the hardware in particular the non-ideal characteristics of RF switches with regard to the switching speed and the rising and falling edges. The use of a switchable LNA has the advantage to reduce the overall noise since the additional noise of the switch is missing, in addition to the reduction of the overall dimensions. The work presented in the thesis is limited to the realization of 4-port switchable LNA device to be used in a future experimental TMA research/applications.

1.3 Thesis Layout

Chapter 2 dealt with the design and construction of reconfigurable wearable all-textile Ultra Wide Band antennas for Wireless Body Area Network (WBAN) applications. This type of antennas were then used in the realization of a wearable radiolocation system based on the principle of the harmonic RADAR described in chapter 3. In chapter 4, the characterization of unconventional dielectric materials, such as fabrics, paper, plastic and organic materials, was studied in depth, with the aim of being able to use them in the design and construction of low cost and low environmental impact sensors and antennas. In this context, research has been extended to the design and construction of low-cost microwave microfluidic sensors for the characterization of acqueous and liquid solutions in general. This study is reported in chapter 5. Chapter 6 describes the design of a completely passive RFId (Radio Frequency Identification) tag that can be used as a sensor in breaking test activities in the laboratory. Chapter 7 describes a particular Low Noise Amplifier (LNA) that can be used in intelligent receiver systems with reconfigurable beam for 5 GHz Wi-Fi applications.

Bibliography

[1]   H. Ghsyvat, S. Mukhopadhyay, X. Gui, and N. Suryadevara.
        *WSN- and IOT-Based Smart Homes and Their Extension to
        Smart Buildings*, Sensors 2015, 15 (5), pp. 10350-10379, May
        2015.

[2]   X. Li, D. Li, J. Wan, A. V. Vasilakos, C. -F. Lai, and S.
        Wang. *A review of industrial wireless networks in the context
        of Industry 4.0*, Wireless Networks (2017) 23, pp. 23-41, Nov.
        2015.

[3]   M. Ilyas, I. Mahgoub. *Handbook of Sensor Networks: Com-
        pact Wireless and Wired Sensing Systems*, CRC Press, July
        2004.

[4]   K. Ashton. *That 'Internet of Things' Thing*, RFID Journal,
        June 2009. (rfidjournal.com/that-internet-of-things-thing)

[5]   P. Magrassi. *Why a Universal RFID Infrastructure Would
        Be a Good Thing*, Gartner research report G00106518, May
        2002.

[6]   P. Magrassi, T. Berg. *A World of Smart Objects*, Gartner
        research report R-17-2243, Aug. 2002.

[7]   Commission of the European Communities. *Internet of
        Things - An action plan for Europe*, June 2009.

[8]   A. Wood. *The internet of things is revolutionizing our lives,
        but standards are a must*, The Guardian, Mar. 2015.

[9]   C. X. Mavromoustakis, G. Mastrorakis, J. M. Batalla. *In-
        ternet of Things (IoT) in 5G Mobile Technologies*, Springer
        Cham Modeling and Optimization in Science and Technolo-
        gies (MOST) Series, Vol. 8, 2016.

[10]   D. Rodenas-Herraiz, A. -J. Garcia-Sanchez, F. Garcia-Sanchez, and J. Garcia-Haro. *Current Trends in Wireless Mesh Sensor Networks: A review of Competing Approaches*, Sensors 2013, 13 (5), pp. 5958-5995, May 2013.

[11]   K. A. Ali, H. T. Mouftah. *Wireless personal area networks architecture and protocols for multimedia applications*, Ad Hoc Networks, Vol. 9, Issue 4, pp. 675-686, June 2011.

[12]   K. Hasan, K. Biswas, K. Ahmed, N. S. Nafi, M. S. Islam. *A comprehensive review of wireless body area network*, Journal of Network and Computer Applications, Vol. 143, pp. 178-198, Oct. 2019.

[13]   R. A. Kahn, A. -S. K. Pathan. *The state-of-the-art wireless body area sensor networks: A survey*, International Journal of Distributed Sensor Networks, Vol. 14 (4), Apr. 2018.

[14]   S. Movassaghi, M. Abolhasan, J. Lipman, D. Smith, and A. Jamalipour. *Wireless Body Area Networks: A Survey*, IEEE Communications Surveys & Tutorials, Vol. 16, Issue 3, pp. 1658-1686, 2014.

[15]   US Federal Communications Commission (FCC), part 15, Oct. 2003. (http://www.fcc.gov/oct/info/rules)

[16]   F. Sabath, E. L. Mokole, and S. N. Samaddar. *Definition and classification of ultra-wideband signals and devices*, URSI Radio Science Bulletin, Vol. 2005, Issue 313, pp. 12-26, June 2005.

[17]   M. Forouzandeh, and N. C. Karmakar. *Chipless RFID tags and sensors: a review on time-domain techniques*, Wireless Power Transfer, Vol. 2, Special Issue 2 (Chipless Technologies), pp. 62-77, Sep. 2015.

[18]   A. Ephremides. *Energy concerns in wireless networks*, IEEE Mag. Wireless Commun., 9, 48-59, Aug. 2002.

[19]   S. Azam, M. A. K. Khan, T. A. Shaem, and A. Z. Khan. *Graphene based circular patch terahertz antenna using novel substrate*, 2017 6th International Conference on Informatics, Electronics and Vision & 2017 7th International Symposium

in Computational Medical and Health Technology (ICIEV-ISCMHT), Sept. 2017.

[20]   R. Bala, and A. Marwaha. *Investigation of graphene based miniaturized terahertz antenna for novel substrate materials*, Engineering Science and Technology, an International Journal, Vol. 19, Issue 1, pp. 531-537, Mar. 2016.

[21]   R. Dewan, M. K. A. Rahim, M. R. Hamid, M. F. M. Yusoff, N. A. Samsuri, N. A. Murad and K. Kamardin. *Artificial magnetic conductor for various antenna applications: An overview*, International Journal of RF and Microwave Computer-Aided Engineering, vol. 27, no. 6, Aug. 2017.

[22]   B. S. Cook and A. Shamim. *Utilizing Wideband AMC Structures for High-Gain Inkjet-Printed Antennas on Lossy Paper Substrate*, IEEE Antennas and Wireless Propagation Letters, vol. 12, pp. 76-79, Jan. 2013.

[23]   X. Y. Liu, Y. -H. Di, H. Liu, Z. -T. Wu and M. M. Tentzeris. *A Planar Windmill-like Broadband Antenna Equipped with Artificial Magnetic Conductor for Off-Body Communications*, IEEE Antennas and Wireless Propagation Letters, vol. 15, pp. 64-67, May 2015.

[24]   K. R. Chudasama, Anupkumar, V. Ram, and S. Kashyap. *Design of Carbon Nanotubes (CNT) Patch Antenna for WLAN Application*, International Journal of Engineering Research & Technology (IJERT), Vol. 2, Issue 4, Apr. 2013.

[25]   Y. -M. Wu, X. Lv, B. K. Tay, H. Wang. *Carbon nanotube-based printed antenna for conformal applications*, 2013 International Conference on Optoelectronics and Microelectronics (ICOM), Oct. 2013.

[26]   E. A. Bengio, D. Senic, L. W. Taylor, R. J. Headrick, M. King, P. Chen, C. A. Little, J. Ladbury, C. J. Long, C. L. Holloway, A. Babakhani, J. C. Booth, N. D. Orloff, and M. Pasquali. *Carbon nanotube thin film patch antennas for wireless communications*, Applied Physics Letters, Vol. 114, Issue 20, May 2019.

[27]   M. Liang, J. Wu, X. Yu, and H. Xin. *3D printing technology for RF and THz antennas*, 2016 International Symposium on Antennas and Propagation (ISAP), Jan. 2017.

[28]   K. N. Paracha, S. K. A. Rahim, H. T. Chattha, S. S. Al-jaafreh, S. ur Rehman, and Y. Chiong Lo. *Low-Cost Flexible Antenna by Using an Office Printer for Conformal Applications*, Hindawi International Journal of Antennas and Propagation, Vol. 2018, Feb. 2018.

[29]   W. G. Whittow. *3D printing, inkjet printing and embroidery techniques for wearable antennas*, 2016 10th European Conference on Antennas and Propagation (EuCAP), June 2016.

Chapter 2

Reversible Structure Wearable All-Textile UWB Antenna

2.1 Introduction

All-textile Ultra Wide Band (UWB) antennas are becoming more and more attractive for on-body short range communication systems like wearable computing, sensor monitoring, health-care assistance and in general for Wireless Body Area Network (WBAN) applications [1], [2]. Because of the easy integration in clothes they permit to achieve comfortable wearability together with a robust assembly with the electronic circuitries for sensing, communications, wireless power transfer or energy harvesting [3], [4]. On the other hand, wearable antennas suffer from the coupling with the human body which may absorb a large part of the radiated electromagnetic field causing the mismatch of the antenna, reduction of efficiency, alteration of radiation pattern with respect to free space condition in addition to potential health risks in case of exposure for prolonged periods of time. For these reasons, planar shaped antennas are preferred because of the easy collocation on the human body while the use of a ground plane strongly reduces the absorption of energy in the body. Resorting to substrate integrated waveguide (SIW) technology the antennas shown in [3] and [5] achieve intrinsic shielding and stable characteristics in proximity of the human body even though the antennas are not UWB but narrow band or multiband. The class of microstrip-like antennas instead, [6]-[9], provided with full ground plane allows low body-antenna interactions and is good candidate for off-body communications in UWB-WBAN typical topology [1] thanks to its characteristics of directivity and good efficiency. The intrinsic drawback of this class of antennas is the narrow bandwidth since they are based on resonance phenomena. Nevertheless, using suitable

modifications and design shrewdness it is possible to extend the bandwidth to cover the entire FCC[1] band. A first class of design methods consists in modifying the antenna geometry with a number of sub-structures having different resonant frequencies that partially overlap over the whole UWB band. This is the case of [6] where folded parts and slots bring more resonances in the radiating patch while parasitic patches surrounding a shaped active one are used in [7], a shaped multi-slot patch, instead, is proposed in [8]. Another design method concerns the use of a planar monopole combined with a reflector and a ground plane that permit to achieve unidirectional radiation pattern preserving the UWB bandwidth and shielding the human body [9]. The dipole-like family of wearable UWB antennas has the advantage of better yield in terms of time-domain performance [10] (e. g. the group delay and the so called System Fidelity Factor) with respect to multi-resonating antennas because a thick dipole (or monopole) is an intrinsic broadband antenna [11], [12]. Wide bandwidths, if fact, can be achieved with planar monopole antenna topology therefore it is frequently used in UWB communication systems. A recurrent design method is based on a flat monopole having various shapes fed by a microstrip line (very often combined with a partial ground plane [11], [13]-[16]) or a Coplanar Wave (CPW) line, e.g. circular disk [12], tapered triangular [17], tapered slot [18]. An alternative design exploits the 3-D dimensions to develop compact broad band antennas like that based on a 3-D slot-loaded folded dipole shown in [19]. Despite the compact size typical of these antennas they have reasonable radiation performance, are frequently realized using rigid substrate but better integration onto clothing has obtained using flexible substrate [18], [20], [23]. A limitation of flat monopole antennas is the alteration of the radiation diagram and impedance matching when worn, in particular for lying parallel to the surface of the body since in that collocation the antenna strongly feels the interaction of the electromagnetic field with the body. On the other hand, it has been demonstrated in [24] that a properly choice of the radiation pattern and polarization of the transmitting and receiving antennas for the different body locations, permits to optimize the WBAN system performance in terms of transmitted power and bit error rate. For on-body communications, it should be favourable to have the radiation pattern omnidirectional in the plane of the body while the polarization vertical with respect to it. A monopole orthogonal to the body surface with a large ground plane is, evidently, a good candidate for this type of systems. In the case of off-body communications instead, unidirectional antennas are preferable because of the increased directivity while the use of a ground plane limits the losses in the body.

---

[1]FCC: Federal Communication Commition.

An important technique that allow to optimize the quality of the radiation pattern of these type of antennas is based on the application of Frequency Selective Surfaces (FSS) [32]-[36]. These surfaces, once positioned between the radiant part of the planar antenna and its ground plane, behave like Artificial Magnetic Conductor (AMC) allowing significant improvements from the point of view of the gain radiation pattern. In this chapter different techniques are described to obtain a all-textile UWB wearable antennas for WBAN that allows to be reconfigured changing from a monopole-like shape to a microstrip-like shape. The change of configuration is simply obtained by raising and lowering a textile flap that contains the main radiating part of the antenna. It behaves like a monopole when arranged orthogonally to the ground plane and like a microstrip patch when placed parallel to the ground. In both configurations the antenna preserves the UWB bandwidth while the radiation pattern changes according to the specific shape: omnidirectional and unidirectional in case of monopole and microstrip configuration, respectively. The proposed type of reconfigurable antenna has been conceived to be used with a device that can switch between a tag mode and sensor mode. In tag mode, the flapping monopole acts as a UWB tag for localization and tracking of personnel, being omnidirectional. In sensor mode, the microstrip-like topology is a part of the air interface of wearable active and passive health sensors that exchange data with an interrogator, away from the body, under the user control.

2.2 Bow-tie Shaped Ground Plane Matching Surface

2.2.1 Antenna Structure and Materials

The antenna is composed of four layers, a schema of the stratigraphy is shown in Fig. 2.2.1. From top to bottom, the first layer is made of conductive fabric, it consists of a CPW line that feeds a circular disk attached over a flapping layer. The flapping part can be rotated around a textile hinge orthogonal to the CPW line in order to accomplish both the monopole and microstrip topology. A part of the ground plane is removed to house the flap when it lays down parallel to the ground in the microstrip topology. The second layer is made of a textile fabric having thickness h_u, that layer hosts on the bottom face a reflector made of conductive fabric and connected to the ground of the CPW line. The reflector has the main function of matching the antenna's impedance in the microstrip topology nevertheless it affects also the radiation pattern as will be shown later on. The third layer is made
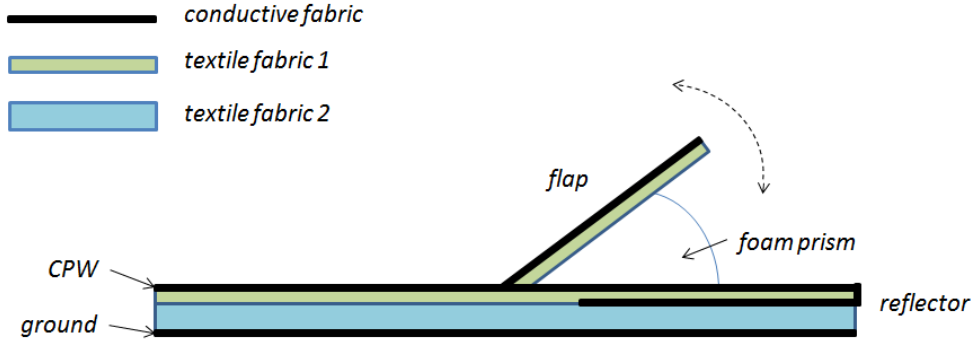
Figure 2.2.1: Schema of the side view of the antenna.

of textile fabric with thickness h_d while the last layer is a reflecting ground made of conductive fabric.

The drawing of the antenna functioning as a monopole is shown in Fig. 2.2.2 a), while the microstrip-like configuration is shown in Fig. 2.2.2 b). Table 2.1 reports the corresponding dimensions in millimeters.

The used conductive textile material is the ShieldIt Super that has surface resistivity < 0.07 Ohm/sq and is 0.17 mm thick [25]. Different textile fabric can be used for the two dielectric layers, we have designed and experimented two different setups: the first uses denim for the first layer and felt for the second one; the other setup, instead, uses denim for both layers. Simulation and experimental measurements have shown similar results in terms of bandwidth and radiation patterns once the thickness and the antenna's dimensions have been optimized. Nevertheless, the use of felt makes the antenna more prone to deformations and mechanical instability (e.g. disjunction of connector) because the felt is softer than denim so that we prefer to use the second setup and we refer to it from now on. The dielectric properties of the used denim are extrapolated using the ring resonator technique described in Chapter 4: its dielectric constant and loss tangent values are, respectively, 1.43 and 0.036, measured at 5 GHz. For the first layer we used a denim fabric having thickness 0.6 mm, the thickness of the fourth layer (h_d), instead, is a parameter to be optimized since it affects the behavior of the antenna, in particular the gain.

To realize the optimized thickness more fabrics have been sewn on top of each other. The flapping part that allows the change from one topology to the other has been made with denim fabric 0.6 mm thick and with a small prism of very light foam. The prism of foam has dielectric constant very near to one and serves to support the flap in the upright position. It acts, in fact, as a spring that is compressed with thin thickness in case of microstrip-like
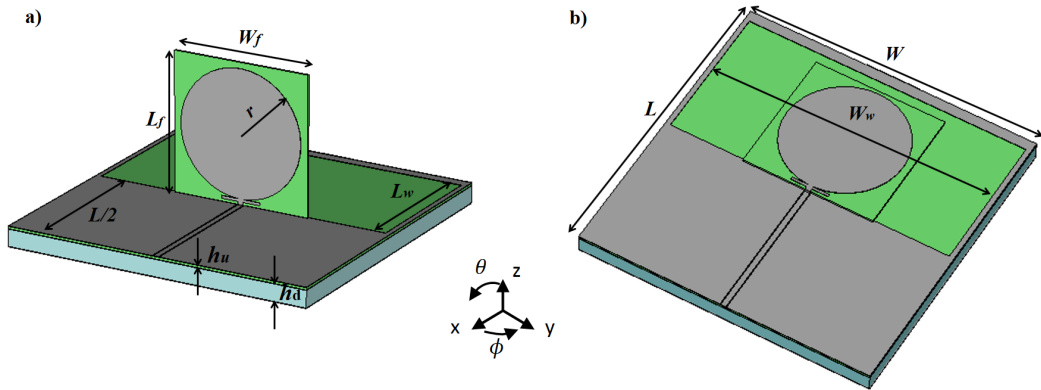
20

Figure 2.2.2: Antenna's drawings: a) monopole configuration; b) microstrip-like configuration.

configuration instead it splays and supports in an almost orthogonal position the flap in case of monopole configuration.

2.2.2 Antenna Design

The design of the antenna has been performed subdividing the task into two almost independent parts: one for monopole topology and one for microstrip topology. In fact, the design of microstrip topology is subsequent to that of the monopole that remains invariant apart from the lying. The electromagnetic analysis has been performed with Ansys HFFS [27] while the optimization of the design of the structures of the antenna has been performed with the genetic algorithm.

2.2.2.1 Monopole Topology

A circular disk orthogonal to a ground plane is an intrinsic broadband radiating structure. When it is CPW-fed the main parameters to optimize the bandwidth are the radius r of the disk that limits the lower frequency of the band, the gap g from the ground plane that has most effects at higher frequencies and the width of the ground plane W. Since the increasing of the size of ground plane gives negligible effects on the monopole behavior after a certain size while it is an important design parameter for the microstrip topology we do not consider it as a design parameter of the monopole and assume it is large enough to not affect the monopole behaviour. The dimension W is determined in the design phase of the microstrip topology making a check of the behavior of the monopole a-posteriori. Since the fabric in the

21

nearness of the hinge of the flap is subjected to bulge when the flap commutates between monopole and microstrip configurations, the gap g might be slightly variable. As a consequence, the bandwidth may become unstable changing every time the flap moves. To avoid that drawback, we introduce in the design of the monopole a couple of thin strips connected orthogonally to the feed line and placed at the intersection point between the disk and the coplanar line. That structure makes the impedance matching of the monopole insensitive to possible variations of the gap but introduces an upper limit to the bandwidth. The length L_s of the strips is the main design parameter that determine the upper frequency, Fig. 2.2.3 shows the details of the structure. The impedance matching of the monopole is independent from the shape and extension of the ground plane opposite to the driven line, i.e. the part of ground plane without the CPW line in Fig. 2.2.2 a). For that reason, the part of the ground plane behind the monopole is free to be modified and can host the microstrip part of the antenna. Nevertheless, the radiating characteristics instead feel the absence of that part of ground plane mainly at lower frequencies, so a floating ground plane is introduced at the bottom side of fourth layer in order to compensate for the lack of that part of CPW ground and to improve the shielding of the body from the electromagnetic field. Table 2.1 shows the optimized values (mm) of the main design parameters in order to achieve the UWB bandwidth.

W	L	W_w	L_w	W_f	L_f	r	h_u	h_d
90	90	87	42	40	40	18.3	0.6	4.8

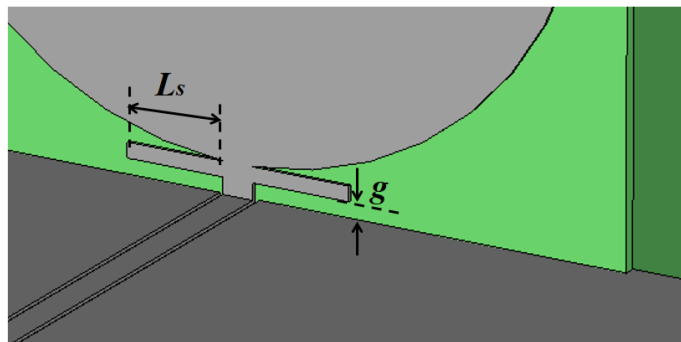Table 2.1: Optimized geometrical values of proposed antenna parts.

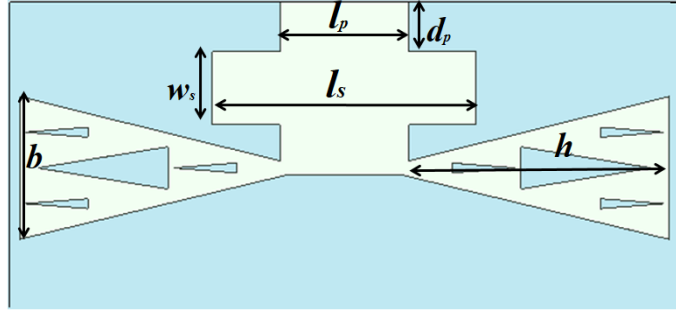Figure 2.2.3: Geometric details of monopole disk.

Figure 2.2.4: Geometric details of shaped reflector.

2.2.2.2 Microstrip Topology

When the denim flap, that contains the radiator disk, is put parallel to the substrate over the CPW ground plane, the input impedance mismatches at some frequency sub-bands. To obtain the UWB bandwidth without changing the geometry of the monopole, the coplanar ground plane has been narrowed along the sides of the substrate in the part opposite to the driven line (Fig. 2.2.2 b)), extended to the back of the top substrate and connected to a shaped reflector that behaves like a broad band matching structure (Fig. 2.2.1). The reflecting structure is placed at the interface between the two textile substrates that have suitable thickness. The thickness (h_u) of the first substrate is kept constant while the thickness of the second substrate (h_d) has been optimized in order to increase the gain of the antenna in that topology.

The geometry of reflector is shown in Fig. 2.2.4, it consists of a main part having the shape of two opposite triangles (like a bowtie) that are connected together by means of a broad line. The line has two large strips orthogonal to its axis and is connected to the coplanar ground plane. The main design parameters that permit the UWB impedance matching are the lengths of the height h and base b of the triangles, the width w_s and length l_s of the strips, the position d_p, of the strips and the length l_p of the line. The dimensions of these parameters have been obtained by means of an optimization having the objective to enlarge as much as possible the bandwidth. That shaping of the reflector permits to achieve a UWB bandwidth apart from some frequencies where the reflection coefficient exceeds the -10 dB threshold. To flat the exceeding parts we punch each triangle with four scaled triangular slots that form a Sierpinsky-like structure. The dimensions of the slots have been obtained after an optimization aimed to flat the reflection coefficient.
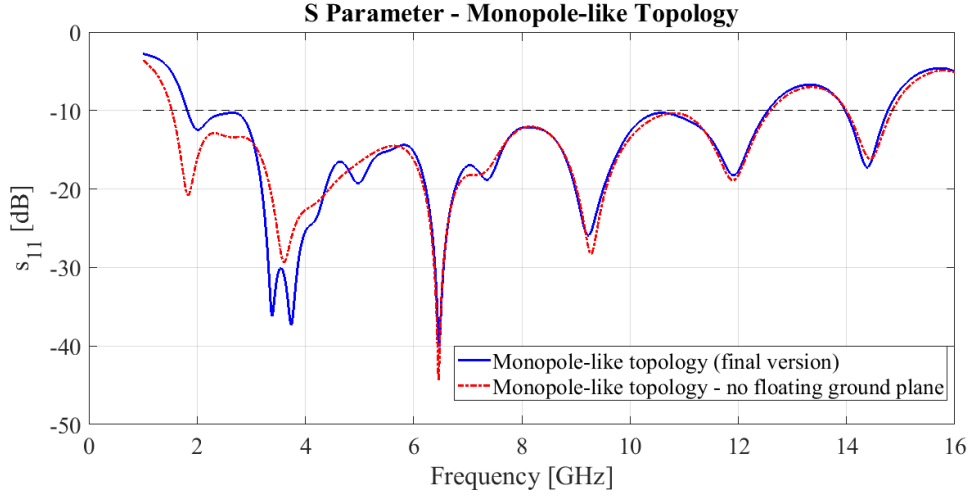
S Parameter - Monopole-like Topology

Figure 2.2.5: Reflection coefficient of the monopole-like antenna: comparison between the final version of the antenna, and the final version of the antenna without floating ground plane.

g	L_s	h	b	w_s	l_s	d_p	l_p
0.9	5	34	18.6	9.5	34.3	6.4	16.8

Table 2.2: Other optimized geometrical values of proposed antenna parts.

2.2.3   Numerical Results

The optimization of the antenna model and the analysis of its behavior in each topology has been performed in free-space, while an a-posteriori check has been performed to test the antenna on body. For on-body simulations we used an equivalent homogeneous body model [30], [31] having volume $130 \times 120 \times 44$ mm³ and simulating a muscle tissue with relative dielectric constant 50 and conductivity 3 S/m. For both topologies, the antenna is centered above the tissue model at a distance of 10 mm that approximates the presence of clothes on the body. Because of the ground plane, simulation results show the antenna is insensitive to the body so that the behavior in terms of reflection coefficient and radiation pattern do not change significantly with or without the body. Since the design of the monopole topology does not require particular efforts we report the obtained results in terms of reflection coefficient and radiation pattern without the description of the evolution of the design. The microstrip-like topology instead requires more design steps and electromagnetic shrewdness therefore we report intermediate results in order to give an in depth description of the evolution of the
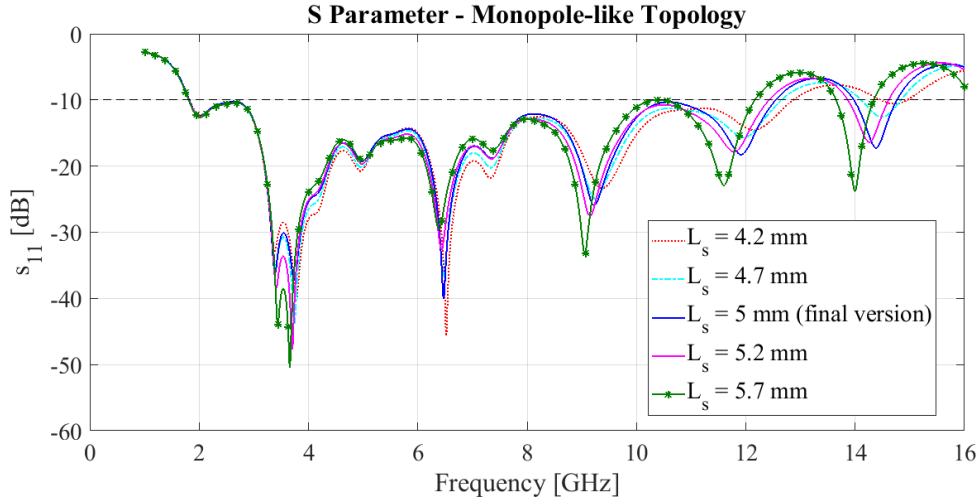
24

Figure 2.2.6: Reflection coefficient of the monopole topology for different lengths of the strips.

design.

2.2.3.1 Reflection Coefficient

The reflection coefficient of the monopole antenna is shown in Fig. 2.2.5, practically, it is insensitive to the floating ground plane. Fig. 2.2.6 shows the reflection coefficient for different lengths (L_s) of the strips placed near the radiating disk. The upper limit of the frequency band is sensitive to the length of the strips, in particular it decreases increasing the length of the strips. For the selected length we obtain an UWB impedance matching larger than the FCC regulations: from 1.82 GHz to 12.55 GHz.

The steps of the design procedure of the microstrip-like antenna are shown in Fig. 2.2.7. The first step (Fig. 2.2.7 a) considers the radiating disk, designed for the monopole topology, is lying over the denim substrate inside a rectangular aperture of the coplanar ground that forms a frame along the sides of the substrate. The corresponding reflection coefficient shown in Fig. 2.2.8 (dotted line) shows two useful bands: one around 4 GHz and the other from about 6 to 10 GHz. The second step introduces inside the aperture and in the bottom side of the substrate a reflector having the shape of a bowtie (Fig. 2.2.7 b). Several alternative shapes have been simulated obtaining a reflection coefficient worse than that the case without the reflector (first step). Instead, the bowtie shaped reflector permits to improve the matching even though the reflection coefficient is larger than the threshold -10 dB over some narrow sub-bands (dashed dot line in Fig. 2.2.8). The third step introduces
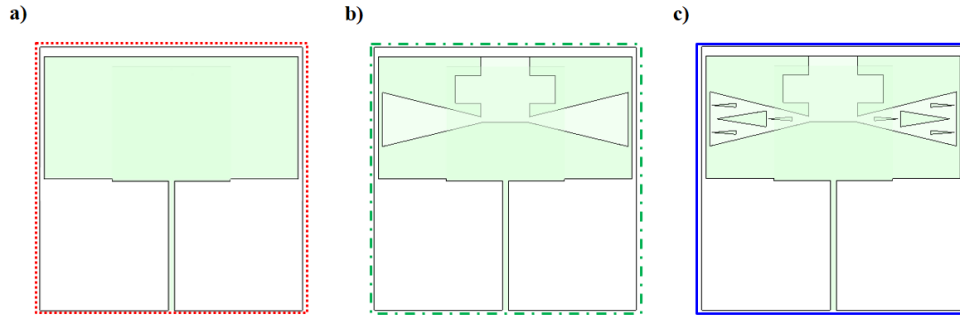
25

Figure 2.2.7: Design steps of the microstrip-like antenna (radiating disk hidden): a) the radiating disk lies over a rectangular aperture of the CPW ground; b) shaped reflector connected to ground; c) final structure with punched reflector.
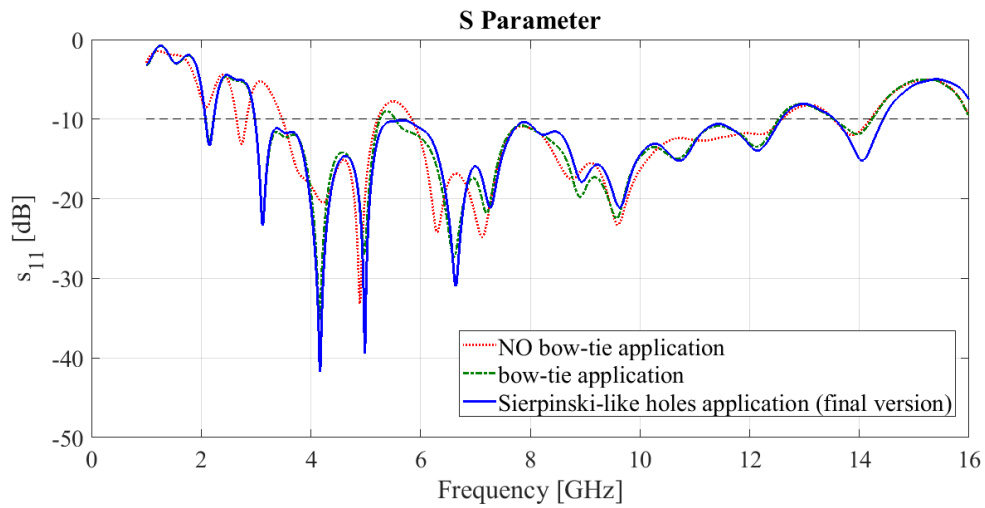

Figure 2.2.8: Evolution of the reflection coefficient of the microstrip-like antenna for the design steps shown in Fig. 2.2.7.
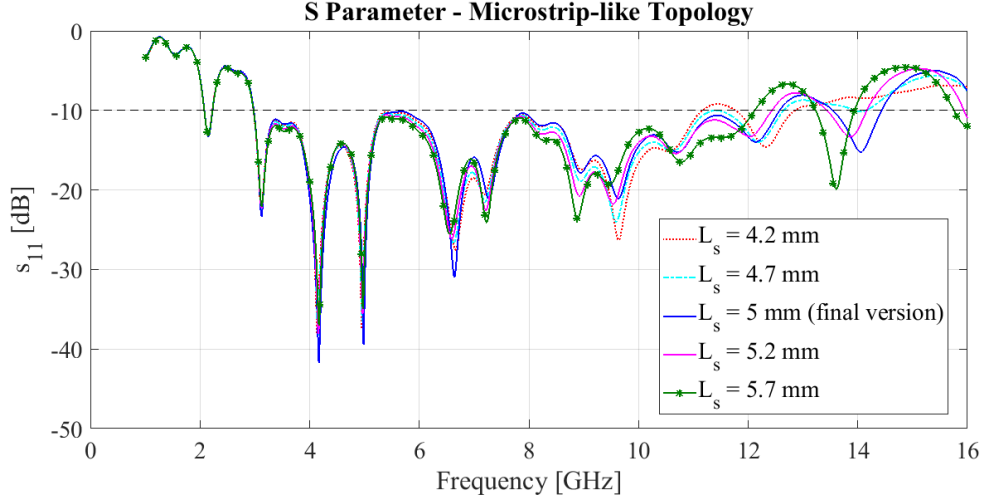
Figure 2.2.9: Reflection coefficient of the microstrip-like antenna for different lengths of the strips near the radiating disk.

a set of slots punched on the reflector, the effect of the slots permits to match the antenna over the full band from 2.98 GHz to 12.57 GHz. Finally, the variation of the reflection coefficient because of the change of the length of the strips (L_s) on the radiating disk is shown in Fig. 2.2.9, similar to the monopole topology the increasing of the length of the strips makes the upper frequency of the band smaller.

2.2.3.2 Radiation Pattern

The 3D gain patterns of the optimized monopole and microstrip-like topologies together with the corresponding current density over the main radiator are shown in Fig. 2.2.10 and Fig. 2.2.11, respectively.

The gain patterns on (z-x) plane (i.e.$\phi = 0°$) of the optimized antennas are shown in Fig. 2.2.12 for the monopole (left) microstrip (right) topologies, at three different frequencies (4.2 GHz, 6.6 GHz, 9.6 GHz). The monopole patterns are almost omnidirectional at lower frequencies while the microstrip-like patterns show higher gain values at slant directions. Fig. 2.2.13 (left) and (right) shows the gain patterns on a plane parallel to (z-y) (i.e. $\phi = 130°$) for monopole (left) and microstrip–like (right) topologies, respectively. Fig. 2.2.14 shows the variation of the maximum gain vs. frequency, it oscillates between 2 dB and 6 dB in case of monopole (up) and between 2 dB and 8 dB for the microstrip (down) topologies.

For microstrip-like topology the main component contributing to the total gain is the θ component a part from three narrow sub-bands near 4 GHz, 6.3
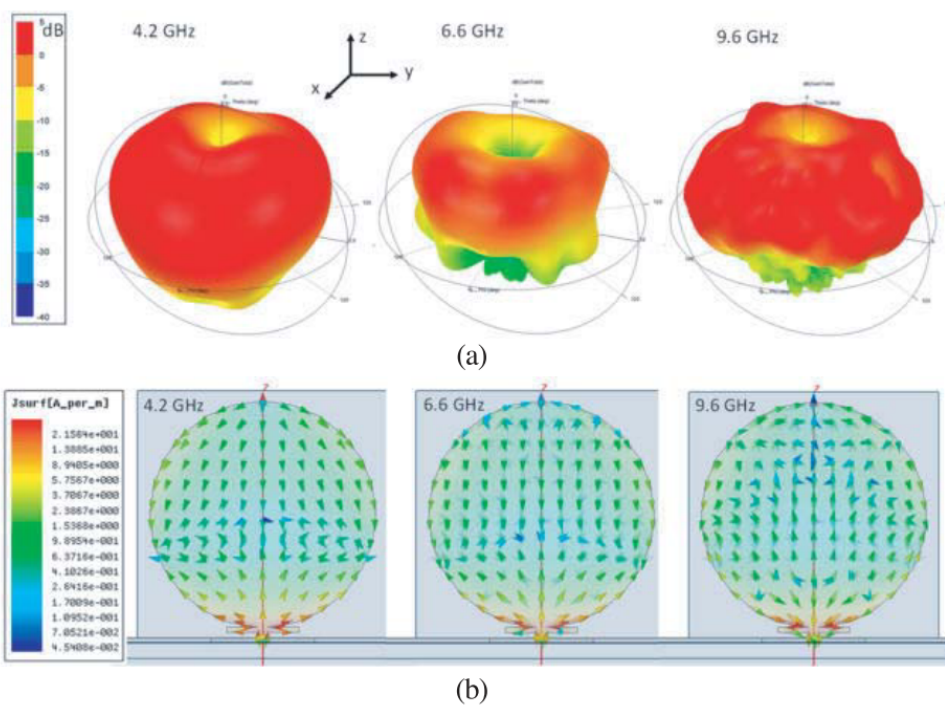
Figure 2.2.10: a) 3-D gain patterns and b) corresponding current distribution for monopole topology at three different frequencies.
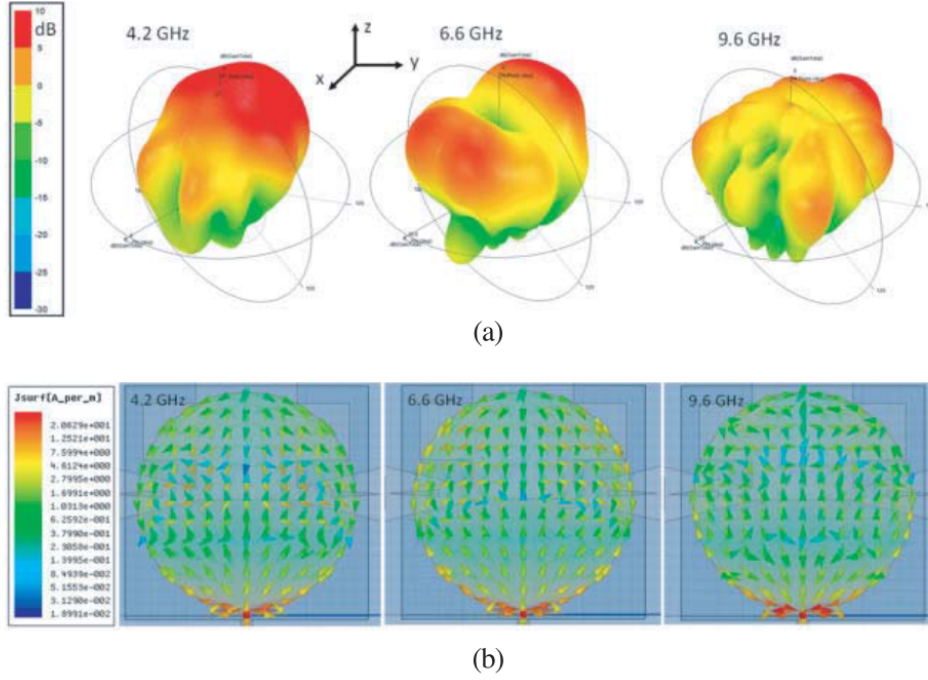
Figure 2.2.11: a) 3-D gain patterns and b) corresponding current distribution for microstrip-like topology at three different frequencies.

GHz and 7.8 GHz. This means that single polarization across the most part of UWB band is obtained. In monopole-like topology, instead, both θ and ϕ components of the gain contribute to the total gain apart from four narrow sub-bands where the θ component is dominant. The effect of the thickness of the substrates has been analysed and shown in Fig. 2.2.15 – Fig. 2.2.18. It is possible to observe that only the thickness of the second substrate has an important effect on the gain of microstrip topology especially at lower frequencies (Fig. 2.2.15). The thickness of $h_d = 4.8$ mm has been chosen because it gives a good trade-off between low and high frequencies.

2.2.3.3 System Fidelity Factor Analysis

In order to estimate the goodness of the designed antennas we simulate the System Fidelity Factor (SFF) in agreement with the procedure [10] that defines the normalized cross-correlation between a transmitted UWB pulse $\hat{T}_s(t)$ and its received version $\hat{R}_s(t+\tau)$:

$$0 \leq SFF = max \int_{-\infty}^{\infty} \hat{T}_s(t)\,\hat{R}_s(t+\tau)\,dt \leq 1 \qquad (2.2.1)$$

a) **Gain pattern (Phi = 90°) - Monopole Topology**   **b)** **Gain pattern (Phi = 90°) - Microstrip-like Topology**
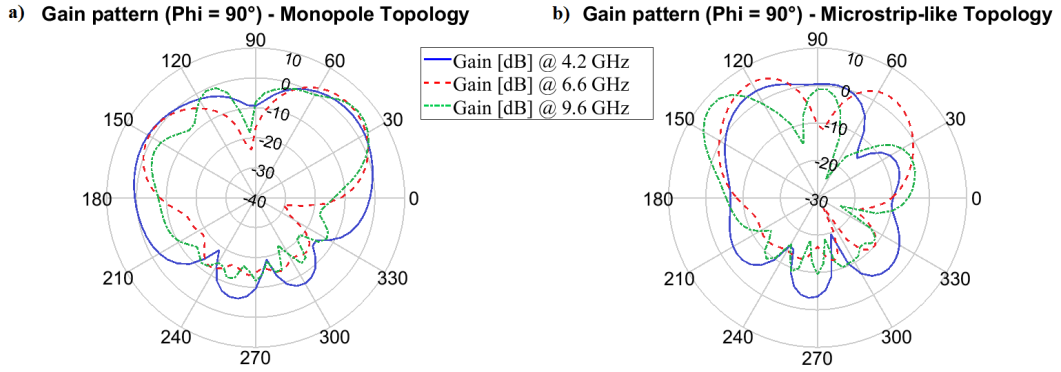
Figure 2.2.12: Zenithal cut of the gain radiation pattern of the monopole-like topology a), and microstrip-like topology b) at 4.2 GHz, 6.6 GHz, and 9.6 GHz.

a) Gain pattern (Theta = 40°) - Monopole Topology   **b) Gain pattern (Theta = 130°) - Microstrip-like Topology**
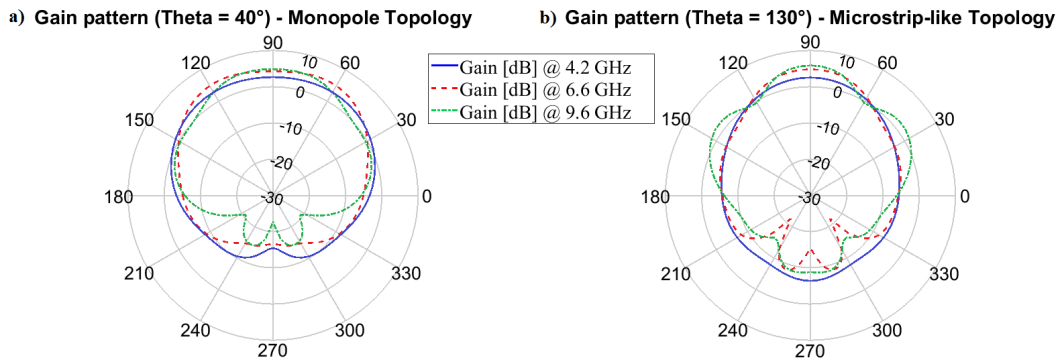
Figure 2.2.13: Azimuthal cut of the gain radiation pattern of the monopole-like topology a), and microstrip-like topology b) at 4.2 GHz, 6.6 GHz, and 9.6 GHz.
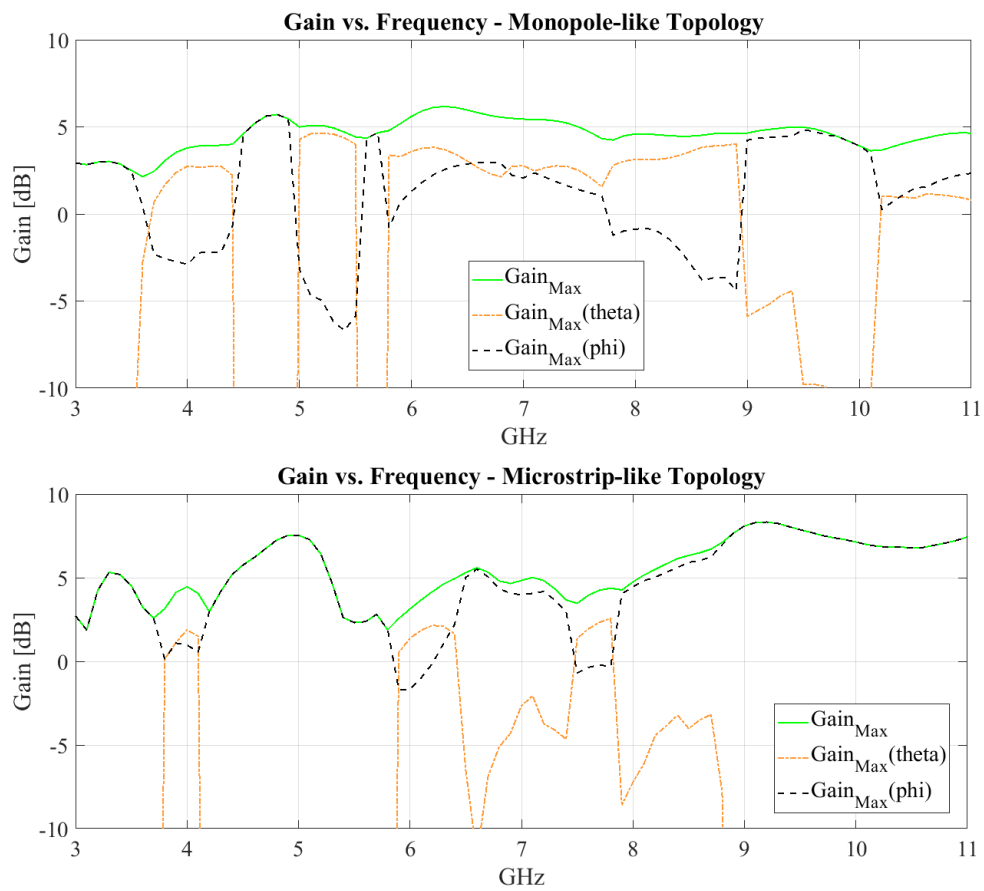
Figure 2.2.14: Maximum gain vs. frequency for monopole (up) and microstrip (down) topologies. Continuous green line total gain; black dash-dotted and orange continuous lines ϕ and θ components, respectively.
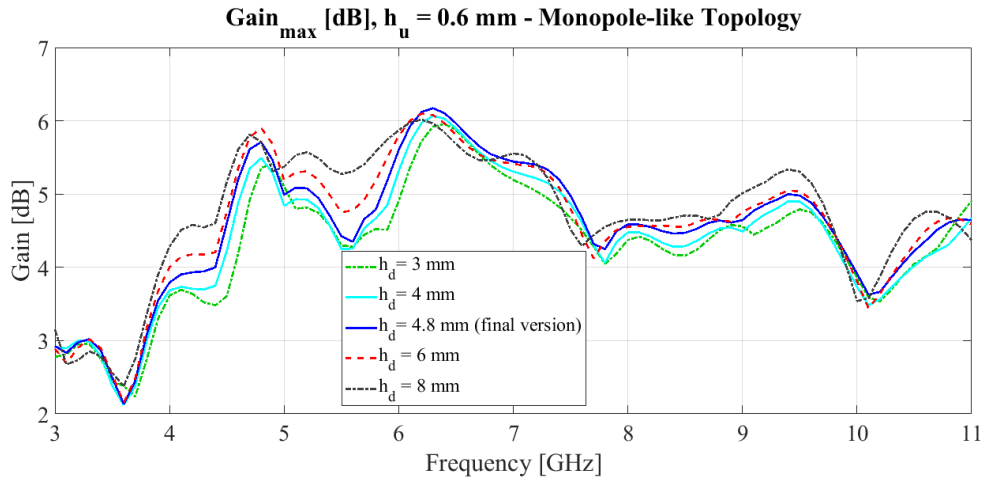
Figure 2.2.15: Maximum gain vs. frequency in case of monopole topology for different thickness of second substrate.
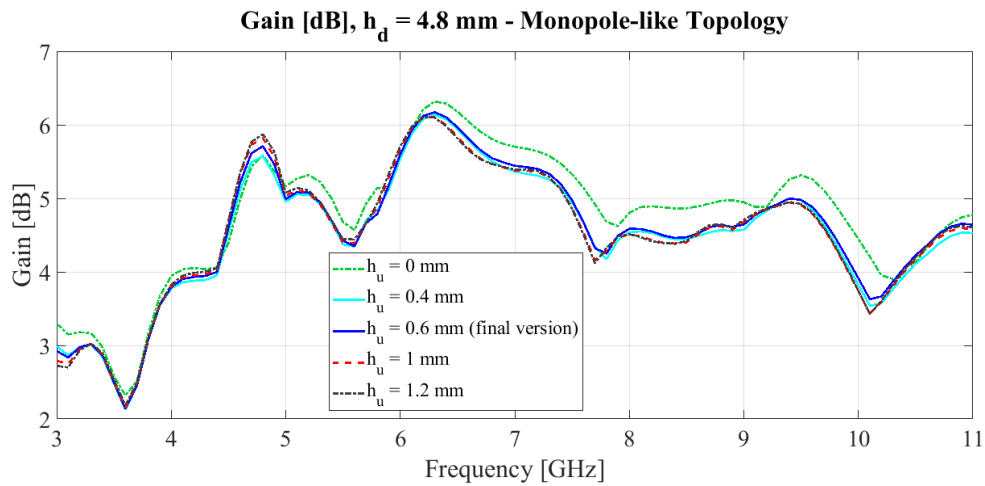
Figure 2.2.16: Maximum gain vs. frequency in case of monopole topology for different thickness of first substrate.
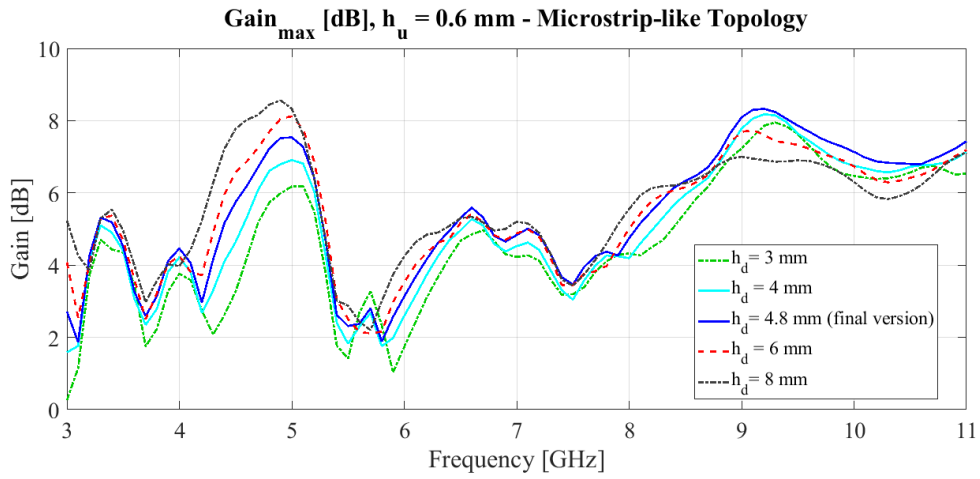
Figure 2.2.17: Maximum gain vs. frequency in case of microstrip-like topology for different thickness of second substrate.
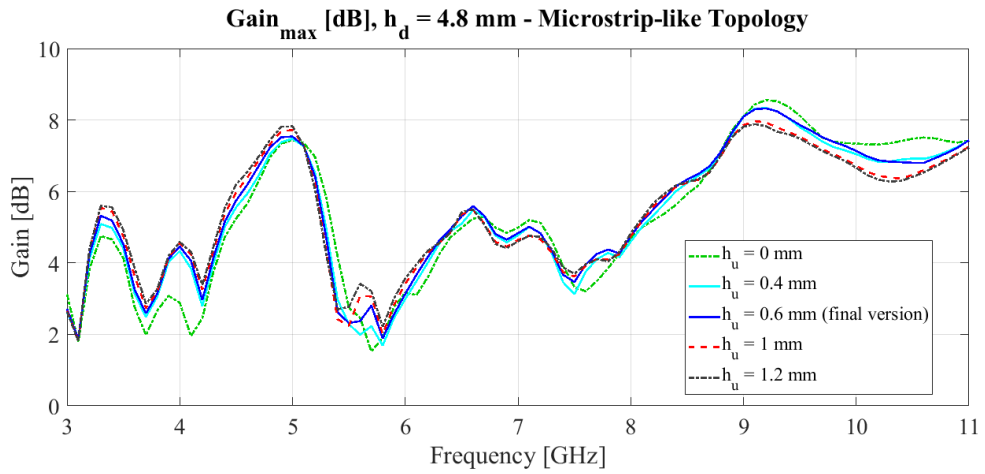
Figure 2.2.18: Maximum gain vs. frequency in case of microstrip-like topology for different thickness of the first substrate.
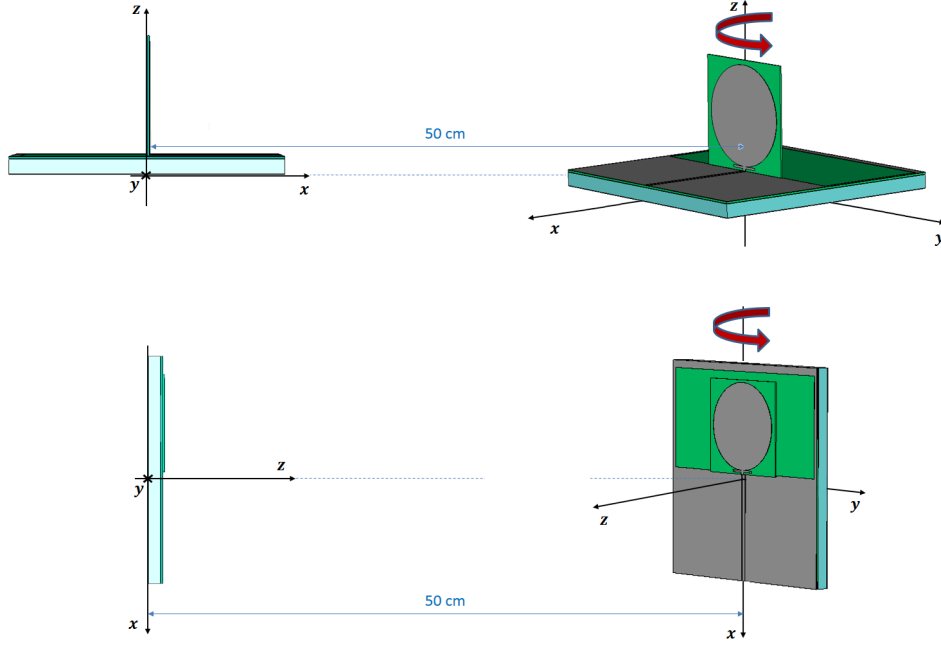
Figure 2.2.19: System Fidelity Factor scenario for the proposed antenna in monopole-like topology, and in microstrip-like topology.

The SFF value strongly depends on the system transfer function $H(\omega)$, defined as:

$$H(\omega) = H_{Tx} H_{CH} H_{Rx} \qquad (2.2.2)$$

where H_{Tx}, H_{CH}, and H_{Rx} are respectively the transmitting antenna transfer function, the channel transfer function, and the receiving antenna transfer function. The used SFF scenario consists of two equal antennas (i.e. same topology) placed at a distance of 0.5 m, one is stationary while the other is rotating around the axis orthogonal to the direction of maximum radiation. In Fig. 2.2.19 a typical SSF scenario is depicted.

As shown in Fig. 2.2.12, when the antenna is configured as a monopole, the maximum of gain radiation pattern does not occur for an elevation angle equal to $\theta = 0°$, but it occur for an elevation angle equal to $\theta = 40°$. In Fig. 2.2.20 SFF scenario for monopole antennas in maximum of gain position is depicted.

A sine-modulated Gaussian pulse is transmitted from the stationary antenna

$$T_s(t) = e^{-((t+a\cdot\tau)/\tau)^2} \cdot sin(2\pi f_r \cdot (t + a \cdot \tau)) \qquad (2.2.3)$$
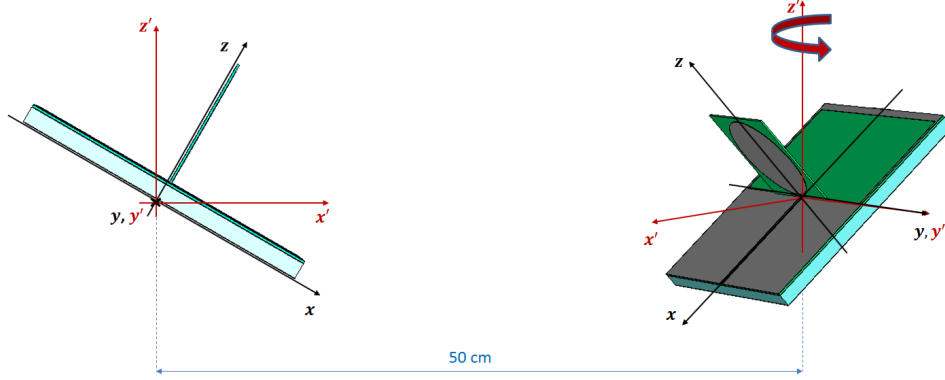
Figure 2.2.20: System Fidelity Factor scenario for the proposed antenna in monopole-like topology, in maximum of gain radiation pattern position.

with $\tau = 210$ ns, $a = 3$, $f_r = 4.5$ GHz.

The results of this analysis gives the SFF for different angles of rotation, it is shown in Fig. 2.2.22 for both topologies. For the microstrip-like topology the SFF value is between 0.29 (at $\pm 145°$ rotation angle) and 0.69 (at $\pm 55°$ rotation angle), while for the monopole topology the SFF value is between 0.3 (at $\pm 70°$ rotation angle) and 0.58 (at $\pm 110°$ rotation angle).

2.2.4 Measurement Results

The realized prototype antenna has been hand-made, all conductive parts are fixed to the fabric substrates by ironing, while the SMA connector is soldered. A picture of the realized antenna is shown in Fig. 2.2.23. The measurements of the reflection coefficient have been performed with Anritsu MS46122B vector network analyzer.

2.2.4.1 Reflection Coefficient

Reflection coefficient measurements have been performed in a laboratory environment with the antenna placed over a hollow cardboard box and, for on-body measurement, over a phantom, far from scattering objects. The phantom has been realized with a very thin plastic box filled with a solution of distilled water and 0.9% sodium chloride. The reflection coefficient of the antenna alone and on-body together with the corresponding simulated result is shown in Fig. 2.2.24 for monopole topology and Fig. 2.2.25 for microstrip topology.
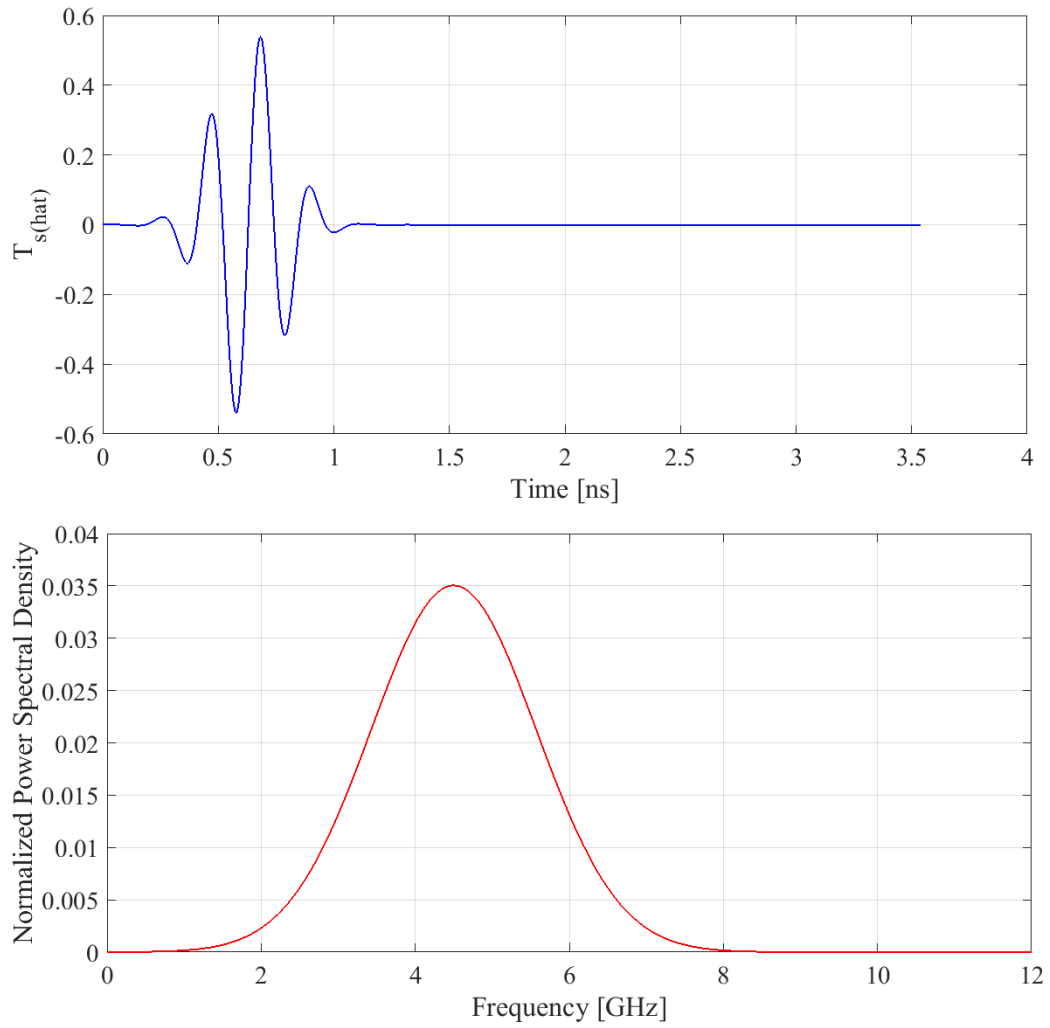
Figure 2.2.21: Sine-modulated Gaussian pulse, and its spectrum.
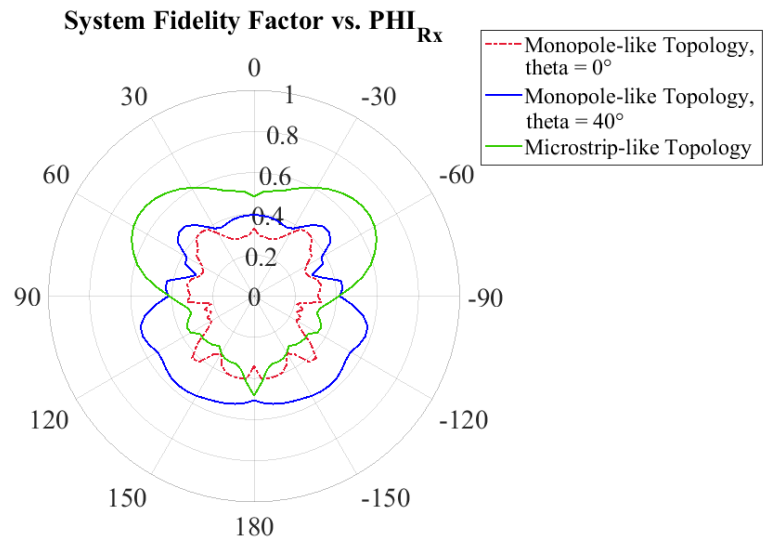
Figure 2.2.22: Simulated System Fidelity Factor results: monopole topology for $\theta = 0°$ (red dashed line), and monopole topology for $\theta = 40°$ (blue continuous line), and microstrip-like topology (green continuous line).
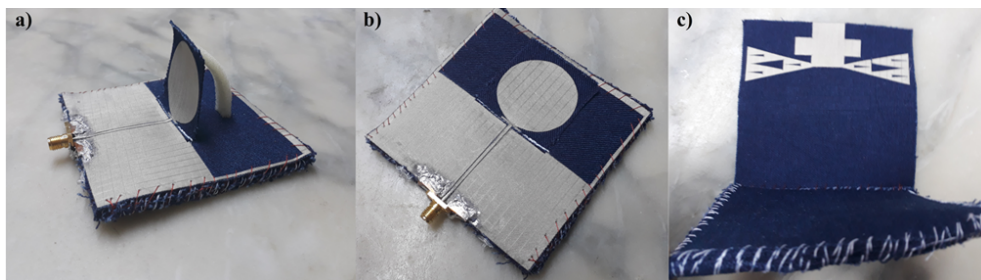
Figure 2.2.23: Realized prototype antenna: a) monopole configuration; b) microstrip configuration; c) underlying shaped reflector.
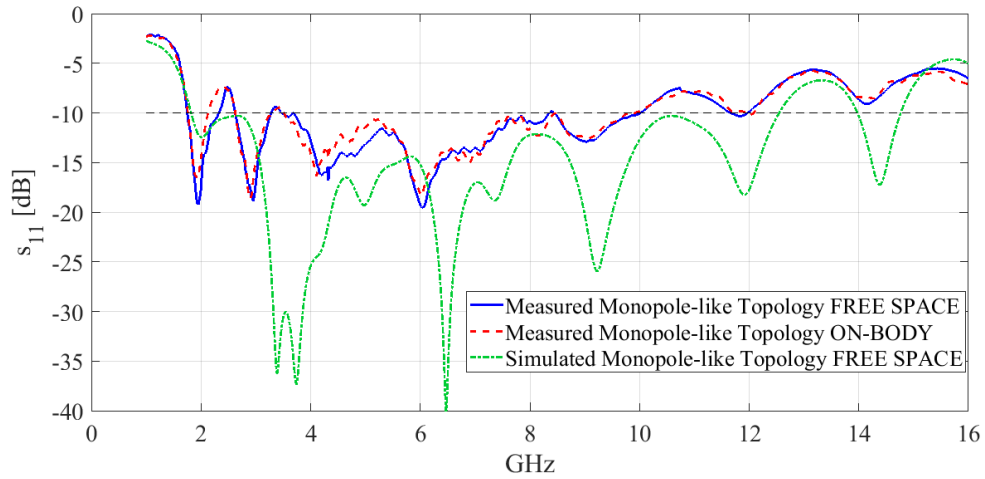
Figure 2.2.24: Measured reflection coefficient of monopole topology for the antenna alone (continuous line), on-body (dashed) and simulated (dash-dotted).
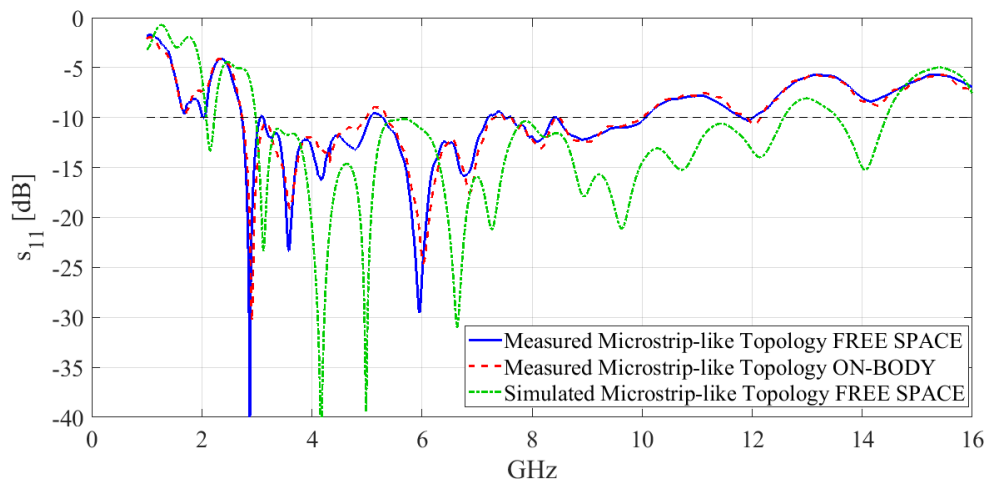
Figure 2.2.25: Measured reflection coefficient of microstrip topology for the antenna alone (continuous line), on-body (dashed) and simulated (dash-dotted).

Figure 2.2.26: On-body measurement set-up for both antenna topologies: a) antenna on an arm; b) antenna on the chest.

The measured reflection coefficient of monopole configuration has a -10 dB bandwidth from 2.62 GHz to 10.1 GHz apart from a slight impedance mismatching near 3 GHz where it is -9 dB for a sub-band of about 30 MHz. The measured bandwidth for microstrip-like topology spans from 2.73 GHz to 10.1 GHz with a slight mismatch for sub-band of about 35 MHz near 5 GHz. For both configurations, negligible differences are visible between the alone and on-body measurements. In comparison with simulated results the measured bandwidths have the upper limit about 1.5 GHz lower than the simulated one. That difference is mainly dependent on the manufacturing inaccuracy of the hand-made prototype: since the reduction of the bandwidth is at higher frequency and have the same value for both configurations it dependents on a part of the antenna common to both configurations. After some checks we have found it is depending on the quality of the soldering of the connector that has main effects at higher frequencies. The behavior of the monopole configuration does not change for slant positions of the flapping part (i.e. the monopole is not exactly orthogonal to the ground plane). Furthermore, the whole behavior of the antenna does not change for moderate bending of its structure.

Fig. 2.2.26 shows the antenna worn on the chest and on an arm where it is moderately bent, and the corresponding reflection coefficients for the two antenna configurations do not change significantly as shown in Fig. 2.2.27 and Fig. 2.2.28.
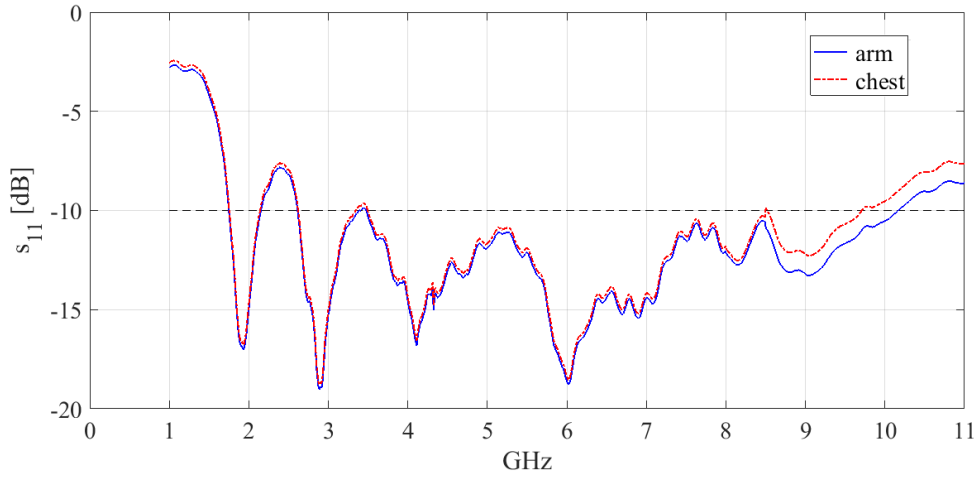
Figure 2.2.27: On-body measured reflection coefficient for monopole topology.
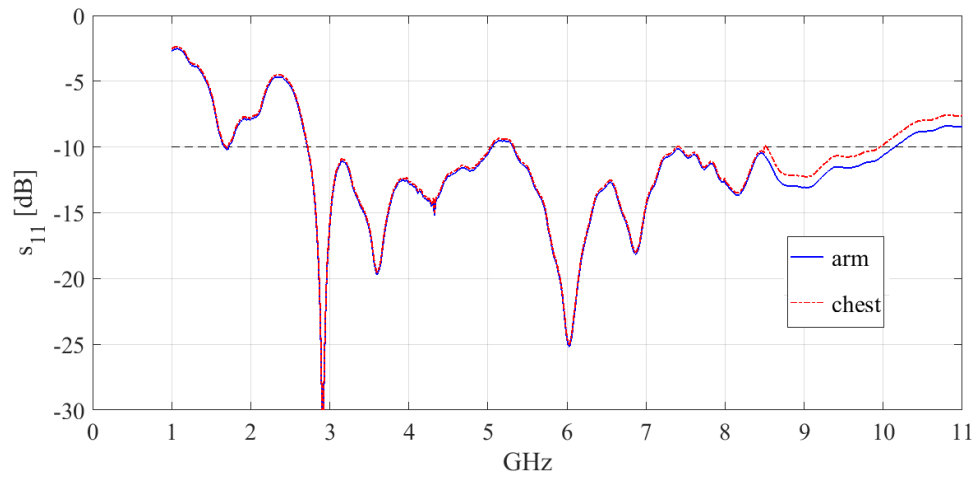
Figure 2.2.28: On-body measured reflection coefficient for microstrip-like topology.

40
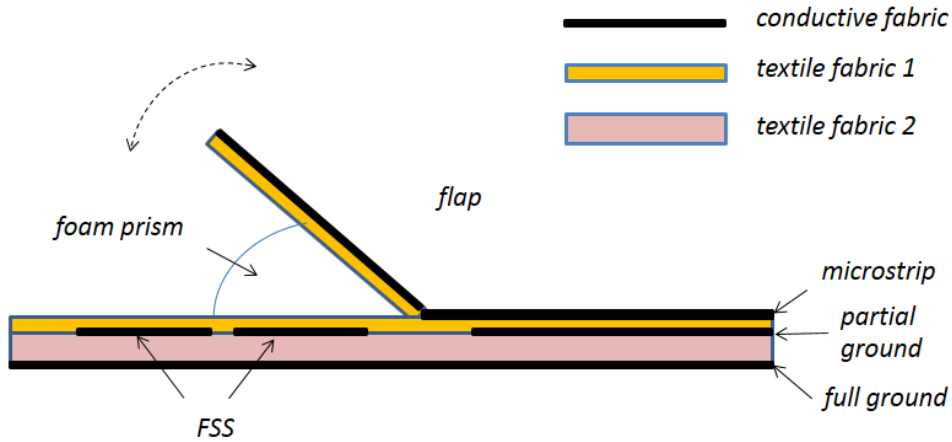
Figure 2.3.1: Schema of the side view of the antenna.

2.3 Artificial Magnetic Conductor Matching Surface

2.3.1 Antenna Structure and Materials

The antenna structure is very similar to the other antenna descripted above. The antenna is composed of five layers, a schema of the stratigraphy is shown in Fig. 2.3.1. From top to bottom, the first layer is made of conductive fabric, it consists of a microstrip line that feeds a circular disk attached over a flapping layer. The flapping part can be rotated around a textile hinge orthogonal to the microstrip line in order to accomplish both the monopole and microstrip topology. The second layer is made of a textile fabric having thickness h_u, that layer hosts on the partial ground plane and on the Frequency Selective Surfaces (FSS) made in conductive fabrics that represent the third layer of the antenna. Unlike what the literature suggests, FSS has the main function of matching the antenna's impedance in a specific sub-band in the microstrip topology rather to improve the gain radiation pattern. The fourth layer is made of textile fabric with thickness h_d while the last layer is a reflecting ground made of conductive fabric. ShieldIt Super conductive textile material (surface resistivity < 0.07 Ohm/sq, thickness of 0.17 mm) [25] was used for ground planes and antenna parts.

The drawing of the antenna functioning in microstrip-like configuration is shown in Fig. 2.3.2 a), while the monopole configuration is shown in Fig. 2.3.2 b). Table 2.3 reports the corresponding dimensions in millimeters. Dielectric properties of denim substrate are the same of the previous antenna

41
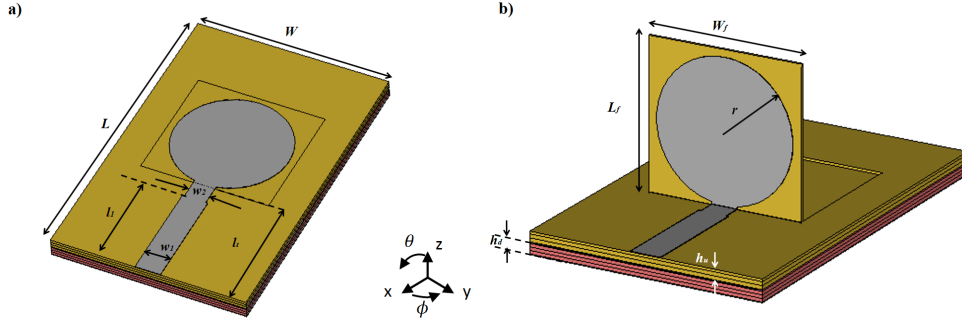
Figure 2.3.2: Antenna's drawings: a) microstrip-like configuration; b) monopole configuration.

(dielectric constant value is 1.43, while its loss tangent value is 0.036 measured at 5 GHz) and are extrapolated using the ring resonator technique descripted in Chapter 4. Exploiting the reduced ground plane technique characteristics [11], [13]-[16], that easily permits to obtain Ultra Wide Band (UWB) response in terms of reflection coefficient, we designed the antenna structure. The global thickness of the structure is an important antenna parameter because has a strong effect on the gain of the antenna. To ensure body shielding from the electromagnetic fields a floating full ground plane was applied in the bottom side of the antenna. The radiator part of the antenna is a disk that is positioned on a 0.6 mm thick flexible mobile part of the substrate in such way that it can acts like a monopole when connected orthogonally to the ground plane and like a microstrip patch when connected parallel to the ground, as seen in the previous antenna design description. For the second layer we used a denim fabric having thickness h_u, while the thickness of the fourth layer is h_d. Both are parameter to be optimized since it affects the behavior of the antenna, in particular the gain.

To realize the optimized thickness more fabrics have been sewn on top of each other. The flapping part that allows the change from one topology to the other has been made with denim fabric 0.6 mm thick and with a small prism of very light foam. The mobile part (flap) was obtained by cutting out a rectangle from the layer placed higher, while the prism of foam has dielectric constant very near to one and serves to support the flap in the upright position. It acts, in fact, as a spring that is compressed with thin thickness in case of microstrip-like configuration instead it splays and supports in an almost orthogonal position the flap in case of monopole configuration.

2.3.2 Antenna Design

The design of the antenna has been performed subdividing the task into two almost independent parts: one for monopole topology and one for microstrip topology. In fact, the design of microstrip topology is subsequent to that of the monopole that remains invariant apart from the lying. The electromagnetic analysis has been performed with Ansys HFFS [27] while the optimization of the design of the structures of the antenna has been performed with the genetic algorithm.

2.3.2.1 Monopole Topology

A circular disk orthogonal to a ground plane is an intrinsic broadband radiating structure. When it is microstrip-fed with partial ground plane on the bottom part of the second layer of the structure, the main parameters to optimize the bandwidth are the radius r of the disk that limits the lower frequency of the band, the gap $l_t - L_{hgp}$ necessary to obtain a wide band impedance matching, and the width of the ground plane W. As described in the previous section, since the increasing of the size of ground plane gives negligible effects on the monopole behavior after a certain size while it is an important design parameter for the microstrip topology, we do not consider it as a design parameter of the monopole and assume it is large enough to not affect the monopole behaviour. The dimension W is determined in the design phase of the microstrip topology making a check of the behavior of the monopole a-posteriori. The impedance matching of the monopole is independent from the application of conductive parts in the area left free by the partial ground plane (Fig. 2.3.2 b)). For that reason, FSS could be applied in this area. Nevertheless, the radiating characteristics instead feel the absence of that part of ground plane mainly at lower frequencies, so a floating ground plane is introduced at the bottom side of fourth layer in order to compensate for the lack of that part of the partial ground and to improve the shielding of the body from the electromagnetic field. Table 2.3 shows the optimized values (mm) of the main design parameters in order to achieve the UWB bandwidth. Table 2.4 shows the optimized values (mm) obtained for the third part of the antenna.

W	L	w_1	w_2	W_f	L_f	r	h_u	h_d	l_l	l_t
57	90	7.4	6.3	38	36	16.8	2.4	2.4	28.8	34.8

Table 2.3: Optimized geometrical values of proposed antenna parts.
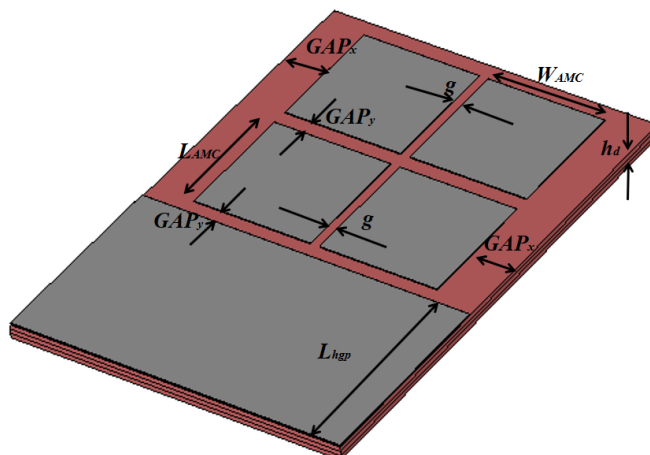
Figure 2.3.3: FSS and partial ground plane view.

GAP_x	GAP_y	g	W_{AMC}	L_{AMC}	L_{hgp}
7.3	2.9	1.6	20.4	22.6	35.9

Table 2.4: Other optimized geometrical values expressed in millimeters.

2.3.3 Microstrip Topology

In this topology, the use of the full ground plane heavily modifies the UWB characteristic of the impedance matching of the antenna. The reflection coefficient presents a wide matched band at higher frequencies while at the lower part of the frequency band it shows a wide mismatch. To remove the impedance mismatching problem a Frequency Selective Surface (FSS) [33] was introduced. In literature [32]-[36], this technique is used especially for radiation diagram improving. In this work FSS was used like an Artificial Magnetic Conductor (AMC) able to introduce a little attenuation in its backscattered reflection coefficient module that allows a good impedance matching in the sub-band of interest. However, this impedance matching property causes a slight deterioration in gain radiation pattern. In the final version of the proposed antenna we introduced four identical rectangular surfaces, properly spaced between them and from the partial ground plane as shown in Fig. 2.3.3. That shaping of the FSS permits to achieve a UWB bandwidth apart from some frequencies where the reflection coefficient exceeds the -10 dB threshold. Differently to the previous antenna, where the thickness (h_u) of the first substrate has been kept constant, in this case is

44

an optimization parameter like the thickness of the second substrate (h_d) in order to increase the gain of the antenna in that topology.

2.3.4 Numerical Results

The optimization of the antenna model and the analysis of its behavior in each topology has been performed in free-space, while an a-posteriori check has been performed to test the antenna on body. For on-body simulations we used an equivalent homogeneous body model [30], [31] having volume 130×120×44 mm³ and simulating a muscle tissue with relative dielectric constant 50 and conductivity 3 S/m. For both topologies, the antenna is centered above the tissue model at a distance of 10 mm that approximates the presence of clothes on the body. Because of the ground plane, simulation results show the antenna is insensitive to the body so that the behavior in terms of reflection coefficient and radiation pattern do not change significantly with or without the body. Since the design of the monopole topology does not require particular efforts we report the obtained results in terms of reflection coefficient and radiation pattern without the description of the evolution of the design. The microstrip-like topology instead requires more design steps and electromagnetic shrewdness therefore we report intermediate results in order to give an in depth description of the evolution of the design.

2.3.4.1 Reflection Coefficient

The reflection coefficient of the monopole antenna is shown in Fig. 2.3.4, practically, it is insensitive to the floating ground plane.

Figure 2.3.5 shows microstrip-like topology reflection coefficient when the FSS is not applied on the antenna structure. As it is possible to see, the antenna in this topology presents a good impedance matching from 2.94 GHz to 3.36 GHz in the first sub-band, from 4.17 GHz to 4.71 GHz in the second sub-band, and from 5.04 GHz to 14.98 GHz in the third sub-band.

This reflection coefficient trend was obtained by the optimization of the shape of the feeding microstrip line. In Fig. 2.3.6, and in Fig. 2.3.7, are depicted the effect introduced by the variation of w_2 and l_l parameters, respectively, on the global matching of the antenna in monopole topology and microstrip topology.

To obtain an FCC compliant UWB response it is necessary to improve the impedance matching of the antenna in the lower part of the reflection coefficient trend (from 2.94 GHz to 5.04 GHz). The idea is to use FSS as an absorber surface, between the disk and the floating full ground plane, in
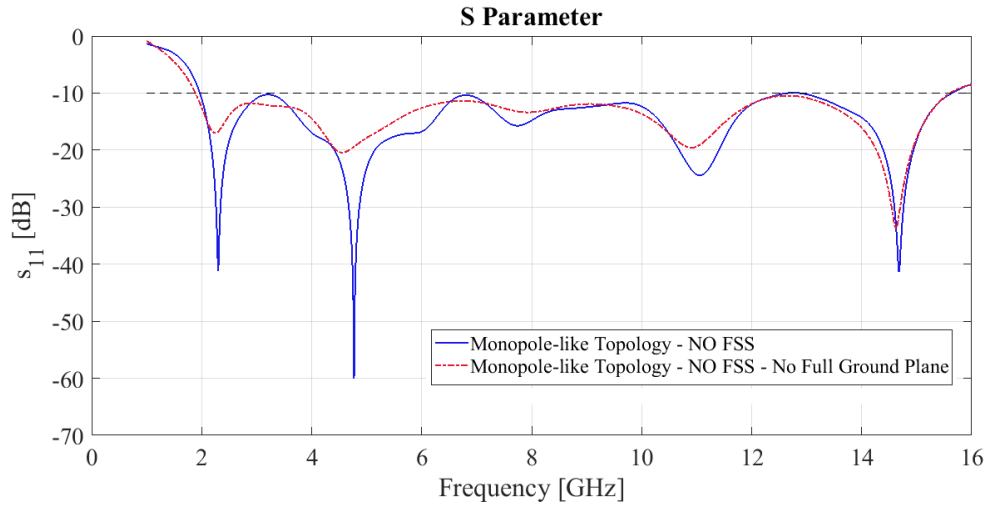
Figure 2.3.4: Reflection coefficient of the monopole-like antenna comparison between the version of the antenna with floating full ground plane, and the version of the antenna without floating ground plane. In both cases FSS are not present in the antenna structure.
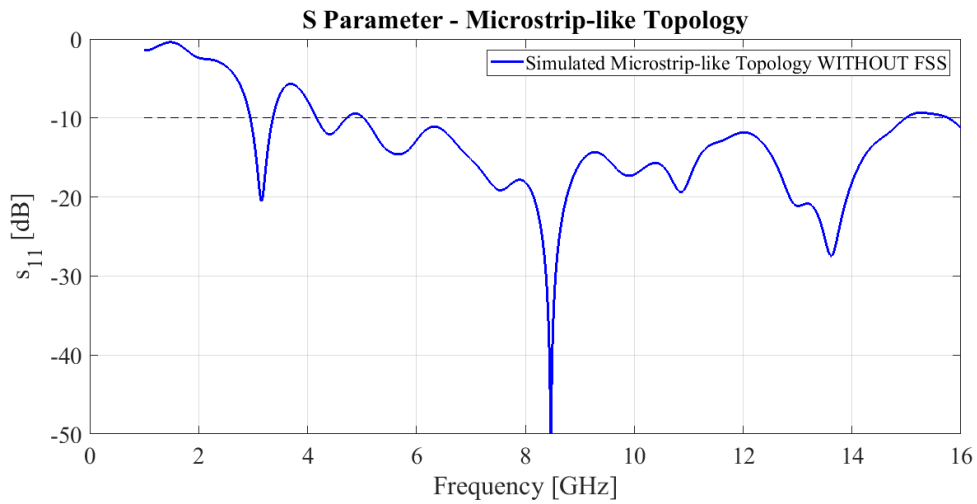
Figure 2.3.5: Reflection coefficient of the antenna in microstrip topology in absence of FSS.
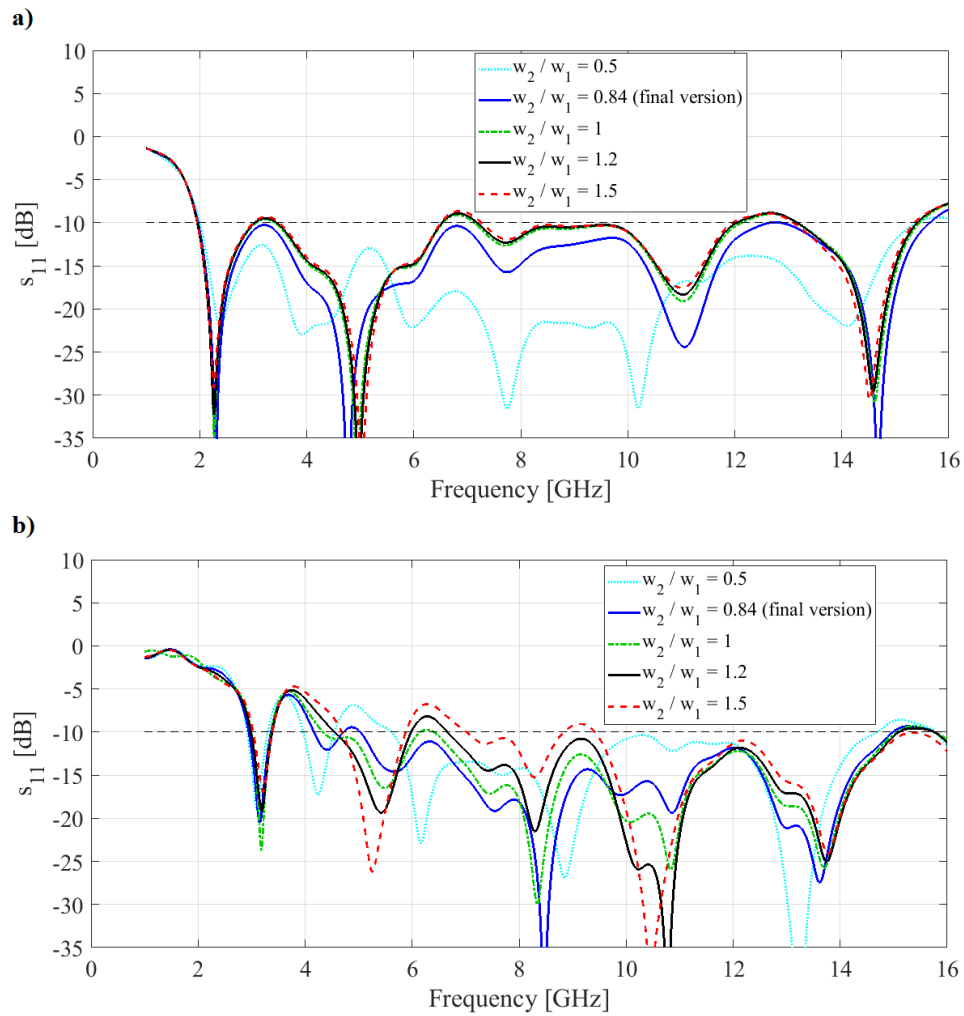
Figure 2.3.6: Reflection coefficient trends at varying of w_2 parameter: a) Monopole-like topology; b) Microstrip-like topology.
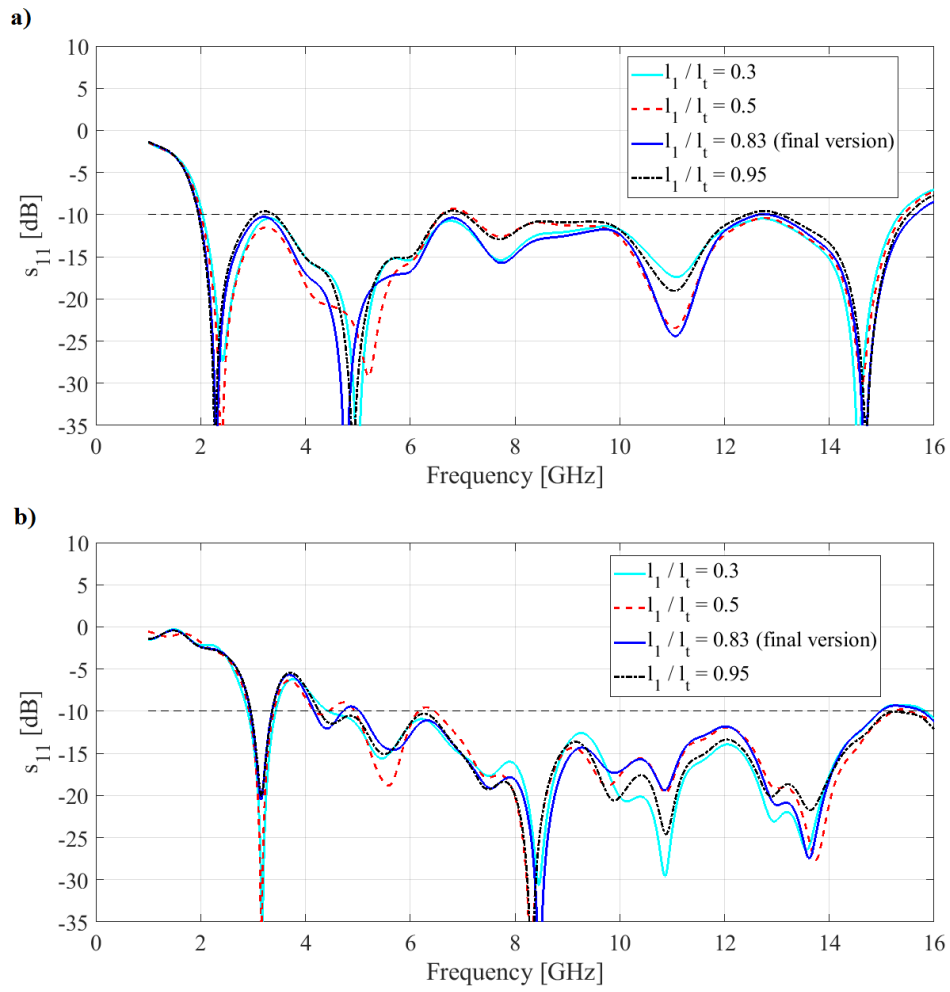
Figure 2.3.7: Reflection coefficient trends at varying of l_l parameter: a) Monopole-like topology; b) Microstrip-like topology.

order to introduce a good impedance matching in a specific sub-band. Fig. 2.3.8 shows the fundamental rectangular FSS cell with its simulated reflection coefficient (magnitude and phase). The FSS applies its influence in a band of frequencies where the extremes are in corrispondence of the phase values ±90° [33]. Usually for antenna gain improving it is necessary to obtain a magnitude value of the reflection coefficient of the single FSS nearest as possible to 0 dB. In our case the FSS must behave like an absorber surface and it is necessary to obtain a reflection coefficient magnitude lower as possible in the sub-band. Main parameters are shown in Fig. 2.3.3, and are FSS dimensions and all the gaps that fix the correct distance between all the Artificial Magnetic Conductor surfaces. The optimized values are reported in Table 2.4. With that values we obtained that the FSS acts its influence in a sub-band from 3.59 GHz to 4.41 GHz. As shown in Fig. 2.3.9, this type of metamaterial was able to matching the reflection coefficient where previously an impedance mismatching occurred (from 2.94 GHz to 5.04 GHz), and the FCC compliant goal was satisfied: in fact a band from 3.01 GHz to 15.39 GHz was obtained for the antenna in microstrip configuration, while for monopole topology a band from 1.98 GHz to 15.75 GHz was obtained.

2.3.4.2 Radiation Pattern

The 3D gain patterns of the optimized monopole and microstrip-like topologies together with the corresponding current density over the main radiator are shown in Fig. 2.3.10 and Fig. 2.3.11, respectively.

The gain patterns on (z-x) plane (i.e. $\phi = 0°$) of the optimized antennas are shown in Fig. 2.3.12 for the microstrip (left) monopole (right) topologies, at three different frequencies (4.4 GHz, 7 GHz, 10.3 GHz). The monopole patterns are almost omnidirectional at lower frequencies while the microstrip-like patterns show higher gain values at slant directions. Fig. 2.3.13 shows the gain patterns on a plane parallel to (z-y) (i.e. $\theta = 110°$) for microstrip (left) and monopole–like (right) topologies, respectively. Fig. 2.3.14 shows the variation of the maximum gain vs. frequency, it oscillates between 0.75 dB and 8.08 dB in case of microstrip (up) and between 3.15 dB and 7.97 dB for the monopole (down) topologies. For microstrip-like topology the main component contributing to the total gain is the ϕ component a part from a single narrow sub-band near 5.5 GHz. This means that single polarization across the most part of UWB band is obtained. In monopole-like topology, the main component contributing to the total gain is the ϕ component a part from four narrow sub-bands where the θ component is dominant near to 3.3 GHz, 5.2 GHz, 6.8 GHz and 10 GHz. The effect of the thickness of the substrates has been analysed and shown in Fig. 2.3.15 – Fig. 2.3.18.
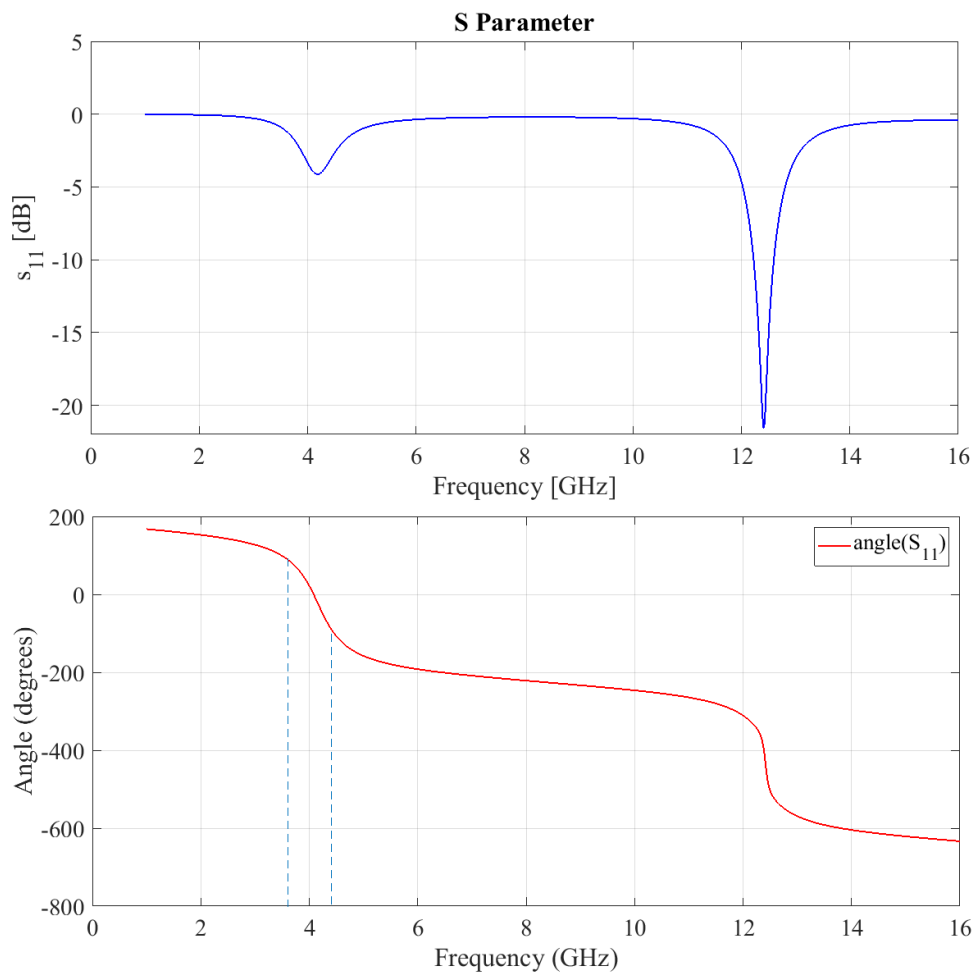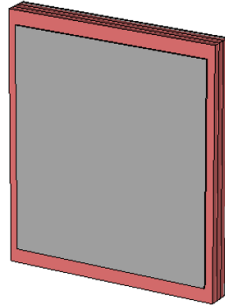
Figure 2.3.8: FSS elementary cell and its reflection coefficient trend (magnitude and phase).
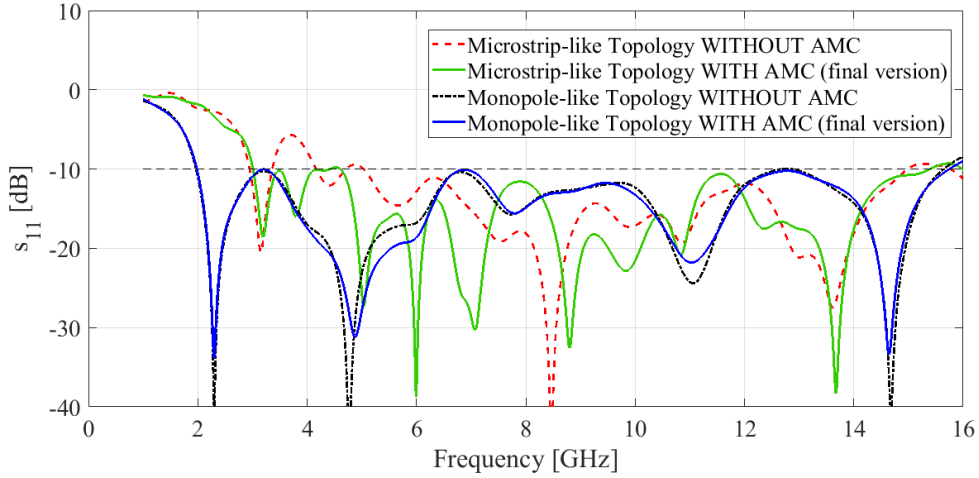
Figure 2.3.9: Microstrip-like and Monopole-like topologies reflection coefficients trends comparison between absence and presence of FSS.

Differently to the previous antenna, in this case it is possible to observe that the thickness of the first substrate (h_u) and the second substrate (h_d) have an important effect on the gain both for microstrip topology and for monopole topology. The thicknesses of $h_u = h_d = 2.4$ mm have been chosen because they give a good trade-off between low and high frequency.

2.3.4.3 System Fidelity Factor Analysis

In order to estimate the goodness of the designed antenna we simulate the System Fidelity Factor (SFF) in agreement with the procedure described in the sub-section 2.2.3.3. The same sine-modulated Gaussian pulse described by equation (2.2.3) is transmitted from the stationary antenna with $\tau = 210$ ns, $a = 3$, $f_r = 4.5$ GHz. The results of this analysis gives the SFF for different angles of rotation, it is shown in Fig. 2.3.19 for both topologies. For the microstrip-like topology the SFF value is between 0.16 (at ±110° rotation angle) and 0.6 (at ±15° rotation angle), while for the monopole topology the SFF value is between 0.32 (at ±95° rotation angle) and 0.59 (at ±135° rotation angle).

2.3.5 Measurement Results

The realized prototype antenna has been hand-made, all conductive parts are fixed to the fabric substrates by ironing, while the SMA connector is soldered. A picture of the realized antenna is shown in Fig. 2.3.20. The

51
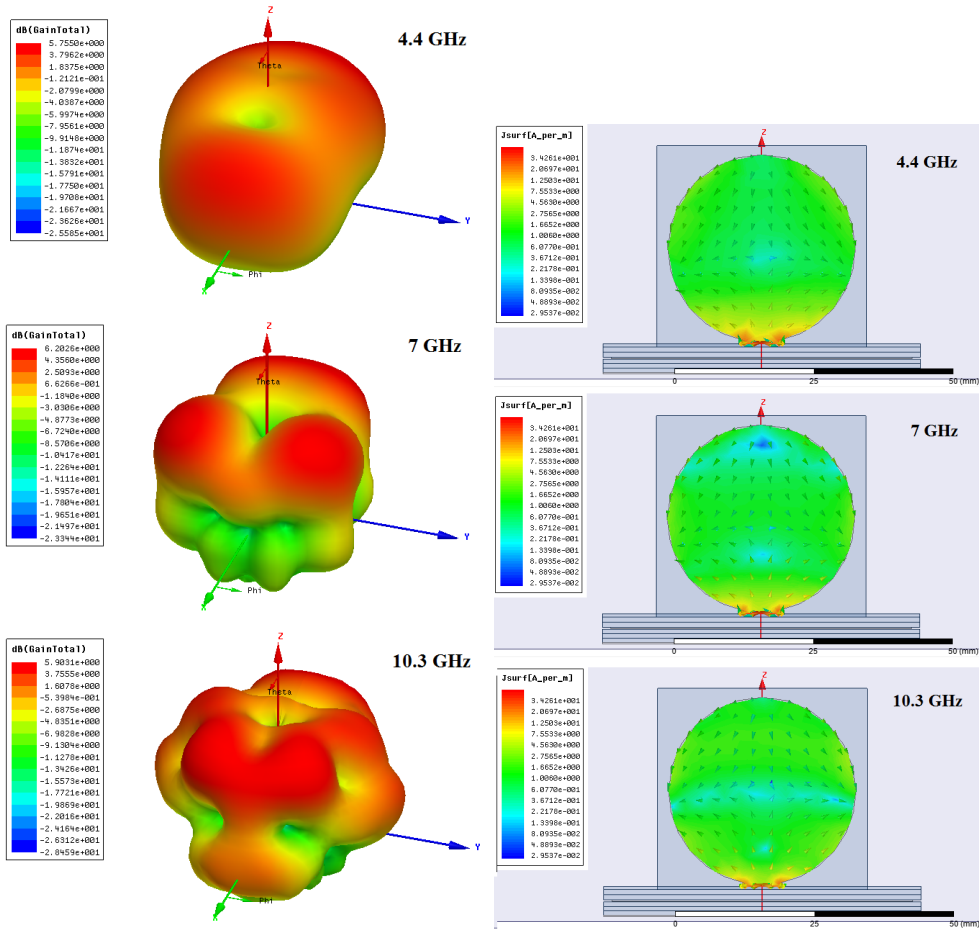
Figure 2.3.10: 3-D gain patterns (left) and corresponding current distribution (right) for monopole topology at three different frequencies.
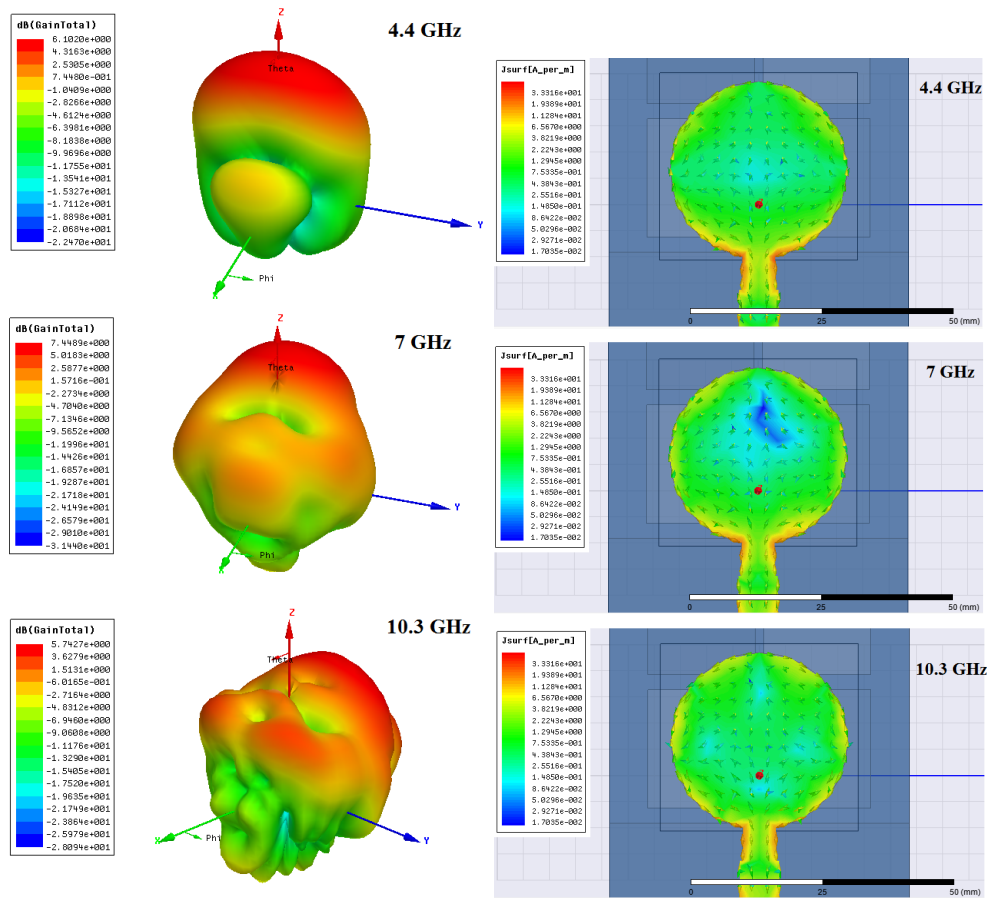
Figure 2.3.11: 3-D gain patterns (left) and corresponding current distribution (right) for microstrip-like topology at three different frequencies.
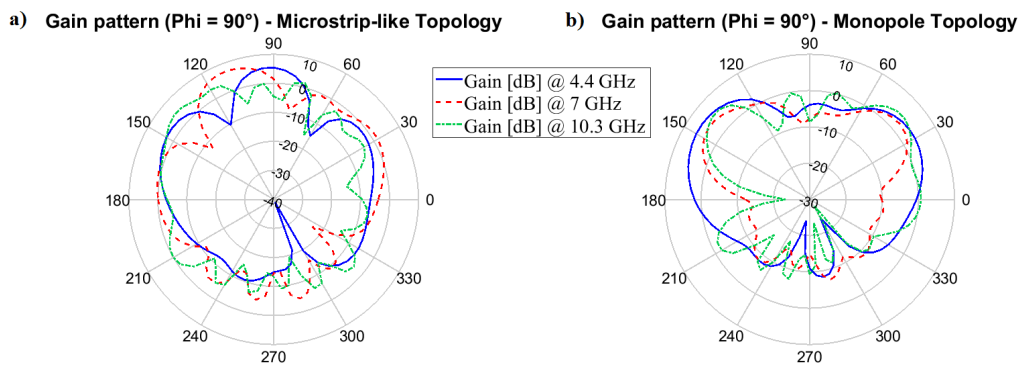
Figure 2.3.12: Zenithal cut of the gain radiation pattern of the microstrip-like topology a), and monopole-like topology b) at 4.4 GHz, 7 GHz, and 10.3 GHz ($\phi = 90°$).

a) **Gain pattern (Theta = 110°) - Microstrip-like Topology** b) **Gain pattern (Theta = 150°) - Monopole Topology**

Legend:
— Gain [dB] @ 4.4 GHz
--- Gain [dB] @ 7 GHz
-·- Gain [dB] @ 10.3 GHz
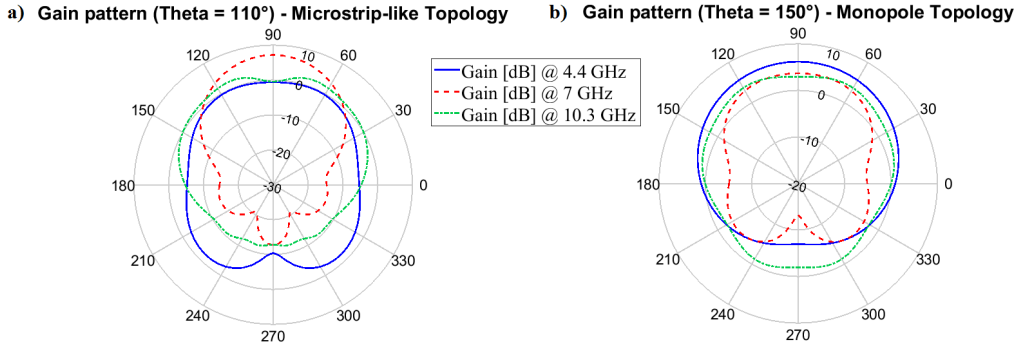
Figure 2.3.13: Azimuthal cut of the gain radiation pattern of the microstrip-like topology a) ($\theta = 110°$), and monopole-like topology b) ($\theta = 150°$) at 4.4 GHz, 7 GHz, and 10.3 GHz.

measurements of the reflection coefficient have been performed with Anritsu MS46122B vector network analyzer.

2.3.5.1 Reflection Coefficient

Reflection coefficient measurements have been performed in a laboratory environment with the antenna placed over a hollow cardboard box and, for on-body measurement, over a phantom, far from scattering objects. The phantom has been realized with a very thin plastic box filled with a solution of distilled water and 0.9% sodium chloride. The reflection coefficient of the antenna alone and on-body together with the corresponding simulated result is shown in Fig. 2.3.21 for microstrip topology and Fig. 2.3.22 for monopole topology.

The measured reflection coefficient of microstrip configuration has a -10 dB bandwidth from 2.41 GHz to 13.94 GHz apart from a slight impedance mismatching near 9 GHz where it is -9 dB for a sub-band of about 620 MHz. The measured bandwidth for monopole-like topology spans from 1.98 GHz to 14.2 GHz with a slight mismatch for sub-band of about 510 MHz near 6 GHz. For both configurations, negligible differences are visible between the alone and on-body measurements. In comparison with simulated results the measured bandwidths have the upper limit about 1.55 GHz lower than the simulated one. Also for this antenna that difference is mainly dependent on the manufacturing inaccuracy of the hand-made prototype: since the reduction of the bandwidth is at higher frequency and have similar values for both configurations it dependents on a part of the antenna common to both configurations. After some checks we have found it is depending on
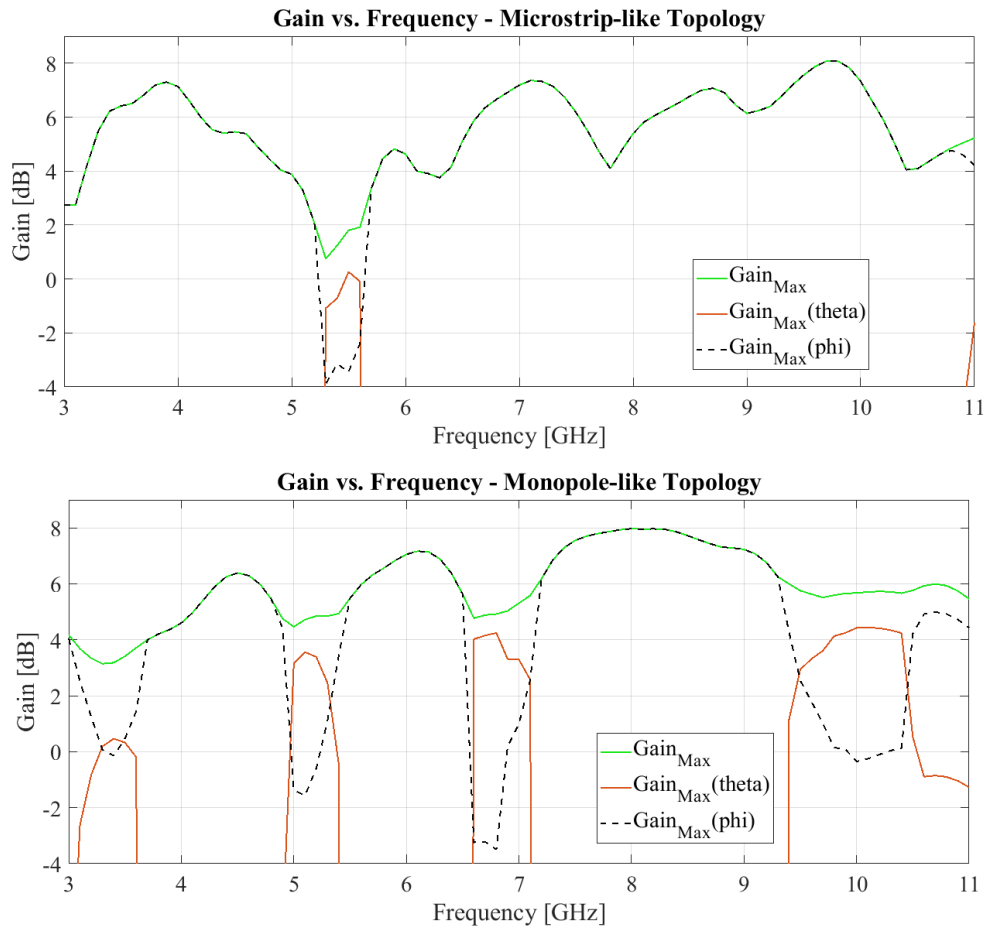
Figure 2.3.14: Maximum gain vs. frequency for microstrip (up) and monopole (down) topologies. Continuous green line total gain; black dash-dotted and orange contiuous lines ϕ and θ components, respectively.
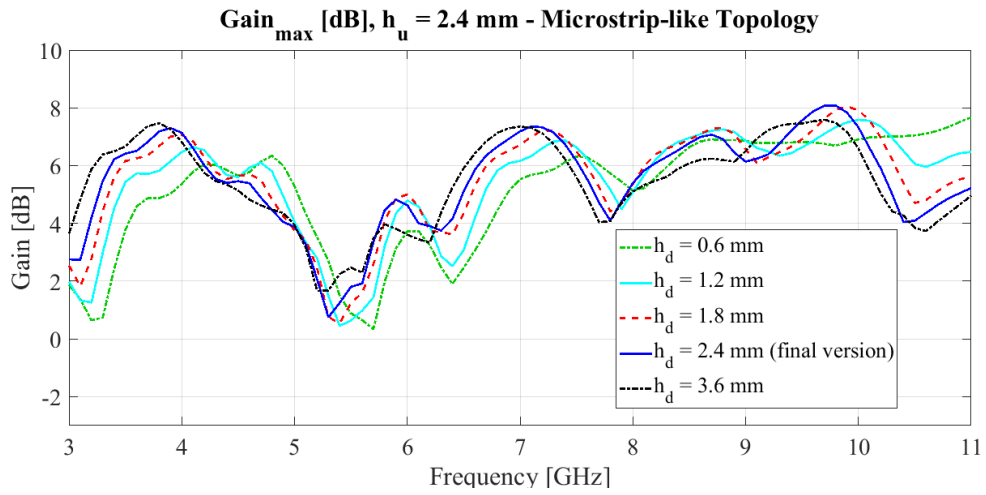
Figure 2.3.15: Maximum gain vs. frequency in case of microstrip-like topology for different thickness of second substrate.
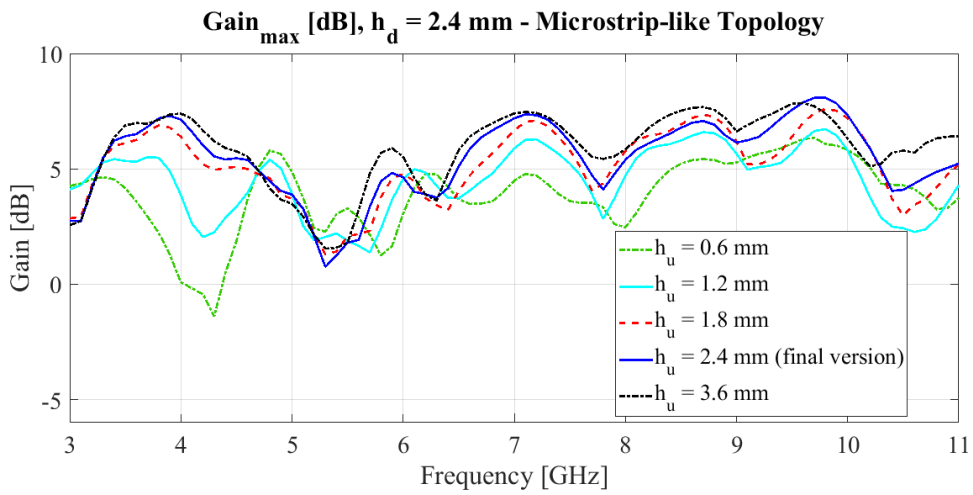
Figure 2.3.16: Maximum gain vs. frequency in case of microstrip-like topology for different thickness of the first substrate.
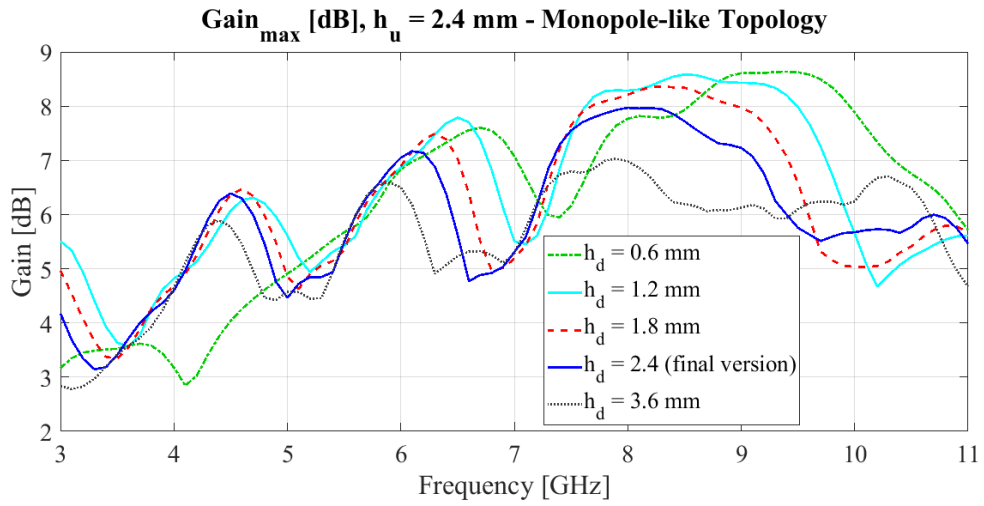
Figure 2.3.17: Maximum gain vs. frequency in case of monopole topology for different thickness of second substrate.
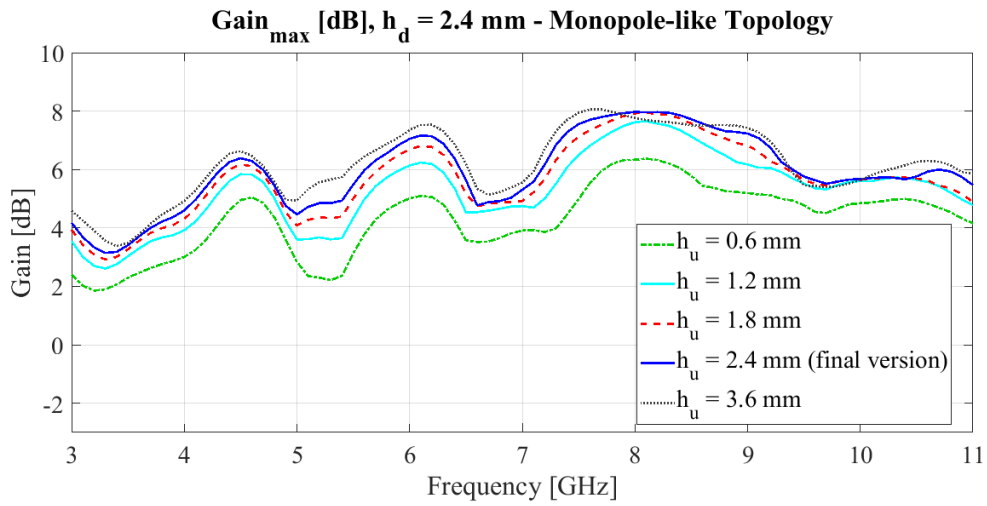
Figure 2.3.18: Maximum gain vs. frequency in case of monopole topology for different thickness of first substrate.
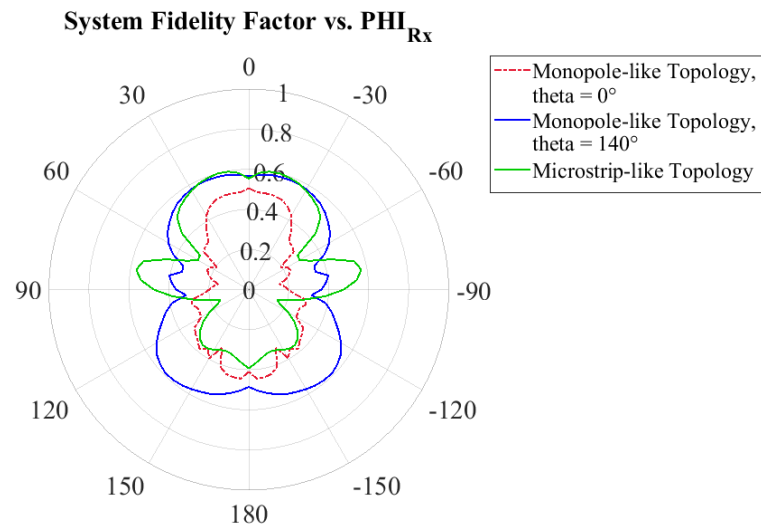
Figure 2.3.19: Simulated System Fidelity Factor results: microstrip-like topology (green continuous line), monopole topology for $\theta = 0°$ (red dashed line), and monopole topology for $\theta = 140°$ (blue continuous line).
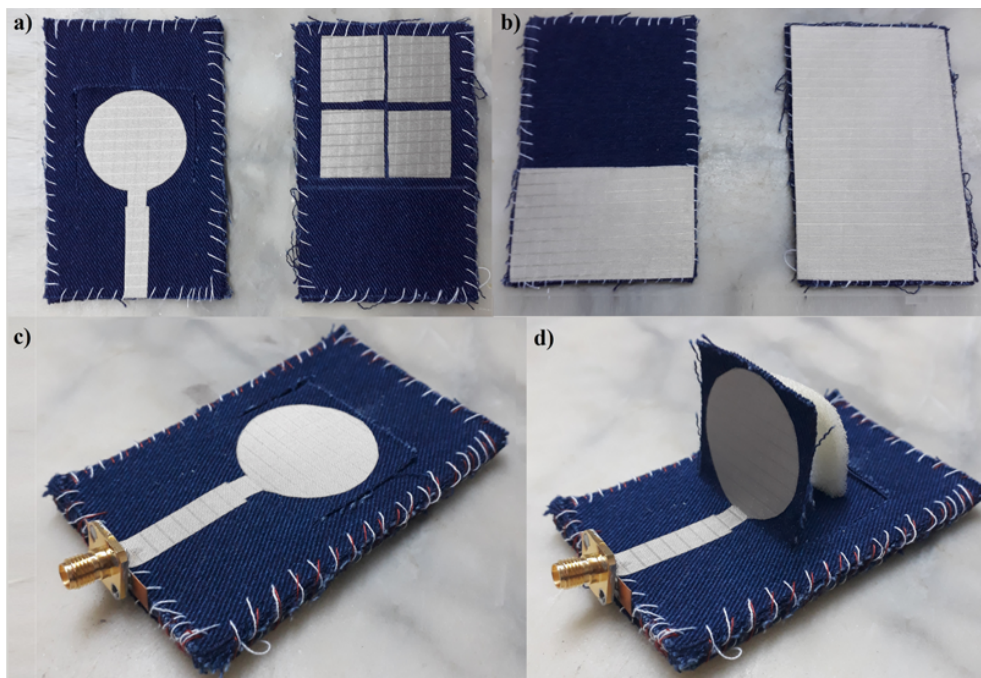
Figure 2.3.20: Realized prototype antenna: (a) circular monopole and squared metamaterial view; (b) half ground plane and floating full ground plane view; (c) microstrip configuration; (d) monopole configuration.
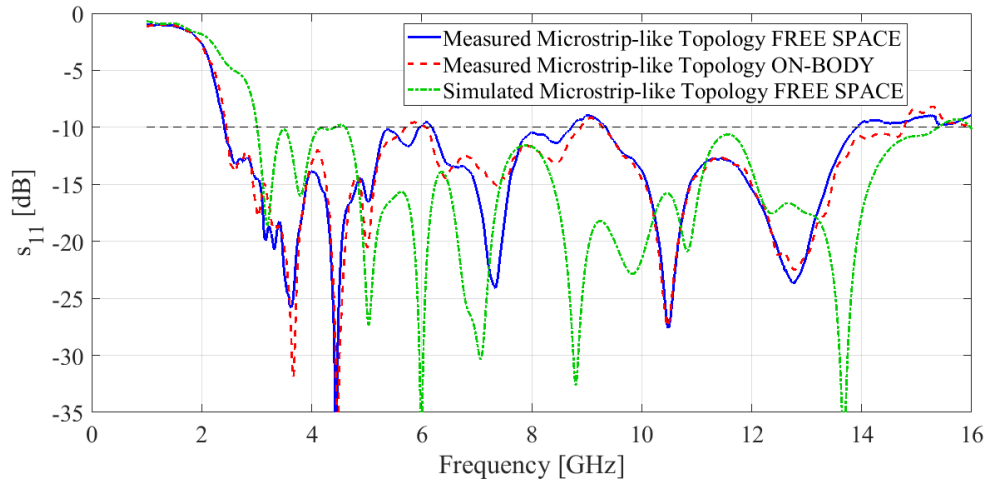
Figure 2.3.21: Measured reflection coefficient of microstrip topology for the antenna alone (continuous line), on-body (dashed) and simulated (dash-dotted).
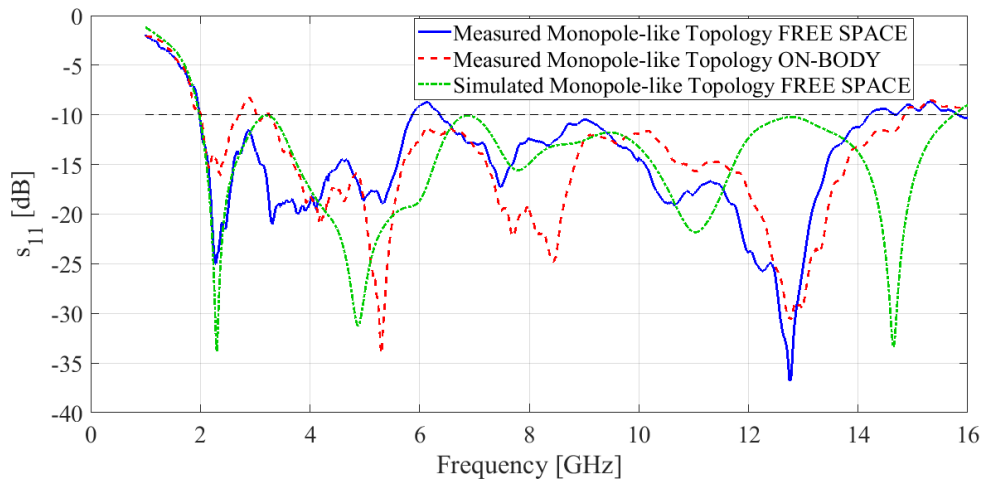
Figure 2.3.22: Measured reflection coefficient of monopole topology for the antenna alone (continuous line), on-body (dashed) and simulated (dash-dotted).

the quality of the soldering of the connector that has main effects at higher frequencies. The behavior of the monopole configuration does not change for slant positions of the flapping part (i.e. the monopole is not exactly orthogonal to the ground plane).

2.4 Conclusions

In this chapter two types of UWB wearable all-textile antenna able to be reconfigured between a monopole and a microstrip-like antenna have been proposed and discussed. These devices are based on a circular radiating disk that works as a monopole when placed orthogonal to a ground plane and as a microstrip patch when it is lying parallel to two different types of matching surfaces: a modified ground plane in the first antenna, and FSS in the second. Thanks to these innovative techniques, numerical analysis shows that both topologies have satisfactory UWB characteristic with bandwidth compliant with FCC regulation and a fair system fidelity factor that allows the antenna as air interface for wearable sensors and short range communication devices. To improve the performance from the point of view of measurements, the use of more accurate tools, like cutting plotter, could be a very good solution for the realization of the conductive parts of the antenna made on conductive fabrics. The antenna connectorization phase remains critical, as tin soldering on conductive fabrics, or the use of conductive glues, often do not provide optimal performance.

Bibliography

[1]   S. Yan, P. J. Soh and G. A. E. Vandenbosh. *Wearable Ul-trawideband Technology—A Review of Ultrawideband Antennas, Propagation Channels, and Applications in Wireless Body Area Networks*, IEEE Access, vol. 6, pp. 42177-42185, July, 2018.

[2]   D. Ghosh and P. K. Sahu. *UWB in healthcare*, International Conference on Electromagnetics in Advanced Applications (ICEAA), Cairns, QLD, 2016, pp. 679-682.

[3]   S. Lemey, F. Declercq, H. Rogier. *Dual-Band Substrate Integrated Waveguide Textile Antenna With Integrated Solar Harvester*, IEEE Antennas Wirel. Propag. Lett. vol. 13, pp. 269–272, 2014.

[4]   A. Dierck, H. Rogier, and F. Declercq. *A Wearable Active Antenna for Global Positioning System and Satellite Phone*, IEEE Trans. Antennas Propag., vol. 61, no. 2, pp. 532-538, Feb. 2013.

[5]   R. Moro, S. Agneessens, H. Rogier, and M. Bozzi. *Wearable Textile Antenna in Substrate Integrated Waveguide Technology*, IET Electron. Lett., vol. 48, no. 16, pp. 985-987, Aug. 2012.

[6]   C.-H. Kang, S.-J. Wu, and J.-H. Tarng. *A novel folded UWB antenna for wireless body area network*, IEEE Trans. Antennas Propag., vol.60, no.2, pp. 1139–1142, Feb. 2012.

[7]   P. B. Samal, P.J. Soh, and G.A.E. Vandenbosch. *A Systematic Design Procedure for Microstrip-Based Unidirectional UWB Antennas*, Progress In Electromagnetics Research, Vol. 143, 105–130, 2013.

[8]   P. B. Samal, P. J. Soh, Z. Zakaria. *Compact and Wearable Microstrip-based Textile Antenna with Full Ground Plane Designed for WBAN-UWB 802.15.6 Application*, European Conference on Antennas and Propagation (EuCAP), 2019, pp. xxx.

[9]   L. A. Y. Poffelie, P. J. Soh, S. Yan, and G. A. E. Vandenbosch. *A high fidelity all-textile UWB antenna with low back radiation for off-body WBAN applications*, IEEE Trans. Antennas Propag., vol. 64, no. 2, pp. 757–760, Feb. 2016.

[10]   G. Quintero, J.-F. Zürcher, and A. K. Skrivervik. *System Fidelity Factor: A New Method for Comparing UWB Antennas*, IEEE Transactions on Antennas and Propagation, vol. 59, no. 7, July 2011.

[11]   A. Dumoulin, M. John, M. J. Ammann and P. McEvoy. *Optimized Monopole and Dipole Antennas for UWB Asset Tag Location Systems*, IEEE Transactions on Antennas and Propagation, vol. 60, no. 6, pp. 2896-2904, June 2012.

[12]   J. Liang, L. Guo, C. C. Chiau, X. Chen and C. G. Parini. *Study of CPW-fed circular disc monopole antenna for ultra wideband applications*, IEEE Proceedings - Microwaves, Antennas and Propagation, vol. 152, no. 6, pp. 520-526, 9 Dec. 2005.

[13]   B. N. Balarami Reddy, P. Sandeep Kumar, T. Rama Rao, T. Ninesh and M. Balachary. *Design an Analysis of Wideband Monopole Antennas for Flexible/Wearable Wireless Device Application*, Progress In Electromagnetic Research M, Vol. 62, pp. 167-174, Nov. 2017.

[14]   M. A. R. Osman, M. K. A. Rahim, N. A. Samsuri, H. A. M. Salim and M. F. Ali. *Embroidered Fully Textile Wearable Antenna for Medical Monitoring Applications*, Progress In Electromagnetic Research, Vol. 117, pp. 321-337, Jan. 2011.

[15]   A. A. Ashraf, K. A. R. Sharul, G. T. Kim, A. W. Reza. *Design of 3.1-12 GHz Printed Elliptical Disc Monopole Antenna with Half Circular Modified Ground Plane for UWB Application*, Wireless Personal Communication, Vol. 69, pp. 535-549, Mar. 2013.

[16]   M. K. Garg. *Partial Ground Microstrip Patch Antenna for Ultra-Wideband Applications*" AKGEC International Journal of Technology, Vol. 6, No. 2, pp. 23-26.

[17]   J. R. Verbiest and G. A. E. Vandenbosch. *A novel small-size printed tapered monopole antenna for UWB WBAN*, IEEE Antennas Wireless Propag. Lett., vol. 5, no. 1, pp. 377–379, Dec. 2006.

[18]   M. Ur-Rehman, Q. H. Abbasi, M. Akram, and C. Parini. *Design of band-notched ultra wideband antenna for indoor and wearable wireless communications*, IET Microw., Antennas Propag., vol. 9, no. 3, pp. 243–251, 2015.

[19]   A. T. Mobashsher and A. M. Abbosh. *Compact 3-D slot-loaded folded dipole antenna with unidirectional radiation and low impulse distortion for head imaging applications*, IEEE Trans.Antennas Propag., vol.64, no.7, pp. 3245–3250, Jul. 2016.

[20]   Y. Sun, S. W. Cheung, and T. I. Yuk. *Design of a textile ultra-wideband antenna with stable performance for body-centric wireless communications*, IET Microw., Antennas Propag., vol. 8, no. 15, pp. 1363–1375, 2014.

[21]   M. Klemm, I. Z. Kovcs, G. F. Pedersen, and G. Troster. *Novel small-size directional antenna for UWB WBAN/WPAN applications*, IEEE Trans. Antennas Propag., vol. 53, no. 12, pp. 3884–3896, Dec. 2005.

[22]   B. N. B. Reddy, S. P. Kumar, T. R. Rao, N. Tiwari, and M. Balachary. *Design and Analysis of Wideband Monopole Antennas for Flexible/Wearable Wireless Device Applications*, Progress In Electromagnetics Research M, Vol. 62, 167–174, 2017.

[23]   M. A. R. Osman, M. K. A. Rahim, N. A. Samsuri, H. A. M. Salim, and M. F. Ali. *Embroidered Fully Textile Wearable Antenna for Medical Monitoring Applications*, Progress In Electromagnetics Research, Vol. 117, 321–337, 2011.

[24]   T. S. P. See, T. M. Chiam, M. C. K. Ho and M. R. Yuce. *Experimental Study on the Dependence of Antenna Type and*

Polarization on the Link Reliability in On-Body UWB Systems, IEEE Transactions on Antennas and Propagation, vol. 60, no. 11, pp. 5373-5380, Nov. 2012.

[25]   lessemf.com/shieldit_super.pdf

[26]   J.-M. Heinola and K. Tolsa. *Dielectric characterization of printed wiring board materials using ring resonator techniques: a comparison of calculation models*, IEEE Transactions on Dielectrics and Electrical Insulation, vol.: 13, Issue: 4, Aug. 2006.

[27]   ansys.com/Products/Electronics/ANSYS-HFSS

[28]   N. Chahat, M. Zhadobov, R. Sauleau, and K. Ito. *A compact UWB antenna for on-body applications*, IEEE Trans. Antennas Propag., vol. 59, no. 4, pp. 1123–1131, Apr. 2011.

[29]   N. M. A. Elaziz, A. J. Alzubaidi, M. A. Hassan. *Performance of the 6th Derivative Gaussian UWB Pulse Shape in IEEE802.15.3a Multipath Fading Channel*, IOSR Journal of Engineering, ISSN (e): 2250-3021, ISSN (p): 2278-8719, vol. 04, Issue 12, pp. 1-12, Dec. 2014.

[30]   A. Alighanbari, C. D. Sarris. *Parallel Time-Domain Full-Wave Analysis and System-Level Modeling of Ultrawideband Indoor Communication Systems*, IEEE Trans. Antennas Propag., vol. 57, no. 1, Jan. 2009.

[31]   Klemm M., and G. Troester. *Textile UWB Antennas for Wireless Body Area Networks*, IEEE Trans. Antennas Propag., vol. 54, no. 11, Nov. 2006.

[32]   R. Dewan, M. K. A. Rahim, M. R. Hamid, M. F. M. Yusoff, N. A. Samsuri, N. A. Murad and K. Kamardin. *Artificial magnetic conductor for various antenna applications: An overview*, International Journal of RF and Microwave Computer-Aided Engineering, vol. 27, no. 6, Aug. 2017.

[33]   B. S. Cook and A. Shamim. *Utilizing Wideband AMC Structures for High-Gain Inkjet-Printed Antennas on Lossy Paper Substrate*, IEEE Antennas and Wireless Propagation Letters, vol. 12, pp. 76-79, Jan. 2013.

[34]   S. Kim, Y. -J. Ren, H. Lee, A. Rida, S. Nikolaou and M. M. Tentzeris. *Monopole Antenna With Inkjet-Printed EBG Array on Paper Substrate for Wearable Applications*, IEEE Antennas and Wireless Propagation Letters, vol. 11, pp. 663-666, June 2012.

[35]   W. Yang, H. Wang, W. Che and J. Wang. *A Wideband and High-Gain Edge-Fed Patch Antenna and Array Using Artificial Magnetic Conductor Structures*, IEEE Antennas and Wireless Propagation Letters, vol. 12, pp. 769-772, June 2013.

[36]   X. Y. Liu, Y. -H. Di, H. Liu, Z. -T. Wu and M. M. Tentzeris. *A Planar Windmill-like Broadband Antenna Equipped with Artificial Magnetic Conductor for Off-Body Communications*, IEEE Antennas and Wireless Propagation Letters, vol. 15, pp. 64-67, May 2015.

Chapter 3

A Rescue Tag Based on Harmonic RADAR Principle

3.1 Introduction

In recent years there has been an exponential increase in the use of wireless sensors that have become fundamental in modern industrial, scientific and home automation environments, leading to the birth of the Internet of Things (IoT). In particular, passive wireless sensors are widely used in many applications because they do not need a local power supply to operate. This leads to rapid installation and low maintenance costs. Although most commercially available passive wireless sensors are chip-based and use digital integrated circuits on the tag, chipless sensors are a current research topic. Chipless systems avoid the use of microchips on tags and could allow them to function, further reducing costs [1]. The proposed sensor can be defined as quasi-chipless, as it does not require any power supply or energy harvesting on the tag, but uses a single unbiased diode to generate the harmonic response. A promising group of chipless sensors is the one operating in the gigahertz frequency range of the radio frequency (RF) spectrum, which uses passive backscattering similar to RADAR technology [2]. These sensors have to cope with strong RADAR disturbances (clutter) that overlap the signal intended for the tag. RADAR clutter limits system capacity, especially in highly reflective and highly dynamic time-variance environments. Making measurements of the RADAR clutter in order to have a reference is a solution to this problem [3], but it makes the system not very scalable, since if there were to be a change in the environment it would be necessary to repeat the measurement of the clutter. To solve the RADAR clutter problem, an approach similar to frequency division duplexing has been presented in [4],

in which RF backscattering is used at a harmonic frequency of the fundamental transmission frequency. In this way, the RADAR clutter that occurs at the fundamental frequency is completely isolated from the backscattered harmonic that carries the desired information. The harmonic RADAR principle was used for the localization and tracking systems [5]. Theoretical work on the combination of harmonic RADAR and detection, based on the coding of the amplitude or phase of the measured value, is presented in [6], and [7]. Unlike [4], it was decided to design a single port sensor to be applied to a wearable Ultra Wide Band (UWB) antenna. The UWB antenna, in fact, being able to receive and transmit on a very wide frequency band, allows to exclude the use of two antennas: one for the transmission of the signal at a given frequency, and the other for the reception of the second harmonic (doubled frequency). The sensor, combined with the wearable UWB antenna, has been designed to be used in radio localization systems for the search and rescue of people buried following natural and man-made disasters such as earthquakes and landslides, terrorist attacks or industrial accidents. Unlike what reported in [8], where active sensors at 434 MHz and 868 MHz were used, in this case a real low-cost, wearable, completely passive and non-invasive S-band transponder would be used for the user.

3.2 Schottky diodes in high frequency applications

A Schottky diode operating at high frequency is usually composed of an n-type gallium arsenide (GaAs) material. Depending on the type of applications they can be biased with small DC forward currents, or, as in our case, without bias. Schottky diodes are usually used to apply a frequency conversion of a given input signal [9]. The three basic frequency conversion operations are: *rectification* (conversion to DC), *detection* (demodulation of an amplitude-modulated signal), and *mixing* (frequency shifting).

A junction diode can be modeled as a nonlinear resistor, with a small-signal V–I relationship expressed as

$$I\left(V\right) = I_S\left(e^{\alpha V} - 1\right) \tag{3.2.1}$$

where $\alpha = \frac{q}{nkT}$, and q is the charge of an electron, k is Boltzmann's constant, T is temperature, n is the ideality factor, and I_S is the saturation current [10]-[12]. Typical values of these quantities are reported in [9]. Fig. 3.2.2, shows a typical diode $V - I$ characteristic for a Schottky diode.

For high frequency applications the Schottky diodes can be represented
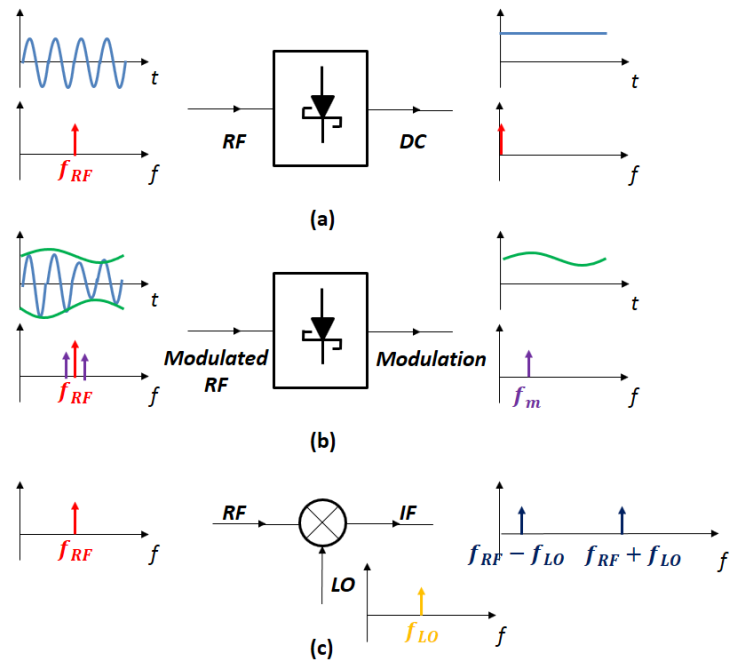
Figure 3.2.1: Basic frequency conversion operations of rectification, detection, and mixing: (a) diode rectifier, (b) diode detector, (c) mixer.
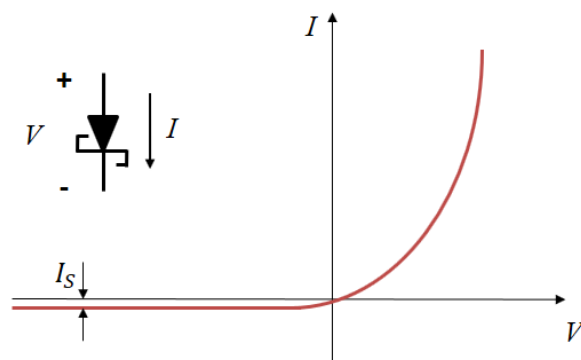
Figure 3.2.2: V–I characteristics of a Schottky diode.

by an equivalent circuit extrapolated from the small-signal approximation. Let the diode voltage be expressed as

$$V = V_0 + v \qquad (3.2.2)$$

where V_0 is a DC bias voltage and v is a small AC signal voltage. Then (3.2.2) can be expanded in a Taylor series about V_0 as follows:

$$I(V) = I_0 + v \frac{dI}{dV}\bigg|_{V_0} + \frac{1}{2} v^2 \frac{d^2 I}{dV^2}\bigg|_{V_0} + \cdots, \qquad (3.2.3)$$

where $I_0 = I(V_0)$ is the DC bias current. The first derivative can be evaluated as

$$\frac{dI}{dV}\bigg|_{V_0} = \alpha I_S e^{\alpha V_0} = \alpha(I_0 + I_S) = G_d = \frac{1}{R_j} \qquad (3.2.4)$$

which defines R_j, the junction resistance of the diode, and G_d which is the dynamic conductance of the diode. The second derivative is

$$\frac{d^2 I}{dV^2}\bigg|_{V_0} = \frac{dG_d}{dV}\bigg|_{V_0} = \alpha^2 I_S e^{\alpha V_0} = \alpha^2(I_0 + I_S) = \alpha G_d = G_d' \qquad (3.2.5)$$

Then (3.2.3) can be rewritten as the sum of the DC bias current, I_0, and an AC current, i:

$$I(V) = I_0 + i + v G_d + \frac{v^2}{2} G_d' + \cdots \qquad (3.2.6)$$

The small-signal approximation is based on the DC voltage–current relationship of (3.2.6), and shows that the equivalent circuit of a diode will involve a nonlinear resistance. In practice, however, the AC characteristics of a diode also involve reactive effects due to the structure and packaging of the diode. A typical equivalent circuit for an RF diode is shown in Fig. 3.2.3.

The leads or contacts of the diode package are modeled as a series inductance, L_s, and shunt capacitance, C_p. The series resistor, R_s, accounts for contact and current-spreading resistance. The junction capacitance, C_j, and the junction resistance, R_j, are bias dependent.

Since our goal was to create a passive harmonic RADAR sensor, the diode was used in the *detection* mode. In this case the nonlinearity of the diode is used to demodulate an amplitude-modulated (AM) RF carrier. In this case, the diode voltage can be expressed as

69
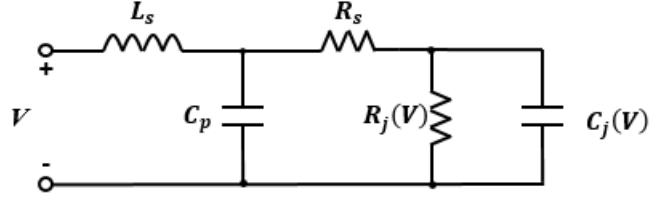
Figure 3.2.3: Equivalent AC circuit model for a Schottky diode.

Frequency	Relative Amplitude
0	$1 + m^2/2$
ω_m	$2m$
$2\omega_m$	$m^2/2$
$2\omega_0$	$1 + m^2/2$
$2\omega_0 \pm \omega_m$	m
$2(\omega_0 \pm \omega_m)$	$m^2/4$

Table 3.1: Frequencies and Relative Amplitudes of the Square-Law Output of a Detected AM Signal.

$$v(t) = v_0 \left[1 + m \cdot \cos(\omega_m t) \cdot \cos(\omega_0 t)\right] \tag{3.2.7}$$

where

$$
\begin{aligned}
i(t) &= v_0 G_d \left[1 + m \cdot \cos(\omega_m t)\right] \cdot \cos(\omega_0 t) + \frac{v_0^2}{2} G_d' \left[1 + m \cdot \cos(\omega_m t)\right]^2 \cos^2(\omega_0 t) \\
&= v_0 G_d \left\{\cos(\omega_0 t) + \frac{m}{2} \cdot \cos\left[(\omega_0 + \omega_m)t\right] + \frac{m}{2} \cdot \cos\left[(\omega_0 - \omega_m)t\right]\right\} \\
&\quad + \frac{v_0^2}{4} G_d' \{1 + \frac{m^2}{2} + 2m \cdot \cos(\omega_m t) + \frac{m^2}{2} \cdot \cos(2\omega_m t) + \cos(2\omega_0 t) \tag{3.2.8} \\
&\quad + m \cdot \cos\left[(2\omega_0 + \omega_m)t\right] + m \cdot \cos\left[(2\omega_0 - \omega_m)t\right] + \frac{m^2}{2} \cdot \cos(2\omega_0 t) \\
&\quad + \frac{m^2}{4} \cdot \cos\left[2(\omega_0 + \omega_m)t\right] + \frac{m^2}{4} \cdot \cos\left[2(\omega_0 + \omega_m)t\right]\}.
\end{aligned}
$$

The frequency spectrum of this output is shown in Fig. 3.2.4. The output current terms that are linear in the diode voltage (terms multiplying $v_0 G_d$) have frequencies of ω_0 and $\omega_0 \pm \omega_m$, while the terms that are proportional to the square of the diode voltage (terms multiplying $v_0^2 G_d'/2$ include the frequencies and relative amplitudes listed in Table 3.1.

The desired demodulated output of frequency ω_m is easily separated from the undesired frequency components with a low-pass filter. Observe that the
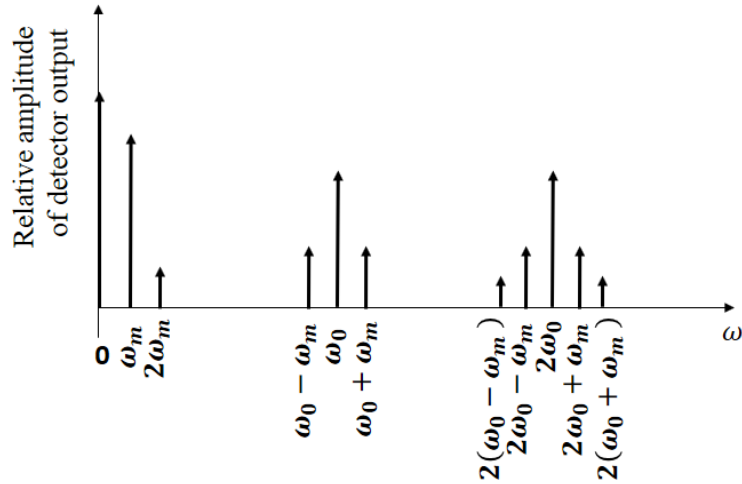
Figure 3.2.4: Output spectrum of a detected AM signal.

amplitude of this current is $mv_0^2 G_d'/2$ which is proportional to the square of the input signal voltage, and hence the input signal power. This square-law behavior is the usual operating condition for detector diodes, but it can be obtained only over a restricted range of input power. If the input power is too large, small-signal conditions will not apply, and the output will become saturated and approach a linear, and then a constant, i versus P characteristic. At very low signal levels the input signal will be lost in the noise floor of the device. Fig. 3.2.5 shows typical v_{out} versus P_{in} characteristic, where the output voltage can be considered as the voltage drop across a resistor in series with the diode. Square-law operation is particularly important for applications where power levels are inferred from detector voltage, as in SWR indicators and signal level indicators. Detectors may be DC biased to an operating point that provides the best sensitivity.

3.3 Sensor design and numerical results

The sensor design starts from a very simple concept. In fact, after choosing the zero bias Schottky diode, we limited to optimizing the rest of the circuit with the aim of matching it to the 50 Ohm (at the port) in correspondance of the frequency of interest and its second harmonic. Therefore the resulting matching network was such as to counterbalance the capacitive reactance of the chosen diode's input impedance. An Avago HSMS-2850 zero bias Schottky diode was chosen, which is a detector that can be used with low input power levels ($P_{in} < -20$ dBm) down to 1.5 GHz. For applications,

71
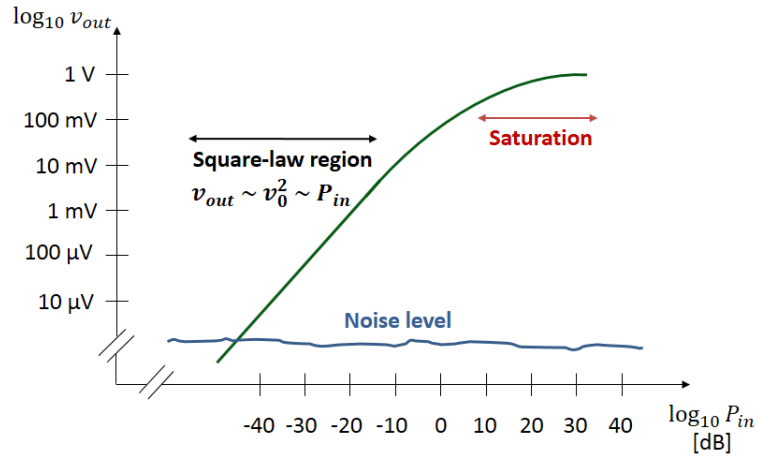
Figure 3.2.5: Square-law region for a typical diode detector.

with power levels greater than -20 dBm, it works well up to 4 GHz and is ideal for RFId (Radio Frequency Identification) and RF passive tags (no DC bias) applications. Fig. 3.3.1 shows the chosen package and the parameters that describe the non-linear behavior of the diode (SPICE parameters). Fig. 3.3.2 shows the input impedance of the Schottky diode at the test frequencies ($f_1 = 2$ GHz, and $f_2 = 2 \cdot f_1 = 4$ GHz). The output impedance matches the input impedance (single port).

As can be seen in Fig. 3.3.2, the chosen Schottky diode has an impedance with strongly capacitive reactance, while the real part is very close to 50 Ohms. The network optimization phase was conducted in Cadence AWR Microwave Office environment [13], in which the SPICE parameters of the diode shown in Fig. 3.3.1 were entered. In order to determine the exact shape of the matching network, sections of transmission lines have been added at the anode and cathode of the detector. Since the sensor has only one port, the cathode of the diode was connected to the ground through a copper via hole having an external diameter of 0.9 mm, and an internal diameter of 0.6 mm. The optimization of the transmission lines was carried out by placing a continuous wave sinusoidal signal with power equal to -40 dBm at 2 GHz at the input of the network, with the aim of obtaining a backscattered signal in the second harmonic (4 GHz) with a power level of at least -65 dBm. The optimization, carried out by means of the *Simplex* and *Random Local* algorithms, made it possible to obtain, for each line section, the optimal characteristic impedance and electrical length value for matching the diode to 50 Ohms. In Fig. 3.3.3 (a), the optimal transmission line circuit is shown. This circuit would have allowed a power level of -62.91 dBm in backscattering

72
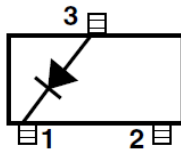
(a)

SPICE Parameters

Parameter	Units	HSMS-285x
B_V	V	3.8
C_{J0}	pF	0.18
E_G	eV	0.69
I_{BV}	A	3 E-4
I_S	A	3 E-6
N		1.06
R_S	Ω	25
P_B (V_J)	V	0.35
P_T (XTI)		2
M		0.5

(b)

Figure 3.3.1: Avago HSMS-2850 zero bias Schottky diode detector: (a) package and pinout (top view), (b) SPICE parameters.
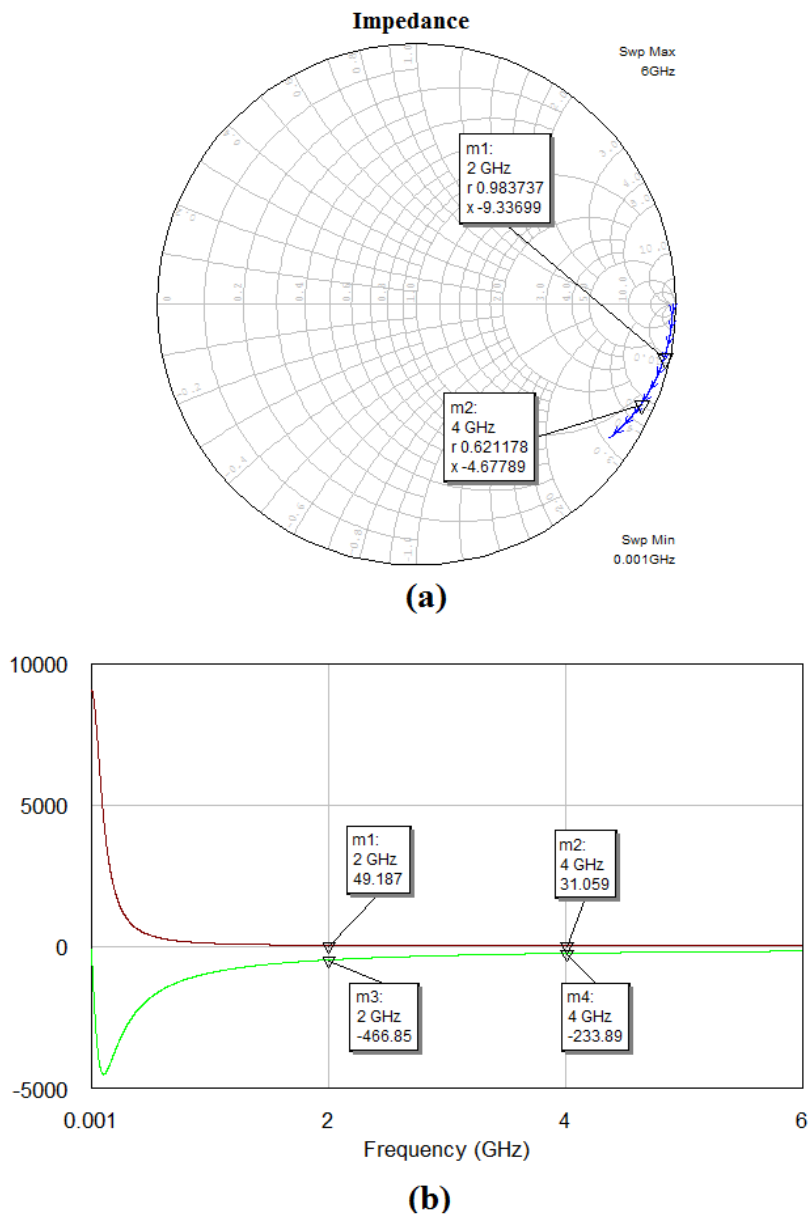
Figure 3.3.2: Input impedance of Avago HSMS-2850 at 2 GHz and 4 GHz:
(a) input impedance on Smith Chart, (b) real part (brown), and imaginary
part (green) of the detector's input impedance.

74
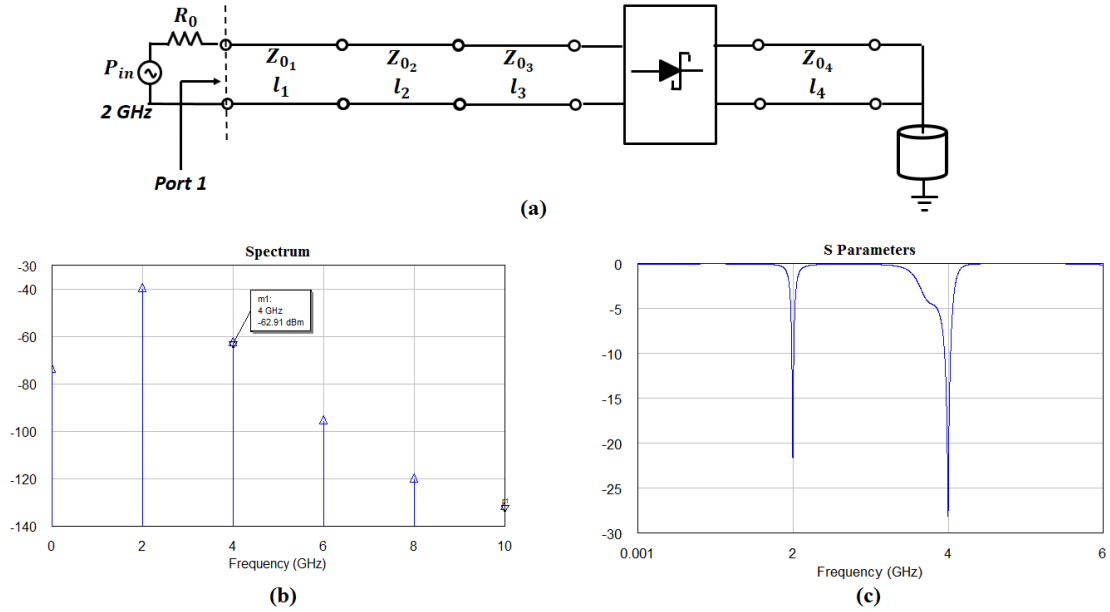
Figure 3.3.3: Optimization results: (a) transmission lines version of the harmonic RADAR sensor, (b) second harmonic backscattered signal spectrum (4 GHz), (c) reflection coefficient.

Z_{0_1} [Ω]	l_1 [deg]	Z_{0_2} [Ω]	l_2 [deg]	Z_{0_3} [Ω]	l_3 [deg]	Z_{0_4} [Ω]	l_4 [deg]
62,93	169,54	10	191,7	62,91	161,35	62,86	75,77

Table 3.2: Transmission lines impedances and phase lengths.

at 4 GHz compared to -40 dBm at 2 GHz expected on the input port. Table 3.2 shows the impedance and phase length values of the transmission lines that make up the circuit.

In order to make it feasible, the obtained transmission line circuit must however be converted into a microstrip circuit. A 0.8 mm thick Rogers RO4003C [14] dielectric substrate was chosen, on which 0.035 mm thick layers of copper are applied. The following design parameters have been set in the simulator: $\varepsilon_r = 3.6$ and $\tan \delta = 0.0024$.

Thanks to TX-Line software [15], the transmission lines were transformed into microstrips placed on RO4003C substrate. The final values of the dimensions of microstrips are reported in Table 3.3. Fig. 3.3.4 shows the resulting layout, the spectrum of the backscattered signal in second harmonic (4 GHz),
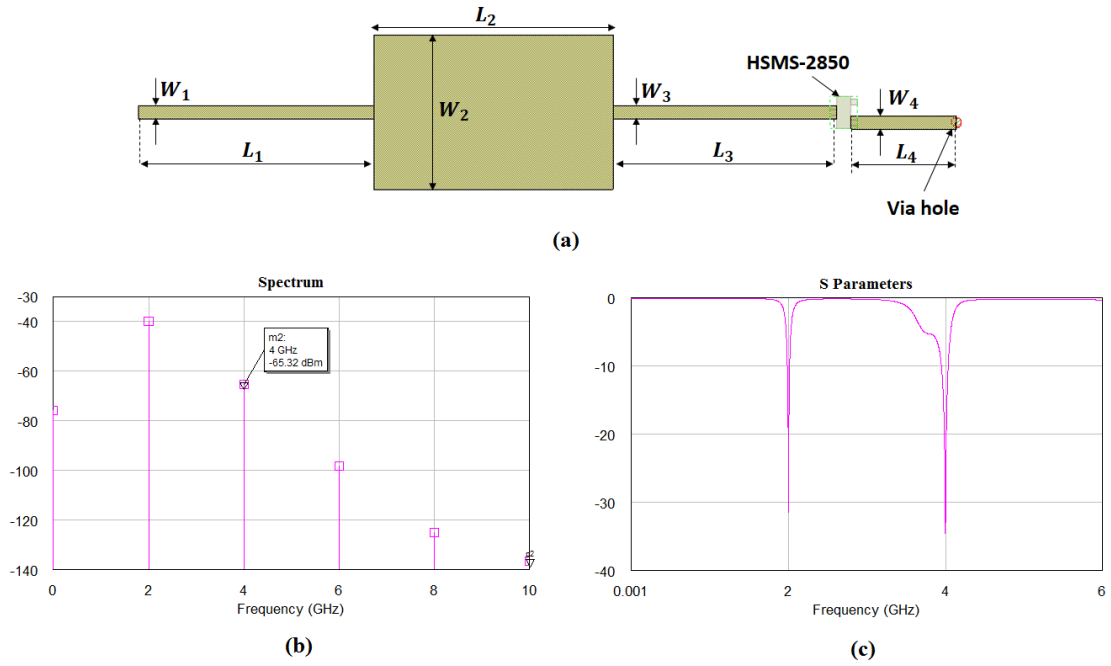
Figure 3.3.4: Microstrip circuit: (a) layout, (b) spectrum of the backscattered signal in second harmonic (4 GHz), (c) reflection coefficient.

and the reflection coefficient of the circuit.

In Fig. 3.3.4 (b) it can be seen how the power level of the backscattered second harmonic signal has dropped by about 3 dB compared to the ideal transmission line circuit. This loss is certainly due to the dielectric losses and to those due to the conductor (copper) that makes up the microstrips. Comparing Fig. 3.3.3 (c) and Fig. 3.3.4 (c), it can be seen that the strong impedance matching in the frequencies of interest (2 GHz and 4 GHz) has remained unchanged.

The microstrips have very different dimensions and therefore very different line impedances, as seen from the values obtained during the optimization

W_1 [mm]	L_1 [mm]	W_2 [mm]	L_2 [mm]	W_3 [mm]	L_3 [mm]	W_4 [mm]	L_4 [mm]
1,158	21,407	14,066	21,745	1,583	20,373	1,16	9,567

Table 3.3: Geometric dimensions of the microstrips corresponding to the four transmission line sections.
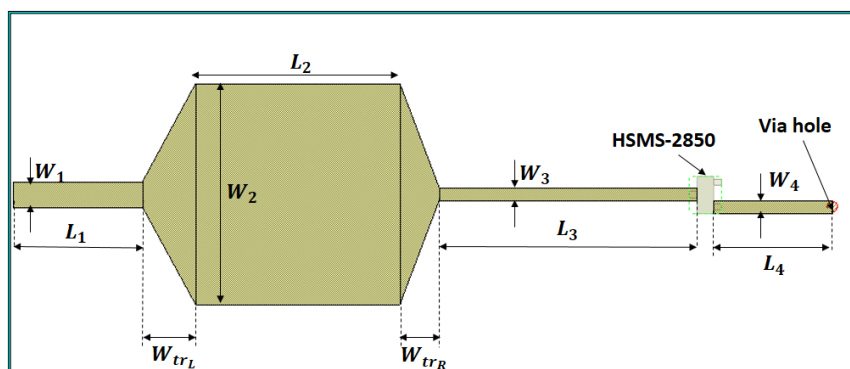
(a)
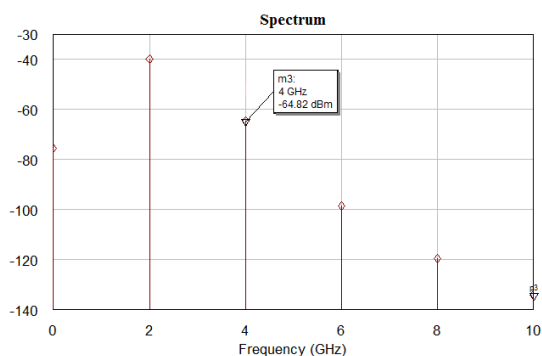
(b)
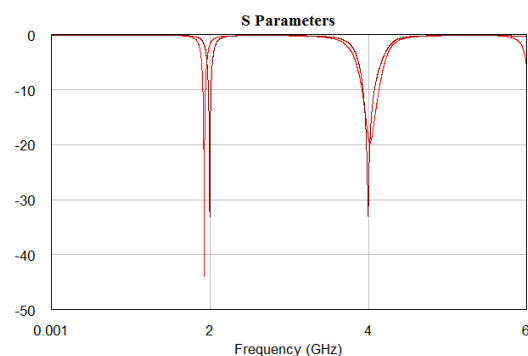
(c)

Figure 3.3.5: Final microstrip harmonic RADAR sensor: (a) circuit layout, (b) spectrum of the backscattered signal in second harmonic (4 GHz), (c) reflection coefficients (AWR simulation (brown line), and AXIEM simulation (red line)).

phase of the circuit with the transmission lines. In order to make the passage of the currents less drastic, it was decided to introduce linear tapers between the various microstrip lines. The final circuit's layout, with the relative spectrum and reflection coefficient are shown in Fig. 3.3.5. Following the introduction of linear tapered lines it was necessary to perform an optimization as previously done with the *Simplex* and *Random Local* algorithms.

The final dimensions of the harmonic RADAR Printed Circuit Board (PCB) are $66 \times 28.2 \times 0.8$ mm^3. In order to have a more accurate representation of its behavior, the sensor was simulated in AXIEM environment [16], which allows to do a planar 3-D electromagnetic analysis of the circuit thanks to the Method of Moments (MoM). Its use is necessary as it allows to take into account electromagnetic phenomena that the AWR simulations

W_1 [mm]	L_1 [mm]	W_{tr_L} [mm]	W_2 [mm]	L_2 [mm]	W_{tr_R} [mm]	W_3 [mm]	L_3 [mm]	W_4 [mm]	L_4 [mm]
1,991	10,062	4,169	15,852	17,169	3	1	20,042	0,9	9,186

Table 3.4: Harmonic RADAR sensor final geometrical dimensions.
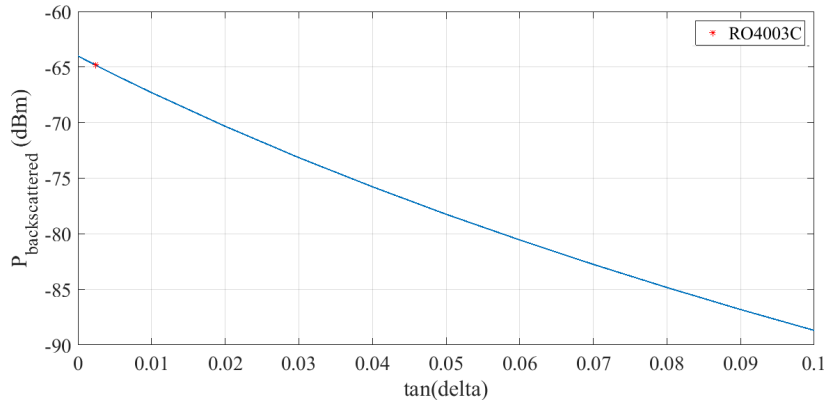
Figure 3.3.6: Second harmonic backscattered signal strenght (4 GHz) vs. loss tangent values of the dielectric substrate that compose the harmonic RADAR.

does not consider (electromagnetic coupling between nearby lines, etc.). In fact, in Fig. 3.3.5 (c) it can be seen how the first resonance frequency obtained in AXIEM is 1.93 GHz instead of 2 GHz. The power of the second harmonic backscattered signal (4 GHz) is equal to -64.82 dBm.

As previously mentioned, the choice of a substrate with low losses led to obtaining a result very close to the ideal one (transmission lines circuit). The dielectric losses, in fact, have a decisive impact on the performance of the harmonic RADAR. In Fig. 3.3.6 it is shown how the power of the backscattered signal varies in second harmonic with the variation of the $\tan \delta$ value of the material composing the substrate, when an incident signal at 2 GHz with a power equal to -40 dBm is applied to the sensor input port. Lower is the loss tangent value and better is the performance in terms of backscattered power signal in the second harmonic (4 GHz).
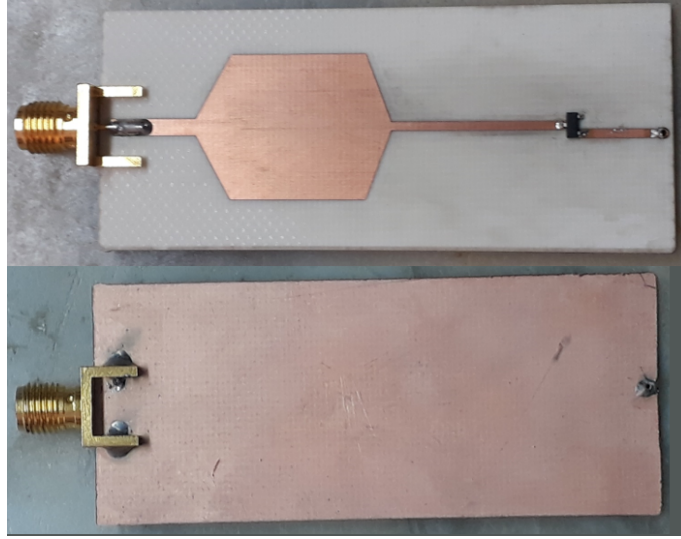
Figure 3.4.1: Realized harmonic RADAR sensor on Rogers RO4003C dielectric substrate.

3.4 Measurement results

3.4.1 RADAR sensor: reflection coefficient

The prototype of the harmonic RADAR circuit was made on Rogers RO4003C substrate thanks to a CNC milling machine. The measurement of the reflection coefficient was carried out with the Anritsu MS46122B vector network analyzer. The results of the measurement are reported in Fig. 3.4.2.

From Fig. 3.4.2 it is possible to see how the first resonance is at 1.8 GHz, while the second harmonic is at 3.6 GHz. The effect of the welds on the diode and the connector led to a strong attenuation in terms of reflection coefficient.

3.4.2 UWB wearable microstrip antenna

The sensor was connected to the Ultra Wide Band antenna described in Chapter 2 section 3, in its microstrip version. Since the wearable antenna had 2.41 GHz - 13.94 GHz band for that configuration, it was necessary to change its size in order to make it work at the first resonance measured for the sensor ($\leqslant$ 1.8 GHz). In this case, the antenna substrate consists of felt (lower substrate) and denim (upper substrate). The two materials were measured with the ring sensor described in Chapter 4 from which they were derived $\varepsilon_{r_{felt}} = 1.19$, $\tan \delta_{felt} = 0.0183$, $\varepsilon_{r_{denim}} = 1.39$, and $\tan \delta_{denim} = 0.015$. The
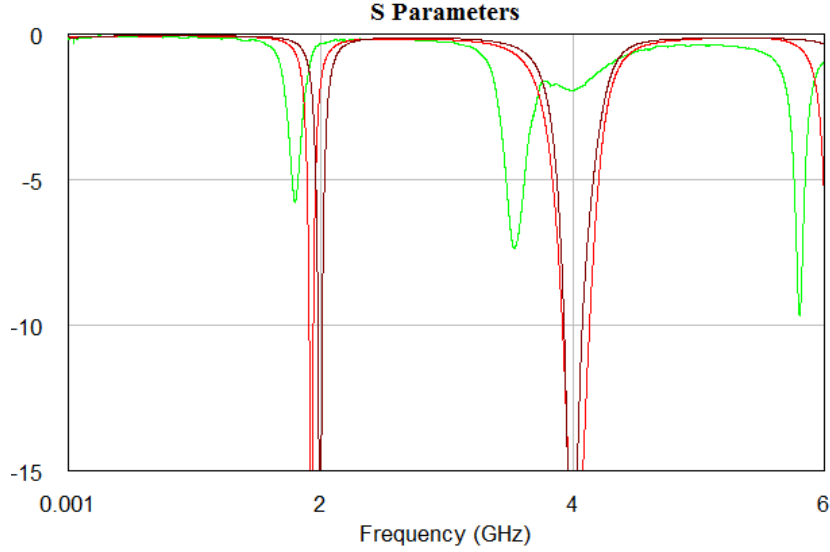
Figure 3.4.2: Harmonic RADAR reflection coefficients: AWR simulated results (brown), AXIEM simulated results (red), and measured results (green).

W	L	w_1	w_2	r	h_u	h_d
115.42	195	10.04	7.14	33.93	2.4	3.4

l_l	l_t	GAP_x	GAP_y	g	W_{AMC}	L_{AMC}	L_{hgp}
64.14	70.17	11.38	6.93	5.41	43.62	48.85	72.11

Table 3.5: Optimized geometrical values of UWB antenna parts.

final dimensions of the various parts of the new version of the antenna are shown in Table 3.5 (see Fig. 2.3.2 and Fig. 2.3.3).

Fig. 3.4.3 shows the simulated and measured reflection coefficients of the new antenna, while Fig. 3.4.4 shows the realized prototype.

The simulated reflection ceofficient shows an UWB impedance matching on a 7.45 GHz band, ranging from 1.74 GHz to 9.19 GHz. In simulated s_{11} [dB] parameter trend, there is a slight mismatch close to the 2.61 GHz - 2.84 GHz band, where the maximum reflection coefficient value is equal to -8.58 dB. In the measurement phase, on the other hand, an impedance match was found on many sub-bands. The impedance mismatch found in several points of the measured reflection coefficient trend may be due to inaccuracies committed during the antenna construction phase. In particular, these effects could be attributed to the imperfect alignement of the frequency selective surfaces (FSS) with the monopole disk present on the upper face of
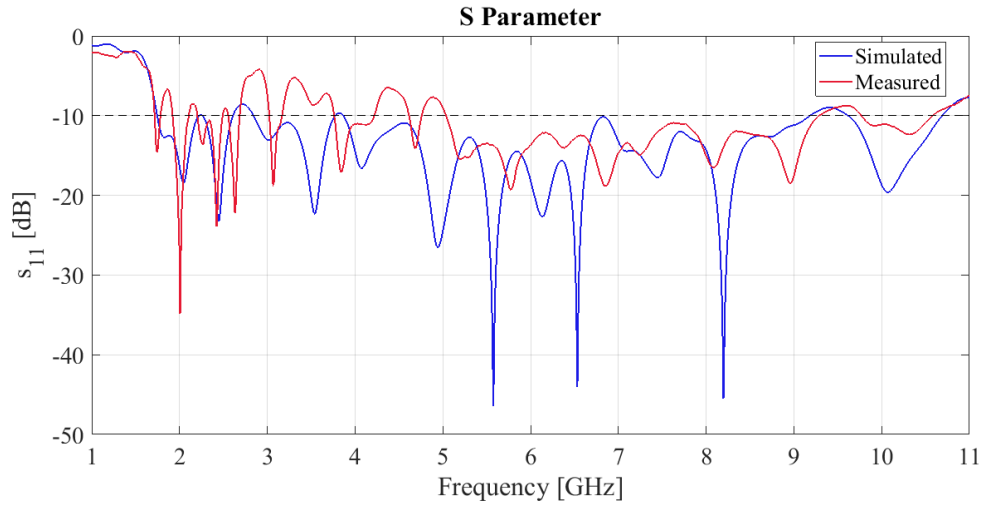
Figure 3.4.3: Wearable scaled UWB antenna reflection coefficients: simulated results (blue), and measured results (red).

the device. Despite this, the antenna has a good impedance matching in the bands in which the frequencies of interest are present (1.8 GHz - 3.6 GHz), and therefore it was possible to use it in the next measurement phase.

As for the original antenna described in Chapter 2 section 3, also in this case the component that contributes entirely to the total gain is the ϕ component and therefore presents a linear polarization along that direction. Fig. 3.4.5 shows the radiation patterns for the simulated gain of the antenna at 1.8 GHz and 3.6 GHz, i.e. at the frequencies corresponding to the peaks of the reflection coefficient of the sensor. Maximum gain at 1.8 GHz is 6.79 dB, while at 3.6 GHz the maximum gain is 8.63 dB.

3.4.3   Harmonic RADAR measurement setup

To test the functionality of the harmonic RADAR sensor combined with the UWB antenna, it was decided to implement the scenario represented in Fig. 3.4.6 in the laboratory. The scenario is made up of a system capable of transmitting a continuous wave signal at a certain frequency, and capable of receiving the backscattered harmonic signal at double frequency compared to the transmitted signal.

In order to have an idea of the power levels of the backscattered signal obtainable in receiving and therefore to define the range of the system, Friis formulas were used:
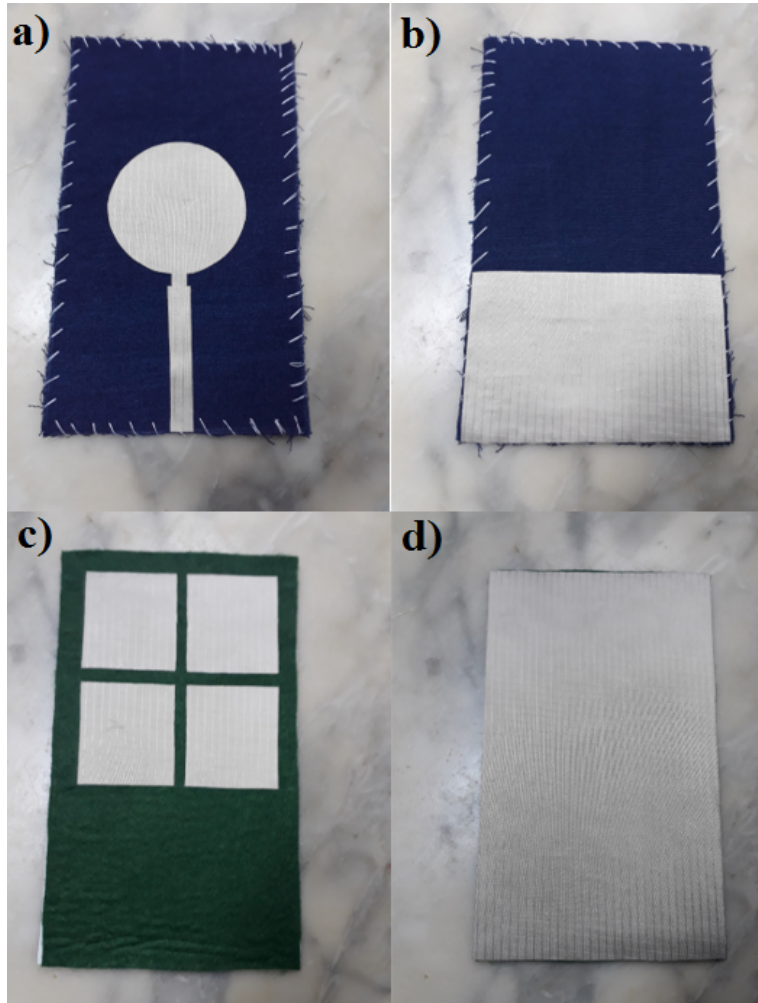
Figure 3.4.4: Realized prototype antenna: (a) circular monopole view; (b) half ground plane view; c) squared metamaterial view; d) floating full ground plane view.
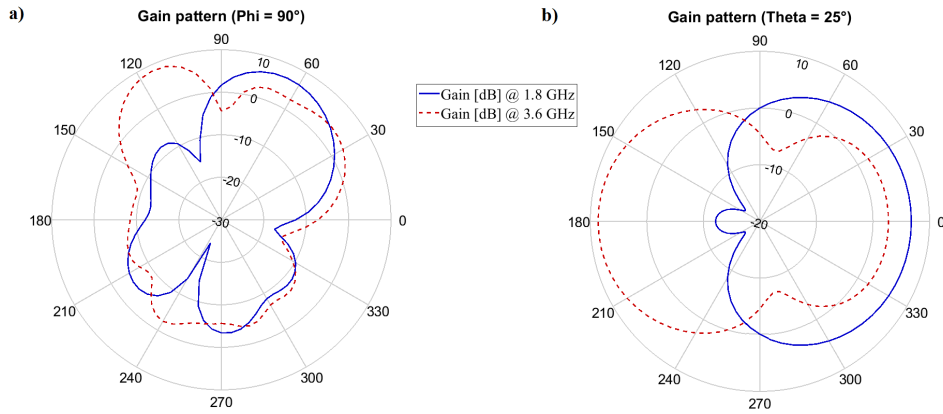
Figure 3.4.5: Gain radiation pattern of the UWB antenna: a) zenithal cut at 1.8 GHz, and 3.6 GHz ($\phi = 90°$); b) azimuthal cut at 1.8 GHz, and 3.6 GHz ($\theta = 25°$).
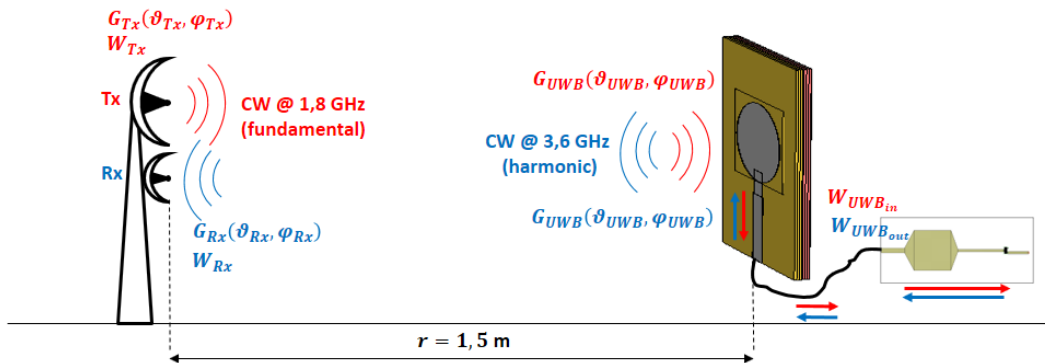
Figure 3.4.6: Harmonic RADAR scenario.

$$W_{Rx} = W_{Tx}G_T\left(\theta_T,\,\phi_T\right)G_R\left(\theta_R,\,\phi_R\right)L_{FS}L_{PA} \qquad (3.4.1)$$

where W_{Tx} and W_{Rx} are, respectively, the transmit and receive power in Watts, $G_T\left(\theta_T,\,\phi_T\right)$ and $G_R\left(\theta_R,\,\phi_R\right)$ are, respectively, the gains of the antenna in transmission and reception, oriented in space according to the given directions, $L_{FS} = \left(\frac{\lambda_0}{4\pi r}\right)^2$ is the free space attenuation due to the length of the link (r in fact is the distance between the transmitting and receiving antennas, λ_0 is the wavelength in the vacuum in which the system operates) and L_{PA} is the path attenuation, which makes it possible to take into account any obstacles or phenomena occurring in the channel.

Friis's formula can be written in decibels

$$\begin{aligned} W_{Rx}\left(dB\right) &= 10\log_{10}\left(EIRP\right) + 10\log_{10}\left(G_R\left(\theta_R,\,\phi_R\right)\right) \qquad (3.4.2) \\ &+ 10\log_{10}\left(L_{FS}\right) + 10\log_{10}\left(L_{PA}\right) \end{aligned}$$

where $EIRP = W_{Tx}G_T\left(\theta_T,\,\phi_T\right)$ is the effective radiated isotropic power.

Thanks to these relationships it is possible to carry out a preliminary analysis, in free space (without obstacles), to determine the range of action of the measuring system. The formulas must be used for the outward journey (Tx antenna → UWB antenna + harmonic RADAR) and for the return journey (UWB antenna + harmonic RADAR → Rx antenna). By setting, for example, $W_{Tx} = -10$ dBm, $G_T\left(\theta_T,\,\phi_T\right) = 6$ dB, $r = 1.5$ m, $G_{UWB}\left(\theta_{UWB},\,\phi_{UWB},\,1.8\,\text{GHz}\right) = 6.79$ dB, $L_{PA} = 0$ dB (free space), at the input of the harmonic RADAR sensor $W_{UWB_{in}} = -38.29$ dBm would be obtained, a close result with the -40 dBm assumed in the sensor design phase. On the return journey, the second harmonic component at 3.6 GHz must be taken into account. From the results reported in Fig. 3.3.5 b), it was placed in (3.4.2), $W_{UWB_{out}} = -63.11$ dBm, $G_{UWB}\left(\theta_{UWB},\,\phi_{UWB},\,3.6\,\text{GHz}\right) = 8.63$ dB, $r = 1.5$ m, $G_R\left(\theta_R,\,\phi_R\right) = 2$ dB, $L_{PA} = 0$ dB, obtaining in reception $W_{Rx} = -99.57$ dBm.

In order to test the wearable harmonic RADAR sensor, the scenario shown in Fig. 3.4.6 was replicated in the laboratory. In Fig. 3.4.7 the measurement scenario is shown where a Vivaldi antenna with a gain of 6 dB at 1.8 GHz and a UWB monopole antenna with a gain of 2 dB at 3.6 GHz were used. The two antennas are placed at a distance of 1.5 m from the wearable UWB antenna with the harmonic RADAR sensor. The signals sent and received were generated through two USRP 2920 of National Instruments [17], thanks to which it was possible to verify and measure the response of the diode placed on the sensor following an interrogation with a continuous wave signal at 1.8 GHz with a power of -10 dBm.
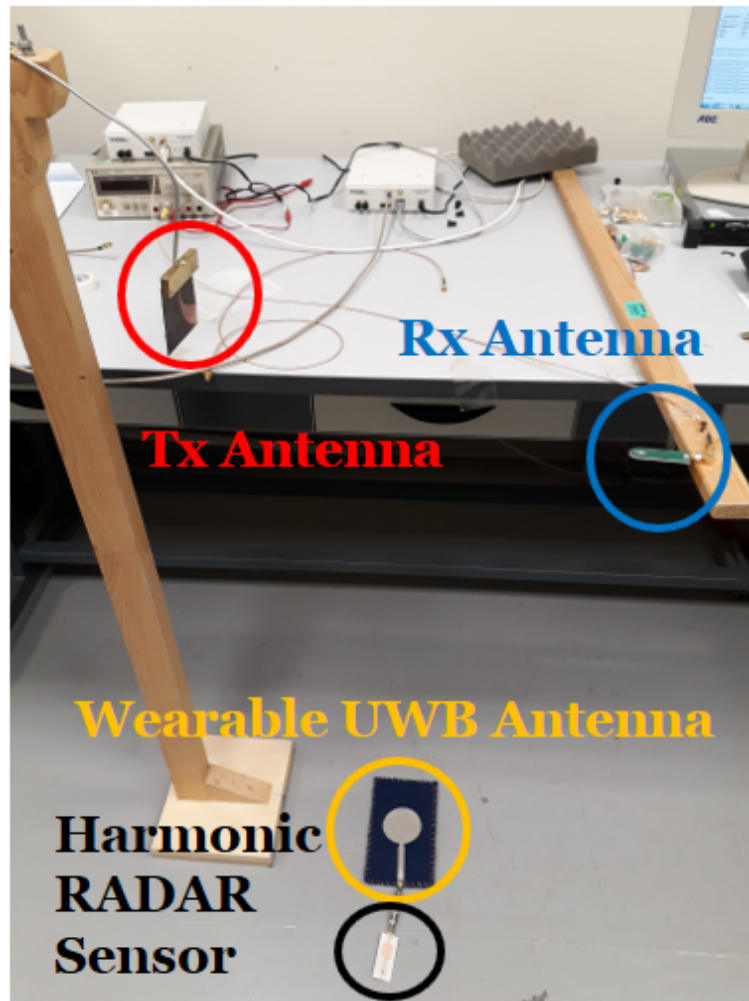
Figure 3.4.7: Realized scenario. The transmitting and receiving antennas are placed at a distance $r = 1.5$ m from the harmonic RADAR sensor.
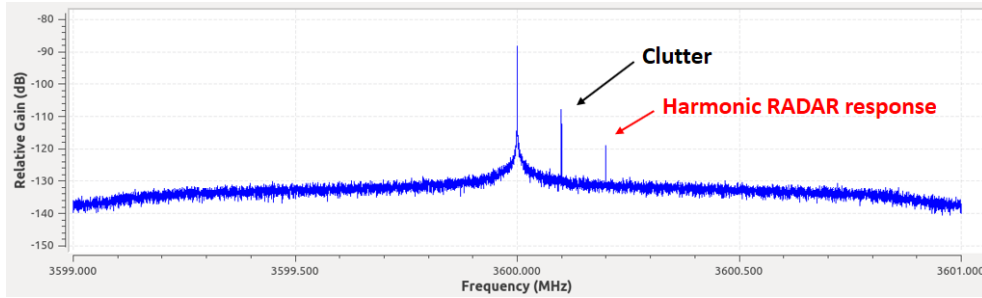
Figure 3.4.8: Harmonic RADAR sensor response at 3600.2 MHz.

Through a software for the management of the two USRP (Universal Software Radio Peripheral) it was possible to measure the continuous wave signal in second harmonic at 3.6 GHz, obtaining a power value, for the signal, equal to about -115 dBm. Fig. 3.4.8 shows the spectrum of the signal received by the USRP associated with the receiver. In order to detect the signal coming from the sensor, a traslated signal of 100 kHz compared to the nominal 1.8 GHz was sent in transmission. In fact, in the second harmonic it was possible to detect the backscattered signal from the antenna at 3600.2 MHz, which is exactly the second harmonic of the interrogating signal.

In Fig. 3.4.8, however, the presence of a spectral component centered around 3600.1 MHz can be seen. That component is probably related to some spurious reflection related to the measurement scenario being backscattered on the wearable UWB antenna receiver.

In order to verify the effective benefit introduced by the use of the matching network designed for the chosen zero bias Schottky diode, a measurement was made by affixing the HSMS-2850 diode to the UWB antenna. In Fig. 3.4.9 it can be seen how the RADAR tag (wearable UWB antenna + diode only), once placed in the same conditions described above, was not able to provide a detectable backscatter response at that distance (it is detected for distances of approximately 0.4 m).

3.5   Possible Upgrade Studies

After being able to create a harmonic RADAR with the characteristics just described, we wanted to investigate the potential of the proposed sensor, in order to be able to use it not only with the simple purpose of being detected, but also with the ability to communicate possible variation introduced by other physical quantities present in the environment in which it would be used. Just think of the more classic forms of commercial sensors, which
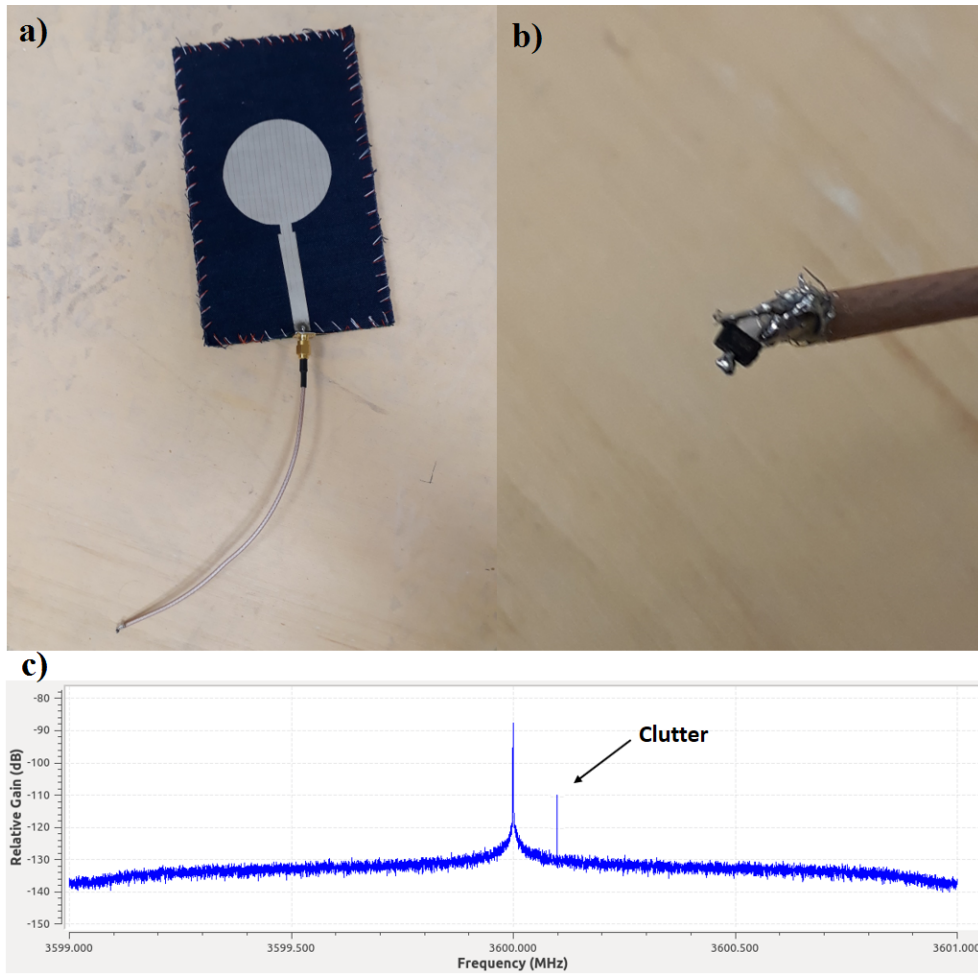
Figure 3.4.9: Measurement without matching network: a) UWB antenna directly connected to the HSMS-2850 zero bias Schottky diode; b) diode soldered directly on coaxial cable; c) detected response (only the clutter component is detected).
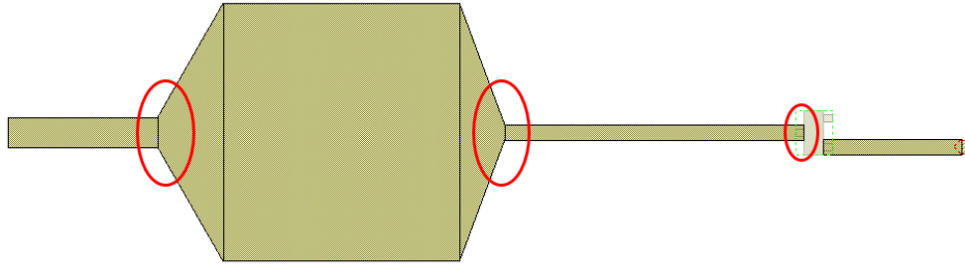
Figure 3.5.1: Possible application points for the ideal capacitor.

may be able to measure physical quantities such as temperature, humidity, brightness, proximity to other objects, and others. At this point, a series of analyzes were carried out on the final structure of the sensor represented in Fig. 3.4.1.

3.5.1 Application of Series Capacitors

The first approaches aimed at verifying the presence of sensitive points to the possible occurrence of physical variations. The approach involved the insertion of an ideal capacitor between the various junctions existing between the three microstrip line sections that precede the Schottky diode's anode.

This approach can be motivated by standing that variations in the capacitance value of the capacitor, placed in one of the positions indicated in Fig. 3.5.1, should have corresponded variations in the impedance seen at the input from the diode. This impedance variation could have resulted in a controlled shift of the intrinsic resonance frequencies of the sensor, from which to obtain information on a possible change in a physical state occurring near the device. After a few attempts, it was found that the most sensitive microstrip line section is the one closest to the anode of the diode (violet microstrip line in Fig. 3.5.2); the others, on the other hand, do not introduce significant variations (almost zero variations).

As can be seen from Fig. 3.5.2, applying the ideal capacitor in the position highlighted in green, small variations and small capacitance values (a few picoFarads) correspond to significant shifts for the first peak of the reflection coefficient (corresponding to the 2 GHz) and least significant shifts on the second peak (at 4 GHz). By positioning the capacitor in the position highlighted in blue (in direct contact with the anode of the diode), an effect practically mirrored was obtained compared to that obtained previously (capacitor in the green highlighted area). In both cases, as the capacitance
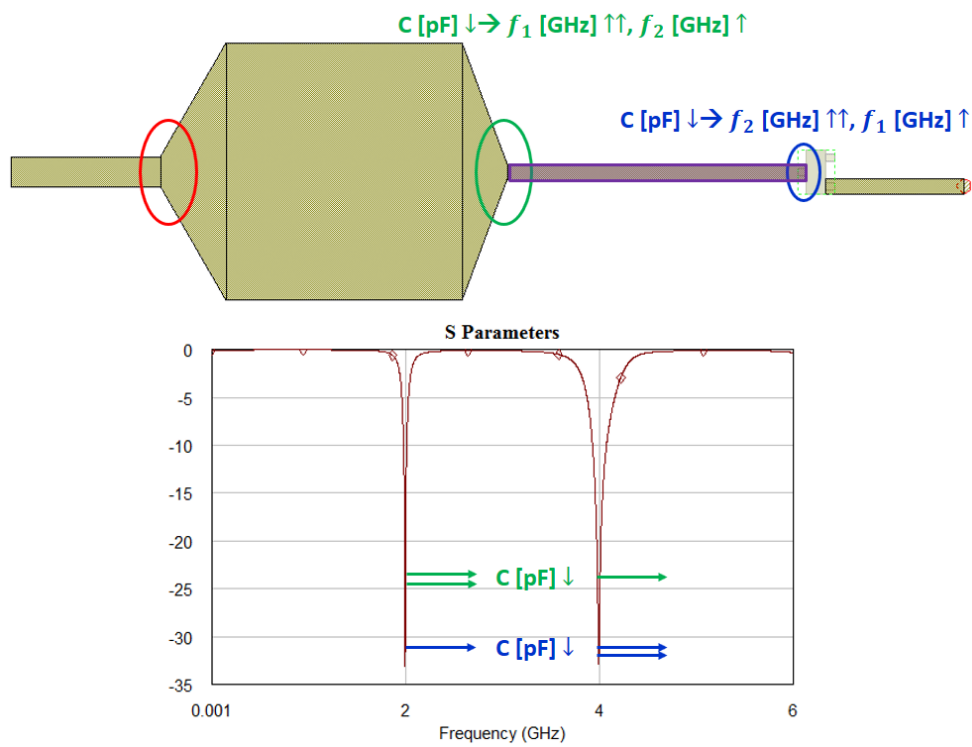
Figure 3.5.2: Sensitive microstrip section and sensitive points of the harmonic RADAR sensor. Effects introduced on s_{11} parameter by the use of capacitors in the points highlighted in green and blue.

f_r [GHz]	$2f_r$ [GHz]	C_1 [pF]	C_2 [pF]
2,015	4,03	140	3,88
2,02	4,04	110	3,07
2,025	4,05	90	2,32
2,03	4,06	80	1,9
2,04	4,08	64,5	1,49
2,05	4,1	47,5	1,23
2,06	4,12	40	1,03
2,07	4,14	33,5	0,85
2,08	4,16	28	0,73
2,1	4,2	23	0,55
2,105	4,21	22	0,52
2,115	4,23	21	0,45
2,12	4,24	20	0,42

Table 3.6: Optimal values of capacitances C_1 and C_2 with which a homogeneous frequency shift with a multiplication factor equal to 2 is obtained.

value decreases, the resonance peaks shift to the right; for high capacitance values (in both cases) the response plotted in Fig. 3.3.5 (c) is obtained.

Given the results obtained from this analysis, it was decided to apply two capacitors simultaneously in the two sensitive positions (green and blue) in order to have a shift effect such that the second resonance peak of s_{11} parameter was always corresponding to double the frequency of first resonance. After some analyzes conducted in AWR simulation environment, it was possible to identify pairs of values for the capacitors C_1 and C_2 for which it would be possible to obtain a simultaneous shift of both peaks of reflection coefficient while maintaining the multiplication factor equal to 2. Table 3.6 shows the capacitance values of the capacitors for which it would be possible to obtain the desired shift.

In Fig. 3.5.3 the curves relating to the two capacitances are represented, the values of which are reported in Table 3.6. Given the similarity of the two trends found for C_1 and C_2, making the ratio between the capacitance values found for the two capacitors, it was possible to extract the proportionality ratio trend. Given that this trend was almost constant, we have considered its average value:

$$\left(\frac{C_2}{C_1}\right)_{average} = 0.0247 \tag{3.5.1}$$
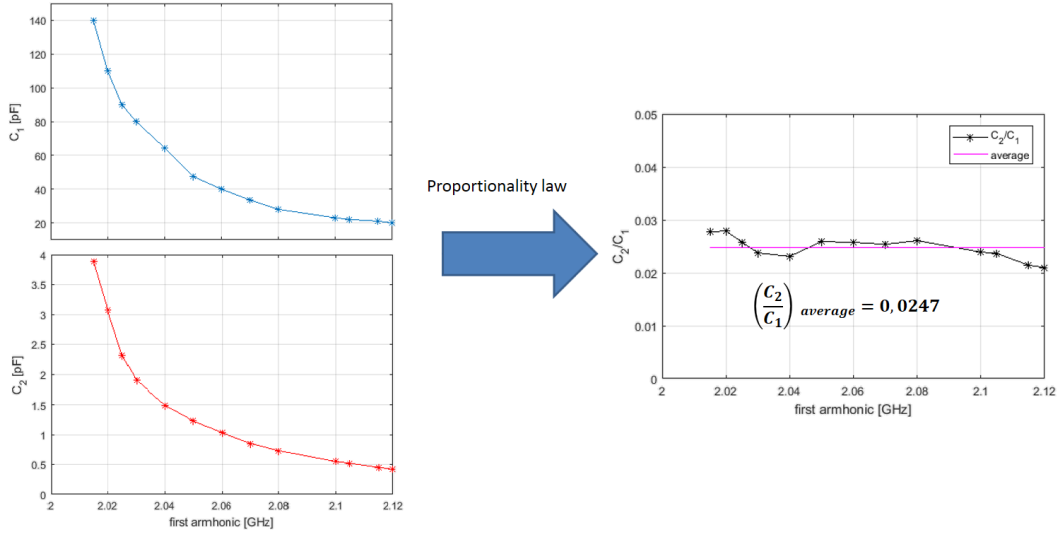
Figure 3.5.3: Trends of the capacitances C_1 and C_2 as the first resonance frequency (first harmonic) varies. On the right is the proportionality law between C_1 and C_2.

This solution would allow, from the theoretical point of view, to have shifts in the reflection coefficient of the harmonic RADAR while maintaining a double proportionality ratio between the resonance frequencies (the second is always double the first). However, if we reasoned from a practical and constructive point of view, the capacitor C_2 would be in a critical position, as it would be welded directly in contact with the anode of the diode. As seen in Fig. 3.4.2 (measured reflection coefficient), the effect introduced by the parasites following the application of a welding, would risk compromising the functioning of the device itself. Even the fact of being able to find capacitors capable of satisfying the condition of proportionality expressed in (3.5.1) is not obvious to obtain.

For these reasons, the structure of the sensor was further investigated, in order to obtain the same effect described above, but trying to use two identical capacitors, i.e. with a proportionality ratio $\left(\frac{C_2}{C_1}\right)_{average} = 1$. Through numerous tests and optimization processes it was possible to find the optimal condition depicted in Fig. 3.5.4.

During the optimization phase it was also realized that the microstrip line that connects the cathode of the Schottky diode to the via hole towards ground, causes variations on the trend of the reflection coefficient of the harmonic RADAR. The greatest effects are produced on the peak centered around 4 GHz, without affecting too much the behavior of the s_{11} coefficient
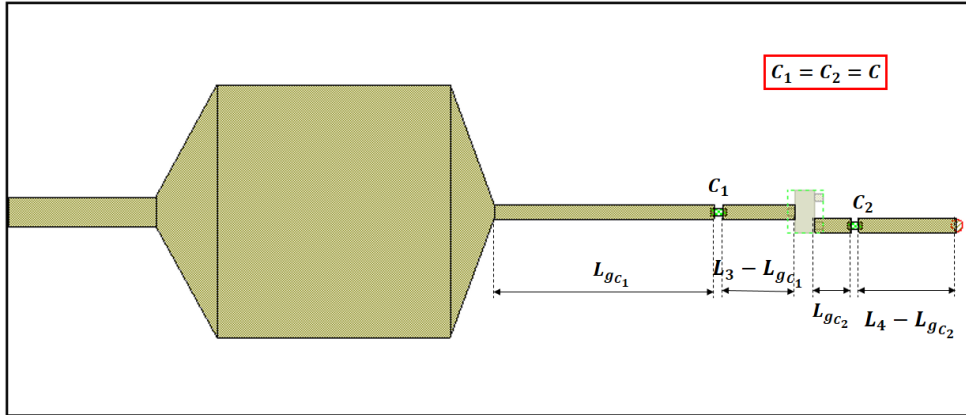
Figure 3.5.4: Harmonic RADAR with capacitors C_1 and C_2 equal to each other.

at 2 GHz. Table 3.7 shows the value of $C_1 = C_2 = C$ for which it is possible to obtain a shift in frequency to the reflection coefficient while maintaining the proportionality ratio equal to 2.

The positions in which the capacitors must be applied are of fundamental importance to achieve the goal. The microstrip lenghts $L_{g_{C_1}} = 15$ mm and $L_{g_{C_2}} = 2.5$ mm were obtained through the use of the *Simplex* and *Random Local* optimizers.

In the next step of the analysis it was thought to insert in the circuit capacitors capable of varying their capacitance value with temperature changes. For this purpose a research was conducted to find commercial capacitors that had this property. The best result was provided by ceramic capacitors in Y5V [18], which, as can be seen from the example graphed in Fig. 3.5.6, show variations in capacitance for certain temperature ranges.

As can be seen in Fig. 3.5.7, however, in the frequency range of interest (GHz) this type of capacitor always has the same capacitance value regardless of the nominal value. This type of capacitors in fact turns out to be efficient for frequencies of the order of MHz or less.

3.5.2   Application of Grounded Shunt Stubs

Based on what was obtained with the introduction of series capacitors in the harmonic RADAR circuit, we tried to find an alternative way to produce the effect of frequency shift of the reflection coefficient while maintaining the proportionality ratio equal to 2. Given the impossibility of using capacitors, it was decided to introduce passive elements into the circuit that would be able to replicate the behavior previously studied. After several attempts and

f_r [GHz]	$2f_r$ [GHz]	C [pF]
2,011	4,017	30
2,017	4,027	20
2,033	4,059	10
2,036	4,067	9
2,041	4,076	8
2,046	4,089	7
2,054	4,105	6
2,063	4,129	5
2,078	4,161	4
2,088	4,182	3,5
2,101	4,208	3
2,118	4,24	2,5
2,142	4,284	2

Table 3.7: Optimal values of the capacitance $C = C_1 = C_2$ with which it is possible to obtain a homogeneous frequency shift with a multiplication factor equal to 2.
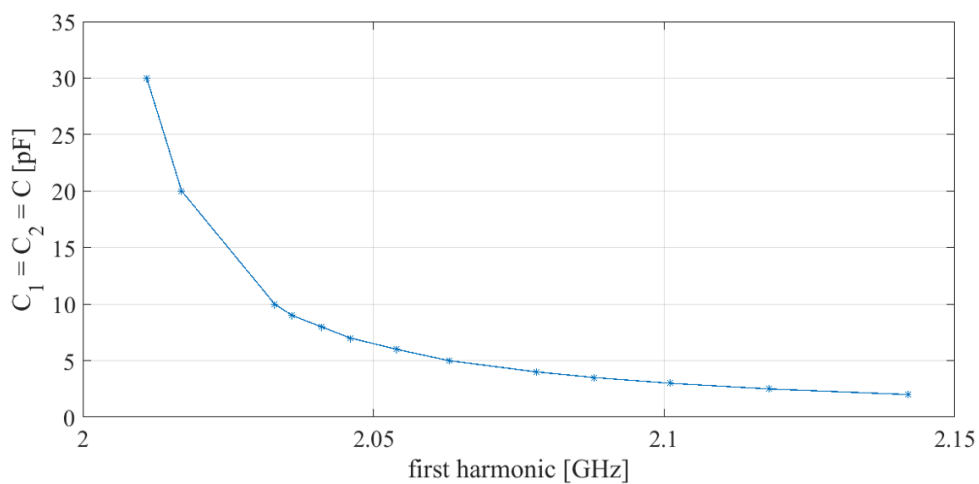
Figure 3.5.5: Trends of the capacitance $C_1 = C_2 = C$ as the first resonance frequency (first harmonic) varies.
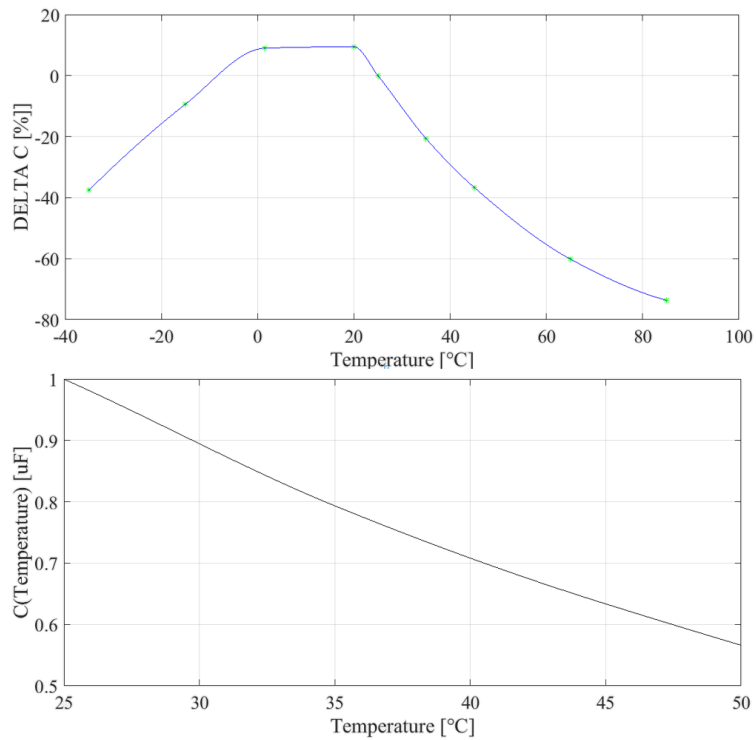
Figure 3.5.6: Example of how the capacitance of a capacitor with a Y5V dielectric, having a nominal value of 1 μF (08053G105ZAT2A), behaves when the temperature varies.
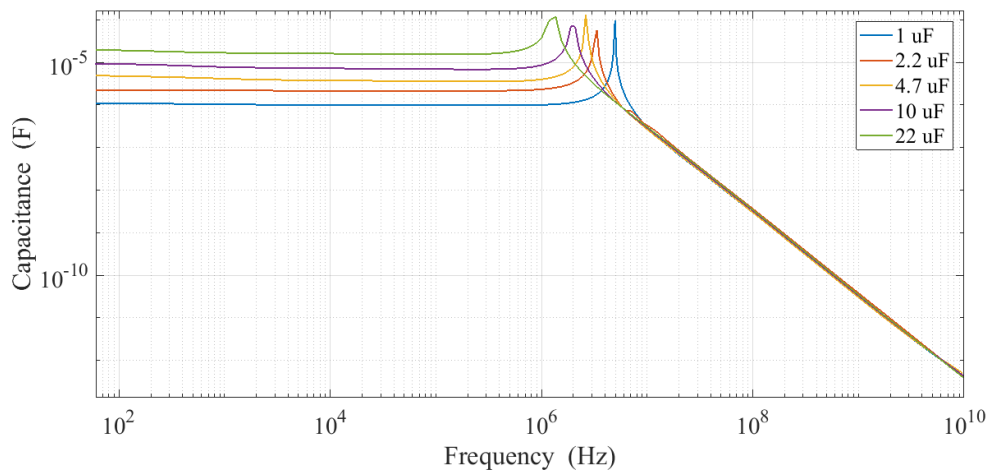
Figure 3.5.7: Behavior of some capacitors with Y5V dielectric as the frequency varies.

optimization processes, the choice fell on the use of stubs having certain geometric dimensions connected to ground through via holes, placed in parallel with respect to the microstrip lines that composes the harmonic RADAR. The optimized circuit is shown in Fig. 3.5.8.

In this case the stubs must be inserted in different points than in the previous case. The quantities $L_{g_{C_1}} = 2$ mm, $L_{g_{C_2}} = 2.5$ mm, $W_{stub} = 1$ mm, and $L_{stub1} = L_{stub2} = 11.4$ mm, were obtained by means of *Simplex* and *Random Local* optimization processes. Unlike the previous case (with capacitors), where the impedance matching in the bands of interest was always preserved as the capacitance varied, in this case the reflection coefficient was consistent with what was desired only for certain lengths of the stubs. Another substantial difference was that the stub placed upstream of the diode anode (*stub1*) was the major responsible for the frequency shift of both resonance peaks. However, the displacement of the second peak occurred enormously if the second stub with a certain length was not affixed. On the other hand, the stub placed downstream of the cathode of the Schottky diode (*stub2*) did not allow, through variations in its length, to shift the second peak as in the case of capacitors. Its purpose was to allow a controlled shift of the second peak once changes were made to the length values of the first stub. From the results obtained from the various simulation processes, it was clear that to obtain frequency shifts with a proportionality factor of 2, it was necessary to leave *stub2* with the optimized fixed length $L_{stub2} = 11.4$ mm, while the length of *stub1* could be varied within certain values. The *stub1* was therefore found to be sensitive element of the sensor, and could be able to detect the occurrence of possible variations of physical phenomena in its vicinity. Table 3.8 shows the values of L_{stub1} within which it was possible to obtain a frequency shift with proportionality equal to 2 without losing the impedance matching (-10 dB was taken as a reference).

As can be read from the columns of Table 3.8 which show the values of the reflection coefficient at f_1 (fundamental frequency), $2 \cdot f_1$ (second harmonic) and f_2 (frequency where the minimum value of the second resonance peak occurs), it has been made sufficient that the value of $s_{11} (2 \cdot f_1)$ [dB] falls in the band centered around f_2 to be able to consider satisfied the principle of frequency shift with double proportionality.

Future studies on this configuration will be carried out in order to be able to exploit it for the detection of variations of physical phenomena present in certain environments and contexts.
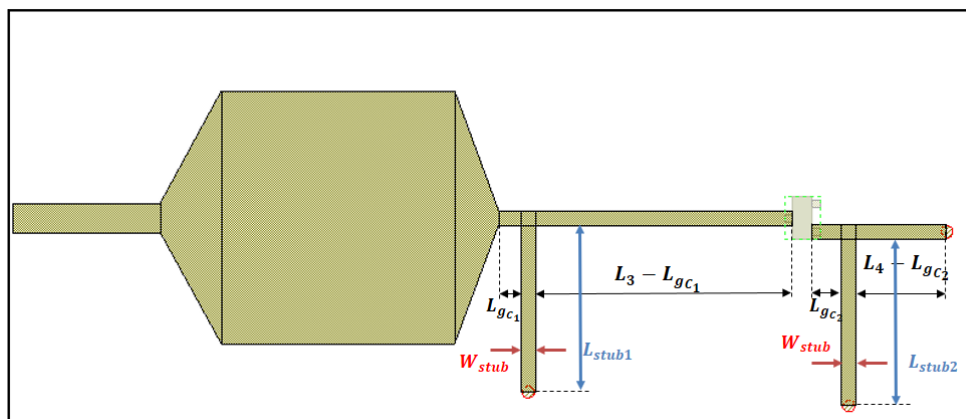
(a)
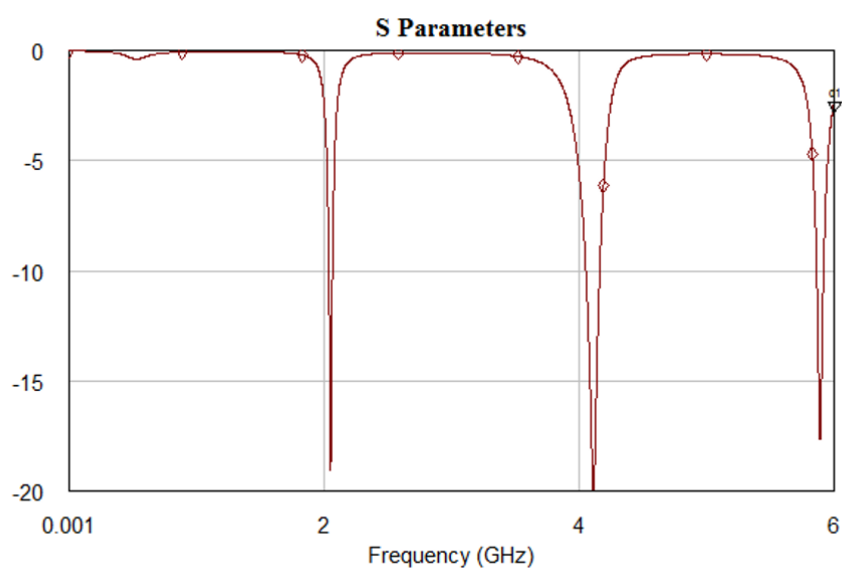
(b)

Figure 3.5.8: Capacitors replacing with a pair of grounded shunt stubs ($L_{stub1} = L_{stub2} = 11.4$ mm): (a) optimized final circuit, (b) reflection coefficient.

L_{stub1} [mm]	f_1 [GHz]	$s_{11}(f_1)$ [dB]	$2 \cdot f_1$ [GHz]	$s_{11}(2 \cdot f_1)$ [dB]	f_2 [GHz]	$s_{11}(f_2)$ [dB]
7	2,078	-12,49	4,156	-9,327	4,118	-17,93
8	2,072	-13,98	4,144	-12,93	4,117	-23,43
9	2,067	-15,44	4,134	-17,64	4,116	-37,2
10	2,062	-16,91	4,124	-23,71	4,116	-28,92
11	2,058	-18,42	4,116	-21	4,117	-21,67
12	2,055	-20,05	4,11	-17,18	4,12	-17,93
13	2,052	-21,79	4,104	-14,16	4,127	-15,5
14	2,049	-23,76	4,098	-11,74	4,138	-13,9
15	2,046	-26,02	4,092	-9,673	4,151	-13,04

Table 3.8: Optimal values of length L_{stub1} with which it is possible to obtain a homogeneous frequency shift with a multiplication factor equal to 2.
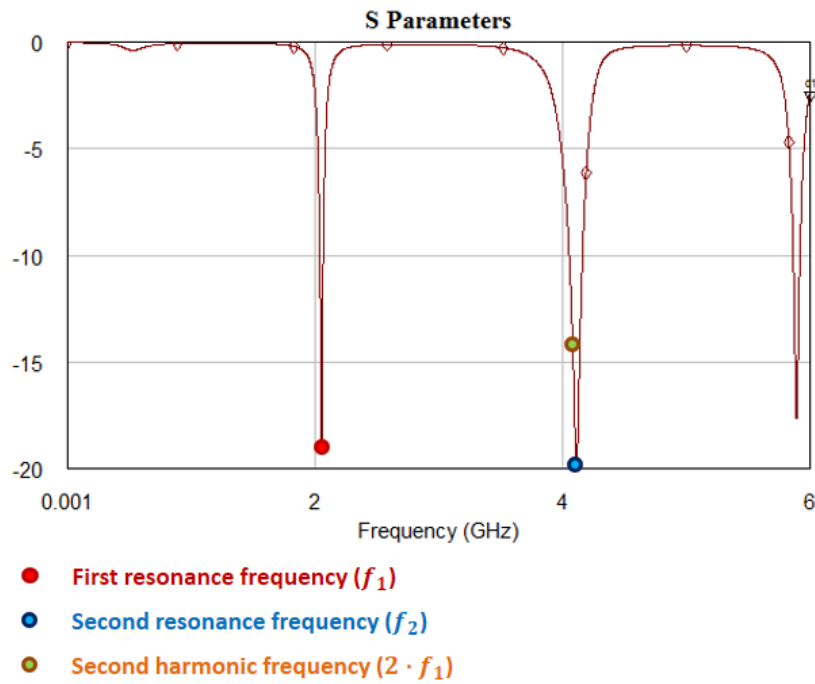

Figure 3.5.9: Definitions of "f_1", "$2 \cdot f_1$", and "f_2".

97

3.6   Conclusions

In this chapter, a sensor operating in the microwave frequency band has been described, which exploits the principle of harmonic RADAR thanks to the detector properties of the zero bias Schottky diode chosen for the application. From the theory of transmission lines, the design phase of the device involved the study and application of a completely passive network which had the purpose of balancing the capacitive reactance of the diode, in order to obtain an impedance match with 50 Ohms. The sensor was made and applied to an enlarged version of the wearable UWB antenna with metamaterials described in Chapter 2 section 3, in order to be used in a detection scenario based on the harmonic RADAR. From the measurements carried out in the laboratory, it was clear the sensor's ability to provide a second harmonic response to the transceiver system that interrogates it, even for low power values of the continuous wave interrogating signal (-10 dBm). The goodness of the results obtained from the measures, comparable with those that were the data estimated in the design phase, suggests that the system may be suitable for use in emergency situations where it is necessary to try to identify and save people in post-disaster scenarios.

Bibliography

[1]   S. Preradovic, and N. C. Karmakar. *Chipless RFID: bar code of the future*, IEEE Microw. Mag., Vol. 11, pp. 87–97, 2010.

[2]   C. Mandel, B. Kubina, M. Schüßler, and R. Jakoby. *Metamaterial-inspired passive chipless radio-frequency identification and wireless sensing*, Ann. Telecommun., Vol. 68, pp. 385–399, 2013.

[3]   A. Vena, E. Perret, and S. Tedjini. *Chipless RFID tag using hybrid coding technique*, IEEE Trans. Microw. Theory Tech., Vol. 59, (Issue: 12), pp. 3356–3364, 2011.

[4]   B. Kubina, J. Romeu, C. Mandel, M. Schüßler and R. Jakoby. *Quasi-chipless wireless temperature sensor based on harmonic radar*, Electronics Letters, Vol. 50, (Issue: 2), pp. 86-88, Jan. 2014.

[5]   B. G. Colpitts, and G. Boiteau. *Harmonic radar transceiver design: miniature tags for insect tracking*, IEEE Trans. Antennas Propag., Vol. 52, (Issue: 11), pp. 2825–2832, 2004.

[6]   R. Baccarelli, G. Orecchini, F. Alimenti, and L. Roselli. *Feasibility study of a fully organic, CNT based, harmonic RFID gas sensor*, IEEE Int. Conf. RFID – Technologies and Applications, Nice, France, November 2012

[7]   F. Alimenti, and L. Roselli. *Theory of zero-power RFID sensors based on harmonic generation and orthogonally polarized antennas*, Prog. Electromagn. Res., Vol. 134, pp. 337–357, 2013.

[8]   A. Di Carlofelice, E. Di Giampaolo, M. Elaiopoulos, M. Feliziani, M. Roselli, and P. Tognolatti. *Localization of radio*

emitters into collapsed buildings after earthquake: measurements of path loss and direction of arrival, International Symposium on Electromagnetic Compatibility - EMC EUROPE, Sept. 2012.

[9]   D. M. Pozar. *Microwave Engineering, 4th Edition*, Wiley, 2011.

[10]   S. Yngvesson. *Microwave Semiconductor Devices*, Kluwer, Norwell, Mass., 1991.

[11]   R. Ludwig and P. Bretchko. *RF Circuit Design: Theory and Applications*, Prentice-Hall, Upper Saddle River, N.J., 2000.

[12]   S. A. Maas. *Nonlinear Microwave and RF Circuits, 2nd edition*, Artech House, Norwood, Mass., 2003.

[13]   awr.com/awr-software/products/microwave-office

[14]   rogerscorp.com/-/media/project/rogerscorp/documents/advanced-connectivity-solutions/english/data-sheets/ro4000-laminates-ro4003c-and-ro4350bdasta-sheet.pdf

[15]   awr.com/awr-software/options/tx-line

[16]   awr.com/awr-software/products/axiem

[17]   ni.com/it-it/shop/wireless-design-test/what-is-a-usrp-software-defined-radio.html

[18]   avx.com/products/ceramic-capacitors/surface-mount/y5v-dielectric

Chapter 4

Microwave Characterization of Unconventional Materials

4.1 Introduction

The accurate estimation and knowledge of the electromagnetic characteristics of dielectrical materials is very important in many fields of application and expecially in microwave circuits, antennas, and sensors design. In fact, relative dielectric constant and loss tangent accurate estimation of the dielectric substrate has a huge impact on design strategies, not only because the final dimensions of the circuit (or antenna) depend on them, but also the final performances depend (gain, impedance matching, noise figure, etc.).

This type of analysis covers many branches of industry and research:

- electronic industries (Integrated Circuits (IC) substrates, innovative materials like graphene, metamaterials, etc.);

- aerospace and defence (absorbtion coefficients determination of the panels that cover the aircraft equipped with stealth technology, radome characterization for RADAR and Telescope antennas coating, etc.);

- materials industry (ceramics, plastics and polymers, liquid crystals, etc.);

- pharmaceutical, biomedical and health safety industry (material characterization for Specific Absorption Rate (SAR) analysis, human tissues characterization, bio-sensors, drugs composition analysis, etc.);

- agri-food industry (food conservation / preservation state analysis, oils composition analysis, etc.).
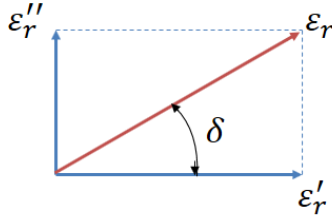
Figure 4.1.1: Relative dielectric constant and loss tangent definitions.

A good estimation of the dielectric parameters of materials, in the band of frequencies of interest, is certainly useful in the simulation phase. An accurate model allows to obtain a more realistic estimate of the subsequent measurement and test steps.

Usually, for the most common materials in microwave design the respective manufacterers provide dielectric characteristics (for some frequencies) in their own technical documentation. However, for design and research needs, it may be necessary to characterize materials (also in common use) whose electromagnetic characteristics are not known.

The parameters that describe a dielectric material from the electromagnetic point of view are the relative dielectric constant and the loss tangent. The relative dielectric constant is defined as a complex quantity defined as:

$$\varepsilon_r = \varepsilon_r^{'} - j\varepsilon_r^{''} \tag{4.1.1}$$

where $\varepsilon_r^{'}$ takes into account the energy stored in the material, and $\varepsilon_r^{''}$ takes into account losses due largely to thermal agitation due to dissipation within the material (it is proportional to the non-ideality of the material).

The ratio between the energy lost per cycle and the energy stored per cycle in the material is the loss tangent:

$$\tan\delta = \frac{\varepsilon_r^{''}}{\varepsilon_r^{'}} = D_f = \frac{1}{Q_d} \tag{4.1.2}$$

where D_f is the dissipation factor, and Q_d is the quality factor due to the dielectric material.

A qualitatively description of the typical behavior of permittivity ($\varepsilon_r^{'}$ and $\varepsilon_r^{''}$) as a function of frequency is depicted in Fig. 4.1.2.

The permittivity of a material is related to a variety of physical phenomena, like ionic conduction, dipolar relaxation, atomic polarizzation, and electronic polarization. In the low frequency range, $\varepsilon_r^{''}$ is dominated by the influence on ion conductivity. The variation of permittivity in the microwave
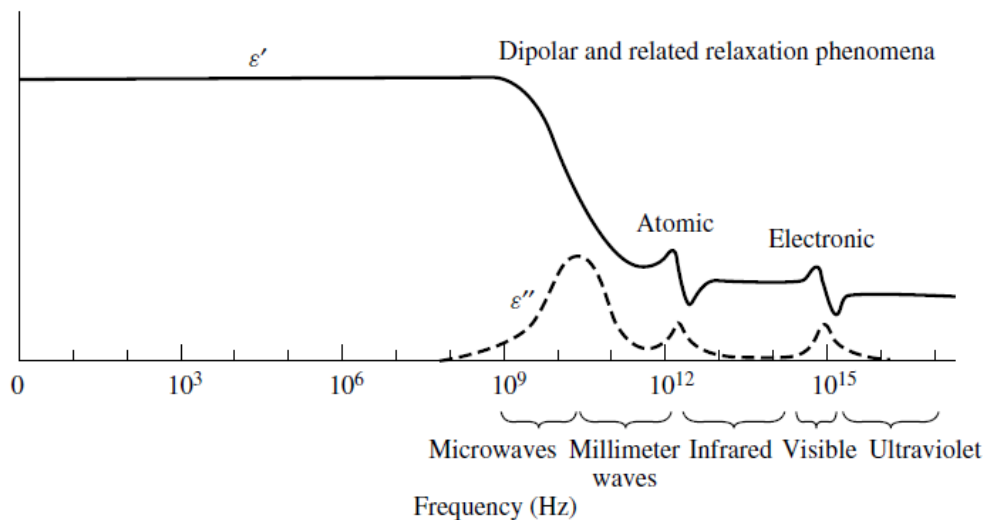
Figure 4.1.2: Frequency dependence of permittivity for a hypotetical dielectric [1].

range is mainly caused by dipolar relaxation, and the absorption peaks in the infrared region and above is mainly due to atomic and electronic polarizations. An accurate description of these phenomena is reported in [2].

There are several methods to extrapolate these characteristics and the use of one rather than the other can depend on the frequencies in which one needs to carry out the analysis (low or high frequencies), and on the type of material (solids, liquid solutions, etc.).

Table 4.1 shows a summary scheme of the "families" of techniques existing in the literature.

This work focuses in particular on the "family" of transmission lines, and specifically in planar microstrip transmission lines "family".

4.2   Microstrip Line

Microstrip line, shown in Fig. 4.2.1, is the most widely used planar transmission structure.

A microstrip line consists of a strip conductor and a ground plane separated by a dielectric substrate. As the dielectric constant of the substrate is usually high, the field is concentrated near the substrate. The wave propagating on this type of structure is not a pure TEM wave but a quasi-TEM mode. Accurate determination of the wave propagation on a microstrip line requires intense numerical simulations. But in engineering design, it is possible take
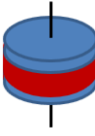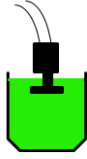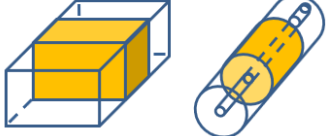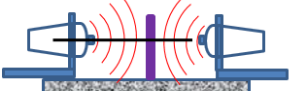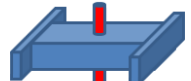
Low Frequency	Parallel Plate		Accurate. Best for low frequencies; thin flat sheets.
High Frequency	Coaxial Probe		Broadband, convenient, non-destructive. Best for lossy Materials Under Tests (MUTs); liquids and semi-solids.
	Transmission Line		Broadband, convenient, non-destructive. Best for lossy to low loss MUTs. Machineable solids.
	Free Space		Broadband; Non-contacting. Best for flats sheets, powder, high temperatures.
	Resonant Cavity		Single Frequency; Accurate. Best for low loss MUTs; small samples.

Table 4.1: Summary scheme of the dielectric parameters extraction techniques existing in literature.
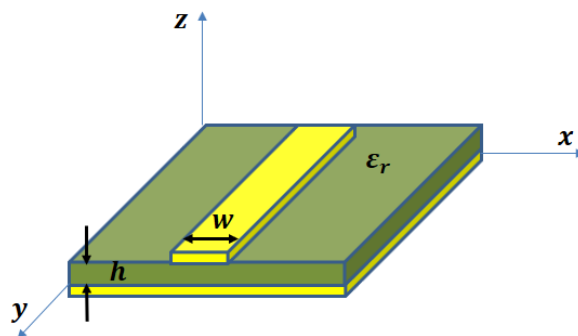
Figure 4.2.1: Microstrip line.
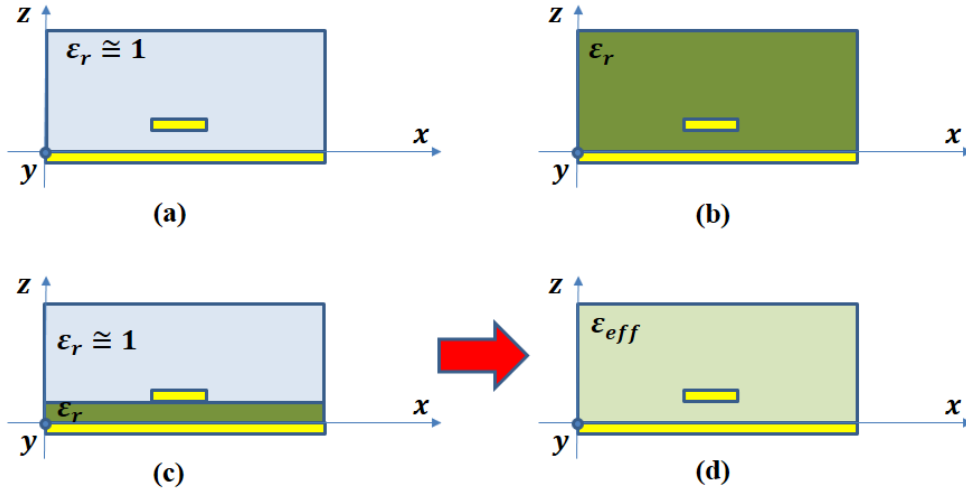
Figure 4.2.2: Effective dielectric constant concept: (a) microstrip fully filled with air, (b) microstrip fully filled with dielectric with permittivity ε_r, (c) microstrip partially filled with dielectric with permittivity ε_r, and (d) microstrip fully filled with dielectric with permittivity ε_{eff}.

the wave in a microstrip line as TEM wave, and use the quasi-static method to calculate the distributed capacitance, and then calculate its propagation constant, wavelength, and characteristic impedance.

In the analysis of microstrip lines using quasi-static method, it is possible to introduce the concept of the effective dielectric constant, as shown in Fig. 4.2.2.

If the filling medium is air ($\varepsilon_r \cong 1$), the microstrip line can support the TEM wave, and its phase velocity equals the speed of light c. If the transmission system is fully filled with a dielectric material with $\varepsilon_r > 1$, the microstrip can support TEM wave, and its phase velocity:

$$v_p = \frac{c}{\sqrt{\varepsilon_r}} \tag{4.2.1}$$

If a microstrip line is partially filled with a dielectric material with dielectric constant ε_r, as shown in Fig. 4.2.2 (c), it is possible to introduce the concept of effective permittivity ε_{eff} to calculate the transmission line wavelength λ_g, phase velocity v_p, and characteristic impedance Z_c:

$$\lambda_g = \frac{\lambda_0}{\sqrt{\varepsilon_{eff}}} \tag{4.2.2}$$

$$v_p = \frac{c}{\sqrt{\varepsilon_{eff}}} \tag{4.2.3}$$

105

$$Z_c = \frac{Z_c^0}{\sqrt{\varepsilon_{eff}}} = \frac{1}{v_p C_l} \qquad (4.2.4)$$

where c is the speed of light, C_l is the distributed capacitance of the microstrip, and Z_c^0 is the characteristic impedance of the microstrip when the filling medium is air.

In the most cases, the thickness of the strip is negligible ($t/h \leq 0.005$). The characteristic impedance and effective permittivity can be calculated using appropriate equations. The dielectric constant and characteristic impedance are given by [3]:

$$\varepsilon_{eff} = \begin{cases} \frac{\varepsilon_r+1}{2} + \frac{\varepsilon_r-1}{2} \left[\left(1 + 12\frac{w}{h}\right)^{-\frac{1}{2}} + 0.041\left(1 - \frac{w}{h}\right)^2 \right], & \text{for } \frac{w}{h} \leq 1 \\ \frac{\varepsilon_r+1}{2} + \frac{\varepsilon_r-1}{2} \left(1 + 12\frac{w}{h}\right)^{-\frac{1}{2}}, & \text{for } \frac{w}{h} > 1 \end{cases} \qquad (4.2.5)$$

$$Z_c = \begin{cases} \frac{60}{\sqrt{\varepsilon_{eff}}} \ln\left(\frac{8h}{w} + \frac{w}{4h}\right) & \text{for } \frac{w}{h} \leq 1 \\ \frac{120\pi}{\sqrt{\varepsilon_{eff}}} \frac{1}{1.393 + \frac{w}{h} + \ln\left(\frac{w}{h} + 1.4444\right)} & \text{for } \frac{w}{h} > 1 \end{cases} \qquad (4.2.6)$$

Actually, the thickness of strip conductor affects the transmission line properties of the microstrip line. It is possible to assume $t < h$ and $t < w/2$. If the thickness of the strip t is not negligible, the effective dielectric constant should be modified [3]:

$$\varepsilon_{eff}(t) = \varepsilon_{eff} - \delta\varepsilon_{eff} \qquad (4.2.7)$$

with

$$\delta\varepsilon_{eff} = (\varepsilon_r - 1) \frac{t}{4.6h\sqrt{\frac{w}{h}}} \qquad (4.2.8)$$

We should also introduce a concept of effective relative strip width w_{eff} :

$$w_{eff} = \begin{cases} w + \frac{1.25t}{\pi} \left[1 + \ln\left(\frac{4\pi w}{t}\right)\right], & \text{for } \frac{w}{h} \leq \frac{1}{2\pi} \\ w + \frac{1.25t}{\pi} \left[1 + \ln\left(\frac{2h}{t}\right)\right], & \text{for } \frac{w}{h} > \frac{1}{2\pi} \end{cases} \qquad (4.2.9)$$

The attenuation factor of microstrip consists of dielectric loss factor $\alpha = \alpha_c + \alpha_d$ [3]. The dielectric loss factor is given by

$$\alpha_d \left[\frac{\text{dB}}{\text{unit length}}\right] = 27.3 \frac{\varepsilon_r}{\varepsilon_r - 1} \frac{\varepsilon_{eff} - 1}{\sqrt{\varepsilon_{eff}}} \frac{\tan\delta}{\lambda_0} \qquad (4.2.10)$$

and the conductor loss factor can be calculated by [4]

$$\alpha_c \left[\frac{\text{dB}}{\text{unit length}} \right] = \begin{cases} \frac{10}{\pi h \ln(10)} \frac{R_s}{Z_c} \frac{32-(w/h)^2}{32+(w/h)^2} \left[1 + \frac{h}{w} \left(1 + \frac{\partial w}{\partial t} \right) \right] & \text{for } \frac{w}{h} \leq 1 \\ \frac{20}{\pi \ln(10)} \frac{\varepsilon_{eff} Z_c R_s}{\eta_0^2} \left\{ \frac{w}{h} + \frac{6h}{w} \left[\left(1 - \frac{h}{w} \right)^5 + 0.08 \right] \right\} \left[1 + \frac{h}{w} \left(1 + \frac{\partial w}{\partial t} \right) \right] & \text{for } \frac{w}{h} > 1 \end{cases}$$

$$(4.2.11)$$

where $R_s = \sqrt{\frac{2\pi f_r \mu_0}{2\sigma_{Cu}}}$ is the surface resistivity of the microstrip, $\eta_0 = \sqrt{\frac{\mu_0}{\varepsilon_0}} \cong 120\pi \cong 377\Omega$ is the characteristic impedance in free space, and

$$\frac{\partial w}{\partial t} = \frac{1}{\pi} \ln \left(\frac{2x}{t} \right) \qquad (4.2.12)$$

with

$$x = \begin{cases} h & \text{for } \frac{w}{h} \leq \frac{1}{2\pi} \\ 2\pi w & \text{for } \frac{w}{h} > \frac{1}{2\pi} \end{cases} \qquad (4.2.13)$$

4.3   Microstrip Ring Resonator

The microstrip ring resonator was first proposed by Troughton [5] for the measurements of phase velocity and dispersion of microstrip lines. Compared to the microstrip linear resonator, the microstrip ring resonator does not suffer from open-ended effects and can be used to give more accurate measurements. Since its introduction the microstrip ring resonator has found applications in determining optimum substrate thickness [6], discontinuity parameters [7], effective dielectric constant and dispersion [8]-[12], and loss and Q-measurements [13]-[15].

The ring circuit is an ideal tool for dispersion, dielectric constant and Q-factor measurements [16]. The typical configuration of the microstrip ring resonator is depicted in Fig. 4.3.1.

The ring resonator is a transmission line formed in a close loop. The basic circuit consists of the feed lines, coupling gaps, and the resonator. The feed lines are separated from the resonator by a distance called the coupling gap. The size of the gap should be large enough such that the fields in the resonator are not appreciably perturbed, yet small enough to allow adequate coupling power. This type of coupling is described in literature as "loose coupling" that is a manifestation of the negligibly small capacitance of the coupling gap. If the feed lines are moved closer to the resonator the coupling becomes tight and the gap capacitance become appreciable. This causes the resonant frequencies of the circuit to deviate from the intrinsic resonant frequencies
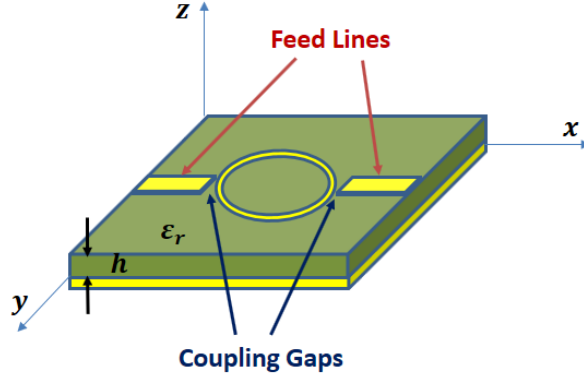
Figure 4.3.1: Typical microstrip ring resonator.

of the ring [17]. The coupling gap equivalent circuit is well defined in [18], where the ring resonator equivalent circuit is described too.

It is usually assumed that the structure would only support waves that have an integral multiple of the guided wavelength equal to the mean circumference. This is expressed as

$$n\lambda_g = 2\pi r \qquad \text{for } n = 1,\ 2,\ 3,\ \ldots \qquad (4.3.1)$$

where n is the mode number or number of wavelengths on the ring, λ_g is the guided wavelength, and r is the mean radius.

There exists in a non-dispersive medium a linear relationship between the frequency and the phase constant or wavenumber, β, where [18]

$$\beta = \frac{2\pi}{\lambda_g} \qquad (4.3.2)$$

If the frequency doubles, then likewise the wavenumber doubles. In a dispersive medium this is not true. The microstrip line is a dispersive medium. The dispersion in a microstrip line can be explained by examining the effective permittivity ε_{eff}. In the case of narrow lines or a very low frequency the field is almost equally shared by the air ($\varepsilon_r \cong 1$) and the substrate so that, at this extreme,

$$\varepsilon_{eff} = \frac{1}{2}\left(\varepsilon_r + 1\right) \text{ as } f \to 0$$

For very wide lines or a very high frequency nearly all of the field is confined to the dielectric substrate, and therefore at this extreme,

$$\varepsilon_{eff} \approx \varepsilon_r \text{ as } f \to \infty$$

108

From this two considerations it turns out that the effective permittivity is frequency dependent, and it increase as the frequency increases.

Inverting (4.2.3), it is possible to extrapolate the effective permittivity

$$\varepsilon_{eff}(f_r) = \left(\frac{c}{v_p}\right)^2 \tag{4.3.3}$$

In the microstrip line the velocity is given by the appropriate frequency-wavelength product. In the microstrip line, the velocity is $v_p = f_r \lambda_g$. Substituting for v_p in (4.3.3) results in the equation

$$\varepsilon_{eff}(f_r) = \left(\frac{c}{\lambda_g f_r}\right)^2 \tag{4.3.4}$$

If we assume that, as in (4.3.1), any microstrip resonator will only support wavelengths that are an integral multiple of the total length, then

$$l_t = n\lambda_g \tag{4.3.5}$$

where l_t is the total length of the resonator. Substituting for λ_g in (4.3.4) yields the equation

$$\varepsilon_{eff}(f_r) = \left(\frac{nc}{f l_{rt}}\right)^2 \tag{4.3.6}$$

The accuracy of the dispersion calculation depends on the accuracy of the measurement of the frequency and the total length of the resonator.

A figure of merit for resonators is the circuit Q-factor as defined by

$$Q = \frac{\omega_0 U}{W} \tag{4.3.7}$$

where ω_0 is the angular resonant frequency, U is the stored energy per cycle, and W is the average power lost per cycle. The three main losses associated with microstrip circuits are conductor losses, dielectric losses, and radiation losses. The total Q-factor, also known as *unloaded* Q-factor, Q_0, can be expressed as

$$\frac{1}{Q_0} = \frac{1}{Q_c} + \frac{1}{Q_d} + \frac{1}{Q_r} \tag{4.3.8}$$

where Q_c, Q_d, and Q_r are the individual Q-values associated with the conductor, dielectric, and radiation losses, respectively [19].

The unloaded Q, Q_0, can also be determined by measuring the loaded Q-factor, Q_L, and the insertion loss of the ring at resonance. Fig. 4.3.2 shows a typical resonator frequency response.
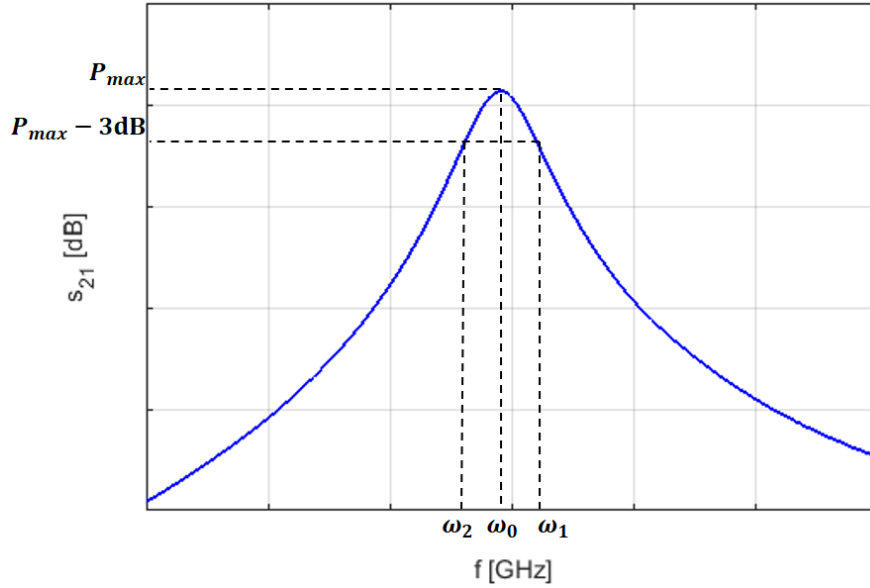
Figure 4.3.2: Example of ring resonator frequency response.

The loaded Q of the resonator is

$$Q_L = \frac{\omega_0}{\omega_1 - \omega_2} \qquad (4.3.9)$$

where ω_0 is the angular resonant frequency and $\omega_1 - \omega_2$ is the 3-dB bandwidth (half power bandwidth).

Normally a high Q_L is desired for microstrip measurements. A high Q_L requires a narrow 3-dB bandwidth, and thus a sharper peak in the frequency response. This makes the resonant frequency more easily determined.

The unloaded Q-factor can be calculated from

$$Q_0 = \frac{Q_L}{(1 - 10^{S_{21max}[dB]/20})} \qquad (4.3.10)$$

where $S_{21max}[dB]$ is the transmission coefficient in correspondance of the peak at frequency ω_0 [20].

The equation to be used to calculate dispersion can be found by combining (4.3.1) and (4.3.4) to yield

$$\varepsilon_{eff}\left(f\right) = \left(\frac{nc}{2\pi f_r r}\right)^2 \qquad (4.3.11)$$

Any ill effect introduced by the ring that might falsify the measure value of wavelength or dispersion can be reduced by correctly designing the circuit.

W	L	r	d	GAP
74	74	15	34	2

Table 4.2: Non-destructive Ring Resonator based sensor dimensions in millimeters.

There are five sources of error that must be considered:

a.   because the transmission line has a curvature, the dispersion on the ring may not be equal to the straight-line dispersion;

b.   field interactions across the ring could cause mutual inductance;

c.   the assumption that the total effective length of the ring can be calculated from the mean radius;

d.   the coupling gap may cause field perturbations on the ring;

e.   nonuniformities of the ring width could cause resonance splitting.

To minimize problems (a.) through (d.) only rings with large diameters should be used. In [5] the author used rings that were five wavelengths long at the frequency of interest. The large ring will reduce (b.) and the effect of (d.) will be minimized because the coupling gap occupies a smaller percentage of the total ring. The effect of the mean radius, (c.), can be reduced by using large rings and narrow line widths. An increased ring diameter will also increase the change of variations in the line width, and the possibility of resonance splitting is increased.

4.4 Multilayer Ring Resonator

The classical version of ring resonator foresees the realization of the ring and of the other parts (50 Ohm microstrips and the ground plane) on the unknown substrate to be measured with consequent "waste" of dielectric material which can no longer be used for other purposes or applications. In some papers [21], [22], the ring resonator was made of known material and it was used to determine the dielectric characteristics of the unknown material to be measured.

Proposed multilayer ring resonator is composed of five different layers, and is depicted in Fig. 4.4.1, and its dimensions are reported in Table 4.2.
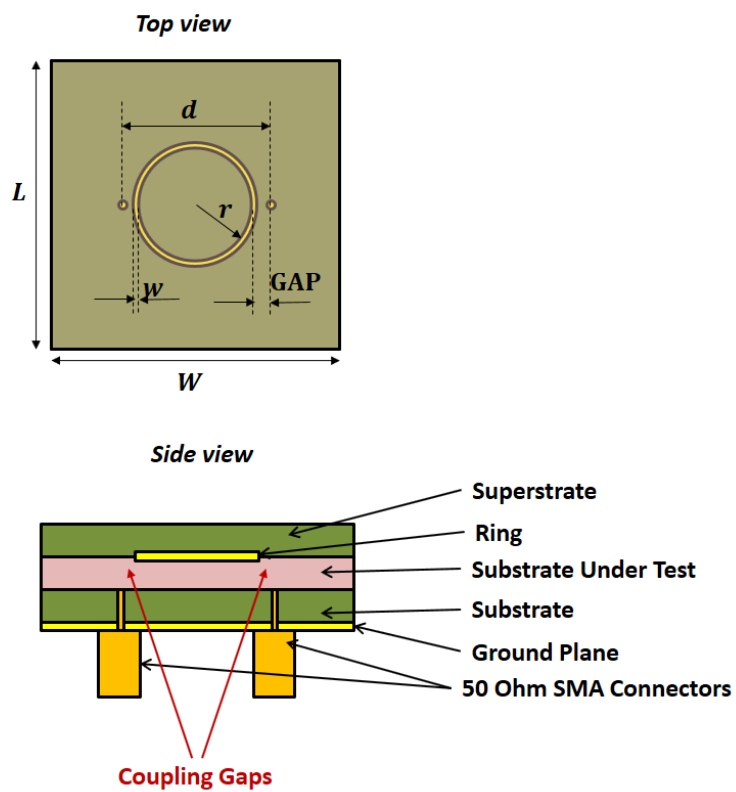
Figure 4.4.1: Proposed Multilayer Ring Resonator. In the top view the unknown substrate and the superstrate are in transparency.

TU-768	DC	@ 500 MHz	@ 1 GHz	@ 2 GHz	@ 5 GHz	@ 10 GHz
ε_r	4,7964	4,62	4,55	4,53	4,3	4,3
$\tan\delta$	0	0,0163	0,0175	0,0184	0,021	0,023

Table 4.3: TU-768 dielectric properties.

The first layer is the metallic ground plane; the second is the known dielectric substrate. The third layer is the unknown dielectric substrate. The ring (fourth layer) is posed under the bottom side of the fifth layer (superstrate), and must be placed on the unknown material in order to carry out the measurement. The second and fifth layers are made of the same material with preferably known dielectric characteristics. Metallic parts are in copper 0.035 mm thick.

Considering the subsequent realization step of the instrument, it was decided to make its fixed parts on a substrate of TU-768 [23], having a thickness of 1.46 mm. The relative permittivity and loss tangent values for various frequencies were collected from the manufacturer's datasheet, and are reported in Table 4.3.

These values have been interpolated with a Piecewise Cubic Interpolating Polinomial (PCHIP) interpolation in MATLAB environment [24]. The dielectric characteristics of this materials are shown in Fig. 4.4.2 as the frequency changes.

The idea is to allow the determination of the dielectric characteristics, in the low microwave band (1 GHz - 3 GHz) of a given substrate without having to redesign, or "waste", the material, the ring, and the other essential parts of the instrument. This resonator is inspired by the multilayer model proposed in [25], [26], in which however the ring is suspended at a certain distance from the material to be measured. This choice was made by the authors to avoid that the unknown material to be measured influenced, with its dielectric properties, the impedance matching at the microstrips that excite the ring resonator. For this reason, given that the ring is expected to rest directly on the material to be measured, it was decided to adopt the excitation model of the resonator with two 50 Ohm SMA connectors placed perpendicular to the ground plane, and with their cores passing through on the substrate [27].

In this way it is possible to measure materials with different thickness simply by placing it between the parts of the measurer with known dielectric characteristics (TU-768). The distance between the two SMA connectors must be large enough to avoid their mutual coupling. One of the most delicate aspects to manage concerns the coupling between the connectors and the ring which in this configuration can vary significantly with the increase of
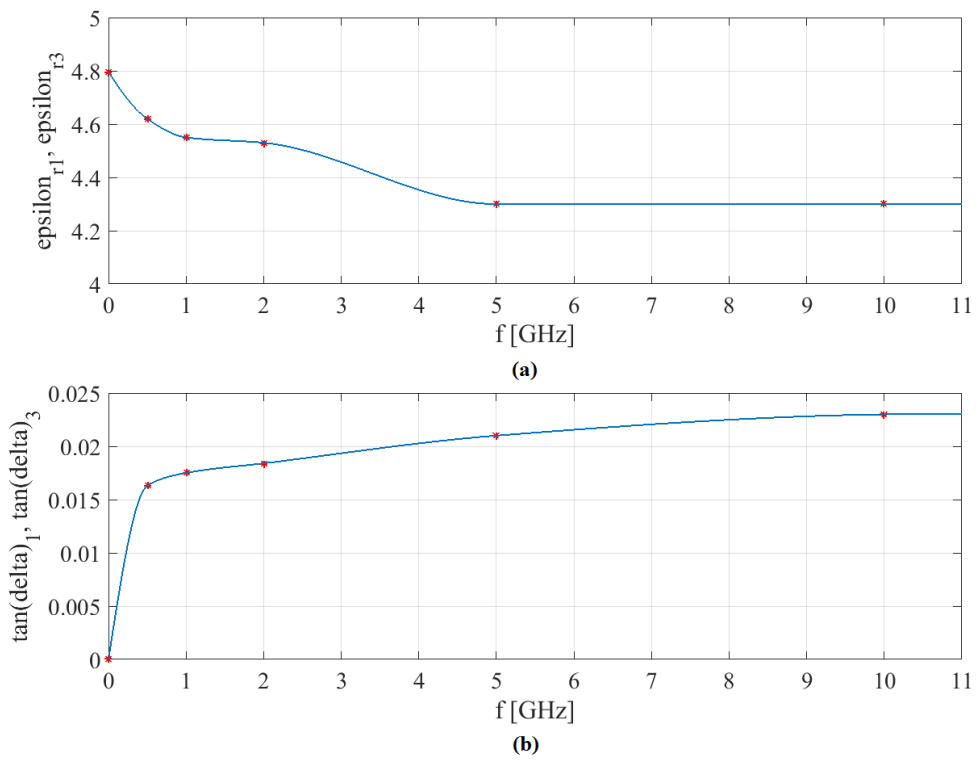
Figure 4.4.2: TU-768 dielectric characteristics: (a) relative permittivity, (b) loss tangent.

the thickness of the unknown substrate and with the increase of its relative dielectric constant. For this reason, in order to obtain good results, it was decided to give a maximum limit of 5 mm to the thickness of the unknown material to be tested, and a maximum of 10 to its relative permittivity value. Consequently, the average radius of the ring r was choosen in order to have a GAP with the core of the SMA connector, such as to allow the maintenance of the loose-loop measurement mode.

4.5   Permittivity Extrapolation Methods

In order to extrapolate the dielectric characteristics of the materials in the 1 GHz - 3 GHz band with the multilayer structure shown in Fig. 4.4.1, it was decided to split the analysis into two distinct steps: the first step involves the calculation of the relative dielectric constant, while the second step involves the extrapolation of the loss tangent value.

For the relative dielectric constant, it was decided to undertake two of the various techinques present in the literature concerning the study of multilayer dielectric structures.

The first branch chosen concerns the study of these composite structures with the *Conformal Mapping Method* [29]-[33]. This method, through the use of the conformal transformations accurately described in [30] and [31], allows to obtain relationships related to the geometric characteristics of the multilayer dielectric structure, the effective dielectric constant. This type of analysis was created with the aim of semplifying the procedure envisaged in the second method chosen for the analysis of multilayer microstrip dielectric systems. This second method is the *Variational Method* [34], [35], in which the study of the composite structure under examination is carried out through the calculation of the potential distribution function, ruled by Poisson's equation, thanks to a set of equations that takes into account the boundary conditions and continuity at the interface between each layer.

These two methods involve the use of static models for the analysis of multilayer dielectric structures, but they can still be used since in the choosen frequency range (1 GHz - 3 GHz) they are still considered reliable. The *Variational Method* turns out to be more accurate then the *Conformal Mapping Method*, but it also turns out to be much more expensive from the computational point of view [32].

Microstrip side view

Air

$\varepsilon_{r_4} \cong 1$

Microstrip Conformal Mapped side view

$w_e/2$

(a)

(b)
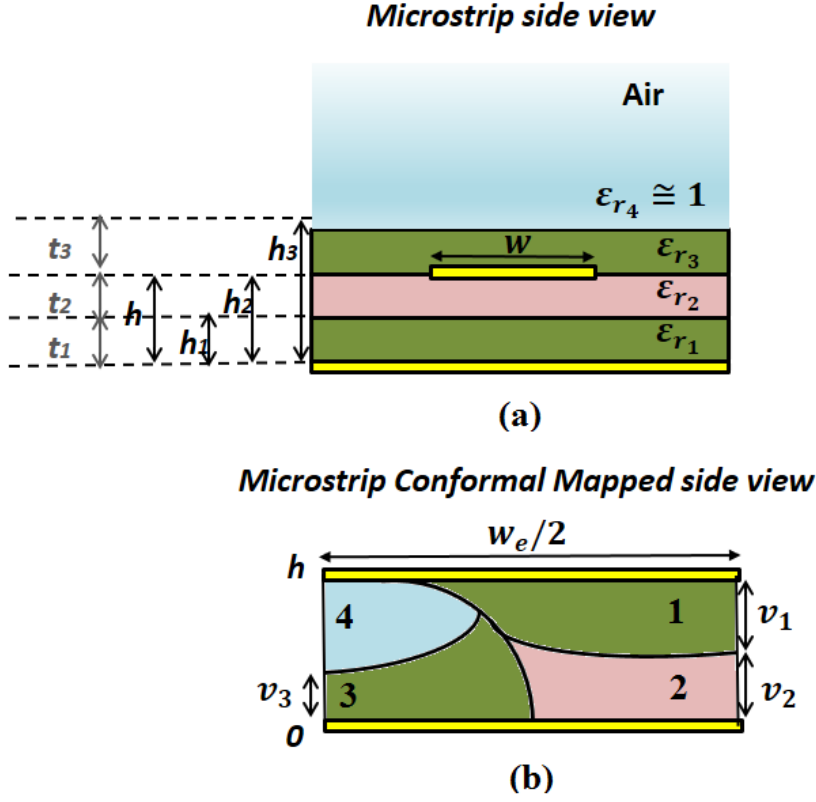
Figure 4.5.1: Multilayer microstrip: (a) Initial structure, (b) Conformal mapped structure.

4.5.1 *Conformal Mapping Method*

The *Conformal Mapping Method* was applied to the proposed measurer (Fig. 4.4.1) following the steps reported in [33]. This method maps the microstrip that composes the ring on another plane with complex variables, the results of which are represented in Fig. 4.5.1.

The filling factors of each dielectric layer are defined, differentiating the cases according to the thickness of the microstrip w.

For wide strips ($\frac{w}{h} > 1$):

$$q_1 = \frac{H_1}{2} \cdot \left[1 + \frac{\pi}{4} - \frac{h}{w_e} \cdot \ln \left(2\frac{w_e}{h} \cdot \frac{\sin\left(\frac{\pi}{2} \cdot H_1\right)}{H_1} + \cos\left(\frac{\pi}{2} \cdot H_1\right) \right) \right] \quad (4.5.1)$$

$$q_2 = 1 - \frac{h}{2w_e} \cdot \ln\left(\pi\frac{w_e}{h} - 1\right) - q_1 \quad (4.5.2)$$

$$q_3 \;=\; \tfrac{h}{2w_e} \cdot \left\{ \ln\left(\pi \tfrac{w_e}{h} - 1\right) - (1+V_3) \cdot \ln\left[2\tfrac{w_e}{h} \cdot \tfrac{\cos\left(\tfrac{\pi}{2}V_3\right)}{2H_3 - 1 + V_3} + \sin\left(\tfrac{\pi}{2} \cdot V_3\right) \right] \right\} \tag{4.5.3}$$

$$q_4 = 1 - \sum_{j=3}^{4} q_j - \sum_{i=1}^{2} q_i \tag{4.5.4}$$

where $H_{i,j} = \tfrac{h_{i,j}}{h}$, and $V_j = \tfrac{v_j}{h}$ with

$$v_j = \frac{2h}{\pi} \arctan\left[\frac{\pi\left(H_j - 1\right)}{\tfrac{\pi}{2} \cdot \tfrac{w_e}{h} - 2} \right] \tag{4.5.5}$$

and the effective line width defined as

$$w_e = w + \frac{2h}{\pi} \cdot \ln\left[17.08\left(\frac{w}{2h} + 0.92 \right) \right] \tag{4.5.6}$$

For narrow strips ($\tfrac{w}{h} \leqslant 1$):

$$q_1 = \frac{\ln\left(A_1\right)}{2 \cdot \ln\left(\tfrac{8h}{w}\right)} \cdot \left[1 + \frac{\pi}{4} - \frac{1}{2} \cdot \arccos\left(\frac{w}{8hH_1} \cdot \sqrt{A_1} \right) \right] \tag{4.5.7}$$

$$q_2 = \frac{1}{2} + \frac{0.9}{\pi \cdot \ln\left(\tfrac{8h}{w}\right)} - q_1 \tag{4.5.8}$$

$$q_3 = \frac{1}{2} - \frac{0.9 + \tfrac{\pi}{4} \cdot \ln\left(B_3\right) \cdot \arccos\left[\left(1 - \tfrac{1 - \tfrac{w}{8h}}{H_3} \right) \cdot \sqrt{B_3} \right]}{\pi \ln\left(\tfrac{8h}{w}\right)} \tag{4.5.9}$$

$$q_4 = 1 - \sum_{j=3}^{4} q_j - \sum_{i=1}^{2} q_i \tag{4.5.10}$$

where

$$A_i = \frac{1 + H_i}{1 - H_i + \tfrac{w}{4h}} \tag{4.5.11}$$

and

$$B_j = \frac{H_j + 1}{H_j + \tfrac{w}{4h} - 1} \tag{4.5.12}$$

From Fig. 4.4.3 (b) it is possible to derive the general relation for the (static) effective permittivity of multilayer microstrip

$$\varepsilon_e\left(0\right) = \frac{\left(q_1+q_2\right)^2}{\frac{q_1}{\varepsilon_{r_1}}+\frac{q_2}{\varepsilon_{r_2}}} + \frac{\left(q_3+q_4\right)^2}{\frac{q_3}{\varepsilon_{r_3}}+\frac{q_4}{\varepsilon_{r_4}}} \tag{4.5.13}$$

which does not take into account the effect due to the frequency behavior of the microstrip.

To take this effect into account, the equations given in [18] (Chapter 2, page 12) can be used:

$$w_e\left(f\right) = w + \frac{w_e\left(0\right)-w}{1+\left(\frac{f}{f_p}\right)^2} \tag{4.5.14}$$

where $w_e\left(0\right)$ is defined by (4.5.6), and

$$f_p = \frac{c}{w_e\left(0\right)\sqrt{\varepsilon_e\left(0\right)}} \tag{4.5.15}$$

However, given the not so high frequency values analyzed, these last two relationships were not considered in the model.

The idea is to derive the relative dielectric constant value of the unknown substrate, starting from the knowledge of its thickness and the dielectric and geometric characteristics of the other layers, simply by inverting the equation (4.5.13).

4.5.1.1   Numerical Results

An electromagnetic model of the structure shown in Fig. 4.4.1 has been created using Ansys HFSS simulator [36].

The electromagnetic analysis in the frequency domain, thanks to the Finite Element Method (FEM), was carried out after inserting the dielectric characteristics of the TU-768 shown in Fig. 4.4.2 in the simulator. In order to test the goodness of the method, widely used in microwave contexts materials have been chosen as unknown substrates, and therefore known, in order to have reliable references regarding their dielectric characteristics. The chosen materials are:

- Mylar-A (thickness: 0.08 mm, $\varepsilon_r = 2.8$, $\tan\delta = 0.008$, @ 1 GHz, [37]);

- Kapton HN200 (thickness: 0.03 mm, $\varepsilon_r = 3.4$, $\tan\delta = 0.0018$, @ 1 kHz, [38]);

Material	h_2 [mm]	f_r [GHz]	ε_e	ε_{r_2}
Mylar-A	0,08	1,5841	4,0321	**62,0132**
Kapton	0,03	1,5617	4,1486	**-9,5958**
RO4003C	0,8	1,6658	3,6465	**4,1096**
TU-768	1,54	1,5829	4,0381	**5,3186**
Alumina	0,63	1,407	5,1111	**11,3996**

Table 4.4: *Conformal Mapping Method* based algorithm: simulation results.

- Rogers RO4003C (thickness: 0.8 mm, $\varepsilon_r = 3.38$, $\tan\delta = 0.0027$, @ 10 GHz, [39]);

- TU-768 (thickness: 1.54 mm, $\varepsilon_r = 4.3$, $\tan\delta = 0.023$, @ 10 GHz, [23]);

- Alumina (thickness: 0.63 mm, $\varepsilon_r = 9.9$, $\tan\delta = 0.0002$, @ 10 GHz, [40]).

The transmission coefficients obtained from the electromagnetic simulations of the proposed measurer model (s_{21} [dB] parameter), have been treated by a special algorithm developed in MATLAB which takes into account the relations (4.5.1)-(4.5.15). In order to derive the relative permittivity of the substrates under test, the effective dielectric constant of the multilayer structure was obtained from the first resonance frequency ($n = 1$) through (4.3.11). After equating (4.3.11) to (4.5.13), from the inversion of the latter it was possible to obtain the relative permittivity to the under test dielectric layer (layer 2). The results obtained from these inversions are reported in Table 4.4.

As it is possible to see from the obtained results, in all cases there are results that turn out to be quite different from what would have been expected: the worst results are obtained in correspondence with very thin substrates (Mylar-A, Kapton HN200). This happened because in the model described in [33], the effect that coupling has on the resonance frequency obtained by the simulator is not taken into account.

To try to reduce the error introduced during the extrapolation of the dielectric characteristics of the substrate under test, it was decided to introduce an auto-calibration mechanism. This step is depicted in Fig. 4.5.2.

Self-calibration consists of putting the two part of the measurer (in TU-768) in contact without introducing any substrate to be measured. In this configuration, the ring is placed at the minimum distance with the SMA
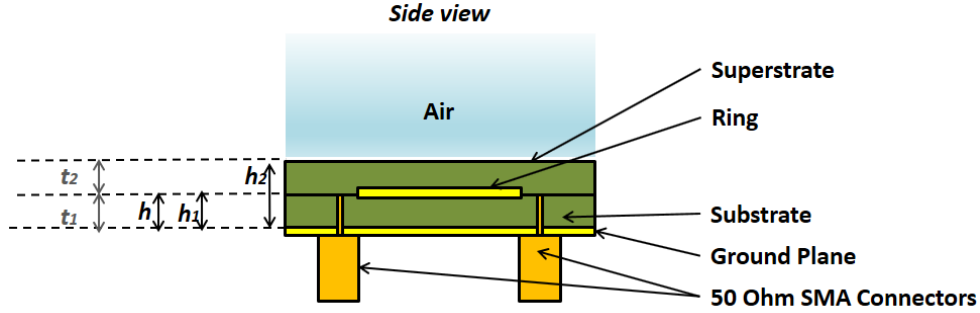
Figure 4.5.2: Auto-calibration setup.

n	f_r [GHz]	ε_e	$\varepsilon_{r_1} = \varepsilon_{r_3}$
1	1,5459	4,2337	5,9125
2	3,161	4,0505	5,6199
3	4,7303	4,0697	5,6506

Table 4.5: Extrapolated values of coupling affected relative permittivity.

connectors, therefore being in the maximum coupling condition. At this point, it will be sufficient to use the formulas treated in [33] for the case shown in Fig. 4.5.2, to extrapolate the relative dielectric constant value of the material composing the instrument affected by the presence of the effect of coupling between the ring and coaxial connectors. In order to have a more exhaustive representation for multiple frequencies, it was decided to extrapolate three dielectric constant values using the first three resonances obtained by the measurer in this configuration ($n = 1, 2, 3$).

The trend of the transmission coefficient for the first three resonances is shown in Fig. 4.5.3 (a), while the relative dielectric constant values affected by the perturbation due to the ring-connector coupling are shown in Table 4.5.

By replacing the values shown in Fig. 4.5.3 (b) in equation (4.5.13), the values shown in Table 4.6 were obtained.

As can be seen from Table 4.6, thanks to the self calibration step, results have been obtained much closer to what the real values should be. The only exception concerns alumina, for which a relative permittivity almost halved compared to the real value has been obtained. This result is related to the definition of effective dielectric constant reported in (4.5.13): looking carefully at the formula, in fact, it is possible to note that as the relative

(a)

(b)
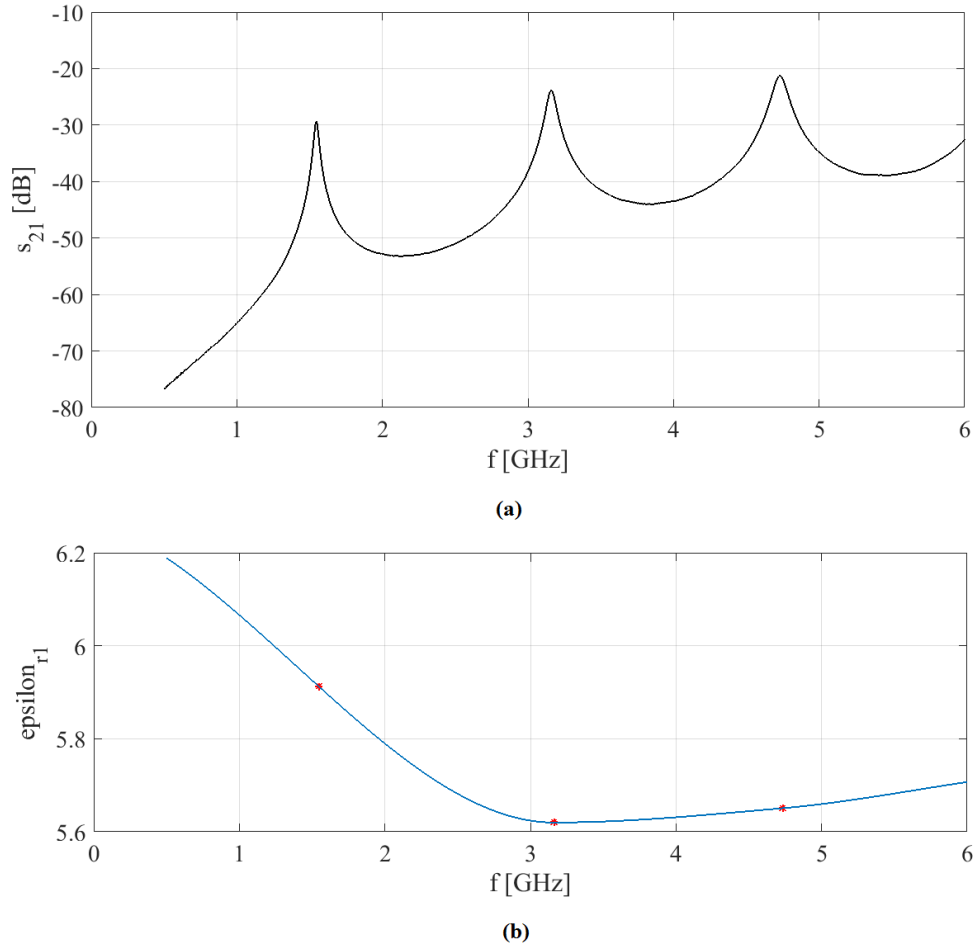
Figure 4.5.3: (a) Measured transmission coefficient of the measurer in auto-calibration configuration, (b) PCHIP interpolation of extrapolated values.

Material	h_2 [mm]	f_r [GHz]	ε_e	ε_{r_2}
Mylar-A	0,08	1,5841	4,0321	**3,0278**
Kapton	0,03	1,5617	4,1486	**2,9874**
RO4003C	0,8	1,6658	3,6465	**3,3439**
TU-768	1,54	1,5829	4,0381	**4,6036**
Alumina	0,63	1,407	5,1111	**6,8196**

Table 4.6: *Conformal Mapping Method* based algorithm with coupling effect consideration results.

Figure 4.5.4: Multilayer Ring resonator in measurement test (Mylar-A).

dielectric constant ε_{r_2} increases (in our case), the ratio $\frac{q_2}{\varepsilon_{r_2}}$, in the term in the denominator, $\frac{q_1}{\varepsilon_{r_1}} + \frac{q_2}{\varepsilon_{r_2}}$, becomes gradually negligible compared to $\frac{q_1}{\varepsilon_{r_1}}$.

4.5.1.2 Measurement Results

To verify what was obtained during the simulation phase, laboratory measurements were carried out with Anritsu MS46112B vector network analyzer.

In Table 4.7 it is possible to see the relative dielectric constant values obtained, which are very similar to the results obtained in simulation confirming the inability of this model to correctly extrapolate too high dielectric constant values.

4.5.2 Variational Method

The *variational method* was used to try to calculate the relative dielectric constant of the unknown dielectric substrate placed inside the ring measurer.

122

Material	h_2 [mm]	f_r [GHz]	ε_e	ε_{r_2} (**no** self-calibration)	ε_{r_2} (self-calibration)
Mylar-A	0,08	1,5834	4,0356	**67,7287**	**3,0405**
Kapton	0,03	1,5624	4,1449	**-9,7634**	**2,9713**
RO4003C	0,8	1,6665	3,6434	**4,1017**	**3,3383**
TU-768	1,54	1,5822	4,0416	**5,3276**	**4,6107**
Alumina	0,63	1,4555	4,7761	**8,7794**	**5,7479**

Table 4.7: Measurement results: no self-calibrated analysis results vs. self-calibrated analysis results.

In [34] and [35], the authors describe the method for calculating the effective dielectric constant of different multilayer microstrip configurations.

The static potential distribution $\phi(x, y)$ in the microstrip line structure satisfies Poisson's equation

$$\nabla^2 \phi(x, y) = -\frac{1}{\varepsilon} \rho(x, y) \tag{4.5.16}$$

and the boundary conditions on the surface of the dielectric material as well as the conductor. Here $\rho(x, y)$ is the charge distribution on the surface of the conducting strip.

The line capacitance can be evaluated by inserting the solution of (4.5.16) in the variational expression

$$\frac{1}{C} = \frac{1}{Q^2} \int_s \rho(x, y)\,\phi(x, y)\,dl \tag{4.5.17}$$

where

$$Q = \int_s \rho(x, y)\,dl \tag{4.5.18}$$

and the integral in (4.5.17) and (4.5.18) are to be taken on all the surfaces over which the charge $\rho(x, y)$ is distributed.

The characteristic impedance of a TEM transmission line in free space (Fig. 4.2.2 (a)) is given by

$$Z_0 = \frac{1}{C_0 c} \tag{4.5.19}$$

where C_0 is the line capacitance of the structure and c is the velocity of light.

When a dielectric material with different characteristics respect to the air is inserted as shown in Fig. 4.2.2 (c), the line capacitance of this new structure C is larger than C_0, while the new guided wavelength λ is smaller than the free space wavelength λ_0. Hence the characteristic impedance of the new line is obtained by modifying (4.5.19) as follows:

$$Z = \left(\frac{C_0}{C}\right)^{\frac{1}{2}} Z_0 \qquad (4.5.20)$$

Similarly, the new guide wavelength is given by

$$\lambda = \left(\frac{C_0}{C}\right)^{\frac{1}{2}} \lambda_0 \qquad (4.5.21)$$

Initially, assume that the strip is infinitely thin. For this case the charge distribution assumes the form

$$\rho\left(x,\, y\right) = f\left(x\right) \delta\left(y - b\right) \qquad (4.5.22)$$

where $\delta\left(y - b\right)$ is Dirac's delta function. Because the symmetry of the problem, $f\left(x\right)$ is an even function of x, and its Fourier transform is

$$\bar{f}\left(\beta\right) = \int_{-\infty}^{\infty} f\left(x\right) e^{j\beta x} dx \qquad (4.5.23)$$

The Fourier transform $\phi\left(\beta,\, y\right)$ of $\phi\left(x,\, y\right)$ is defined by

$$\phi\left(\beta,\, y\right) = \int_{-\infty}^{\infty} \phi\left(x,\, y\right) e^{j\beta x} dx \qquad (4.5.24)$$

The transforming (4.5.16) according to (4.5.24) gives

$$\left(-\beta^2 + \frac{d^2}{dy^2}\right) \phi\left(\beta,\, y\right) = 0 \qquad y \neq b,\, h \qquad (4.5.25)$$

For the proposed multilayer structure, referred to Fig. 4.4.1, the equation (4.5.25) becomes

$$\left(-\beta^2 + \frac{d^2}{dy^2}\right) \phi\left(\beta,\, y\right) = 0 \quad y \neq h_1,\, h_2,\, h_3,\, t_4 \qquad (4.5.26)$$

The general solution of this differential equation is a linear combination of $\exp\left(\beta y\right)$ and $\exp\left(-\beta y\right)$ in a bounded region. When t_4 is taken as infinity, the solution takes a form of $\exp\left(-\left|\beta\right| y\right)$ in the unbounded region. The boundary and continuity conditions in the Fourier transformed domain are

$$\phi\left(\beta,\, 0\right) = 0 \tag{4.5.27}$$

$$\phi\left(\beta,\, \infty\right) = 0 \tag{4.5.28}$$

$$\phi\left(\beta,\, h_1 + 0\right) = \phi\left(\beta,\, h_1 - 0\right) \tag{4.5.29}$$

$$\varepsilon_{r_2}\frac{d}{dy}\phi\left(\beta,\, h_1 + 0\right) = \varepsilon_{r_1}\frac{d}{dy}\phi\left(\beta,\, h_1 - 0\right) \tag{4.5.30}$$

$$\phi\left(\beta,\, h_2 + 0\right) = \phi\left(\beta,\, h_2 - 0\right) \tag{4.5.31}$$

$$\varepsilon_{r_3}\frac{d}{dy}\phi\left(\beta,\, h_2 + 0\right) = \varepsilon_{r_2}\frac{d}{dy}\phi\left(\beta,\, h_2 - 0\right) \tag{4.5.32}$$

$$\phi\left(\beta,\, h_3 + 0\right) = \phi\left(\beta,\, h_3 - 0\right) \tag{4.5.33}$$

$$\varepsilon_{r_4}\frac{d}{dy}\phi\left(\beta,\, h_3 + 0\right) = \varepsilon_{r_3}\frac{d}{dy}\phi\left(\beta,\, h_3 - 0\right) \tag{4.5.34}$$

$$\frac{d}{dy}\phi\left(\beta,\, h_2 + 0\right) = \frac{d}{dy}\phi\left(\beta,\, h_2 - 0\right) - \frac{1}{\varepsilon_{r_3}\varepsilon_0}\bar{f}\left(\beta\right) \tag{4.5.35}$$

where ε_{r_1}, ε_{r_2} and ε_{r_3} are the relative dielectric constants. $\varepsilon_{r_4} \cong 1$ is the air relative permittivity.

Substituting these conditions to the general solution, one obtains a set of linear inhomogeneous simultaneous equations for the coefficients of potential functions. The solution of the potential distribution on the strip is

$$\phi\left(\beta,\, h_2\right) = \frac{1}{\varepsilon_0}\bar{f}\left(\beta\right)\bar{g}\left(\beta\right) \tag{4.5.36}$$

where $\bar{g}\left(\beta\right)$ is a complicated equation derived from (4.5.27)-(4.5.36).

For the calculation of the line capacitance the MATLAB Partial Differential Equation Toolbox [41] was used.

Using this tool that allow to solve partial differential equations with the Finite Element Method (FEM), it was possible to derive the electrostatic effective dielectric constant $\varepsilon_e\left(0\right)$.

4.5.2.1 Numerical Results

Thanks to the MATLAB PDE toolbox, a code was created in which it was possible to define the multilayer dielectric structure represented in Fig. 4.4.1. In the developed script file were defined geometrical variables (such as the thickness of each layer, and the position and width of the microstrip), and the dielectric properties of each of the materials that make up the structure. This tool is usually used to calculate the effective dielectric constant of dielectric structures (simple or composite) such as the ratio between the line capacitance calculated for the presence of one or more dielectric layers, and the line capacitance calculated in the presence of air only:

$$\varepsilon_e(0) = \frac{C}{C_0} \tag{4.5.37}$$

In order to obtain the relative permittivity value of the unknown layer, it was necessary to develop the following algorithmic procedure:

- starting from the transmission coefficient (s_{21} [dB] parameter) obtained from simulations or measurements, the $\varepsilon_e(f)$ was calculated thanks to equation (4.3.11);

- subsequently the thickness of each dielectric layer, the dielectric properties of the layers 1 and 3 (made in TU-768, see Fig. 4.4.2 and Table 4.3), and a fictitius value of dielectric constant for the unknown substrate (layer 2), were inserted in the PDE toolbox; the dielectric constant of air for layer 4 was also inserted without specifying the thickness (ideally tends to infinity);

- the difference between the effective dielectric constant obtained from (4.3.11) and the effective dielectric constant obtained by the *variational method* (4.5.37) initially set to zero was defined;

- once the new $\varepsilon_e(0)$ value, due to the ε_{r_2} value initially set, has been obtained, the algorithm proceeds until the difference between $\varepsilon_e(f)$ and $\varepsilon_e(0)$ becomes less than the desired minimum error threshold.

Fig. 4.5.5 shows a flow chart which summarizes what has just been described.

As for the *conformal mapping method*, also in this case we started from the results obtained from the simulations made with the electromagnetic model, and we proceeded with the calculation by applying the described algorithm. The results are reported in Table 4.8.

From the results obtained from the transmission coefficients obtained by the electromagnetic model, it was clear that the proposed algorithm offered

126
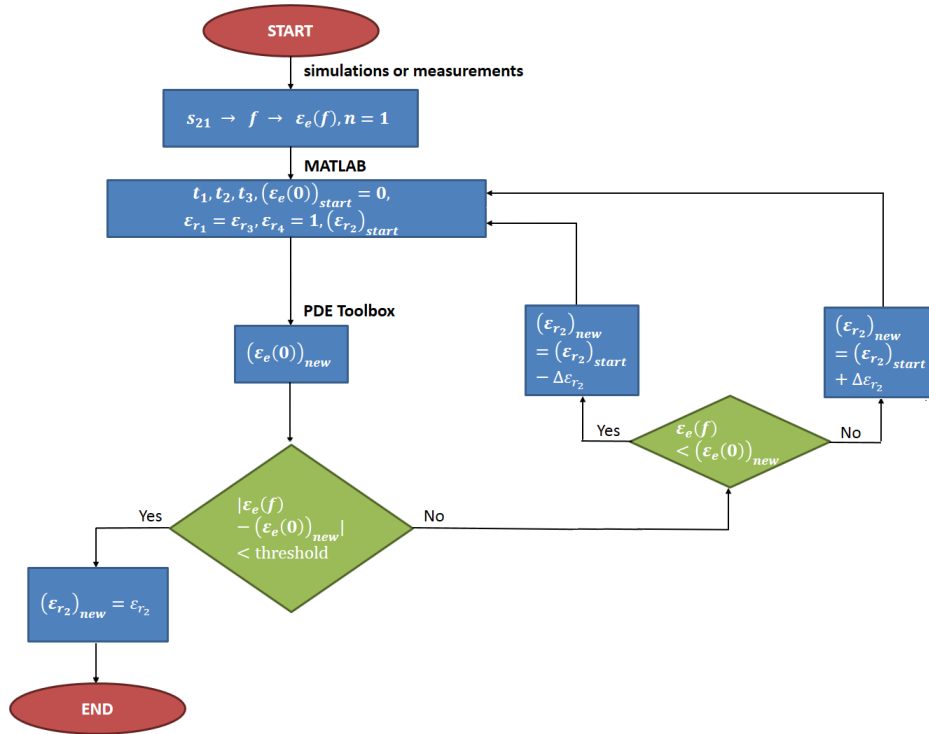
Figure 4.5.5: Flowchart of the algorithm for *variational method* implemented in MATLAB/PDE toolbox

Material	h_2 [mm]	f_r [GHz]	ε_e	ε_{r_2}
Mylar-A	0,08	1,5841	4,0321	**2,8172**
Kapton	0,03	1,5617	4,1486	**3,222**
RO4003C	0,8	1,6658	3,6465	**3,3289**
TU-768	1,54	1,5829	4,0381	**4,6092**
Alumina	0,63	1,407	5,1111	**9,2223**

Table 4.8: *Variational method* based algorithm: simulation results.
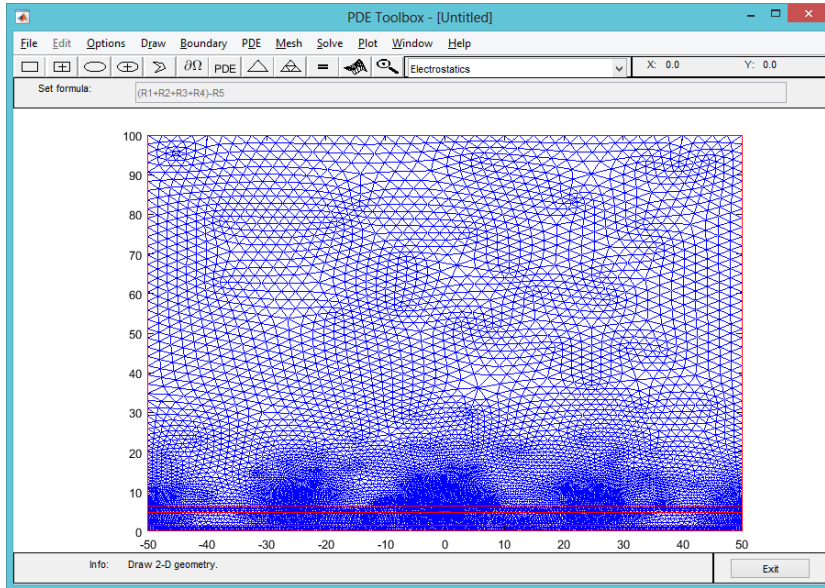
(a)
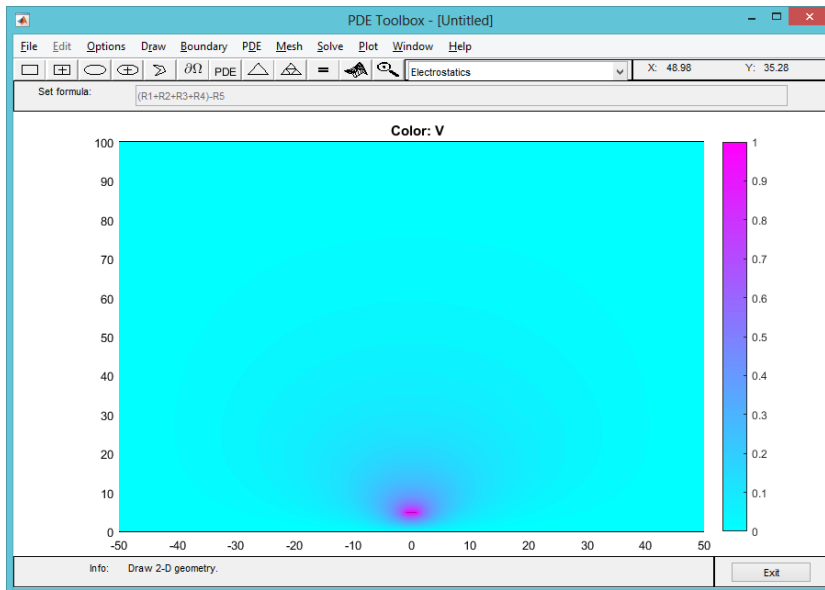
(b)

Figure 4.5.6: Multilayer structure in MATLAB PDE toolbox: (a) mesh view, (b) static potential distribution view.

Material	h_2 [mm]	f_r [GHz]	ε_e	ε_{r_2}
Mylar-A	0,08	1,5834	4,0356	**2,8461**
Kapton	0,03	1,5624	4,1449	**3,142**
RO4003C	0,8	1,6665	3,6434	**3,3215**
TU-768	1,54	1,5822	4,0416	**4,6177**
Alumina	0,63	1,4555	4,7761	**7,3547**

Table 4.9: *Variational method* based algorithm: measurement results.

results similar to those obtained with the previous method (*conformal mapping method*). There are slight differences for Mylar-A and Kapton HN200, while a much better, albeit non-exhaustive, result is obtained in the extraction of alumina permittivity. Compared to the algorithm developed with the *conformal mapping method*, this algorithm is much slower and computationally more expensive, especially in the analysis of very thin substrates. The explanation lies in the fact that the mesh generated with MATLAB's PDE tool is very dense when the thickness of the unknown substrate is reduced. In this case a self-calibration step was not necessary.

4.5.2.2 Measurement Results

Given the found efficacy in the extrapolation of the permittivity values, the relative dielectric constant values of the selected substrates, have been extrapolated starting from the measurement made with the real measurer. The results of the extrapolations carried out with the algorithm based on the *variational method* are reported in Table 4.9.

4.5.3 Electromagnetic Map Extraction Method

The *conformal mapping method* and the *variational method* provide good results in the extrapolation of the relative dielectric constant of the selected substrates. The *variational method* provides results closer to the real values than the *conformal mapping method*, but has very long calculation times. As seen, the first method fails in the case of substrates under test with high relative permittivity (alumina), while the second method is very close to the expected value.

To try to have better results it was thought to extrapolate a surface (map) of data directly from the electromagnetic simulator. In this way it was possible to take into account, not only the dielectric and geometric characteristics

of the entire structure (measurer and unknown substrate), but also all aspects related to other electromagnetic phenomena present in the structure that could not be taken into account with the two previous methods (for example, presence of surface waves, ring - SMA connectors coupling, SMA connector - SMA connector coupling, etc.).
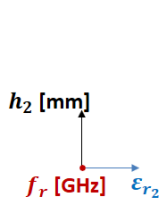
The *electromagnetic map extraction method* consists in the extrapolation of a surface having, respectively, relative dielectric constants and thicknesses of the unknown substrate on the x-y plane of a corresponding Cartesian plane, and on the z axis the value of the resonance frequencies obtained by the various combinations of the other two parameters. For the fixed parts of the instrument (in TU-768), the model uses the same data shown in Fig. 4.4.2.

First of all, material models have been identified with different dielectric costants which are different from each other in the Ansys HFSS environment. Specifically, the following material models were chosen:

- Air ($\varepsilon_r = 1.00059$, $\tan \delta = 0$);

- Teflon ($\varepsilon_r = 2.1$, $\tan \delta = 0.0002$);

- Taconic TLX-8 ($\varepsilon_r = 2.55$, $\tan \delta = 0.0019$);

- Rogers RO4003C ($\varepsilon_r = 3.39$, $\tan \delta = 0.0027$);

- TU-768 ($\varepsilon_r = 4.54$, $\tan \delta = 0.017$, inserted on the basis of the data shown in Fig. 4.4.2);

- Arlon AR-600 ($\varepsilon_r = 6$, $\tan \delta = 0.0035$);

- Preperm L700HF ($\varepsilon_r = 7$, $\tan \delta = 0.0006$);

- Dupont 951 ($\varepsilon_r = 7.8$, $\tan \delta = 0.0015$);

- Heracus CT2000 ($\varepsilon_r = 9.1$, $\tan \delta = 0.002$);

- Alumina ($\varepsilon_r = 9.9$, $\tan \delta = 0.0001$).

In the material model, the characteristics just reported were almost constant in the frequency band examinated (1 GHz - 3 GHz). For the thicknesses of the unknown substrate, the vector [0, 0.01, 0.02, 0.03, 0.04, 0.05, 0.1, 0.5, 1, 1.5, 2, 2.5, 3, 4, 5] (in millimeters) was be taken as a reference.

Electromagnetic simulations were carried out for each of the materials listed above, for each of the thicknesses reported in the vector just described, in order to extrapolate, for each combination of parameters, the resulting

					ε_{r_2}					
f_r [GHz]	1,00059	2,1	2,55	3,39	4,54	6	7	7,8	9,1	9,9
0	1,5495	1,5495	1,5495	1,5495	1,5495	1,5495	1,5495	1,5495	1,5495	1,5495
0,01	1,6051	1,6093	1,5941	1,5868	1,5568	1,5521	1,5421	1,5978	1,5835	1,5238
0,02	1,6198	1,5988	1,5936	1,5752	1,5558	1,5463	1,5374	1,573	1,569	1,5206
0,03	1,633	1,5941	1,582	1,5747	1,5631	1,5379	1,5363	1,57	1,5685	1,5259
0,04	1,6477	1,6046	1,5941	1,5736	1,5589	1,5379	1,5327	1,5673	1,5675	1,5227
0,05	1,6697	1,6057	1,5931	1,5721	1,5605	1,5448	1,53	1,5565	1,538	1,5217
0,1	1,7327	1,6414	1,6062	1,5847	1,5621	1,539	1,5258	1,5357	1,525	1,5038
0,5	2,0262	1,7663	1,7044	1,6356	1,5668	1,5064	1,477	1,4678	1,4417	1,4104
1	2,1926	1,8582	1,7726	1,6723	1,5731	1,4886	1,4429	1,4295	1,391	1,3463
1,5	2,2813	1,9075	1,8183	1,696	1,582	1,4797	1,424	1,402	1,35	1,3117
2	2,3464	1,9448	1,8503	1,7164	1,5862	1,4828	1,4172	1,3838	1,3262	1,2891
2,5	2,3821	1,9705	1,8697	1,7311	1,5957	1,4744	1,4088	1,3738	1,318	1,2739
3	2,4184	1,9873	1,8881	1,7369	1,5988	1,4681	1,3993	1,3665	1,3035	1,2592
4	2,4551	2,0267	1,907	1,7537	1,988	1,4618	1,3888	1,3555	1,2868	1,2439
5	2,4756	2,034	1,9033	1,7516	1,5978	1,4571	1,3794	1,3393	1,2662	1,2277

h_2 [mm]

f_r [GHz] ε_{r_2}

h_2 [mm]

Table 4.10: Resonance frequencies extrapolated from the electromagnetic simulations carried out when the materials placed in the intermediate layer and the reference thicknesses vary.

transmission coefficients of the whole structure. From these data, as done in the methods described above, it was possible to extrapolate the frequencies of the first resonance (parameter on the z axis). The first resonance frequency values ($n = 1$) corresponding to the other two reference quantities are shown in Table 4.10. In Fig. 4.5.7 the surface obtained by combining the quantities of which we have so far taken into consideration (proto-surface) is reported.

The *electromagnetic map extraction method* therefore allows to extrapolate the relative dielectric constant of the intermediate substrate (unknown substrate) starting from the knowledge of its thickness and from the resonance frequency extrapolated from the transmission coefficient obtained from the real measurement phase (or from the simulation phase).

In order to have a surface with a more marked detail, a fitting was applied to the data extrapolated from the electromagnetic simulations, and then interpolated thanks to the MATLAB's Curve Fitting tool. After some tests, *biharmonic* interpolation was the most effective interpolation. In Fig. 4.5.8 the interpolated surface is shown. Thanks to these two steps, a relative dielectric constant extrapolation with an accuracy up to the third decimal place was made possible.
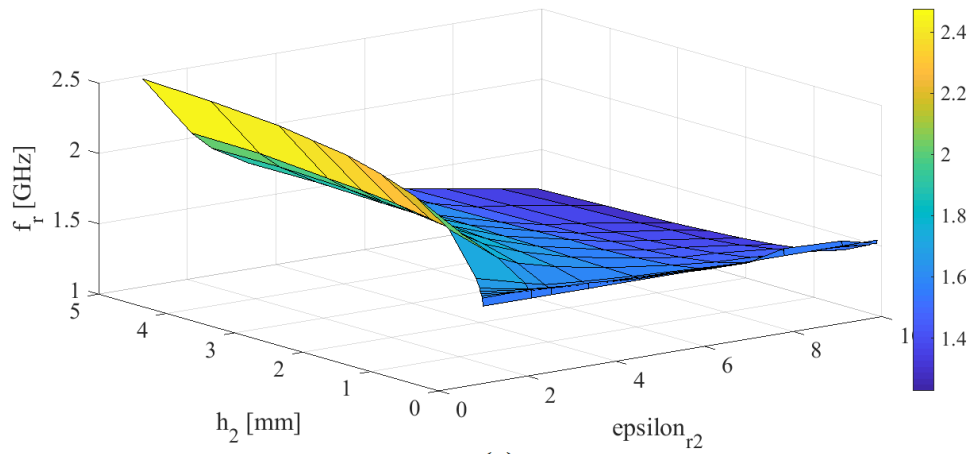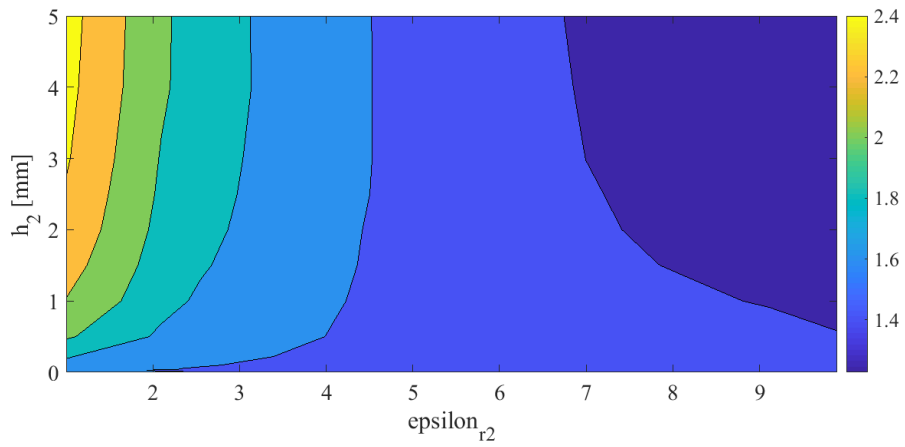
Figure 4.5.7: Surface (map) of the resonance frequencies obtained as a function of the relative permittivity and of the thicknesses fixed for the intermediate layer of the resonant structure: (a) 3D map, (b) 2D map.

Figure 4.5.8: Fitted and interpolated surface: (a) 3D map, (b) 2D map; relative permittivity sensitivity of extrapolation to the third decimal place.

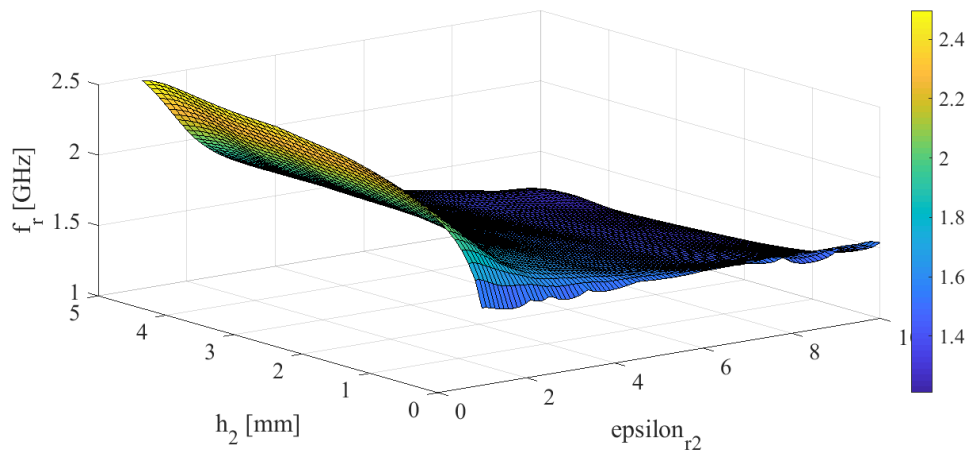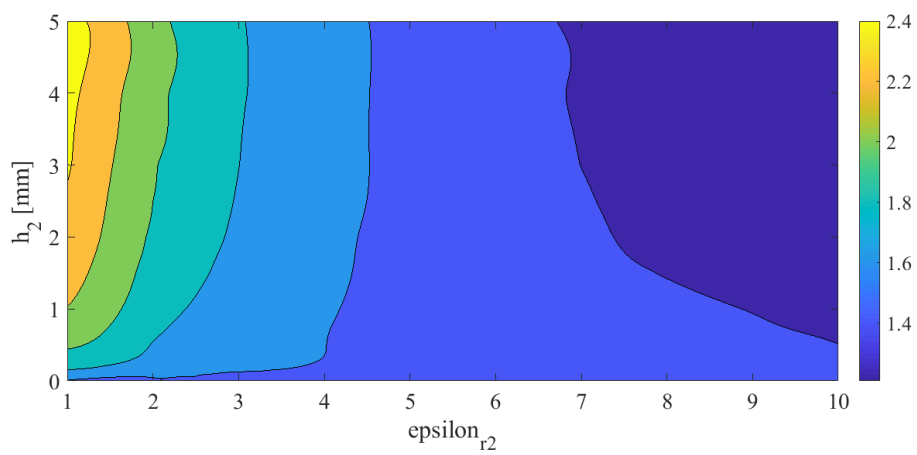| Material	h_2 [mm]	f_r [GHz]	ε_e	ε_{r_2}
Mylar-A	0,08	1,5834	4,0356	**2,776**
Kapton	0,03	1,5624	4,1449	**3,304**
RO4003C	0,8	1,6665	3,6434	**3,28**
TU-768	1,54	1,5822	4,0416	**4,542**
Alumina	0,63	1,4555	4,7761	**7,5780**

Table 4.11: *Electromagnetic map extraction method*: measurement results.

From the comparison between Fig. 4.5.7 (b) and Fig. 4.5.8 (b), it is possible to see the benefits introduced by the fitting on the final interpolation of the surface.

4.5.3.1   Measurement Results

For this method, the transmission coefficients obtained during the measurement phase were directly analyzed. The results are reported in Table 4.11.

As can be seen from the results obtained, this method permits to obtain values even closer to those declared by the manufacturers of the dielectric materials chosen and examinated. Although minimal, there continue to be inaccuracies also due to truncation errors in the various calculation phases provided for in the algorithm. The results are however very satisfactory. For the alumina sample, results very similar to those obtained with the *variational method* were obtained. However, in this case, the value returned for the dielectric constant is slightly greater than that obtained with the other method. Once extrapolated the grid of Table 4.10, this method presents rather short processing times, even if slightly longer than the algorithm that takes into account the *conformal mapping method*. Electromagnetic simulation times, on the other hand, are very long, especially when the substrate under test in the simulations has a high relative dielectric constant (AR-600, Preperm L700HF, Dupont 951, Heracus CT2000, alumina).

4.5.4   Alumina measurements consideration

From the comparison of the results obtained from the simulations and from the measurements for alumina with the three methods described above, it is possible to notice how the resonance frequencies are very different from each other ($f_{r_{simulated}} = 1.407$ GHz, and $f_{r_{measured}} = 1.4555$ GHz). This diversity has led to the extrapolation of the data from the transmission coefficient,

dielectric constant values lower than the real ones of alumina. The problem lies in the fact that small imperfections in the materials that make up the multi-layer structure have allowed the air to permeate inside, altering the measurement result. In this case, this problem can also occur during the measurement of other materials, but the effect introduced by the presence of air will be greater the greater the value of the dielectric constant of the material to be measured. Thanks to simulations carried out in Ansys HFSS environment, it was possible to verify the effect introduced by the application of very thin layers of air between the alumina sample and the layers adjacent to it. As can be seen from Fig. 4.5.9, very few hundredths of a millimeter are sufficient to be able to have significant variations in the position of the resonant frequency.

If we consider the resonance frequency obtained for the simulated alumina sample ($f_{r_{simulated}} = 1.407$ GHz), the extrapolated dielectric constant value is equal to $\varepsilon_{r_{2_{simulated}}} = 9.552$, which confirms the goodness of the *Electromagnetic Map Extraction Method.*

4.6   Loss Tangent Extrapolation Methods

The calculation of the relative dielectric constant of a dielectric material is only the first part of the analysis that is usually carried out on this type of materials. The other important parameter to be determined is the loss tangent value expressed through the definition of $\tan \delta$ seen in (4.1.2). Also in this case other algorithms have been developed suitably used together with those described for the calculation of the relative permittivity. Specifically, for each of the methods seen above, a relative technique will be added for the determination of the loss tangent value.

4.6.1   *Schneider's Method*

Starting from the trend of the transmission coefficient (s_{21}[dB]) obtained from the electromagnetic simulation phase (or from the measurement phase), thanks to the relations (4.3.8)-(4.3.10), and taking into account the equations (4.2.10)-(4.2.13) it is possible to obtain the value of $\tan \delta$ contained in the equation (4.2.10).

Since the structure to be considered is multilayer and is composed of different dielectric materials, the loss tangent value obtained from the simulation or measurement phases is the effective loss tangent value:
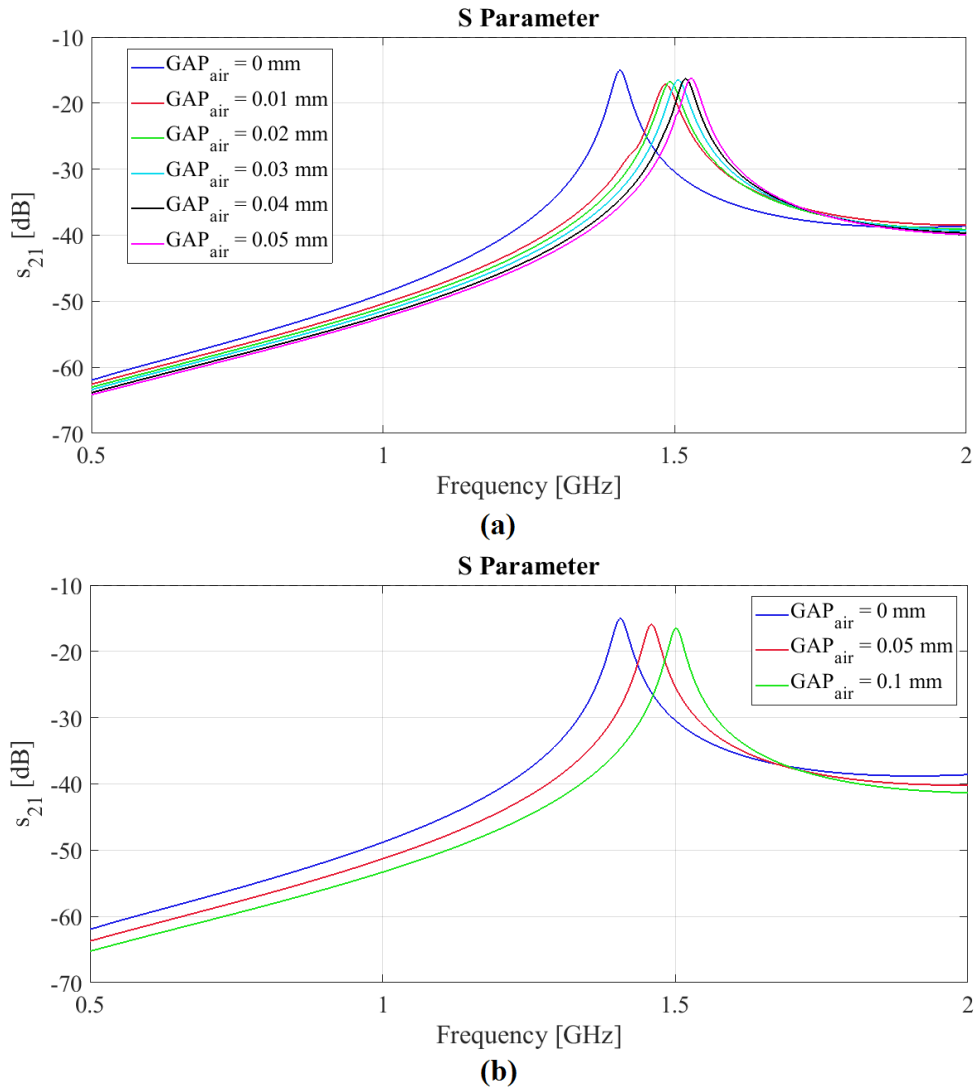
$$Q_d = \frac{1}{\tan \delta_e} \tag{4.6.1}$$

Figure 4.5.9: Resonance frequency shift effect due to the presence of thin layers of air: (a) air between the ring and the alumina sample; (b) air between the alumina sample and the TU-768 substrate. Simulation results.

Following what reported in [42], the effective loss tangent can be calculated through a linear combination of the effects introduced by the loss tangent factors of each of the dielectric layers that make up the entire structure:

$$\tan \delta_e = \frac{1}{\varepsilon_e} \sum_{i=1}^{4} p_i \tan \delta_i \qquad (4.6.2)$$

where the p_i coefficients are multiplicative factors (also called filling factors) which depend on the dielectric and geometric characteristics of the multilayer structure, similarly to what was done in [33] for the calculation of the relative dielectric constant, and are calculated as:

$$p_i = \varepsilon_{r_i} \frac{\partial \varepsilon_e}{\partial \varepsilon_{r_i}} \qquad , \, i = 1, \, 2, \, 3, \, 4 \qquad (4.6.3)$$

The term $\frac{\partial \varepsilon_e}{\partial \varepsilon_{r_i}}$ can be defined as [43]:

$$\frac{\partial \varepsilon_e}{\partial \varepsilon_{r_i}} = \frac{\hat{\varepsilon}_{e_i} - \varepsilon_e}{\hat{\varepsilon}_{r_i} - \varepsilon_{r_i}} \qquad , \, i = 1, \, 2, \, 3, \, 4 \qquad (4.6.4)$$

where

$$\hat{\varepsilon}_{r_i} = \varepsilon_{r_i} + \Delta \varepsilon_r \qquad , \, i = 1, \, 2, \, 3, \, 4 \qquad (4.6.5)$$

with $\Delta \varepsilon_r$ infinitesimal increase in the relative dielectric constant (for example $\Delta \varepsilon_r = 0.01$), and

$$\hat{\varepsilon}_{e_i} = \varepsilon_e|_{\varepsilon_{r_i} = \hat{\varepsilon}_{r_i}} \qquad , \, i = 1, \, 2, \, 3, \, 4 \qquad (4.6.6)$$

is the effective dielectric constant value calculated for $\varepsilon_{r_i} = \hat{\varepsilon}_{r_i}$.

In the specific case, these equations were used in combination with the algorithm based on the *conformal mapping method*. So the relationship of the effective dielectric constant that has been taken into account is defined in the equation (4.5.13).

4.6.1.1   Measurement results

Starting from the transmission coefficients obtained in the measurement phase, the loss tangent relative to the intermediate (unknown) substrate was extrapolated by inverting equation (4.6.2). The results obtained for the dielectric materials taken as reference are reported in Table 4.12.

The results obtained are not good and the only material for which reasonable results are obtained is Mylar-A.

Material	h_2 [mm]	f_r [GHz]	ε_e	ε_{r_2}	$\tan \delta_e$	$\tan \delta_2$
Mylar-A	0,08	1,5834	4,0356	**3,0405**	0,0158	**0,0095**
Kapton	0,03	1,5624	4,1449	**2,9713**	0,0172	**0,0142**
RO4003C	0,8	1,6665	3,6434	**3,3383**	0,0144	**0,0155**
TU-768	1,54	1,5822	4,0416	**4,6107**	0,0286	**0,0406**
Alumina	0,63	1,4555	4,7761	**5,7479**	0,0139	**0,0109**

Table 4.12: *Schneider's method* applied with autocalibrated *conformal mapping method* algorithm: measurement results.

The ineffectiveness of this method of determining the loss tangent is certainly due to the fact that the equations taken from [42] and [43] have been developed for multilayer structures having the microstrip placed on the uppermost layer of the dielectric stack and therefore in direct contact with the air. In our case, given the presence of the cover in TU-768 on the ring resonator, the *Schneider's method* does not allow to correctly extrapolate the loss tangent values of the unknown substrate.

4.6.2 *Upgraded Variational Method*

Following the theory and the steps listed in the description of the *variational method* for determining the relative permittivity of the unknown substrate, it was decided to upgrade the model developed in MATLAB and with the aid of the PDE tool, allowing insertion into the algorithm of complex dielectric constants. In fact, using the definition of dielectric constant described by equation (4.1.1), it was possible to insert also the immaginary part of the permittivity starting from the insertion of the value of $\tan \delta$. The procedure is completely identical to that described in the paragraph relating to the *variational method* for permittivity. The results are reported in Table 4.13.

Also in this case the results obtained are not encouraging and differ from those declared by the manufacturers of the respective analyzed materials.

4.6.3 *Svačina and Schneider mixed method*

In order to complete the characterization of the materials through the *electromagnetic map extrapolation method*, it was decided to combine the relationships used in the algorithm based on the *conformal mapping method* [33] and the relationships described in [42], and reported previously. The idea was that if relative permittivity (real part) can be treated with confor-

Material	h_2 [mm]	f_r [GHz]	ε_e	ε_{r_2}	$\tan\delta_e$	$\tan\delta_2$
Mylar-A	0,08	1,5834	4,0356	**2,8461**	0,0158	**0,0038**
Kapton	0,03	1,5624	4,1449	**3,142**	0,0172	**0,0193**
RO4003C	0,8	1,6665	3,6434	**3,3215**	0,0144	**0,0111**
TU-768	1,54	1,5822	4,0416	**4,6177**	0,0286	**0,0418**
Alumina	0,63	1,4555	4,7761	**7,3547**	0,0139	**0,0076**

Table 4.13: *Variational method* for complex permittivity determination: measurement results.

Material	h_2 [mm]	f_r [GHz]	ε_e	ε_{r_2}	$\tan\delta_e$	$\tan\delta_2$
Mylar-A	0,08	1,5834	4,0356	**2,797**	0,0158	**0,0089**
Kapton	0,03	1,5624	4,1449	**3,297**	0,0172	**0,0211**
RO4003C	0,8	1,6665	3,6434	**3,279**	0,0144	**0,0031**
TU-768	1,54	1,5822	4,0416	**4,542**	0,0286	**0,0194**
Alumina	0,63	1,4555	4,7761	**7,578**	0,0139	**0,0038**

Table 4.14: Svačina and Schneider mixed method for loss tangent extraction: measurement results.

mal transformations, then the same thing could be possible for its imaginary part and therefore for the loss tangent (equation (4.1.2)).

First of all the filling factors [33] were calculated thanks to the equations (4.5.1)-(4.5.12), and then they were used in the final equation for the calculation of the effective loss tangent in the *Schneider's method* [42]:

$$\tan\delta_e = \frac{1}{2\cdot\varepsilon_e}\sum_{i=1}^{4} q_i \tan\delta_i \qquad (4.6.7)$$

Term $\frac{1}{2}$ has been included as it will help to provide better results in loss tangent extraction as we will see below. The results of the extrapolation are shown in Table 4.14.

The results obtained are very close to those provided by the manufacturers. The combination of the *electromagnetic map extraction method* and the *Svačina and Schneider mixed method* allows to have very good approximations of relative dielectric constant and loss tangent.

4.7 Common use materials and fabrics dielectric characterization

After having seen the results obtained by the three pairs of methods described, for the dielectric materials most widely used for microwave applications, we wanted to move on to the characterization of materials that are used daily, such as paper, cardboard, plexiglass, etc.. The purpose is to understand if it could be possible to use them as a substrate for the realization of low cost microwave devices (antennas, sensors, etc.). The analysis was also conducted on various textile materials, such as fleece fabric, cotton, satin, silk, felt, etc., with the aim of being able to use them in the realization of microwave wearable devices. The results obtained by combining all the methods seen so far, and more precisely:

- *conformal mapping method* (relative dielectric constant) + *Schneider's Method* (loss tangent value);

- *upgraded variational method* (relative dielectric constant + loss tangent value);

- *electromagnetic map extraction method* (relative dielectric constant) + *Svačina and Schneider mixed method* (loss tangent value).

4.7.1 Common use materials

The materials chosen for the determination of their dielectric characteristics are paper, polystirene, teflon, polylactic acid (PLA), cardboard, plexiglass, and FR4. In the literature there are several studies in which numerous approaches are described in the characterization of their dielectric properties, and we will use their results as a reference terms to verify the goodness of the data obtained. Table 4.15 shows the results obtained using the first combination of methods, namely *conformal mapping method + Schneider's method*, while Table 4.16 shows the extrapolated results obtained with the *upgraded variational method*. Table 4.17 shows the results obtained with the *electromagnetic map extraction method* and the *Svačina and Schneider mixed method*.

By making a quick comparison between the three sets of values obtained from the extrapolations, it can be seen that the data obtained from the last pair of methods is the closest to the values disseminated in the literature. It is obvious that small differences can however be found in that these materials can have varying densities and composition, and therefore non-standardized dielectric characteristics.

Material	h_2 [mm]	f_r [GHz]	ε_e	ε_{r_2}	$\tan \delta_e$	$\tan \delta_2$	ε_r Bibliographic value	$\tan \delta$ Bibliographic value
Paper	0,08	1,6225	3,8433	**2,4653**	0,0201	**0,029**	**1,7-2,2** @ 1 GHz **[44]**	**0,011-0,032** @ 1 GHz **[44]**
Polystyrene (transparent part of a jewel case)	1,14	2,0416	2,4275	**1,6871**	0,0161	**0,0224**		
Teflon	2,17	1,9671	2,6148	**2,3403**	0,0174	**0,0241**	**2** from 10 kHz to 25 GHz **[45]**	≤ **0,0006** from 10 kHz to 25 GHz **[45]**
Polylactic Acid (PLA)	1,63	1,8793	2,8648	**2,5614**	0,0176	**0,0252**	**2,533** from 1,7 GHz to 4 GHz **[46]**	**0,0395** from 1,7 GHz to 4 GHz **[46]**
Cardboard	1,65	2,2039	2,0832	**1,4017**	0,0284	**0,0504**		
Plexiglass	2,75	1,887	2,8417	**2,8452**	0,0238	**0,034**	**2,7276** @ 1,1048 GHz **[47]**	**0,0032** @ 1,1048 GHz **[47]**
FR4	1,49	1,675	3,6062	**3,7591**	0,0231	**0,0318**		

Table 4.15: Common use materials measurements results. Adopted methods: *conformal mapping method + Schneider's method.*

Material	h_2 [mm]	f_r [GHz]	ε_e	ε_{r_2}	$\tan \delta_e$	$\tan \delta_2$	ε_r Bibliographic value	$\tan \delta$ Bibliographic value
Paper	0,08	1,6225	3,8433	**1,7445**	0,0201	**0,0441**	**1,7-2,2** @ 1 GHz **[44]**	**0,011-0,032** @ 1 GHz **[44]**
Polystyrene (transparent part of a jewel case)	1,14	2,0416	2,4275	**1,4078**	0,0161	**0,0168**		
Teflon	2,17	1,9671	2,6148	**2,0435**	0,0174	**0,0197**	**2** from 10 kHz to 25 GHz **[45]**	≤ **0,0006** from 10 kHz to 25 GHz **[45]**
Polylactic Acid (PLA)	1,63	1,8793	2,8648	**2,2857**	0,0176	**0,0199**	**2,533** from 1,7 GHz to 4 GHz **[46]**	**0,0395** from 1,7 GHz to 4 GHz **[46]**
Cardboard	1,65	2,2039	2,0832	**1,1685**	0,0284	**0,044**		
Plexiglass	2,75	1,887	2,8417	**2,5351**	0,0238	**0,0315**	**2,7276** @ 1,1048 GHz **[47]**	**0,0032** @ 1,1048 GHz **[47]**
FR4	1,49	1,675	3,6062	**3,6162**	0,0231	**0,0311**		

Table 4.16: Common use materials measurements results. Adopted method: *upgraded variational method.*

Material	h_2 [mm]	f_r [GHz]	ε_e	ε_{r_2}	$\tan\delta_e$	$\tan\delta_2$	ε_r Bibliographic value	$\tan\delta$ Bibliographic value
Paper	0,08	1,6225	3,8433	**2,26**	0,0201	**0,0418**	**1,7-2,2 @ 1** GHz **[44]**	**0,011-0,032** @ 1 GHz **[44]**
Polystyrene (transparent part of a jewel case)	1,14	2,0416	2,4275	**1,569**	0,0161	**0,0021**		
Teflon	2,17	1,9671	2,6148	**2,066**	0,0174	**0,0057**	**2** from 10 kHz to 25 GHz **[45]**	**≤ 0,0006** from 10 kHz to 25 GHz **[45]**
Polylactic Acid (PLA)	1,63	1,8793	2,8648	**2,275**	0,0176	**0,0065**	**2,533** from 1,7 GHz to 4 GHz **[46]**	**0,0395** from 1,7 GHz to 4 GHz **[46]**
Cardboard	1,65	2,2039	2,0832	**1,282**	0,0284	**0,0137**		
Plexiglass	2,75	1,887	2,8417	**2,5**	0,0238	**0,0145**	**2,7276** @ 1,1048 GHz **[47]**	**0,0032** @ 1,1048 GHz **[47]**
FR4	1,49	1,675	3,6062	**3,565**	0,0231	**0,0147**		

Table 4.17: Common use materials measurements results. Adopted methods: *electromagnetic map extraction method + Svačina and Schneider mixed method.*

4.7.2   Fabrics materials

The textile materials chosen for the characterization of their dielectric properties are silk, satin, wool, cotton, denim (pure cotton), linen, viscose (95% cotton - 5% viscose), felt, and stretch denim (cotton and polyester). Also for these materials there are numerous studies in the literature that have be taken as a reference to verify the validity of the data obtained from extrapolations. As in the case of commonly used materials, the results of the dielectric characterization of the fabrics are reported in Table 4.18, Table 4.19 and Table 4.20, respectively related to the three pairs of extrapolation methods listed at the beginning of the Section.

Also in this case the combination of *electromagnetic map extraction method* and the *Svačina and Schneider mixed method* provides values very close to those found in the literature.

4.8   Conclusions

In this chapter a new way of measuring dielectric materials having dielectric constants between 1 and 10, and thicknesses between 0 mm and 5 mm has been described. A strenght of this measurement technique lies in the fact

Material	h_2 [mm]	f_r [GHz]	ε_e	ε_{r_2}	$\tan\delta_e$	$\tan\delta_2$	ε_r Bibliographic value	$\tan\delta$ Bibliographic value
Silk	0,18	1,7314	3,3754	**2,0686**	0,167	**0,0177**	**1,75 [48]**	**0,012 [48]**
Satin	0,08	1,6225	3,8433	**2,4653**	0,0196	**0,0266**	**2,74 @ 330 GHz [49]**	**0,0274 @ 330 GHz [49]**
Fleece fabric	0,48	1,9175	2,7519	**1,9092**	0,0178	**0,022**	**1,25 @ 2,4 GHz [50]**	**0,007 @ 2,4 GHz [50]**
Cotton	0,36	1,8854	2,8464	**1,8147**	0,0224	**0,0318**	**1,6 @ 2,6 GHz [51]**	**0,04 @ 2,6 GHz [51]**
Denim (Cotton)	0,8	2,0429	2,4243	**1,4802**	0,0133	**0,0164**	**1,6 @ 2,3 GHz [52]**	**0,05 @ 2,3 GHz [52]**
Linen	0,38	1,9003	2,8019	**1,7964**	0,0194	**0,0253**		
95% Cotton – 5% Viscose	0,35	1,9080	2,7795	**1,7057**	0,0193	**0,0252**		
Felt	3,4	2,3556	1,8234	**1,3283**	0,0288	**0,0537**	**1,22 @ 1 GHz [52]**	**0,016 @ 1 GHz [52]**
Denim (Cotton & Polyester)	0,75	2,0569	2,3916	**1,4029**	0,0261	**0,0437**	**1,6 @ 2,4 GHz [53]**	**0,02 @ 2,4 GHz [53]**

Table 4.18: Textile materials measurements results. Adopted methods: *conformal mapping method + Schneider's method.*

Material	h_2 [mm]	f_r [GHz]	ε_e	ε_{r_2}	$\tan\delta_e$	$\tan\delta_2$	ε_r Bibliographic value	$\tan\delta$ Bibliographic value
Silk	0,18	1,7314	3,3754	**1,3608**	0,167	**0,0164**	**1,75 [48]**	**0,012 [48]**
Satin	0,08	1,6225	3,8433	**1,7445**	0,0196	**0,039**	**2,74 @ 330 GHz [49]**	**0,0274 @ 330 GHz [49]**
Fleece fabric	0,48	1,9175	2,7519	**1,2528**	0,0178	**0,0201**	**1,25 @ 2,4 GHz [50]**	**0,007 @ 2,4 GHz [50]**
Cotton	0,36	1,8854	2,8464	**1,1646**	0,0224	**0,0335**	**1,6 @ 2,6 GHz [51]**	**0,04 @ 2,6 GHz [51]**
Denim (Cotton)	0,8	2,0429	2,4243	**1,1959**	0,0133	**0,0093**	**1,6 @ 2,3 GHz [52]**	**0,05 @ 2,3 GHz [52]**
Linen	0,38	1,9003	2,8019	**1,1467**	0,0194	**0,0248**		
95% Cotton – 5% Viscose	0,35	1,9080	2,7795	**1,0631**	0,0193	**0,0246**		
Felt	3,4	2,3556	1,8234	**1,1257**	0,0288	**0,045**	**1,22 @ 1 GHz [52]**	**0,016 @ 1 GHz [52]**
Denim (Cotton & Polyester)	0,75	2,0569	2,3916	**1,1173**	0,0261	**0,0403**	**1,6 @ 2,4 GHz [53]**	**0,02 @ 2,4 GHz [53]**

Table 4.19: Textile materials measurements results. Adopted method: *upgraded variational method.*

Material	h_2 [mm]	f_r [GHz]	ε_e	ε_{r_2}	$\tan\delta_e$	$\tan\delta_2$	ε_r Bibliographic value	$\tan\delta$ Bibliographic value
Silk	0,18	1,7314	3,3754	**1,73**	0,167	**0,0015**	**1,75 [48]**	**0,012 [48]**
Satin	0,08	1,6225	3,8433	**2,26**	0,0196	**0,0366**	**2,74 @ 330 GHz [49]**	**0,0274 @ 330 GHz [49]**
Fleece fabric	0,48	1,9175	2,7519	**1,537**	0,0178	**0,0022**	**1,25 @ 2,4 GHz [50]**	**0,007 @ 2,4 GHz [50]**
Cotton	0,36	1,8854	2,8464	**1,494**	0,0224	**0,0211**	**1,6 @ 2,6 GHz [51]**	**0,04 @ 2,6 GHz [51]**
Denim (Cotton)	0,8	2,0429	2,4243	**1,376**	0,0133	**0,015**	**1,6 @ 2,3 GHz [52]**	**0,05 @ 2,3 GHz [52]**
Linen	0,38	1,9003	2,8019	**1,464**	0,0194	**0,0074**		
95% Cotton – 5% Viscose	0,35	1,9080	2,7795	**1,36**	0,0193	**0,0051**		
Felt	3,4	2,3556	1,8234	**1,191**	0,0288	**0,0183**	**1,22 @ 1 GHz [52]**	**0,016 @ 1 GHz [52]**
Denim (Cotton & Polyester)	0,75	2,0569	2,3916	**1,283**	0,0261	**0,0171**	**1,6 @ 2,4 GHz [53]**	**0,02 @ 2,4 GHz [53]**

Table 4.20: Textile materials measurements results. Adopted methods: *electromagnetic map extraction method + Svačina and Schneider mixed method.*

that it has a real instrument that allows to not to "waste" every time a piece of sample on which it would have been necessary to make the measurer in order to identify its dielectric properties. Three pairs of algorithms were presented in order to derive the relative dielectric constant and loss tangent values. Several simulations tests were carried out and then the measurement phase. As it is possible to see from various results tables, the combination of the *electromagnetic map extraction method* and the *Svačina and Schneider mixed method* manages to return values of relative dielectric constant and loss tangent close to what they should be. The *conformal mapping method*, combined with *Schneider's method*, and the *updated variational method* also manage to give an idea of what the real relative permittivity and loss tangent values could be. The *upgraded variational method*, however, even if it returns values slightly closer to *electromagnetic map extraction method* for intermediate permittivities ($\varepsilon_r = 3 \div 5$), can provide dielectric constant values too low and close to 1 in cases where a low relative dielectric constant material is being measured ($\varepsilon_r = 1.2 \div 1.6$). The processing times are also very high compared to all other methods, which makes it "inconvenient" for carrying out preliminary analyzes. To reduce the analysis times it may be better to use the *conformal mapping method* (in the case of relative dielectric constant values $\leqslant 5$), and then move on to the use of the *electromagnetic map extraction method.* As regards the extrapolation of the loss tangent value, the *Svačina and Schneider mixed method* is the one that among the analyzed methods, is closest to the real values.

Bibliography

[1]   S. Ramo, J. R. Whinnery and T. Van Suzer. *Fields and Waves in Communication Electronics*, 3rd edition, John Wiley & Sons, Inc., New York, Feb. 1994.

[2]   L. F. Chen, C. K. Ong, C. P. Neo, V. V. Varadan, V. K. Varadan. *Microwave Electronics: Measurement and Materials Characterization*, John Wiley & Sons, Inc., New York, Apr. 2004.

[3]   T. K. Ishii. *Handbook of Microwave Technology, Vol. 1*, Academic Press, San Diego, CA, 1995.

[4]   J. -M. Heinola, P. Silventoinen, K. Latti, M. Kettunen, and J. -P. Strom. *Determination of Dielectric Constant and Dissipation Factor of a Printed Circuit Board Material Using a Microstrip Ring Resonator Structure*. Microwaves, Radar and Wireless Communications, 2004. MIKON-2004. 15th International Conference on. Warsaw, Poland: IEEE.

[5]   P. Troughton. *Measurement technique in microstrip*, Electron. Lett., Vol. 5, No. 2, pp. 25–26, January 23, 1969.

[6]   K. Chang, F. Hsu, J. Berenz, and K. Nakano. *Find optimum substrate thickness for millimeter-wave GaAs MMICs*, Microwaves & RF, Vol. 27, pp. 123–128, September 1984.

[7]   W. Hoefer and A. Chattopadhyay. *Evaluation of the equivalent circuit parameters of microstrip discontinuities through perturbation of a resonant ring*, IEEE Trans. Microwave Theory Tech.,Vol. MTT-23, pp. 1067–1071, December 1975.

[8]   T. C. Edwards. *Foundations for Microstrip Circuit Design*, Wiley, Chichester, England, 1981; 2d ed., 1992.

[9]   J. Deutsch and J. J. Jung. *Microstrip ring resonator and dispersion measurement on microstrip lines from 2 to 12GHz*, Nachrichtentech. Z., Vol. 20, pp. 620–624, 1970.

[10]   I.Wolff and N. Knoppik. *Microstrip ring resonator and dispersion measurements on microstrip lines*, Electron. Lett.,Vol. 7, No. 26, pp. 779–781, December 30, 1971.

[11]   H. J. Finlay, R. H. Jansen, J. A. Jenkins, and I. G. Eddison. *Accurate characterization and modeling of transmission lines for GaAs MMICs*, in 1986 IEEE MTTS Int. Microwave Symp. Dig., New York, pp. 267–270, June 1986.

[12]   P. A. Bernard and J. M. Gautray. *Measurement of relative dielectric constant using a microstrip ring resonator*, IEEE Trans. Microwave Theory Tech., Vol. MTT-39, pp. 592–595, March 1991.

[13]   P. A. Polakos, C. E. Rice, M. V. Schneider, and R. Trambarulo. *Electrical characteristics of thin-film Ba2YCu3O7 superconducting ring resonators*, IEEE Microwave Guided Wave Lett.,Vol. 1, No. 3, pp. 54–56, March 1991.

[14]   M. E. Goldfarb and A. Platzker. *Losses in GaAs Microstrip*, IEEE Trans. Microwave Theory Tech.,Vol. MTT-38, No. 12, pp. 1957–1963, December 1990.

[15]   S. Kanamaluru, M. Li, J. M. Carroll, J. M. Phillips, D. G. Naugle, and K. Chang. *Slotline ring resonator test method for high-Tc superconducting films*, IEEE Trans. App. Supercond.,Vol. ASC-4, No. 3, pp. 183–187, September 1994.

[16]   T. S. Martin. *A study of the microstrip ring resonator and its applications*, M.S. thesis, Texas A&M University, College Station, December 1987.

[17]   A. Bogner, C. Steiner, S. Walter, J. Kita, G. Hagen, and R. Moos. *Planar Microstrip Ring Resonators for Microwave-Based Gas Sensing: Design spects and Initial Transducers for Humidity and Ammonia Sensing*, Sensors, Vol. 17(10): 2422, Oct. 2017.

[18]   K. Chang, L -H. Hsieh. *Microwave Ring Circuits and Related Structures*, Wiley & Sons, Inc., Apr. 2004.

147

[19]   E. Belohoubek and E. Denlinger. *Loss considerations for microstrip resonators*, IEEE Trans. Microwave Theory Tech.,Vol. MTT-23, pp. 522–526, June 1975.

[20]   K. Chang, F. Hsu, J. Berenz, and K. Nakano. *Find optimum substrate thickness for millimeter-wave GaAs MMICs*, Microwaves & RF, Vol. 27, pp. 123–128, September 1984.

[21]   A. Rashidian, M. T. Aligodarz, and D. M. Klymyshyn. *Dielectric Characterization of Materials using a Modified Microstrip Ring Resonator Technique*, IEEE Transaction on Dielectrics and Electrical Insulation, Vol. 19, Issue: 4, pp. 1392-1399, Aug. 2012.

[22]   M. T. Jilani, W. P. Wen, M. A. Zakariya, and L. Y. cheong. *Microstrip Ring Resonator Based Sensing Technique for Meat Quality*, 2013 IEEE Symposium on Wireless Technology & Applications (ISWTA), pp. 220-224, Sept. 2013.

[23]   tuc.com.tw/en-es/products-detail/id/24/index/7/title/TU-768

[24]   mathworks.com

[25]   I. Waldron. *Ring Resonator Method for Dielectric Permittivity Measurement of Foams*, Master Degree Thesis, May 2006.

[26]   I. Waldron, S. N. Makarov, S. Biederman, and R. Ludwig. *Suspended Ring Resonator for Dielectric Constant Measurement of Foams*, IEEE Microwave and Wireless Components Letters, Vol. 16, No. 9, pp. 496-498, Sept. 2006.

[27]   K. Sarabandi and E. S. Li. *Microstrip Ring Resonator for soil Moisture Measurements*, IEEE Transactions on Geoscience and Remote Sensing, Vol. 35, No. 5, pp. 1223-1231, Sept. 1997.

[28]   J. -M. Heinola and K. Tolsa. *Dielectric Characterization of Printed Wiring Board Materials Using Ring Resonator Techniques: A Comparison of Calculation Models*, IEEE Transactions on Dielectrics and Electrical Insulation, Vol. 13, No. 4, pp. 717-726, Aug. 2006.

[29]   K. C. Gupta, R. Garg, and I. J. Bahl. *Microstrip Lines and Slot-Lines*, Dedham, MA: Artech House, 1979.

148

[30]   H. A. Wheeler. *Transmission Line Properties of Parallel Wide Strips by a Conformal Mapping approximation*, IEEE Trans. Microwave Theory Tech., Vol. MTT-12, No. 3, p. 280, 1964.

[31]   H. A. Wheeler. *Transmission Line Properties of Parallel Strips Separated by a Dielectric Sheet*, IEEE Trans. Microwave Theory Tech., Vol. MTT-13, No. 2, p. 172, 1965.

[32]   J. Svačina. *Analysis of Multilayer Microstrip Lines by a Conformal Mapping Method*, IEEE Transactions on Microwave Theory and Techniques, Vol. 40, No. 4, pp. 769-772, Apr. 1992.

[33]   J. Svačina. *A Simple Quasi-Static Determination of Basic Parameters of Multilayer Microstrip and Coplanar Waveguide*, IEEE Microwave and Guided Wave Letters, Vol. 2, No. 10, October 1992.

[34]   E. Yamashita, *Variational Method for the Analysis of Microstrip-Like Tranmission Lines*, IEEE Trans. Microwave Theory Tech., Vol. MTT-16, No. 8, pp. 529-535, 1968.

[35]   E. Yamashita and K. Atsuki. *Strip Line with Rectangular Outer Conductor and Three Dielectric Layers*, IEEE Trans. Microwave Theory Tech., Vol. MTT-18, No. 5, pp. 238-244, 1970.

[36]   ansys.com/Products/Electronics/ANSYS-HFSS

[37]   usa.dupontteijinfilms.com/wp-content/uploads/2017/01/Mylar_Electrical_proper

[38]   materials-direct.com/wp-content/uploads/2019/08/DEC-Kapton-HN-datasheet.pdf

[39]   rogerscorp.com/-/media/project/rogerscorp/documents/advanced-connectivity-solutions/english/data-sheets/ro4000-laminates-ro4003c-and-ro4350b—dasta-sheet.pdf

[40]   rf-microwave.com/it/nbp/nmp/lastra-allumina-bianca-vergine/alm-05/

[41]   mathworks.com/products/pde.html

[42]   M. V. Schneider. *Dielectric Loss in Integrated Microwave Circuits*, The Bell System Technical Journal, Vol. 48, Issue: 7, pp. 2325-2332, Sept. 1969.

[43]   B. E. Spielman. *Dissipation Loss Effects in Isolated and Coupled Transmission Lines*, IEEE Transactions on Microwave Theory and Techniques, Vol. MTT-25, No. 8, Aug. 1977.

[44]   V. Mandrić Radivojević, S. Rupčic, M. Snorvić, and G. Benšić. *Measuring the Dielectric constant of Paper Using a Parallel Plate Capacitor*, International Journal of Electrical and Computer Engineering Systems, Vol. 9, No. 1, Jan. 2018.

[45]   R. G. Geyer. *Dielectric Characterization and Reference Materials*, National Institute of Standards and Technology (NIST) Technical Note 1338, Apr. 1990.

[46]   J. Bjorgaard, M. Hoyack, E. Huber, M. Mizaree, Y. -H. Chang, and S. Noghanian. *Design and Fabrication of Antennas Using 3D Printing*, Progress In Electromagnetic Research C, Vol. 84, pp. 119-134, 2018.

[47]   E. Tanabe and W. T. Joines. *A Nondestructive Method for Measuring the Complex Permittivity of Dielectric Materials at Microwave Frequencies Using an Open Transmission Line Resonator*, IEEE Transaction on Instrumentation and Measurement, Vol. IM-25, No. 3, pp. 222-226, Sept. 1976.

[48]   S. Dhupkariya, V. K. Singh, and A. Shukla. *A review of Textile Materials for Wearable Antenna*, Journal of Microwave Engineering & Technologies, ISSN: 2349-9001 (online), Vol. 1, Issue: 3, www.stmjournals.com, Mar. 2014.

[49]   B. Kapilevich, B. Litvak, M. Anisimov, D. Hardon, and Y. Pinhasi. *Complex Permittivity Measurements of Textiles and Leather in a Free Space: An Angular-Invariant Approach*, International Journal of Microwave Science and Technology 2012 (11), Aug. 2012.

[50]   F. Declercq, H. Rogier, and C. Hertleer. *Permittivity and Loss Tangent Characterization for Garment Antennas Based on a New Matrix-Pencil Two-Line Method*, IEEE Transaction on Antenna and Propagation, Vol. 56, No. 8, pp. 2548-2554, 2008.

[51]   R. Salvado, C. Loss, R. Goncalves, and P. Pinho. *Textile Materials for the Design of Wearable Antennas: A Survey*, Sensors 12 (11): 15841-57, Dec. 2012.

[52]   M. Mantash, A. -C. Tarot, S. Collardey, and K. Mahdjoubi. *Investigation of Flexible Textile Antennas and AMC Reflectors*, International Journal of Antennas and Propagation 2012 (11), May 2012.

[53]   M. L. Scarpello, I. Kazani, C. Hertleer, H. Rogier, and D. V. Ginste. *Stability and Efficiency of Screen-Printed Wearable and Washable Antennas*, IEEE Antennas and Wireless Propagation Letters, Vol. 11, pp. 838-841, 2012

Chapter 5

Microwave Microfluidic Sensors for Medical and Chemical Analysis

5.1 Introduction

The novel medical and healthcare applications involving in situ diagnosis systems (e. g., Point-of-Care testing systems) for rapid detection and diagnosis of diseases and biomedical surveillance systems for monitoring vital health parameters demand for new generation of compact, cost effective and reliable sensors. The objective is the development of high sensitive and accurate biosensors that permit to perform biochemical analysis with the same reliability of the bioanalytical laboratories and with the advantage of using extremely small volume of the samples. A class of sensors suitable for that kind of applications is based on microfluidic systems that exploits different technologies [1]. Optical and electronic technologies are largely used for implementing the detection part of microfluidic sensors nevertheless, microwave and radio frequency techniques have also been exploited recently. Microwave sensors rely either on the measurement of relative permittivity and conductivity of the sample or the detection of their variation as a consequence of changes of the analyte. The most sensitive microwave sensor devices are based on resonant structures like cavities, rings and metamaterial inspired shapes [2], [3]. The resonant frequency and the merit factor of the resonator are the measuring values used to perform the analysis of the sample. The sensitivity depends on the value of the merit factor and on the rapidity of the change of the resonant frequency with respect to the variation of the analyte. In this chapter simple microfluidic microwave sensors that have the poten-

tiality to be used as disposable sensors in chemical and biological analysis are described. The basic sensor structure is flat and very thin, it is based on a microstrip structure to be specifically realized using 3D printing technology or assembling minute parts constructed in advance. The behaviour of this type of sensors have been analysed by means of numerical methods showing a good performance in differentiating a large class of analytes from chemical solvents to aqueous solutions and organic liquids. Low-cost laboratory prototypes have been developed and the experimental measurements confirmed the simulated performances.

5.2 Design and theoretical considerations

Planar, and in particular microstrip transmission lines, are largely exploited to measure the dielectric properties of laminated materials using resonator methods and resonant-perturbation methods. In case of resonant methods, the material under test is used as the substrate and the properties of the material are calculated from the resonant frequency and quality factor of the resonator [4]. In a resonant-perturbation method, the sample under test is brought close to a microstrip resonator, and the properties of the sample are derived from the change of resonant frequency and quality factor of the resonator due to the presence of the sample [3]. The idea is to modify the T-resonator method shown in [4] into a resonant-perturbation method able to detect the characteristics of the liquids inside a microfluidic channel. As shown in Fig. 5.2.1, the T-resonator is actually an open-end transmission-line stub that resonates approximatively at odd-integer multiples of its quarter-wavelength frequency and gives a transmission coefficient S_{21} having a band-stop response. Near the resonance the S_{21} is

$$S_{21} = \frac{2Z_{in}}{2Z_{in} + Z_0} \qquad (5.2.1)$$

where Z_0 is the characteristic impedance of the measurement transmission line. Z_{in} is the equivalent input impedance of a series lumped resonant circuit representing the behavior of the stub, i.e.,

$$Z_{in} = R_0 \left(1 + j2Q_0 \frac{\Delta\omega}{\omega_0} \right) \qquad (5.2.2)$$

where Q_0 is the unload Q-factor of the resonator, ω_0 is the resonant frequency and $2\Delta\omega$ is the "twice power" bandwidth for which the magnitude of S_{21} is equal to its minimum value times the square root of 2. That resonator permits to determine the effective dielectric constant of the substrate under
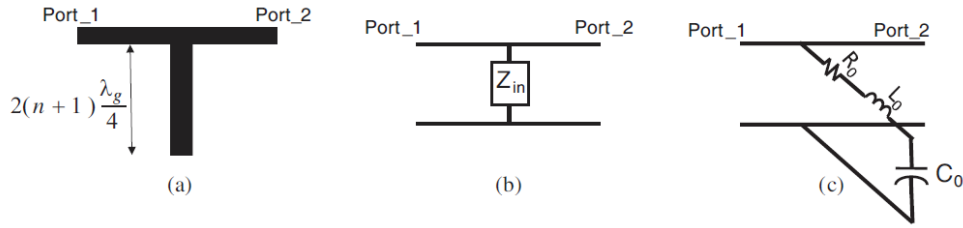
Figure 5.2.1: Schema of microstrip T-resonator (a) and its equivalent circuits (b)-(c).

test (i.e. the substrate where it is placed on) through the resonant frequency and the known length of the stub. The measured Q-factor togheter with the calculated effective dielectric constant permits to determine the transmission line attenuation.

Making the substrate (hosting the stub) inhomogeneous by introducing under the stub line, inside the substrate material, a microfluidic channel we perturb the behavior of the resonator by changing the local dielectric properties of the material as shown in Fig. 5.2.2. The first effect of the perturbation is the changing of the resonant frequency, in fact the channel under the stub changes the capacitance to ground of the microstrip which is very sensitive to the dielectric properties of the material inside the channel. Evidently, the measurement of the changing of the resonant frequency permits to distinguish among different materials inside the channel. The measurement of the Q-factor is an additional information that account for the losses of the material inside the channel even though it is not directly exploitable because of the losses of the surrounding substrate. To minimize the undesired losses of the substrate and in order to increase the strength of the electric field inside the channel we resort to a substrate having a honeycomb structure.

An ad-hoc substrate including both the honeycomb structure and the microfluidic channel has been realized using a 3D printer as shown in Fig. 5.2.2. The material of that substrate is a Polylactic Acid (PLA) polymer resin, the diameter of the channel is about 0.5 mm while the thickness of the substrate is about 0.8 mm. The ground and the microstrip line are made of adhesive copper.

154
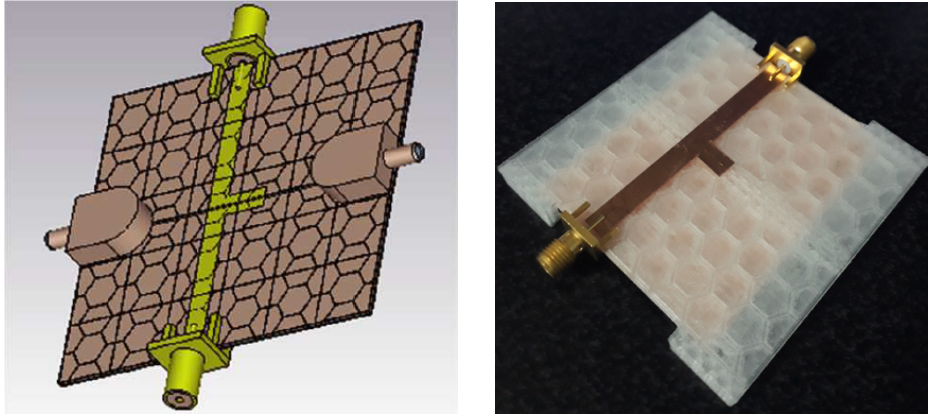
Figure 5.2.2: Design of microfluidic sensor. The microfluidic channel is connected to external tubes by means of special connectors. The substrate is a honeycomb structure. On the right side the realized prototype is depicted.

5.3 Preliminary numerical and experimental results

The proposed microfluidic sensor has been modelled by means of numerical tools (CST Microwave Studio [5], Altair FEKO [6]) in order to determine its behavior and to improve its sensitivity by tuning the characterizing parameters. The model accounts for the permittivity of the 3D-printed substrate that has been measured in advance by means of the ring-resonator method [7]. Fig. 5.2.3 shows the calculated transmission coeffcient on a large bandwidth including both the first and the second resonant mode. The microfluidic channel has been filled with different (organic and aqueous) materials as shown in the legend of Fig. 5.2.3. Each material is distinguished from the others by the frequency of the minimum of the S_{21} and for the width of the twice power band. Both resonant modes permit to have a clear distinction of the materials but the resonant mode at higher frequency permits to have a better resolution since the peaks of the minima are spread over a larger bandwidth (about 1.5 GHz).

Fig. 5.3.2 shows the measured transmission coeffcient in case of 6 aqueous and solvent liquids. The minima of the transmission coeffcients do not correspond in frequency to the simulative results (of Fig. 5.3.1) because the length of the stub is shorter than the simulated one (to include only one resonance). It's worth observing the ability to discriminate with good resolution different kind of water: distilled water, tap water and physiological saline water. That behavior makes us confident to use the sensor in real applications.

155
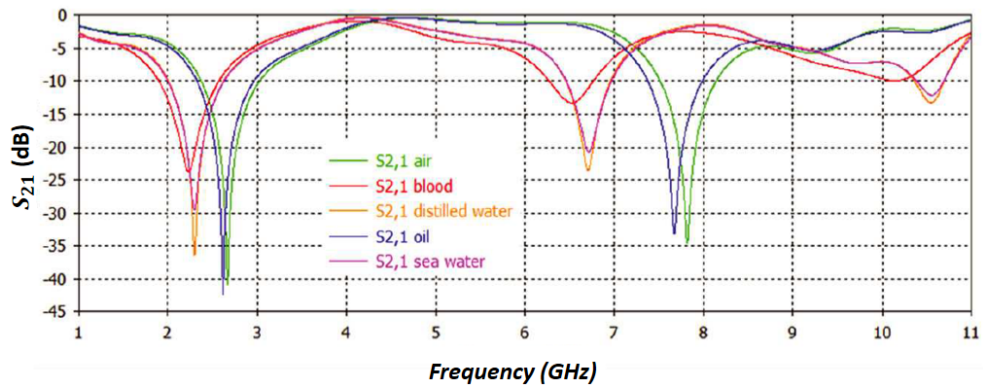
Figure 5.3.1: Transmission coefficient over a bandwidth including the first two resonant modes.
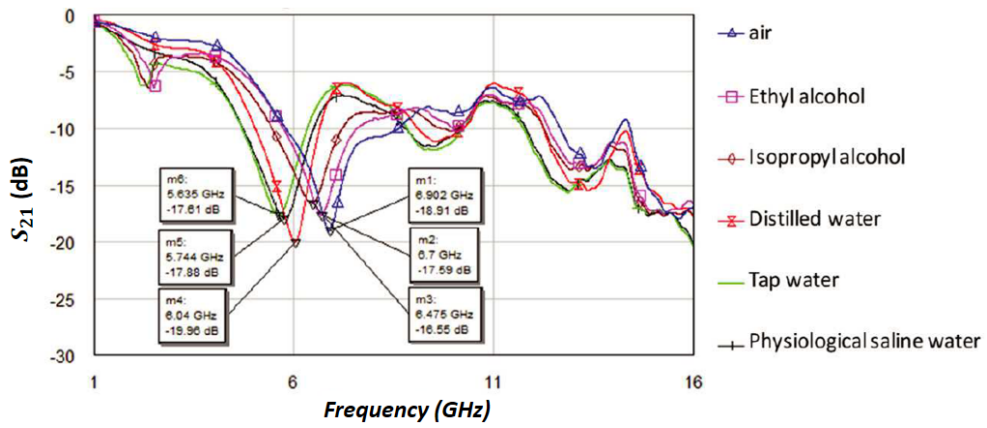
Figure 5.3.2: Measured transmission coeffcient for the realized microfluidic sensor in case of 6 different materials inside the channel. The insets report the values of the peaks of minima.

5.4 PLA material considerations

Polylactic acid (PLA), used in the construction of the microfluidic sensor, is a polyester polymer produced by the condensation of lactic acid that is derived from microbial fermentation of renewable agriculture resures. As reported in various studies in literature PLA plastics are very sensitive to moisture and heat [8]-[12]. In [8], the temperature and humidity resistance properties of PLA were studied for different types of plastics, finding that the greatest strength was obtained for those materials whose molecular density had been increased. However, whitin a few weeks there was still a structural deterioration of the plastic material. Very similar results are also reported in [9], in which the analysis was conducted considering also the direct effects that water, in its liquid state, causes on the molecular stability of PLA.

In our case, PLA was used for the realization, not only of the honeycomb substrate of the sensor, but also of the microfluidic channel in which the liquids to be analyzed are made to flow. Based on what has been said, there was a risk that as the number of measurements made increased, the device could lose reliability during the measurement phase. This aspect was found during the measurement phase, in which it happened not to obtain, for the same liquid, a representative resonance frequency identical to that measured the previous time. For this reason, and as reported in chapter 4, it was decided to proceed towards the realization of another low-cost microfluidic sensor with unconventional substrates for the microwave frequency band.

5.5 New low-cost microwave microfluidic sensor

To overcome the problems associated to the use of PLA, it was necessary to choose a material that would permit to realize a low cost and low environmental impact device. From the data reported in Table 4.17, the choice fell on the cardboard, as it had very low dielectric constant and losses ($\varepsilon_r = 1.28$, $\tan \delta = 0.0065$). As in the case of honeycomb PLA, even the common cardboard has periodic structures inside it that allow air to flow inside. This feature then allowed the application of a small chemical laboratory glass tube, having internal and external diameters respectively equal to $d_i = 0.5$ mm, $d_o = 1$ mm. As in the case of PLA sensor, the presence of cavities inside the cardboard would allow the application of multiple channels in order to carry out simultaneous analysis of different liquids at multiple frequencies. The thickness of the cardboard chosen was 1.7 mm, while the conductive parts were in 0.035 mm thick copper. Fig. 5.5.1 shows the layout of the new
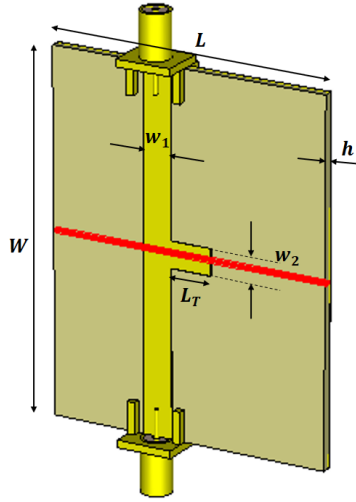
Figure 5.5.1: Cardboard based microfluidic sensor drawing.

W	L	h	w_1	w_2	L_T
61	48	1,7	5	4,5	7,5

Table 5.1: Geometrical values of proposed microfluidic sensor parts in millimeters.

microfluidic sensor, while Table 5.1 shows the final dimensions of the various parts that make up the device.

The microfluidic sensor having the characteristics just described was simulated in CST Microwave Studio environment. For the glass tube, present inside the substrate $\varepsilon_r = 4.82$, and $\tan\delta = 0.0054$ have been set. The simulation was made with a frequency domain analysis using the Finite Element Method (FEM) which better allows to analyze the resonant structures. Fig. 5.5.2 depicts the results of simulation, which show the lower and upper limits of the frequency band within which the resonance peak can move as the dielectric characteristics of the material that flow inside the tube vary. The resonance frequency obtained in the case of an empty pipe (air inside it) is found at 7.56 GHz, while in the case of distilled water ($\varepsilon_r = 68.49$, $\sigma = 11.11$ [S/m], at 20 °C) the resonance frequency is at 7.34 GHz.

Given the ability to detect the presence of different types of liquids inside the microfluidic tube, the set goal for this new sensor was to be able to detect different concentrations of solute within solutions where the solvent was distilled water. Specifically, solutions based on sodium chloride (NaCl) were analyzed.
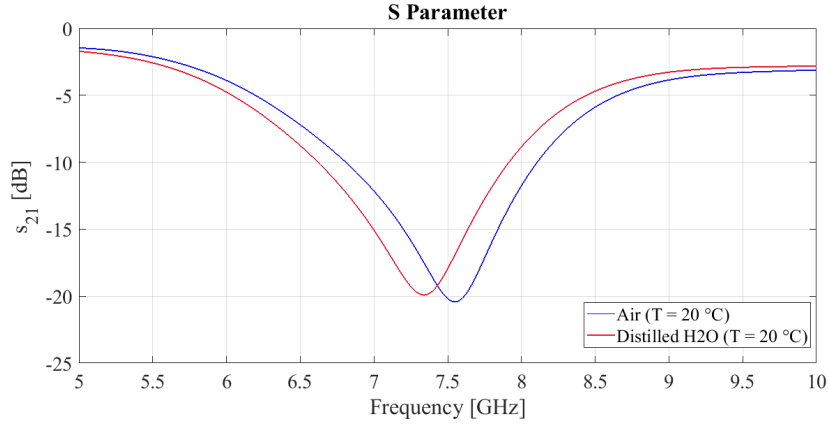
Figure 5.5.2: Simulated transmission coefficient of the new microfluidic sensor.

5.6 Sodium cloride microfluidic analysis

5.6.1 Numerical results

In order to be able to estimate the sensor's ability to distinguish the different concentrations of sodium chloride (NaCl) whitin a solution whose solvent was distilled water, electromagnetic simulations were performed. In order to be able to insert the correct dielectric constant and conductivity values of the liquid to be analyzed in the simulator, reference was made to the model describer by Stogryn [13].

The electrical conductivity is obtained starting from the definition of frequency-dependent dielectric constant:

$$\varepsilon\left(\omega\right) = \varepsilon^{'}\left(\omega\right) - j\varepsilon^{''}\left(\omega\right) = \varepsilon_r\left(\omega\right) - j\frac{\sigma\left(\omega\right)}{\varepsilon_0 \cdot \omega} \tag{5.6.1}$$

where $\omega = 2\pi f$, ε_r is the relative dielectric constant corresponding to the real part $\varepsilon^{'}$, ε_0 is the dielectric constant of vacuum, and σ is the electrical conductivity.

As can be seen from (5.6.1), the electrical conductivity is related to the imaginary part of the frequency-dependent dielectric constant and thus describes the losses of the material. Considering only the imaginary part of the dielectric constant $\varepsilon\left(\omega\right)$ it is possible to derive the electrical conductivity:

$$\sigma\left(\omega\right) = \varepsilon_0\varepsilon^{''}\omega \tag{5.6.2}$$

The Stogryn model very faithfully describes the trend of the real and imaginary parts of the dielectric constant of saline solutions, also taking into

159

mol/L	g/L
0,125	7,305
0,25	14,61
0,5	29,22
1	58,44
3	175,32

Table 5.2: Saline solutions considered.

account the temperature: in our case we have set $T = 20$ °C. Fig. 5.6.1 show the trends of the relative dielectric constant and of the electrical conductivity of the water as the frequency varies for different quantities of sodium chloride dissolved in it (number of moles per liter). For convenience, the conversion formula from mol/# to g/# is reported (where # is the volume expressed in liters or its multiples or submultiples):

$$C_{mol} = \frac{C_g}{m} \tag{5.6.3}$$

where C_{mol} is the molar concentration, C_g is the mass concentration, and m is the molar mass which in the case of NaCl is equal to 58.44. In Table 5.2 the quantities of solute considered in mol/l and in g/l are reported.

The curves shown in Fig. 5.6.1 (a-b) were imported into the electromagnetic simulator and simulations were carried out for each molar concentration shown in Table 5.2. The results are reported in Fig. 5.6.2, where the effect produced by the salt concentration inside the acqueous solution can be seen. As the NaCl concentration increases, the resonant frequency increases. This effect is linked to the variation of the relative dielectric constant and the electrical conductivity. As the presence of NaCl becomes more sustained, the permittivity of the liquid decreases, while the conductivity increases (for constant temperature). The relative dielectric constant and electrical conductivity values of the various solutions obtained from the Stogryn model are shown in Table 5.3.

5.6.2   Measurement results

The new microfluidic sensor was made on a cardboard substrate on which the metal parts (T resonator and ground plane) were made of adhesive copper with the aid of a cutting plotter. The measurements of the various saline solutions were carried out in the laboratory thanks to Anritsu MS46122B
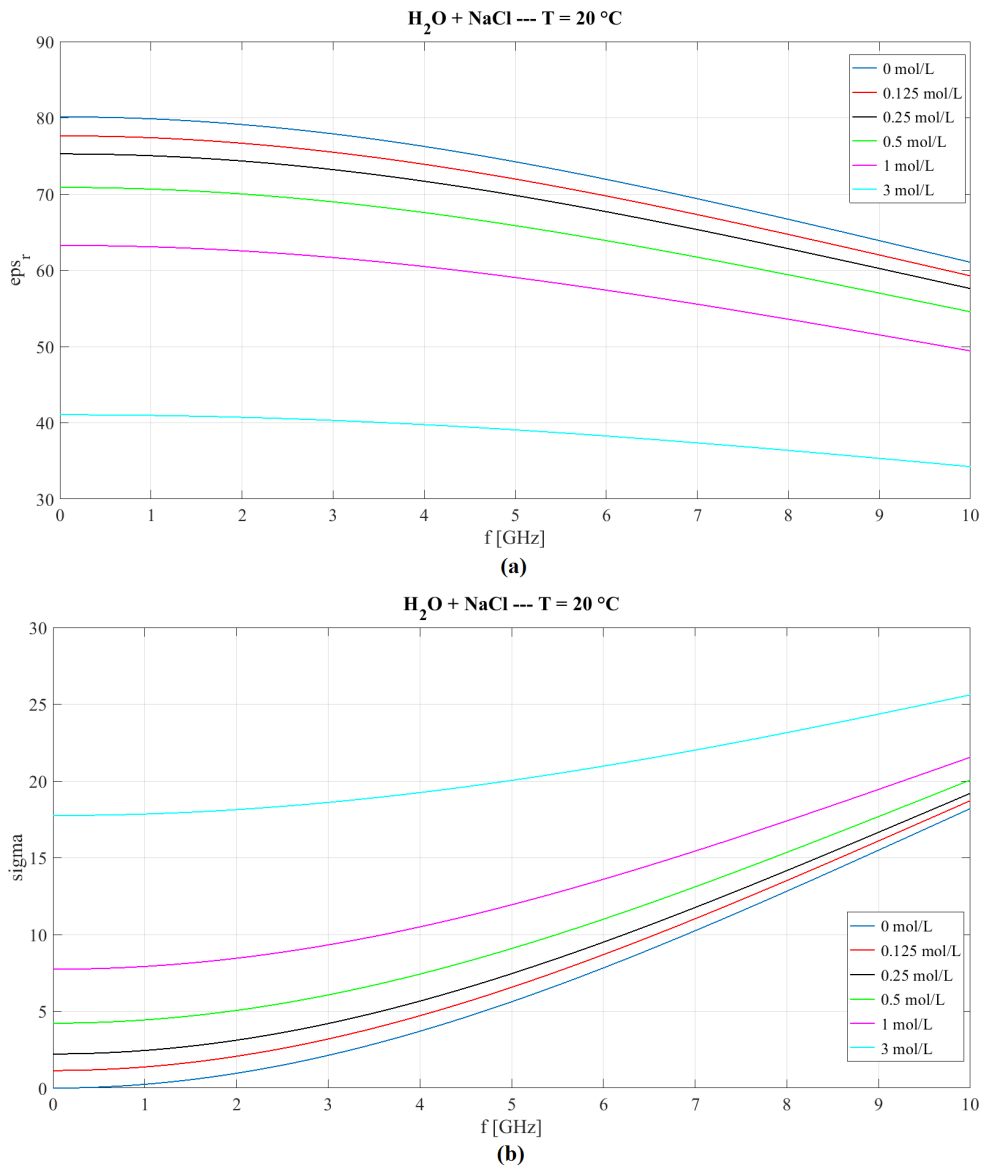
Figure 5.6.1: Stogryn trends for a sodium chloride quantity variation in a water solution at 20 °C: (a) relative dielectric constant, (b) electric conducibility [S/m].
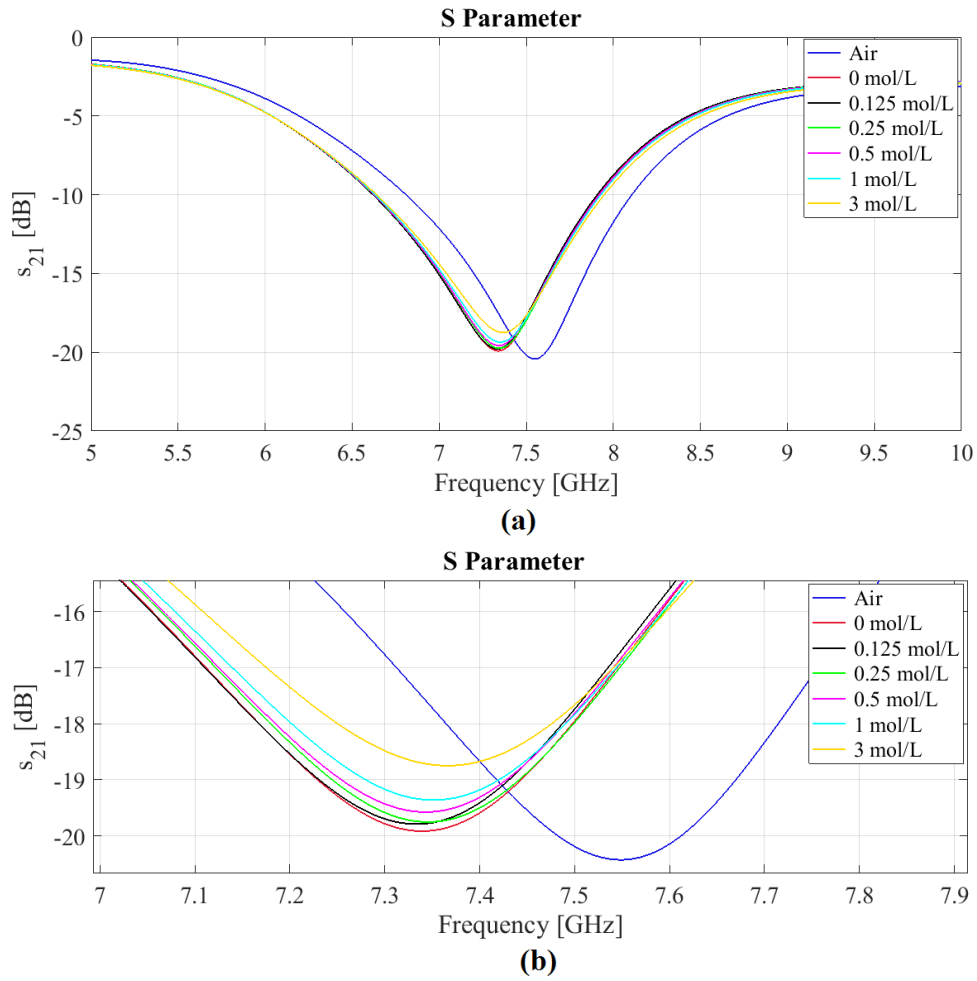
Figure 5.6.2: Simulation results. (a) Transmission coefficients as salinity changes, (b) zoom on resonance peaks.

Solution	C_m [mol/L]	C_g [g/L]	f_r [GHz]	ε_r	σ [S/m]
Air	-------	-------	7,56	1,00059	0
$H_2O + NaCl$	0	0	7,34	68,49	11,11
$H_2O + NaCl$	0,125	7,305	7,343	66,43	11,87
$H_2O + NaCl$	0,25	14,61	7,349	64,48	12,59
$H_2O + NaCl$	0,5	29,22	7,351	60,92	13,88
$H_2O + NaCl$	1	58,44	7,359	54,86	16,13
$H_2O + NaCl$	3	175,32	7,366	37,01	22,42

Table 5.3: Dielectric parameters of the various saline solutions obtained thanks to the Stogryn model. Simulation results.

162

Solution	C_m [mol/L]	C_g [g/L]	f_r [GHz]	ε_r	σ [S/m]
Air	-------	-------	7,3801	1,00059	0
$H_2O + NaCl$	0	0	7,1255	69,06	10,56
$H_2O + NaCl$	0,125	7,305	7,1262	66,99	11,34
$H_2O + NaCl$	0,25	14,61	7,1266	65,03	12,06
$H_2O + NaCl$	0,5	29,22	7,1305	61,43	13,39
$H_2O + NaCl$	1	58,44	7,1333	55,3	15,69
$H_2O + NaCl$	3	175,32	7,1335	37,24	22,16

Table 5.4: Dielectric parameters of the various analyzed solutions obtained thanks to the Stogryn model. Measurement results.

vector network analyzer. The sensor and the measuring system are shown in Fig. 5.6.3. In order to insert the small quantities of liquid inside the glass channel, small medical syringes were used (one for each solution). After each measurement, the channel was washed with distilled water and dried with compressed air, in order to leave nothing of the previous liquid.

Fig. 5.6.4 shows the results obtained by measuring the transmission coefficients obtained by the sensor as the NaCl concentrations in the solution vary. As it is possible to see, the results are very similar to those obtained in simulation. If we exclude a slight shift in frequency, probably due to the effect of the presence of the SMA connectors, and soldering that could have introduced parasitic capacitance on the ports of the device, a behavior similar to that seen in the simulation phase was obtained.

Thanks to the Stogryn model it was possible to estimate the dielectric characteristics of the various solutions used in the measurement phase (see Table 5.4).

5.7 Conclusions

The study has investigated the design of a microfluidic sensor based on microstrip T-resonator. The sensor has been realized using a 3D printing technique, it has a compact and thin structure allowing a useful channel of about 12 μl. Numerical and experimental results show a very large variation of the resonant frequency passing from low permittivity low loss liquids to water based liquids. Given the goodness of the results obtained, we wanted to use the sensor to identify the percentages of a known solute dissolved in an acqueous solution. Considering the poor resistance properties of PLA to the presence of water and humidity, it was decided to create a new low-cost sen-
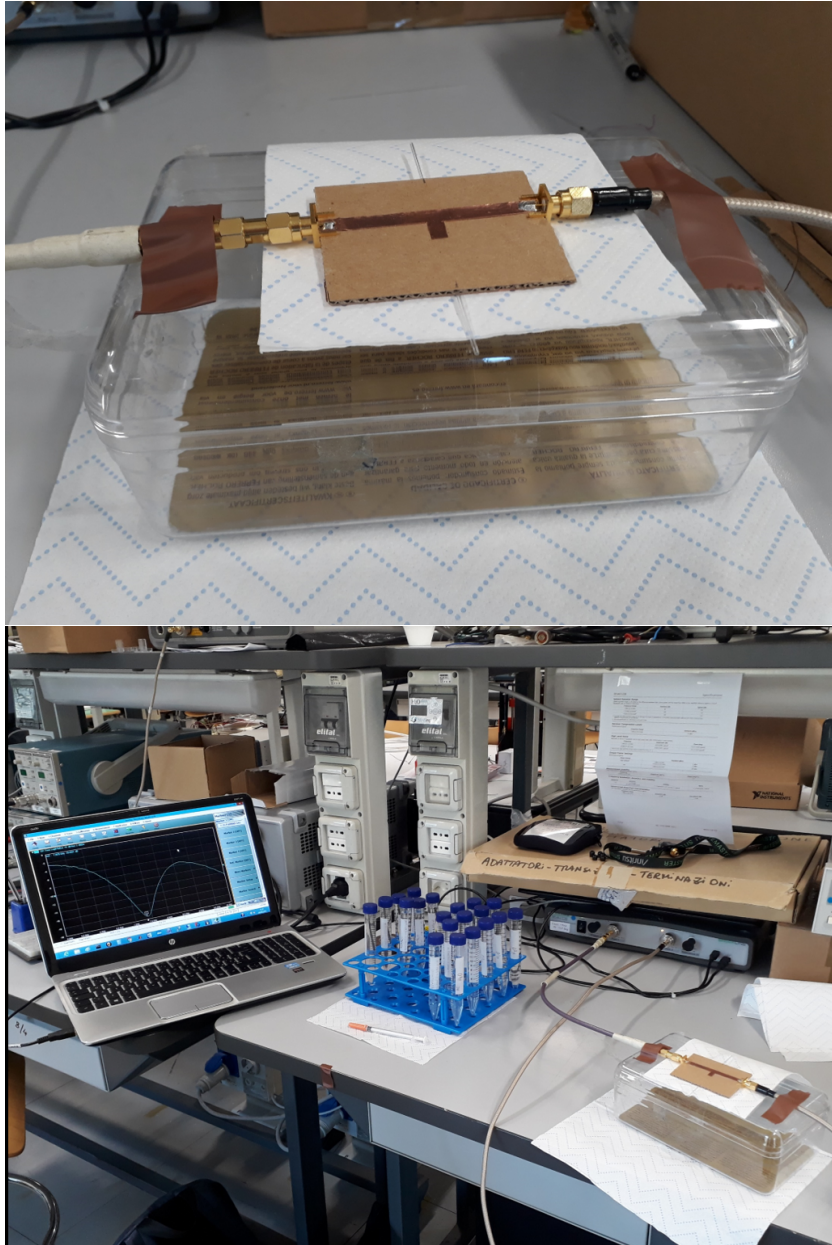
Figure 5.6.3: Microwave microfluidic cardboard based sensor (top). Measurement setup (down).
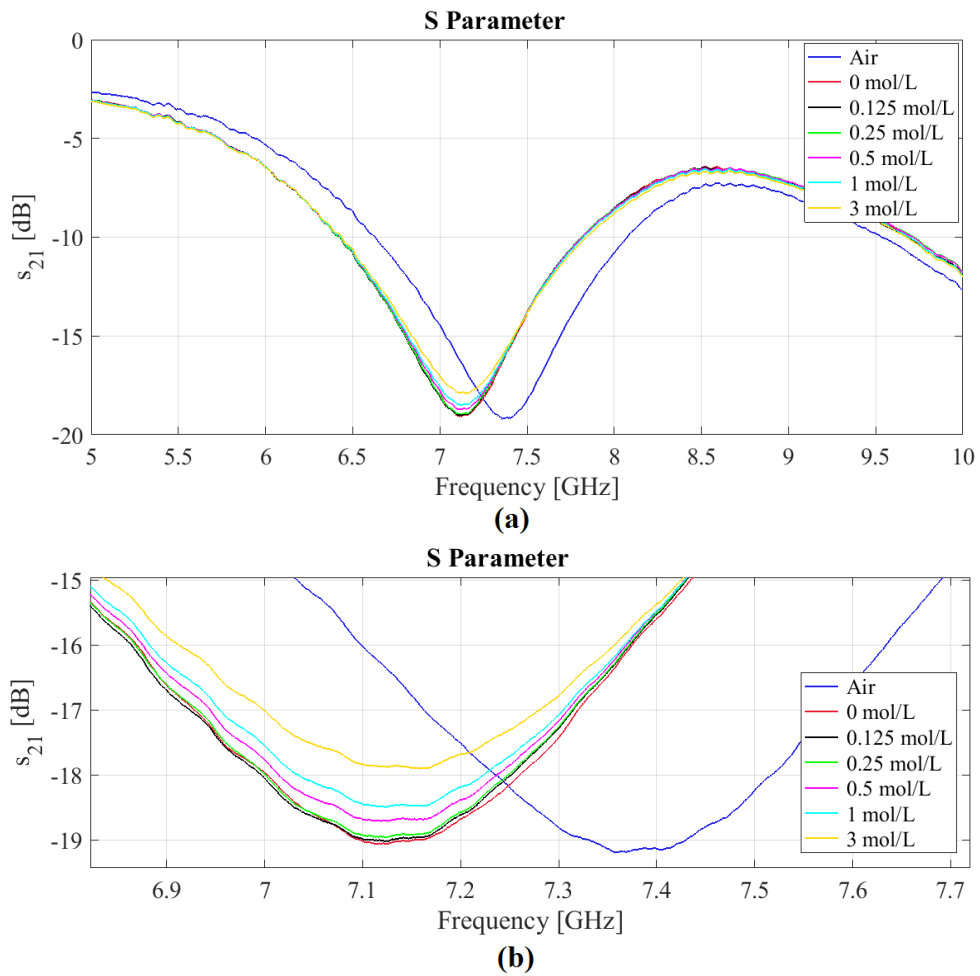
Figure 5.6.4: Transmission coefficients as salinity changes. (a) Measurement results at 20 °C, (b) zoomed version of the measured results.

sor in cardboard, with a microfluidic channel made with a small tube used in chemical laboratories. Through the results obtained during the simulation phase, then confirmed by the measurements, the ability of the instrument to be able to detect small variations in the concentration of dissolved solute in an acqueous solution was evident. The structure of the sensor permits to include multiple microfluidic channels allowing the simultaneous analysis at different frequencies and/or different analytes.

Bibliography

[1]   G. M. Whitesides. *The origins and the future of microfluidics*, Nature, Vol. 442, pp. 368-373, 2006.

[2]   V. Rawat, S. Dhobale, and S. N. Kale. *Ultra-fast-selective sensing of ethanol and petrol using microwave-range metamaterial complementary split-ring resonators*, Journal of Applied Physics, Vol. 116, pp. 1-6, 2014.

[3]   A. A. Abduljabar, D. J. Rowe, A. Porch, and D. A. Barrow. *Novel microwave microfluidic sensor using a microstrip split-ring resonator*, IEEE Transactions on Microwave Theory and Techniques, Vol. 62, pp. 679-688, 2014.

[4]   J. Carrol, M. Li, and K. Chang. *New technique to measure transmission line attenuation*, IEEE Transactions on Microwave Theory and Techniques, Vol. 43, No. 1, pp. 219-222, 1995.

[5]   www.cst.com

[6]   altair.com/feko/

[7]   P. A. Bernard and J. M. Gautray. *Measurement of dielectric constant using a microstrip ring resonator*, IEEE Transactions on Microwave Theory and Techniques, Vol. 30, No. 3, pp. 592-595, Mar. 1991.

[8]   K. -L. G. Ho, A. L. Pometto III, and P. N. Hinz. *Effects of Temperature and Relative Humidity on Polylactic Acid Plastic Degradation*, Journal of environmental polymer degradation, Vol. 7, No. 2, pp. 83-92, 1999

[9]   J. R. Rocca-Smith, N. Chau, D. Champion, C. -H. Brachais, E. Marcuzzo, A. Sensidoni, F. Piasente, T. Karbowiak, F. Debeaufort. *Effect of the state of water and relative humidity on*

ageing of PLA films, Food Chemistry, Vol. 236, pp. 109-119, Dec. 2017.

[10] A. Copinet, C. Bertrand, S. Govindin, V. Coma, Y. Couturier. *Effects of ultraviolet light (315 nm), temperature and relative humidity on the degradation of polylactic acid plastic films*, Chemosphere, Vol. 55, Issue 5, pp. 763-773, May 2005.

[11] V. K. Holm, S. Ndoni, J. Risbo. *The Stability of Poly(lactic acid) Packaging Films as Influenced by Humidity and Temperature*, Journal of Food Science, Vol. 71, Issue 2, pp. E40-E44, Mar. 2006.

[12] M. -K. Mitchell, D. E. Hirt. *Degradation of PLA fibers at elevated temperature and humidity*, Polymer Engineering & Science, Vol. 55, Issue 7, pp. 1652-1660, July 2015.

[13] A. Stogryn. *Equations for Calculating the Dielectric Constant of Saline Water*, IEEE Transactions on Microwave Theory and Techniques, Vol. 19, Issue 8, Aug. 1971.

Chapter 6

An RFId-Based Breaking Test Sensor

6.1 Introduction

The growth of connectivity in the last decade and the introduction of the Internet of Things (IoT) concept have made it necessary to rapidly increase the development of pervasive sensors [1]. As already mentioned in Chapter 1, Radio Frequency Identification (RFId) technology is playing an important role in many sectors, thanks to its widespread use in logistics. A typical RFId system is represented in Fig. 6.1.1.

As it is possible to see, a typical RFId system is composed of one or more trasponders (tags) placed on the objects or in the environments from which we need to obtain information, an interrogator (reader) capable of interrogating the tags, and a system for the collection and processing of the
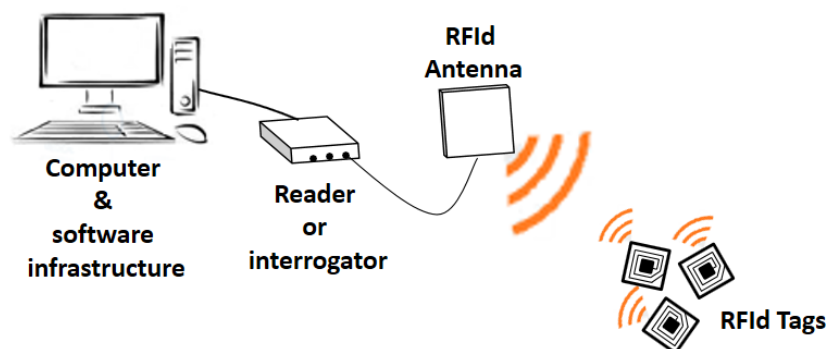
Figure 6.1.1: Principle diagram of an RFId system.

received data. The types of tags can be grouped into three large families:

- active tags: they contain an embedded power source and a CPU[1] that allows autonomous data processing. They have an active transmitter on board and take the energy necessary for data transmission directly from the battery. This means that the tags can communicate with the readers even at a great distance (in some cases even for distances of a few kilometers);

- semi-passive tags: they are equipped with a battery used only to power a microchip (which allows to perform more complex functions and to operate even when the reader is not transmitting) or other auxiliary sensors, but not to power the actual communication device. In this latter aspect they are very similar to passive tags. The advantage of using these tags is that of being able to mount higher capacity memories (also rewritable); an example of application would be that of environmental sensors for monitoring temperature, pressure and movement;

- passive tags: they have no power supply and derive the energy for operation from the RF signal (generally from the carrier) coming from the reader. The operating principle of these tags can be summarized in two main phases: one where the tag collects energy and remains silent, and the other where it responds to the reader query by releasing the energy accumulated in the first phase. The various blocks that make up this type of transponder concern the antenna, the signal receiver, the power supply, and the transmission. Low maintenance costs make this type of tag a great choice for many applications, even if their communication range and computing capabilities are limited. Their sizes vary from a few tens of mm^2 (in the UHF[2] operating band (300 MHz - 3 GHz)) up to a few microns.

Each of these types of tags has its own fields of application and research lines have been developed for each of them. Recent examples of RFId systems and devices that perform sensing and data logging using a wireless powered data logger are reported in [2] and [3], while [4] describes a battery-assisted two-chip data logger for packaging surveillance applications. Another example of use of RFId active sensors is reported in [5]. While on the one hand the active and semi-passive sensors present advanced performances allowing the digital recording of sensor data and the possibility to manage a storage memory, on the other hand they include batteries and/or complicated energy harvesting

---

[1]CPU: Central Processing Unit.
[2]UHF: Ultra High Frequency.

circuits for powering the processing unit on board (usually a microcontroller). From a pervasive point of view they are not the best solution as their construction and maintenance costs would become prohibitive. In the lastest years, passive RFId sensors, instead, collecting a steady increase in interest thanks to the lower cost and to the long lifetime, which are possible because of the absence of the battery and of complicated circuitry. The basic operation principle [6] requires a sensor or a sensor-like component capable of modifying the antenna properties (e.g., the impedance or the gain) of the RFId tag. Such variation can be remotely detected and stored by interrogating the RFId sensor tag with a reader and by processing the backscattered signal. This method brings the advantage of simplicity and low cost, even if the use of passive sensors implies a communication degradation due to varying impedance or gain. A tradeoff analysis for the two contrasting requirements can be found in [7], with guidelines to minimize the communication degradation while amplifying the power oriented sensing. In recent years, it has been shown how mutual coupling effects between two closely spaced tags can help in compensating the impedance variation due to the sensing process [8]. Engineered coupling can enable a stable communication while at the same time obtaining sensing through variations of the phase of the RFID signal. In that case, the two antennas played as transducers themselves converting the change of the environment into a controlled modulation of the backscattered signal. In other implementations, instead, it is preferred to include a specific sensor into the antenna, for instance a lumped element, in order to provide a more specific detection of the physical phenomenon. Some examples are humidity-sensor polymer drops [9], thermistors [10], and substrates [11] comprising vapor-sensitive polymers.

In [12] a generic synthesis methodology suitable for RFId tags with an embedded lumped sensor that rely on phase monitoring. The phase of the backscattered system is mathematically manipulated to make explicit the effect of the change of the impedance of the lumped sensing element. A suitable pole/zero representation, originating from the multiport tag theory [13], [14], allowed to formalize a constrained synthesis of the RFId tag to balance the minimum allowed read range with the dynamic range of the phase sensing.
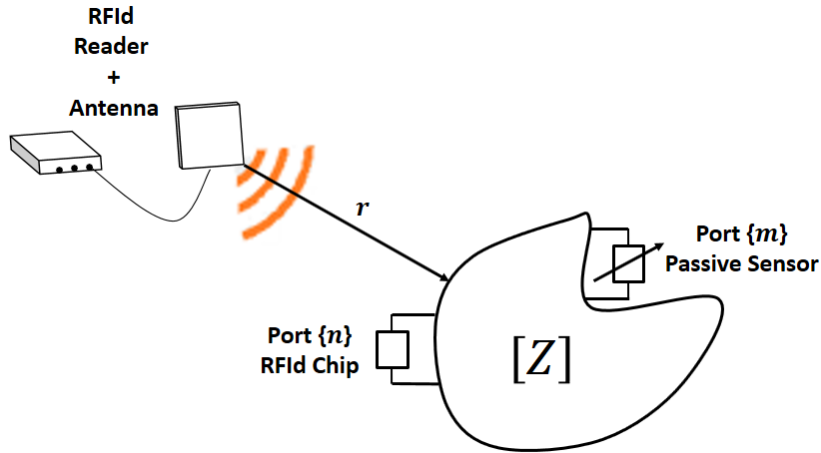
Figure 6.2.1: Representation of a 2-port sensor: one port is connected to an RFId chip and the other is connected to a variable passive sensor.

6.2 Mathematical formulation of 2-port tag response

In this research work we wanted to exploit the mathematical representation reported in [12] for 2-ports scatterers such as those reported in Fig. 6.2.1.

As can be seen from Fig. 6.2.1, one port is connected to the RFId microchip and a second port is connected to a variable load, i.e., the passive lumped sensor of impedance Z_L. The radiating part of the structure could be implemented as either two strongly coupled scatterers or by a unique conductor provided with two terminals. In both cases, due to the electromagnetic coupling among the two ports, the variation of the impedance of the load will influence the induced current over the whole system and thus the power collected by the microchip. As a result, the amplitude and phase of the backscattered signals will be accordingly modified.

6.2.1 Phase response

As indicated in [12], the antenna mode signal due to a 2-port RFId tag can be expressed in terms of impedance matrix and chip impedance as in [8]. If we consider the two ports of the tag (named n and m) as sufficiently close to each other in order to be electromagnetically coupled. Port n is associated to an UHF microchip, while the port m is teminated on a load, which is variable according some receptor. The signal received at the reader due to antenna mode can be written as

$$V_{R,(n)}^{ON/OFF}(\Psi) = \frac{Z_{nn} + Z_{mm} - 2Z_{mn} + Z_L(\Psi) + Z_{Cn}^{ON/OFF}}{\left(Z_{nn} + Z_{Cn}^{ON/OFF}\right)(Z_{mm} + Z_L(\Psi)) - Z_{mn}^2} \cdot f(r) \quad (6.2.1)$$

where Z_{mn} $\{m,\, n = 1,\, 2\}$ are, respectively, self $(m = n)$ and mutual $(m \neq n)$ impedances, $Z_{Cn}^{ON/OFF}$ and $Z_L(\Psi) = R_L(\Psi) + jX_L(\Psi)$ are, respectively, the chip impedance in the two ON and OFF states and the load impedance on port m, with Ψ the analyte, i.e., the physical parameter to monitor. $f(r)$ is a function whose phase only depends on the reader-to-tags distance r and on the effective heights of tags and reader

$$f(r) \propto \left(\frac{\lambda}{4\pi r}\right)^2 G_R R_n^{rad} G_n \left(\hat{\underline{h}}_n \cdot \hat{\underline{h}}_R\right)^2 \sqrt{P_{in} P_R^{rad}/2} \quad (6.2.2)$$

where λ is the wavelength, P_{in} is the power supplied by the reader, R_R^{rad}, $\hat{\underline{h}}_R$, and G_n are instead the radiation resistance, the polarization unitary vector and the radiation gain of the tag antenna when the port m is in open circuit condition.

The phase measured by the RFId reader can hence be written as

$$\varphi_n[Z_L(\Psi)] = \arg\left\{V_{R,(n)}^{OFF}[Z_L(\Psi)] - V_{R,(n)}^{ON}[Z_L(\Psi)]\right\} \quad (6.2.3)$$

where the dependence from $Z_L(\Psi)$ has been made clear.

It is assumed that the radiating body has a symmetric geometry with respect to the two ports, hence $Z_{11} = Z_{22} = Z_S$ and $Z_{21} = Z_M$. Phase becomes, therefore

$$
\begin{aligned}
\varphi_n[Z_L(\Psi)] \;=\; &\arg\left\{-\frac{2Z_s - 2Z_M + Z_L(\Psi) + Z_{Cn}^{OFF}}{\left(Z_S + Z_{Cn}^{OFF}\right)(Z_S + Z_L(\Psi)) - Z_M^2}\right. \quad (6.2.4)\\
&\left. + \frac{2Z_s - 2Z_M + Z_L(\Psi) + Z_{Cn}^{ON}}{\left(Z_S + Z_{Cn}^{ON}\right)(Z_S + Z_L(\Psi)) - Z_M^2}\right\} + \varphi_0
\end{aligned}
$$

$\varphi_0 = \arg\{f(r)\}$ can be considered a constant with respect to variations of $Z_L(\Psi)$, because the polarization unitary vector $\hat{\underline{h}}_n$ in (6.2.2), is defined when port m is in open circuit and thus it does not depend on the load of port m. Moreover, if the measurement setup is kept fixed along with the sensing process, φ_0 will not vary at all (it only depends on the distance between reader and tag).

The variations of the phase will be due only to variations of $Z_L(\Psi)$ and hence information on such load variations will be remotely retrievable by measuring the phase of the tag as received by the reader.

6.2.2 Amplitude response

On the other hand, communication properties for downlink limited passive systems are controlled by the realized gain, which can be conveniently expressed in the following form [15]:

$$
\begin{aligned}
\widetilde{G}_n \left[Z_L \left(\Psi \right) \right] &= G_n \chi_n \widetilde{\tau}_n &\text{(6.2.5)} \\
&= G_n \chi_n 4 R_{Cn}^{ON} R_S^{rad} \left| \frac{Z_S - Z_M + Z_L \left(\Psi \right)}{\left(Z_S + Z_{Cn}^{ON} \right) \left(Z_S + Z_L \left(\Psi \right) \right) - Z_M^2} \right|^2
\end{aligned}
$$

χ_n is the polarization factor and

$$
\widetilde{\tau}_n = 4 R_{Cn}^{ON} R_S^{rad} \left| \frac{Z_S - Z_M + Z_L \left(\Psi \right)}{\left(Z_S + Z_{Cn}^{ON} \right) \left(Z_S + Z_L \left(\Psi \right) \right) - Z_M^2} \right|^2
$$

is the embedded power transfer coefficient.

Equation (6.2.5) shows how also the realized gain depends on the variable load of the sensing port m and will, therefore, need to be properly engineered to avoid substantial degradation along the sensing process. It is worth clarifying that $\widetilde{\tau}_n$ is a mathematical function, different from the conventional ratio between the power absorbed by the chip impedance and the power collected by the antenna.

Since the reader/tag is kept at fixed distance and the gains and effective heights are defined in open circuit condition for port m, the realized gain will only experience changes by means of variations of the lumped impedance $Z_L \left(\Psi \right)$ of the sensor.

6.2.3 Pole/Zero representation

Equations (6.2.4) and (6.2.5) are the key equations for sensing and communication properties, respectively. After simple mathematical manipulations, they can be rewritten in the more compact form

$$
\varphi_n \left[Z_L \left(\Psi \right) \right] = \arg \left\{ \frac{d \cdot \left[Z_L \left(\Psi \right) - z \right]^2}{c^{ON} c^{OFF} \left[Z_L \left(\Psi \right) - P^{OFF} \right] \left(Z_L \left(\Psi \right) - P^{ON} \right)} \right\} + \varphi_0
$$

$$\text{(6.2.6)}$$

$$
\widetilde{\tau}_n \left[Z_L \left(\Psi \right) \right] = \frac{4 R_{Cn}^{ON} R_S^{rad}}{\left| c^{ON} \right|^2} \left| \frac{Z_L \left(\Psi \right) - z}{Z_L \left(\Psi \right) - P^{ON}} \right|^2 \qquad \text{(6.2.7)}
$$

where

$$z = -Z_S + Z_M \qquad (6.2.8)$$

$$P^{ON} = \frac{-\left(b^{ON} + a\right)}{c^{ON}} \qquad (6.2.9)$$

$$P^{OFF} = \frac{-\left(b^{OFF} + a\right)}{c^{OFF}} \qquad (6.2.10)$$

and

$$a = (Z_S + Z_M)(Z_S - Z_M)$$

$$b^{OFF/ON} = \left(Z_S Z_{Cn}^{OFF/ON}\right)$$

$$c^{OFF/ON} = \left(Z_S + Z_{Cn}^{OFF/ON}\right)$$

$$d = \left(Z_{Cn}^{ON} - Z_{Cn}^{OFF}\right).$$

The performance features both for sensing and for communication can hence be expressed in terms of poles ($\left\{P^{ON},\ P^{OFF}\right\}$) and zeros ($z$), with the purpose of allowing an esier and fully mathematical control of their trends. It is worth noticing that (6.2.6) and (6.2.7) both have two coinciding zeroes. Equation (6.2.6) has two different poles P^{ON} and P^{OFF}, while (6.2.7) has two coinciding poles in P^{ON}. The presence of poles in (6.2.7) may in theory allow the $\widetilde{\tau}_n$ to be arbitrary large for a suitable choice of the load impedance $Z_L(\Psi)$ (i.e., it may tend to infinite). However, based on what has been said in [12], this possibility vanishes for fisical feasible antennas and passive loads. Indeed, a feasible antenna impedance [16] requires that:

- the self resistance $R_S > 0$ due to passivity;

- the self and mutual impedance to be subjected to the constraints $|R_M| < |R_S|$, $|X_M| < |X_S|$.

Accordingly, it has been proved numerically that the poles will always lay in the negative resistance half-space of the complex load impedance plane. As a consequence of the imposed constraints, also the zero $z = -Z_S + Z_M$ will have negative real part.

In such conditions, therefore, the embedded power transfer coefficients will never grow indefinitely using only passive devices, as expected from common sense: $\widetilde{\tau}_n$ in fact would tend to the pole only for negative values
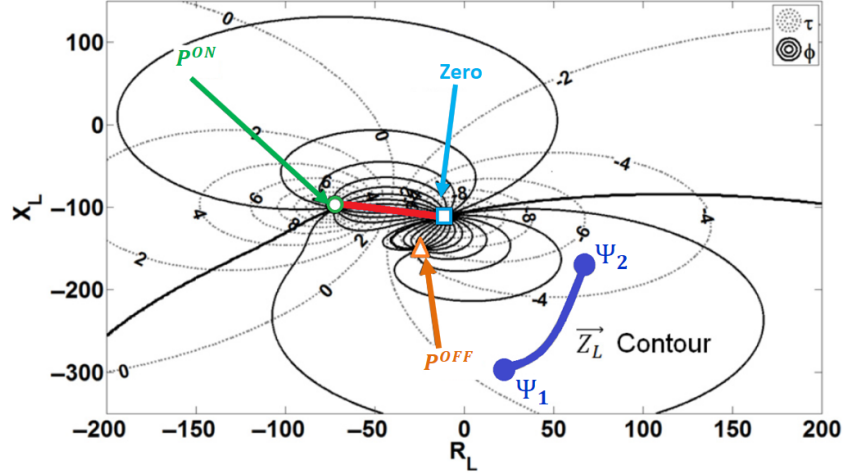
Figure 6.3.1: Example of $\widetilde{\tau}_n - \varphi_n$ nomogram over a complex Z_L plane, when $z = -10 - j110$ Ω and $P^{ON} = -70 - j100$ Ω and $Z_C^{ON} = 15 - j135$ Ω, $Z_C^{OFF} = 150$ Ω. Phase isolines are plotted every 25° while $\widetilde{\tau}_n$ isolines are expressed in dB. The thick blue line indicates a qualitative $\overrightarrow{Z_L}(\Psi)$ contour, while the red line is the $P^{ON} - z$ axis.

of R_L, i.e. for negative load resistances, not admissible for passive devices. Although poles and zeroes belong to the $R_L < 0$ half-plane, nevertheless they will influence the phase and power transmission coefficient trends on the half-plane $R_L > 0$ as well.

6.3 The $\widetilde{\tau}_n - \varphi_n$ nomogram

The concurrent control of the variation of the phase of the backscattered signal (sensing) and of the embedded power transfer coefficient (communication) is here implemented through the representation of all the involved functions over the complex plane of the load impedance. The response of the lumped sensor to the physical parameter under observation can be hence mapped on the Z_L-plane as an oriented contour $\overrightarrow{Z_L}(\Psi) = R_L(\Psi) + jX_L(\Psi)$ with $\Psi_1 < \Psi < \Psi_2$, where $\{\Psi_1, \Psi_2\}$ are the initial and final states of the analyte as in [7]. By plotting the isolines of $\widetilde{\tau}_n$ and φ_n functions over the Z_L-plane, a nomogram is obtained (Fig. 6.3.1).

The dynamic range of the tag, in its behavior of phase-based sensor, and its read distance are hence dependent on the intersection between the sensor contour $\overrightarrow{Z_L}(\Psi)$ and the $\widetilde{\tau}_n - \varphi_n$ nomogram. The position of poles and zeroes on the Z_L-plane will affect the shape and orientation of isolines and their
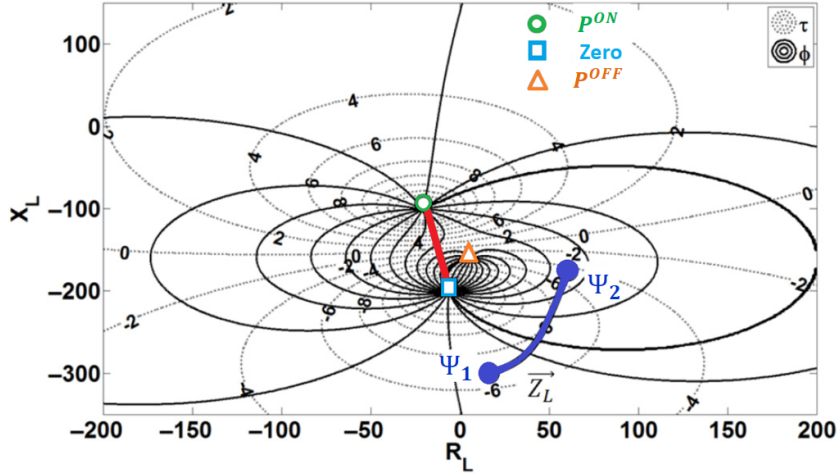
Figure 6.3.2: $\widetilde{\tau}_n - \varphi_n$ nomogram over a complex Z_L plane corresponding to a different position of zero and poles with respect to Fig. 6.3.1 (e.g., $z = -5 - j200$ Ω and $P^{ON} = -20 - j100$ Ω) that produces a near 90° rotation of the $P^{ON} - z$ axis (red line). Also in this case $\widetilde{\tau}_n$ isolines are expressed in dB.

intersection with the $\overrightarrow{Z_L}(\Psi)$ profile, and ultimately the device performance. Phase and $\widetilde{\tau}_n$ isolines have approximately a simmetrical circular shape, in particular, the symmetry axis of $\widetilde{\tau}_n$ isolines lays on the conjunction line between P^{ON} and z, while the phase, though having a more complicated behavior due to its dependence also from P^{OFF}, has a symmetry axis almost perpendicular to black that of $\widetilde{\tau}_n$ isolines. Since phase isolines are almost perpendicular to $\widetilde{\tau}_n$ ones, phase and $\widetilde{\tau}_n$ exhibit different trends along a specific path on the Z_L plane: for instance, if $\overrightarrow{Z_L}(\Psi)$ draws a path that follows a single $\widetilde{\tau}_n$ isoline, it will cross several phase isolines and vice versa.

A change in the position of poles and zero, which is controlled by the electromagnetic interaction among the two ports of the sensor (Z_S, Z_M) and by the chip impedance $Z_C^{ON/OFF}$, thus provokes a rescaling and a rotation of the nomogram with respect to the contour $\overrightarrow{Z_L}(\Psi)$ of the sensor response. For instance, by perturbing the values of zeroes and poles of Fig. 6.3.1, the map of Fig. 6.3.2 will be produced. Now, the symmetry axes of the nomogram are rotated with respect to the previous case, due to ratation of the line between P^{ON} and z. The result is that the contour $\overrightarrow{Z_L}(\Psi)$ now intersects a region with much denser isolines of phase and accordingly the $\widetilde{\tau}_n - \varphi_n$ response to the physical parameter to monitor will be sharper than in Fig. 6.3.1. It is, therefore, intuitive that the sensor's response and communication features

177

can be mathematically manipulated by a proper placement of zero and poles on the complex impedance plane.

6.4   Design method

The design method reported in [12] and used in this work, comprises two steps:

- a mathematical placement of poles and zeros on the complex plane to properly steer the $\widetilde{\tau}_n - \varphi_n$ nomogram;

- an electromagnetic design to shape a 2-port antenna having the required feasible impedance matrix that has been derived from the first step.

The overall design is constrained to conditions over the sensing range and minimum communication distance.

6.4.1   Design constraints

The placement of poles and zeroes in the Z_L plane is subject to desired requirements on sensing accuracy and communication distance. Such constraints are expressed in terms of minimum power transmission coefficient $\widetilde{\tau}_{n,min}$

$$\widetilde{\tau}_{n,min} = \frac{p_{c,n}}{\left(\frac{\lambda}{4\pi r_0}\right)^2 P_{in} G_n G_R \chi_n} \tag{6.4.1}$$

that assures the required read range r_0, and the minimum span of the measurable phase variation $\triangle\varphi_{n,min}$

$$\triangle\varphi_{n,min} = \frac{\delta\varphi}{\delta\Psi}\left(\Psi_2 - \Psi_1\right) \tag{6.4.2}$$

that permits to achieve the required resolution $\delta\Psi$ in the measurement of the analyte [6], $\delta\varphi$ being the phase resolution of the reader.

The aim of the design is, therefore, a radio-sensor satisfying the following conditions:

$$\begin{cases} \varphi_n\left[Z_L\left(\Psi_2\right)\right] - \varphi_n\left[Z_L\left(\Psi_1\right)\right] \geqslant \triangle\varphi_{n,min} \\ \widetilde{\tau}_n\left[Z_L\left(\Psi\right)\right] \geqslant \widetilde{\tau}_{n,min} \end{cases} \tag{6.4.3}$$

for the whole range of the sensing process, i.e. $\forall\,\Psi \in [\Psi_1,\,\Psi_2]$.

6.4.2 Positioning of poles and zeros

In general, a fully numerical pole/zero search procedure [17], aiming at shifting and rotating nomograms with respect to the sensor response $\overrightarrow{Z_L}(\Psi)$ can be applied to find the optimal parameters $\{z, P^{ON/OFF}\}$ that satisfy the requirements in (6.4.3). At each step of the search, self and mutual impedance required for the 2-port tag are derived from (6.2.8) to (6.2.10) by using the following formulas:

$$Z_{S,\omega} = \frac{P^{ON} Z_C^{ON} - z^2}{2z - P^{ON} - Z_C^{ON}} \qquad (6.4.4)$$

$$Z_{M,\omega} = Z_S + z \qquad (6.4.5)$$

and conditions have to be enforced so that mutual impedances are physically meaningful, as discussed above.

In order to obtain reliable communication (i.e., high and stable $\widetilde{\tau}_n$) and fine sensing (i.e., strongly variable φ_n) and thus satisfy the requirements in (6.4.3), it is beneficial that the path of $\overrightarrow{Z_L}(\Psi)$ is far away from the position of the zero where very low $\widetilde{\tau}_n$ values are expected and where the communication should be accordingly very poor. On the other hand, having both $\widetilde{\tau}_n$ and φ_n a common pole (P^{ON}), a path of $\overrightarrow{Z_L}(\Psi)$ in its vicinity would guarantee strong phase variation (as phase isolines are particularly dense in the vicinity of the pole) and high $\widetilde{\tau}_n$ values. The two extreme cases of resistive and reactive behavior of the sensor are reported in [12].

6.5 Rational of the Method

From the map of Fig. 6.5.1 that is the nomogram for the specific case of two coupled half-wavelength dipole antennas (Fig. 6.5.2) we observe there are different zones useful for achieving a specific design objective.

Inside the green dotted region $(R_L < 0)$ there is a large zone where the embedded power transfer coefficient τ_n is larger than 0 dB. It may be useful to improve the realized gain but requires a sensor done with active components in order to obtain a negative input resistance. For that reason it is not considered in this analysis that is restricted to the half-space $R_L > 0$. Nevertheless, for $R_L > 0$ there is a small region with $\tau_n > 0$ dB, highlighted in yellow in Fig. 6.5.1, that can be exploited for passive sensors. The size of that region depends mainly on the position of the poles and zeros, it assumes its maximum possible extension in the limit the real part of the poles and zeros approaches zero. The size of that region can be enlarged
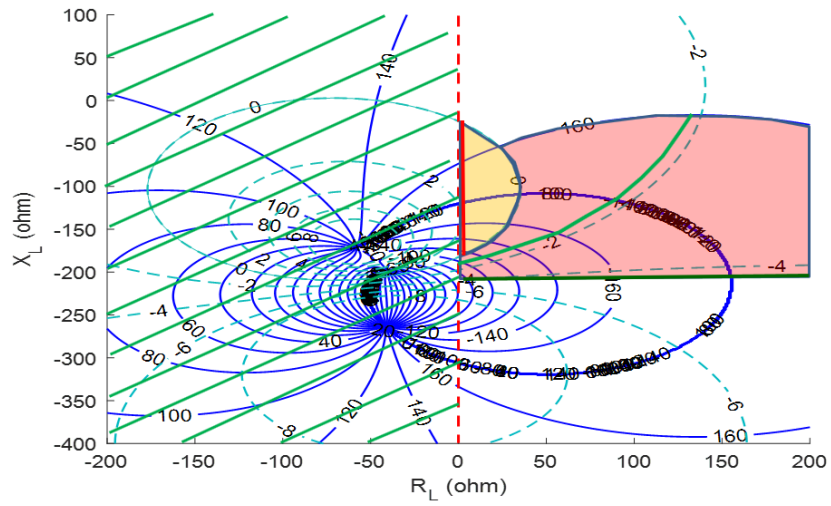
Figure 6.5.1: Interesting design regions: yellow $\tau_n > 0$ dB, red $0 < \tau_n < -4$ dB.
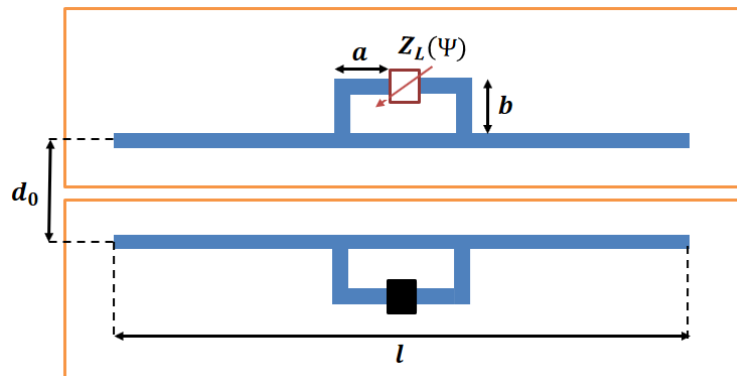
Figure 6.5.2: Proposed couplet consisting of dipole antennas with T-match circuit.

only by means of a suitable design of the coupled antennas. A sensor that varies a purely reactive input impedance is included within that yellow area, i.e. the red path of Fig. 6.5.1 and can be designed using passive components. That kind of sensor has the advantage of an improved realized gain but it is not constant for different values of the physical parameter to monitor i.e. different values of the input impedance of the sensor. On the contrary, to obtain a constant τ_n it is required the input impedance of the sensor has to have both resistive and reactive components following a path coincident with a $\tau_n = const$ contour as highlighted by the light green line inside the red region of Fig. 6.5.1. The impedances inside that red region have the drawback to obtain $\tau_n < 0$ dB but it is sufficiently high to not compromise the realized gain. The dark green path on the boundary of the red region has the peculiarity to correspond to a resistive sensor with a constant $\tau_n < 0$ dB and a constant reactance.

6.5.1   Purely reactive sensor

Let us consider the design of a purely reactive sensor based on an open circuit transmission line. In fact, the input impedance of an open circuit transmission line is purely capacitive:

$$Z_{in} = -jZ_c \cot(\beta l) \qquad (6.5.1)$$

where Z_c, β and l are, respectively, the characteristic impedance, the propagation constant and the length of the transmission line. The input impedance can change for two effects: the change of the length and the change of the characteristic impedance. So that a simple capacitive sensor can be realized if either or both Z_c and l are depending on the physical phenomenon to measure. Let us consider the case of a bifilar transmission line made with a good conductor (Fig. 6.5.3), its characteristic impedance is

$$Z_c = \frac{120}{\sqrt{\varepsilon_r}} \cdot \text{arcosh}\left(\frac{d}{D}\right) \qquad (6.5.2)$$

where D, d and ε_r are the diameter of the wire, the distance between the wires and the permittivity of the medium, respectively. Evidently, the change of one or more of that parameters causes the change of Z_c, in particular Z_c increases for increasing d and for the decreasing of D and ε_r as shown in Fig. 6.5.4 and Fig. 6.5.5.

The input impedance (6.5.1) is very sensitive to the change of the length in particular when it approaches half-wavelength because of the rising of the stationary wave over the line. Fig. 6.5.6 shows the input impedance (6.5.1)

181
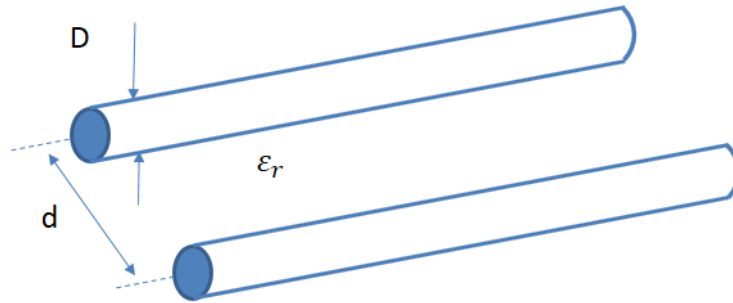
Figure 6.5.3: Design parameters of a bifilar transmission line.
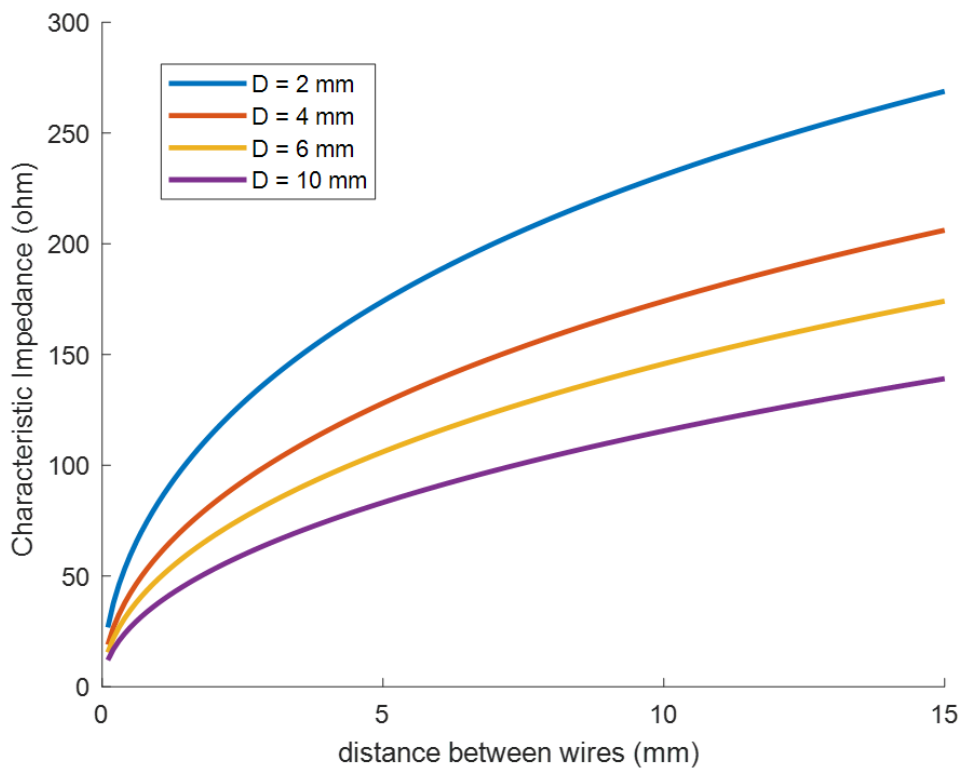
Figure 6.5.4: Z_c for $\varepsilon_r = 1$, when the distance between the wires increases and for different values of the wire's diameter.
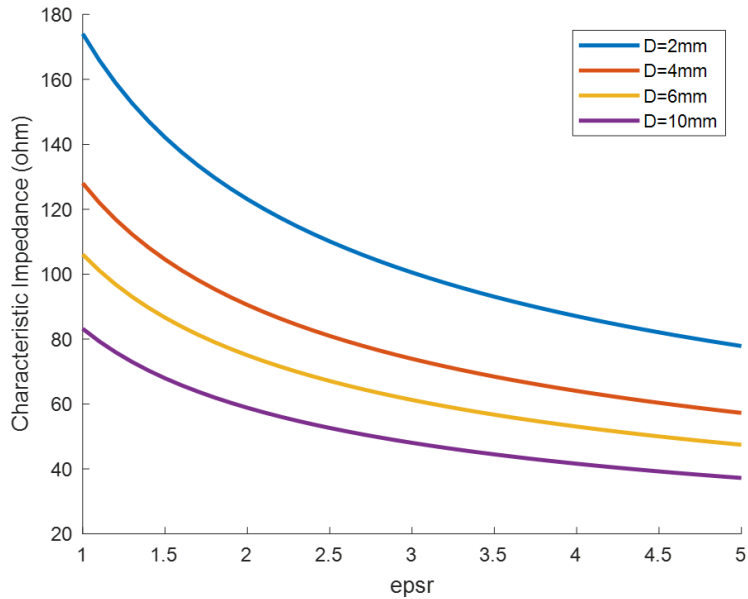
Figure 6.5.5: Z_c for $d = 5$ mm, when permittivity increases and for different values of the wire's diameter.

for a line in free space at frequency of 867 MHz and for different values of Z_c.

A reactive filter can be realized by associating the variation of the phenomenon to be measured with the variation of one or more of the design parameters above described. It requires a design strategy specific for the particular physical phenomenon considered in order to achieve the desired characteristics of the sensor. As an example we consider the design of a breaking test sensor i.e. a sensor that permits to detect the arising and the growth of a fracture in an object subjected to mechanical stress under controlled conditions. For that purpose, we may exploit the variation of the characteristic impedance of the transmission line by varying the distance between the two conductors when they are subjected to the movement of the fracture. That structure, however, has the disadvantage of requiring a sliding connection of the end points of the line to the antenna terminals that instead are fixed. To avoid that drawback, we resort to a tapered transmission line where two end points of the line are fixed to the antenna's terminals while the rest of the line diverges under the movement of the fracture of the object (Fig. 6.5.7).

The behaviour of a tapered transmission line can be modelled with a Riccati's equation that has a not simple resolution in closed form. A numerical model based on a method of moments, instead, permits a quick and accu-
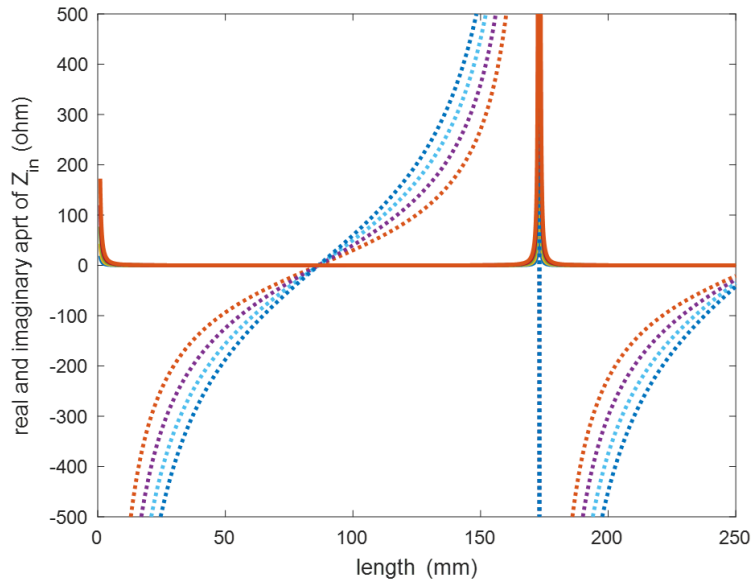
Figure 6.5.6: Input impedance Z_{in} (real and imaginary parts) vs. the length of a line having different values of Z_c at 867 MHz.
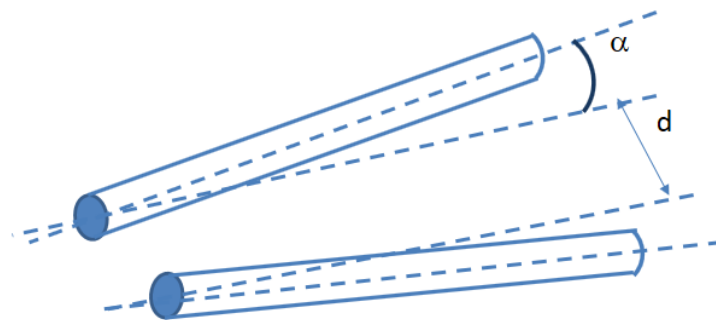
Figure 6.5.7: A tapered line realized by bending the wires by an angle α.
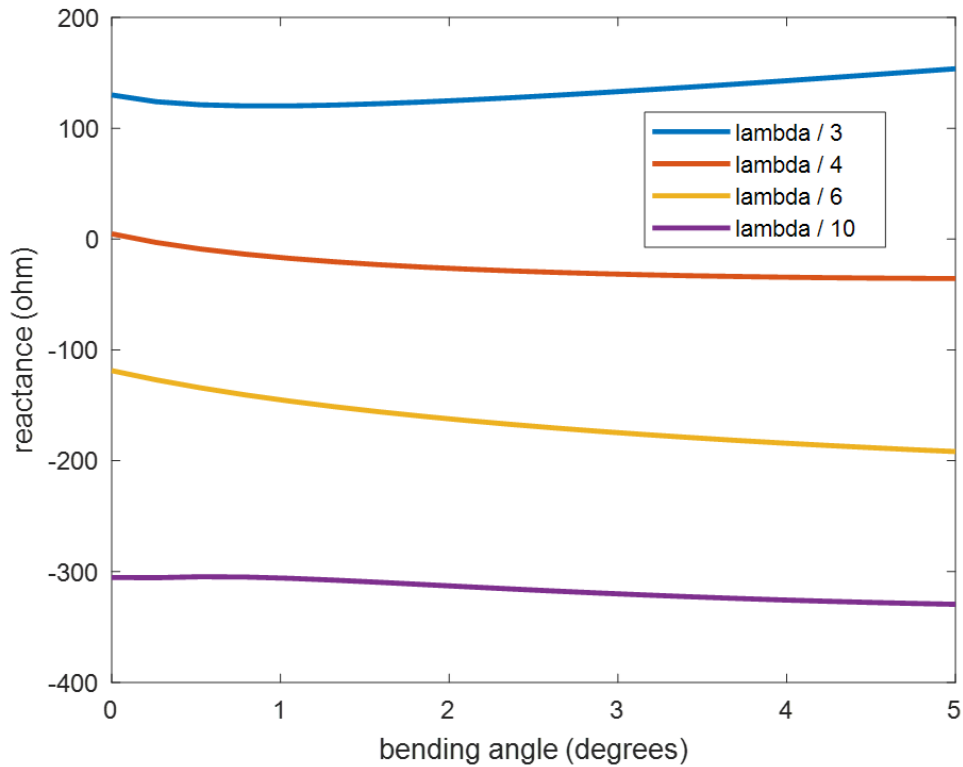
Figure 6.5.8: Imaginary part of the input impedance Z_{in} of a tapered transmission line vs. the bending angle for different lengths of the wires. For wires made of good conductors the real part of Z_{in} is negligible.

rate resolution as shown in Fig. 6.5.8. Wires made of good conductor as copper are subjected to very low losses and therefore the real part of the impedance has negligible values in the order of few ohm. The imaginary part instead is not negligible and its sign depends on the length of the line, so it is capacitive for lines long less than a quarter of wavelength and inductive for lengths between a quarter of wavelength and half wavelength. In case of capacitive impedance, it is interesting to observe that as the value of the bending angle (α in Fig. 6.5.7) increases the reactance decreases because of the increasing of the characteristic impedance of the line. From the results shown in Fig. 6.5.8 it appears that the slope of the capacitive reactance is higher for lengths of the line in the nearness of $\lambda/6$, so that it may be taken as a reference length to develop the breaking test sensor.
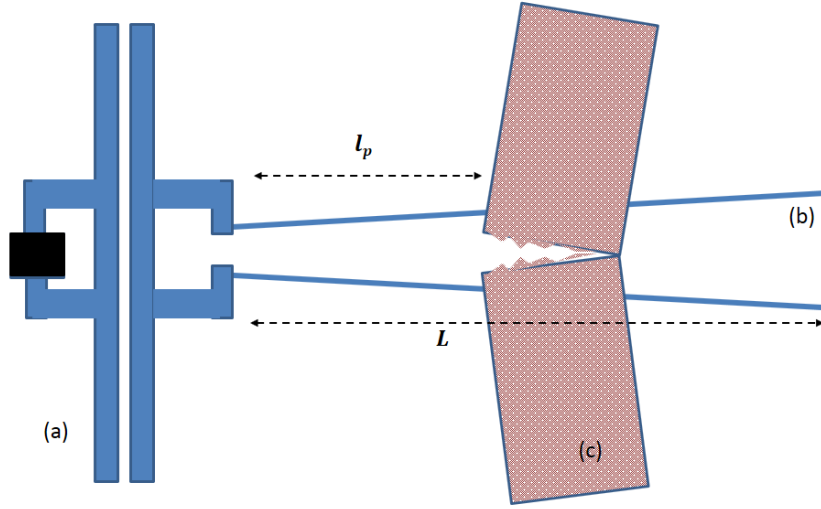
Figure 6.5.9: Schema of the breaking test sensor: (a) RFID couplets; (b) tapered transmission line behind the material under test (c). L length of the line, l_p distance of the anchor point.

6.5.2   Breaking-test sensor

A schema of the breaking test sensor is shown in Fig. 6.5.9, it is composed of an RFID couplet (a), the tapered transmission line (b) and the material under test (c).

Couplet geometries and relative dimensions are reported respectively in Fig. 6.5.2 and in Table 6.1. These values were obtained through the synthesis process described in [12], where the authors tried to obtain values of Z_S and Z_M ($Z_S = 35 + j208$ Ω, and $Z_M = -6 - j56$ Ω), as close as possible to the desired values $Z_{S,\omega}$ and $Z_{M,\omega}$($Z_{S,\omega} = 26 + j192$ Ω, and $Z_{M,\omega} = -13 - j48$ Ω), at the frequency $f_{RFId} = 867$ MHz. The first dipole that compose the couplet is connected to the NXP G2XM RFId chip [18] ($Z_C^{ON} = 16 - j156$ Ω, and $Z_C^{OFF} = 150$ Ω at $f_{RFId} = 870$ MHz). The divergence of the couple of wires depends on both the largeness of the fracture and the position of the fixing point along the line, i.e. l_p in Fig. 6.5.9 so that the distance l_p is a further degree of freedom that permits the tuning of the sensibility of the sensor. We can define, in fact, the sensibility as the ratio between the variation of the measured quantity, i.e. the phase φ of the backscattered signal, and the variation of the quantity under test, i.e. the largeness p of the fracture. The decreasing of l_p permits to increase that ratio, i.e. $S = \frac{\partial \varphi}{\partial p}$, as it will be demonstrated later on.

The input reactance vs. the bending angle (α) for a line long $L = \lambda/6$

l	a	b	d_0
122	18	10	4

Table 6.1: Couplet geometrical values in millimeters.

l_p	S [°/mm]	Resolution (mm)
$\lambda/6$	16	0.3
$\lambda/12$	32	0.15
$\lambda/20$	53	0.1

Table 6.2: Sensibility S and resolution as l_p varies.

@ 867 MHz is shown in Fig. 6.5.10, it spans from about -120 Ω to -190 Ω for a variation of the bending angle from 0 to 5 degrees. The real part of the input impedance instead has a negligible value. The collocation of that reactance over the nomogram of the considered RFID couplet is shown in Fig. 6.5.11, it is almost all within the region with $\tau_n > 0$ dB (the part outside that region corresponds to the interval 3.5° - 5°). The variation of the backscattered phase and the corresponding embedded power transfer coefficient are shown in Fig. 6.5.12 and Fig. 6.5.13, respectively. The phase spans over an interval of about 80 degrees with an almost linear variation while the coefficient τ_n has a not monotonic behaviour being it maximum (about 2 dB) for bending angles in the nearness of 1 degree while it decreases linearly becoming negative for angles larger than 3.5 degrees. The variation of the phase of the backscattered field vs. the displacement of the fracture is shown in Fig. 6.5.14 for different values of the length l_p, in particular $l_p = \lambda/6$ corresponds to the case of material under test fixed at the end points of the line while shorter lengths corresponds to fixing points in intermediate positions. Evidently the sensibility $S = \frac{\partial \varphi}{\partial p}$ doubles by halving l_p as shown in Table 6.2.

The phase measurement is affected by the noise that typically introduces an uncertainty of about +/-5° while an off-the-shelf reader typically has a measurement accuracy of about +/-3°, the smallest change that can be measured i.e. the resolution is strongly affected by the sensibility. In case of sensibility of 16°/mm the resolution is about 0.3 mm while it improves to 0.15 mm and 0.1 mm for $S = 32$ and $S = 53$, respectively.
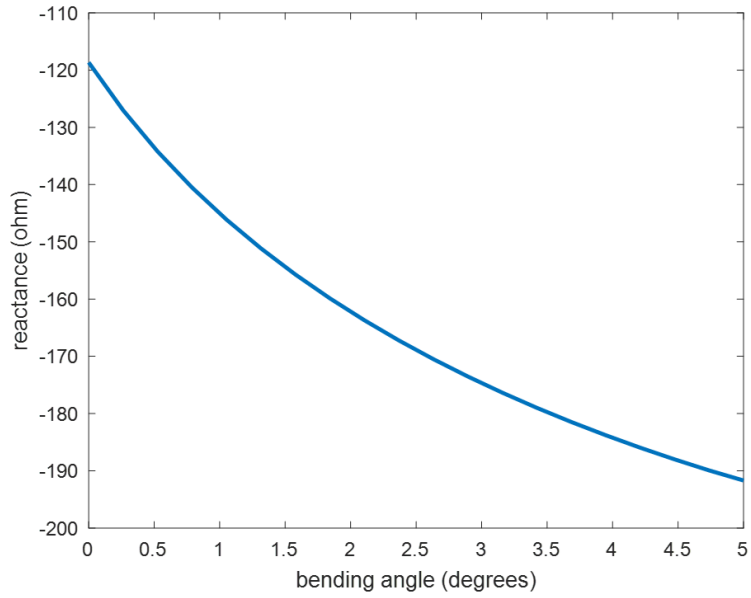
Figure 6.5.10: Reactance of a $\lambda/6$-long tapered transmission line vs. the bending angle. $l_p = L$.
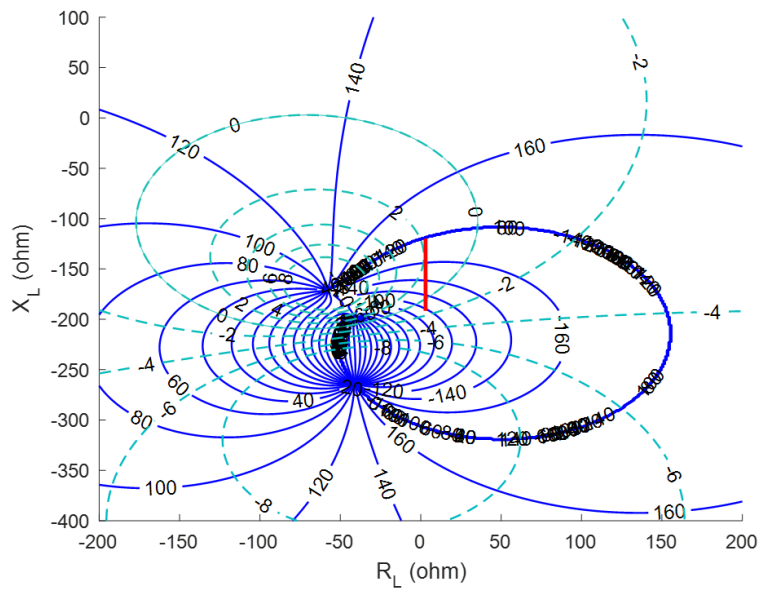
Figure 6.5.11: Collocation of reactance of Fig. 6.5.9 (red segment) on the nomogram.
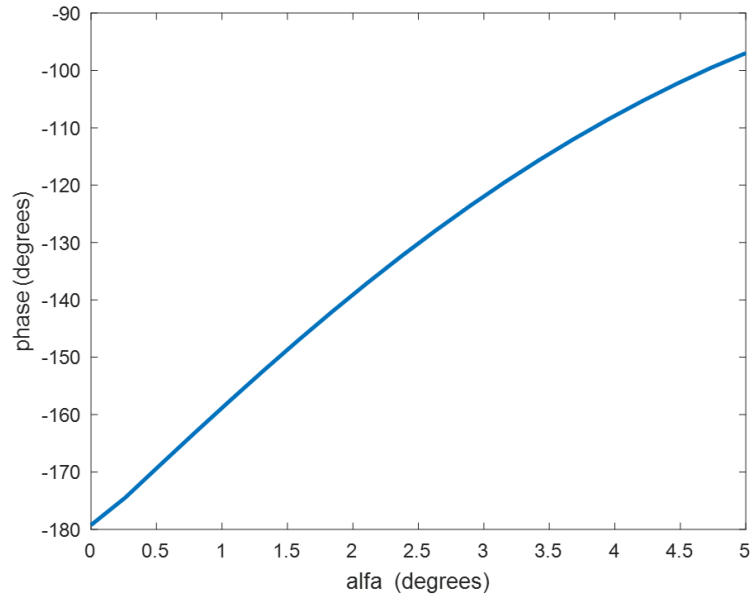
Figure 6.5.12: Phase variation vs. bending angle.
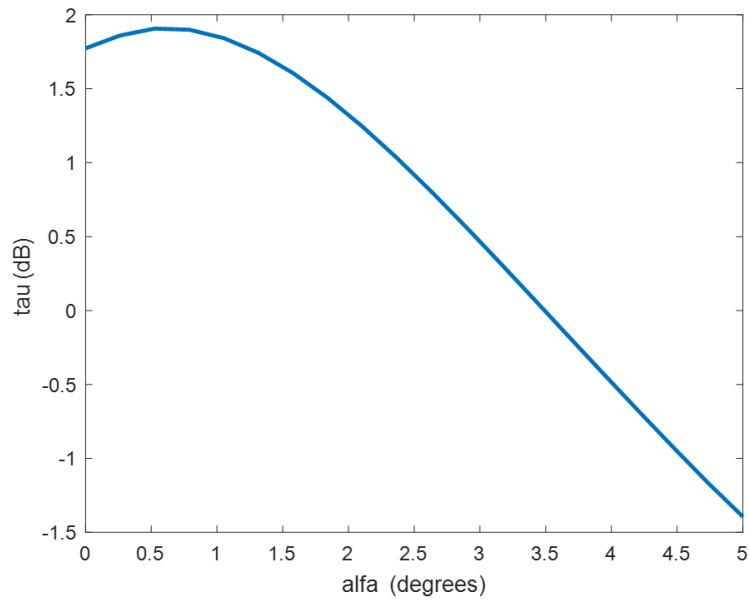
Figure 6.5.13: Variation of the embedded power transfer coefficient vs. bending angle.
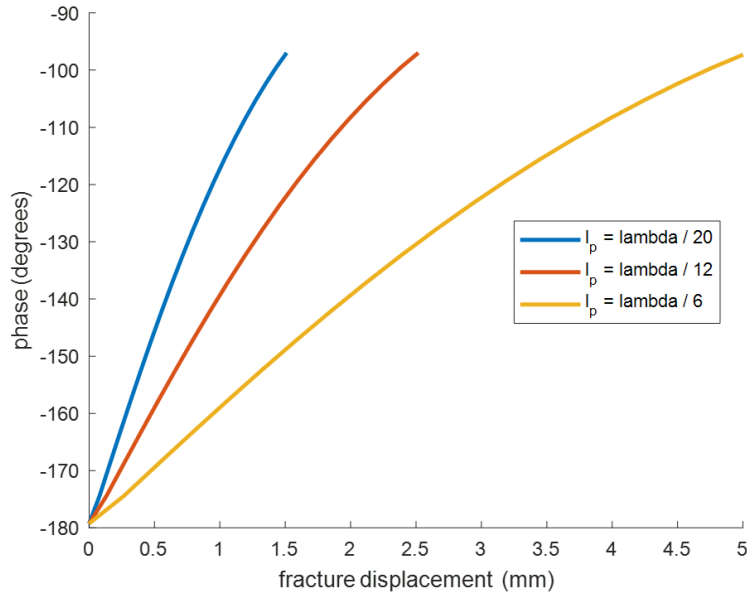
Figure 6.5.14: Variation of the phase vs. fracture displacement for different values of l_p.

6.6 Measurement results

The above described breaking test sensor has been realized and tested in laboratory under controlled condition (Fig. 6.6.1). The length of the bifilar line is about 5.5 cm i.e. about $\lambda/6$, it is realized with copper wire having 0.8 mm of diameter and it soldered to the free terminals of the RFID couplet. An arm of the bifilar line is glued to a narrow strip made of polypropylene that is connected to a sliding small wooden jig by means of paper support. The jig is moved by means of a differential screw having sub-millimeter step (not visible in the picture) while it moving permits to increase or decrease the distance between the two wires. The sensor is placed on a wooden table while the reader's antenna is at a distance of about 50 cm from it with the input power at 16 dBm.

In a first experiment the plastic strip has been fixed at the free end point of a wire, it is moved by rotating the screw while the other wire remains standing. The phase and the RSSI[3] of the backscattered signal are collected for a set of different distances between the standing and moving end points of the line. For each distance the measured value is obtained as an average among 10 independent interrogations. Results are shown in Fig. 6.6.2 and

---

[3]RSSI: Received Signal Strength Indication.
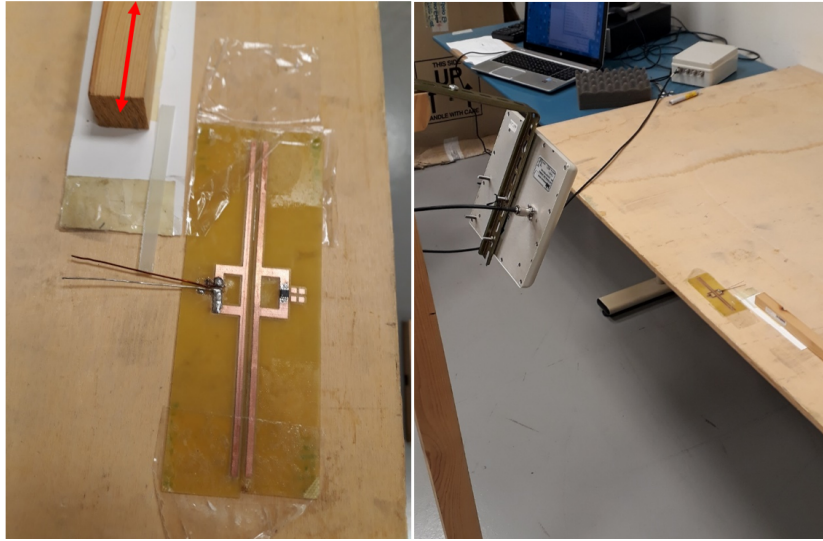
Figure 6.6.1: Picture of realized prototype connected to the sliding jig (left). Realized prototype sensor in the RFId interrogation scenario (right).

Fig. 6.6.3 where error bars concern the standard deviation of the measurements. The phase (Fig. 6.6.2) shows a monotonic behaviour over an interval of about 65 degrees for a variation of the distance between the end points between 0 and 4 mm. In average the slope of the curve interpolating the set of measured data is about 16 °/mm and corresponds to the theoretical value shown in Table 6.2. For fixed input power at the reader's antenna, the collected RSSI is proportional to the embedded power transfer coefficient, Fig. 6.6.3 shows the collected RSSI has a behaviour similar to the theoretical one shown in Fig. 6.5.12. The experiment has been repeated fixing the plastic strip in the middle of the wire, i.e. it halves the length l_p , results are shown in Fig. 6.6.4 and Fig. 6.6.5 for phase and RSSI, respectively. Evidently, the slope of the phase is about 32°/mm confirming the theoretical value shown in Table 6.2 while the RSSI remains almost unchanged.

6.7 Conclusions

In this chapter a new method for the design of a completely passive RFId tag for breaking test of materials has been described. Starting form the mathematical formulation that makes the behavior of a generic 2-port device representable, the goal was to synthesize the tag through the matrix representation of its intrinsic impedances. Thanks to this method it was possible to represent and interpret the phase and amplitude response (in terms of
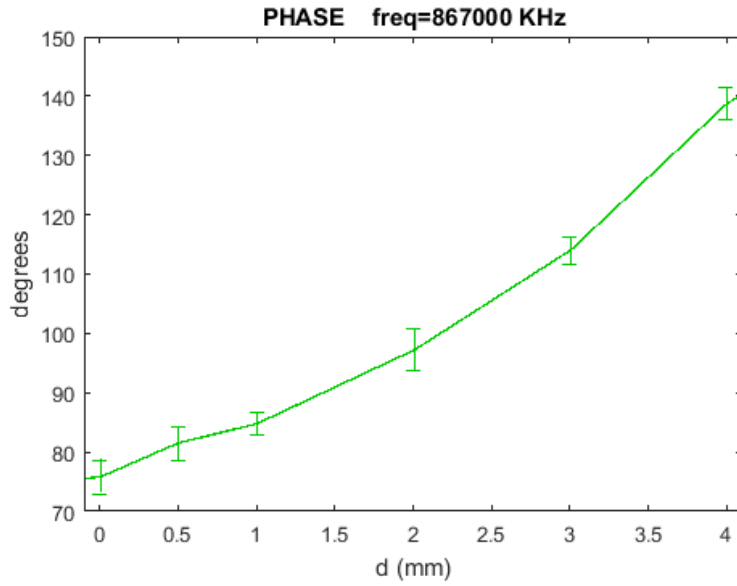
Figure 6.6.2: Measured phase vs. the distance between the end points of the line. Error bars show the standard deviation of the measurements.
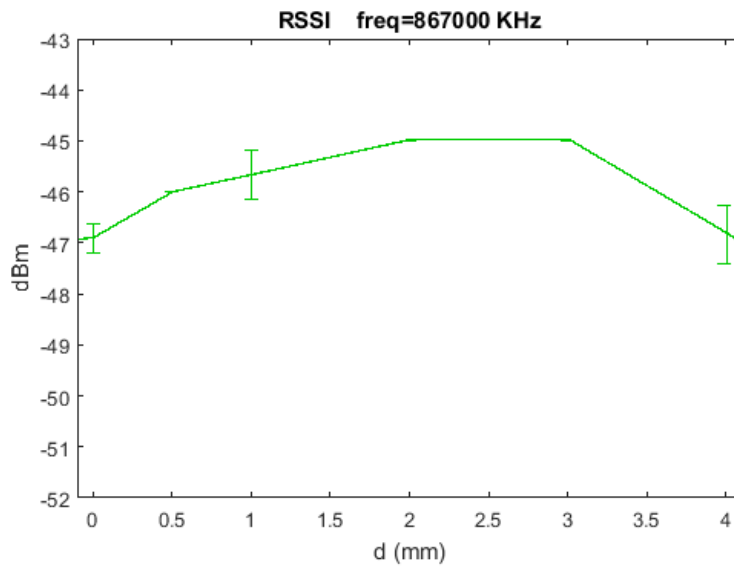
Figure 6.6.3: Measured RSSI vs. the distance between the end points of the line. Error bars show the standard deviation of the measurements.
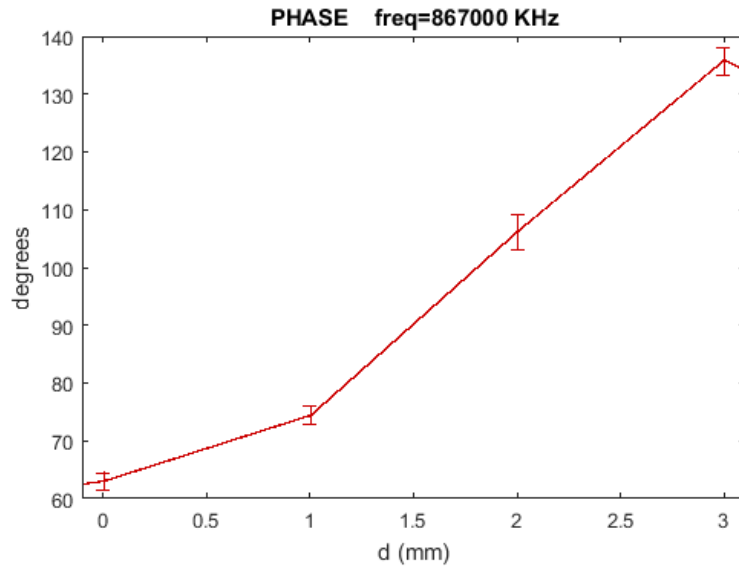
Figure 6.6.4: Measured phase vs. the distance between the middle points of the line. Error bars show the standard deviation of the measurements.
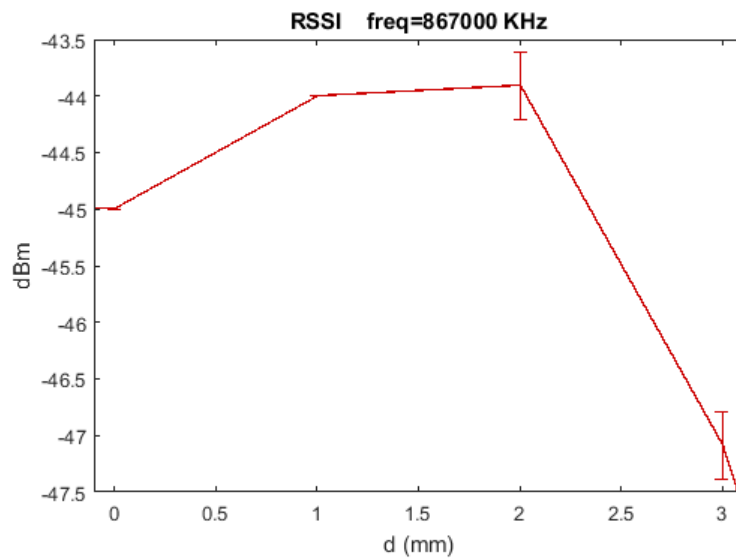
Figure 6.6.5: Measured phase vs. the distance between the middle points of the line. Error bars show the standard deviation of the measurements.

gain) of the 2-port device, allowing stronger control in the design phase of the tag/device. The resulting $\widetilde{\tau}_n - \varphi_n$ nomogram is the map through which it was possible to synthesize the couplet composed of two dipoles with T-match circuits, which together with the chosen RFId chip, led to the realization of the basic structure of the proposed passive tag. Through the study of the possible behaviors carried out on the $\widetilde{\tau}_n - \varphi_n$ nomogram it was decided to use the tag as a sensor for the breaking test of materials. In particular, by analyzing the behavior of the impedance of the port left free, a pair of copper-based filiform conductors were finally applied in order to detect the impedance variations obtained as a result of the spreading apart of the two terminals themselves. The spreading would emulate the behavior that would occur following a breakage of the material under test. The prototype was interrogated with a reader placed 50 cm from the sensor in the laboratory. The measurements confirmed what was achieved in the study analysis phases carried out during the simulation phase.

Bibliography

[1]   C. Perera, A. Zaslavsky, P. Christen, and D. Georgakopou-
        los. *Sensing as a service model for smart cities supported by
        Internet of Things*, Trans. Emerging Telecommun. Technol.,
        Vol. 25, No. 1, pp. 81-93, Jan. 2014.

[2]   D. J. Yeager, P. S. Powledge, R. Prasad, D. Wetherall, and
        J. R. Smith. *Wirelessly-charged UHF tags for sensor data
        collection*, in Proc. IEEE Int. Conf. RFID, Las Vegas, NV,
        USA, pp. 320-327, Apr. 2008.

[3]   J. R. Smith. *Wirelessly Powered Sensor Networks and Com-
        putational RFID*, Berlin, Germany: Springer-Verlag, 2013.

[4]   T. Unander, J. Siden, and H. E. Nilsson. *Designing of RFID-
        based sensor solution for packaging surveillance applications*,
        IEEE Sens. J., Vol. 11, No. 11, pp. 3009-3018, Nov. 2011.

[5]   M. S. Khan, M. S. Islam, and H. Deng. *Design of a reconfig-
        urable RFID sensing tag as a generic sensing platform toward
        the future Internet of Things*, IEEE Internet Things J., Vol.
        1, No. 4, pp. 300-310, Aug. 2014.

[6]   C. Occhiuzzi, S. Caizzone, and G. Marrocco. *Passive UHF
        RFID antennas for sensing applications: Principles, methods
        and classifications*, IEEE Antennas Propag. Mag., Vol. 55,
        No. 6, pp. 14-34, Dec. 2013.

[7]   C. Occhiuzzi and G. Marrocco. *Constrained design of passive
        UHF RFID sensor antennas*, IEEE Trans. Antennas Propag.,
        Vol. 61, No. 6, pp.2972-2980, Jun. 2013.

[8]   S. Caizzone, E. Di Giampaolo, and G. Marrocco. *Wireless
        crack monitoring by stationary phase measurements from*

coupled RFID tags, IEEE Trans. Antennas Propag., Vol. 62, No. 12, pp. 6420-6412, Dec. 2014.

[9]   S. Manzari, C. Occhiuzzi, S. Nawale, A. Catini, C. Di Natale, and G. Marrocco. *Humidity sensing by polymer-loaded UHF RFID antennas*, IEEE Sens. J., Vol. 12, No. 9, pp. 2851-2858, Jun. 2012.

[10]   S. Manzari, S. Caizzone, C. Rubini, and G. Marrocco. *Feasibility of wireless temperature sensing by passive UHF-RFID tags in ground satellite test beds*, in Proc. IEEE Conf. Wireless Space Extreme Environ. (WiSEE), pp. 1-6, Oct. 2014.

[11]   R. A. Potyrailo et al.. *Selective quantitation of vapors and their mixtures using individual passive multivariate RFID Sensors*, in Proc. IEEE Int. Conf. RFID, Orlando, FL, USA, pp. 22-28, Apr. 2010.

[12]   S. Caizzone, E. Di Giampaolo, and G. Marrocco. *Constrained Pole-Zero Synthesis of Phase-Oriented RFID Sensor Antennas*, IEEE Trans. on Antennas and Propagation, Vol. 64, No. 2, pp. 496-503, Feb. 2016.

[13]   G. Marrocco. *RFID grids - Part I: Electromagnetic theory*, IEEE Trans. Antennas Propag., Vol. 59, No. 3, pp. 1019-1026, Mar. 2011.

[14]   S. Caizzone and G. Marrocco. *RFID grids - Part II: Experimentations*, IEEE Trans. Antennas Propag., Vol. 59, No. 8, pp. 2896-2904, Aug. 2011.

[15]   S. Caizzone, E. Di Giampaolo, and G. Marrocco. *Passive RFID couplets as wireless interface for sensor applications*, in Proc. Eur. Conf. Antennas Propag. (EUCAP), pp. 1-4, Apr. 2015.

[16]   C. Balanis. *Antenna Theory: Analysis and Design*, Hoboken, NJ, USA: Wiley.

[17]   M. H. Tu and C. -M. Lin. *Synthesis of pole/zero assignement control law with minimum control input*, IEE Proc. Control Theory Appl., Vol. 139, No. 3, pp. 291-295, May 1992.

[18]   nxp.com/products/rfid-nfc/ucode-rain-rfid-uhf/ucode-g2xm-and-g2xl:SL3ICS1002_1202

Chapter 7

Switchable Low Noise Amplifier

7.1 Introduction

A low noise amplifier (LNA) is a particular type of amplifier that is usually used in the receive chains in a data transmission / reception system. Its task, in fact, is to amplify the weak signals picked up by the antenna by introducing as little noise as possible. In fact, in the path between the transmitting and receiving antenna, the signal is attenuated due to the distance and losses introduced by the transmission medium. The goodness of a LNA is established mainly on the basis of the Noise Figure (NF) parameter expressed in decibels, whose typical values are $NF = 1 \div 2$ [dB]. Other important parameters to consider during the design phase are the gain (e. g. 10 [dB]), a large inter-modulation and compression point (IP3 and P1dB, respectively), the stability over the widest possible frequency band, and a good impedance matching on the input and output ports so as to ensure maximum power transfer for the incoming and outgoing (amplified) signal in the amplifier.

This chapter will describe a particular operating technique for the LNA: the *switching* technique. If we refer to Fig. 7.1.1, which shows the block diagram of a receive-transmission system in which the antenna can be used both to transmit (Tx) and to receive (Rx), it can be seen that a switch is needed to allow switching from one block to the other.

In Fig. 7.1.2, an example of a 2.4 GHz microwave switch is shown. As it is possible to see, it is composed of three branches: the branch for the Tx part of the system, the branch for the Rx part of the system, and the antenna branch. The PIN diodes, which are usually used in this type of circuits, are used to allow the passage from the Tx branch to the antenna in the case of transmission, avoiding allowing the signal to reach the Rx part of the chain (where the LNA is contained) and vice versa. The isolation implemented by
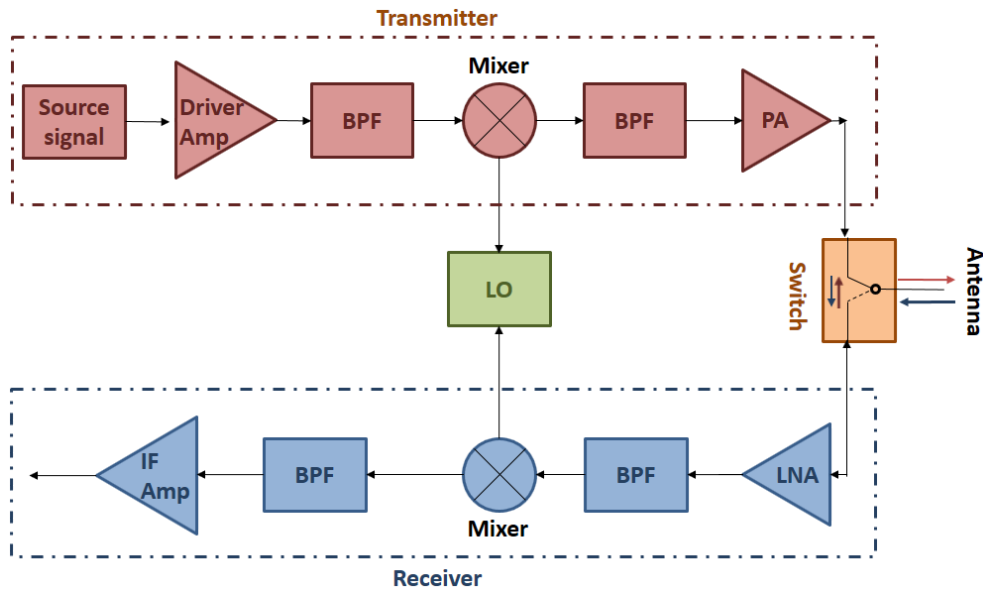
Figure 7.1.1: Block diagram of a receive-transmission chain with single antenna. A microwave circulator could also be used instead of the switch.

the switch is in any case not infinite, and therefore there will always be effects due to the tansmitted signals on the Rx branch and vice versa. Furthermore, the switches are made with components that still introduce noise, as well as the copper microstrips that connect them together.

The idea is precisely to introduce an LNA with switching capability in order to eliminate the switch. Obviously on the transmission chain it is necessary to have a power amplifier (PA) with the same skill.

7.2 Design parameters of a Low Noise Amplifier

In a radio communication system it is very important to try to have as little distortion in reception as possible on the signals sent from the transmitting side. The LNA is therefore the most important device in the reception chain as it has the dual function of amplifying the very weak signals sent by the transmitting system and introducing as little noise as possible. In the microwave frequency range, amplifier design involves the careful balancing of numerous design parameters that determine their correct operation. The most important are:

- the noise figure (NF), whose typical values usually must not exceed 1

(a)

(b)
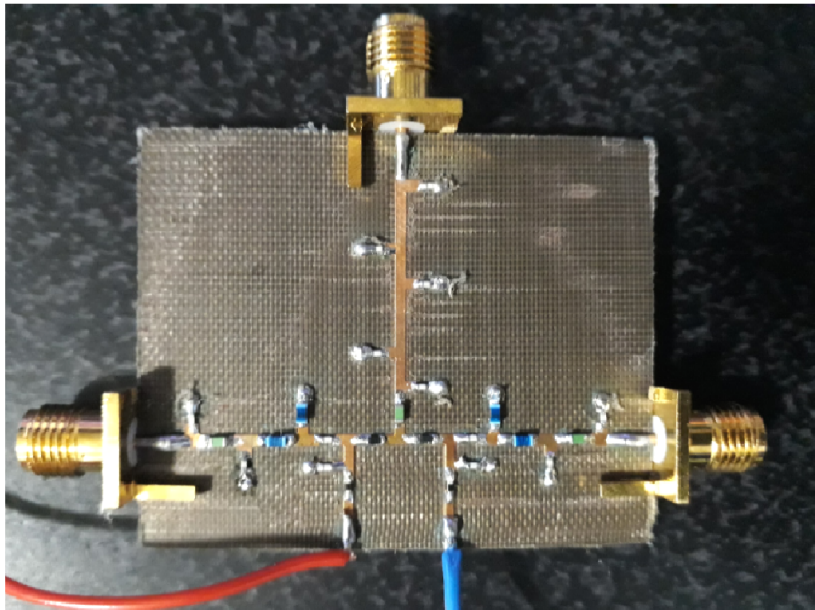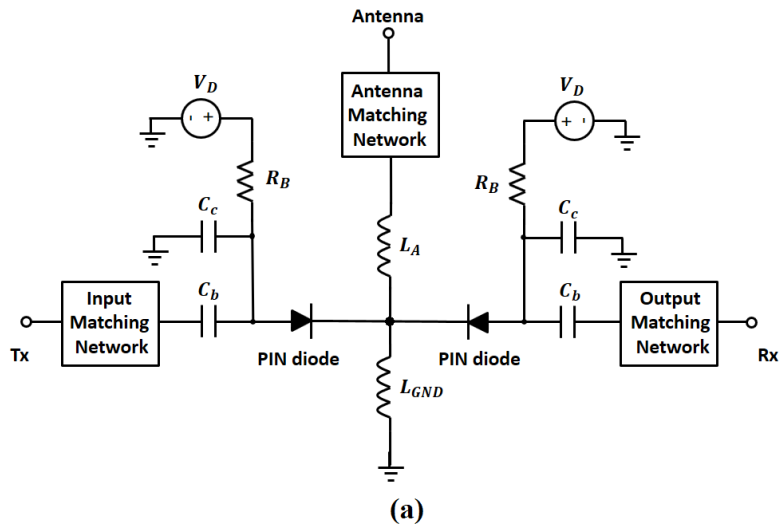
Figure 7.1.2: Example of a 2.4 GHz microwave switch: (a) concept circuit, (b) realized circuit.

- 2 dB, which precisely characterizes this type of amplifier;

- stability: in the microwave range, the circuit must be stable over the entire frequency range, as if this condition is not respected oscillations could occur which would compromise the functioning of the LNA;

- the gain typically not less than 9 - 10 dB in single stage;

- good impedance matching to the input and output ports of the amplifier, to ensure that the signal that arrives and that, once amplified, leaves the LNA reaches its destination as less attenuated and distorted as possible.

7.2.1   Noise in amplifiers

The noise generated inside an amplifier becomes a problem when the signal to be amplified has such a small amplitude that it is confusing and comparable to that of the amplifier noise itself. The quantitative measure of the effect of noise on the signal is the signal-to-noise ratio (S/N), i.e. the ratio between the power of the treated signal and the power generated by the noise in the circuit. In general, its minimum value depends on the application and the context, so much so that it does not have a standardized minimum value. Since most applications use signals available within a limited band, noise and signal strength are usually only evaluated within that specific band for each of the available frequencies. Outside the band of interest, a filtering action is usually applied.

The signal to be amplified, as mentioned, is itself affected by noise and therefore the signal arriving from the transmitting chain itself has a S/N ratio. Once amplified, both the signal and the associated noise are amplified, but the S/N ratio is not altered. However, the additional noise generated by the amplifier itself is added to that contained in the signal, and therefore we obtain:

$$\frac{S_o}{N_o} = \frac{G \cdot S_i}{G \cdot N_i + N_{ampl}} > \frac{S_i}{N_i} \tag{7.2.1}$$

where S_i and S_o are, respectively the powers of the input and output signals, G is the gain of the amplifier, and N_{ampl} is the noise power introduced by the amplifier itself.

The measure of the deterioration of the S/N ratio after amplification is the Noise Figure (NF), which is the ratio between the S/N ratio before amplification and the S/N ratio after the amplifier:
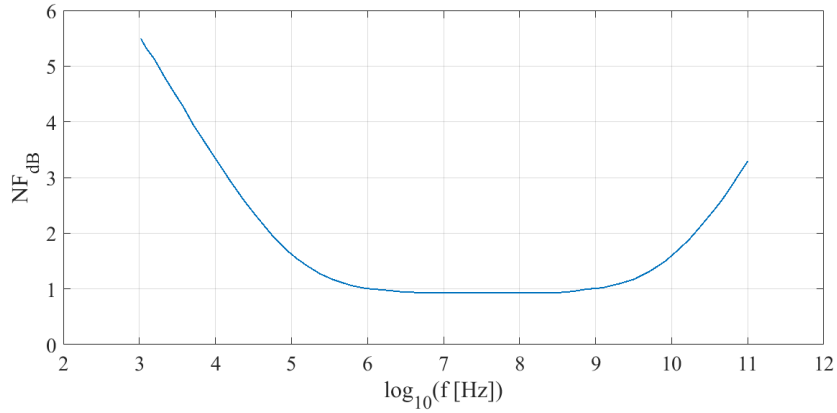
Figure 7.2.1: Noise Figure of a transistor as a function of frequency.

$$NF = \frac{S_i/N_i}{S_o/N_o} > 1 \qquad (7.2.2)$$

which in dB is expressed as:

$$NF_{dB} = \left(\frac{S_i}{N_i}\right)_{dB} - \left(\frac{S_o}{N_o}\right)_{dB} > 0 \qquad (7.2.3)$$

Without discussing the physical origins of noise within an amplifier, suffice it to say that it is not the same at all frequencies. Noise sources are essentially resistors and active components. The resistors contribute with their so called thermal noise, which is constant at all frequencies and substantially depends on the temperature: in fact the higher the temperature, the higher the noise will be. In active components, the noise power is high at low frequencies, and decreases as the reciprocal of the frequency: it is known as 1/f noise contribution. At certain frequencies the noise power becomes approximately constant with respect to the frequency (typically in the MHz range), well below the microwave region. In the GHz region the noise power usually begins to increase, and the NF_{dB} has an approximately linear dependence on frequency.

The noise is also dependent on the bias current in active devices: it is very high for very low currents, while it decreases as the bias current increases until the minimum required value is reached, and then grows again. The optimal bias current value for the noise is usually indicated in the data sheet of the selected active component.

Noise added by an amplifier can be minimized by proper design. First of all, the amplifier should not include resistors; if this is not possible, these

Noise Figure $NF_{min} = f(I_C)$, $V_{CE} = 3$ V, $Z_S = Z_{opt}$ Power Gain G_{ma}, $G_{mS} = f(I_C)$, $V_{CE} = 3$ V, $f =$ Parameter in GHz
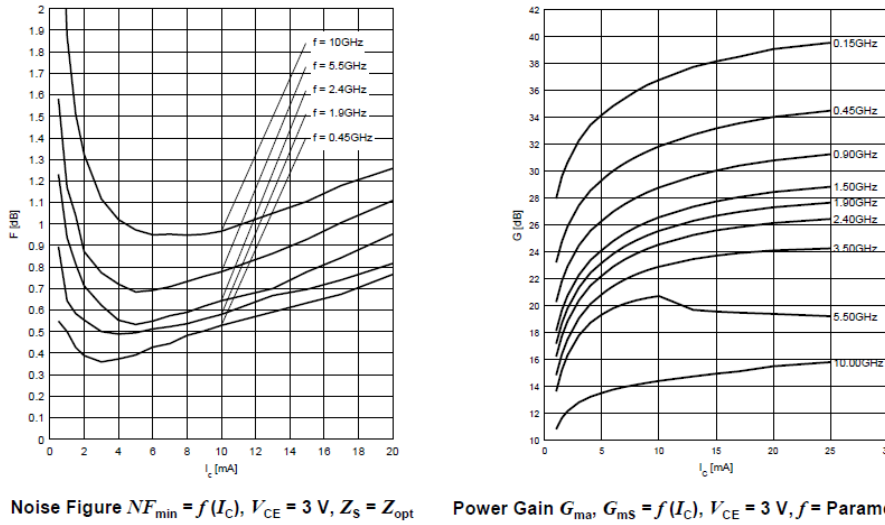
Figure 7.2.2: Minimum noise figure and associated gain of a transistor (Infineon BFP720) as a function of the bias current, for several frequencies.

should be affixed to the output network, as their noise would not be amplified. Similarly, all passive components (capacitors, inductors, lines, etc.) must have very low losses and therefore very low resistivities. The active component, therefore, must be biased to the optimum current (suggested by the supplier).

7.2.2 Stability

The stability of a low noise amplifier, as well as for all amplifiers, is an essential characteristic without which the device would become an oscillating circuit and therefore not suitable for signal amplification. The parameter that gives an indication of the stability of an amplifier operating in microwaves is the k factor, also known as the Rollet factor. In order to define the stability factor it is necessary to consider the amplifier and the matching networks (without losses) as a 2-port device, as shown in Fig. 7.2.3.

The Rollet factor in the case of Fig. 7.2.3 is expressed on the basis of the S parameters representative of the network [1]:

$$k = \frac{1 + |D|^2 - |S_{11}|^2 - |S_{22}|^2}{2 \cdot |S_{21}| |S_{12}|} \tag{7.2.4}$$

where

$$D = S_{11}S_{22} - S_{21}S_{12} \tag{7.2.5}$$

203
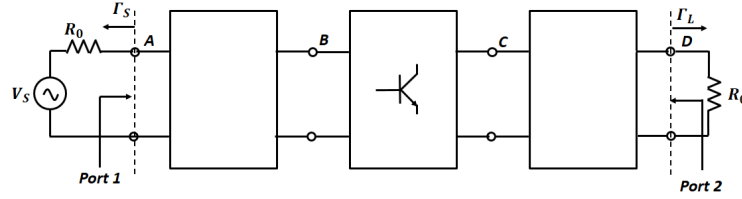
Figure 7.2.3: 2-port reference network.

There are four possible cases that can arise in a scenario like the one represented:

- $k > 1$ on a limited number of frequencies thanks to the choice of certain pairs of Γ_S and Γ_L; for the other frequencies there are oscillations and therefore there is potential instability;

- $k > 1$ on all frequencies; in this case the chosen values of Γ_S and Γ_L do not allow the triggering of oscillations and therefore there is unconditional stability;

- $-1 < k < 1$ for some pairs of Γ_S and Γ_L; in this case the circuit is conditionally stable, but it is potentially unstable;

- $k < -1$ for all pairs of Γ_S and Γ_L: the circuit is unconditionally unstable.

Despite all these recommendations, it is a good design practice (even if not mandatory), to try to obtain $k > 1$ on all frequencies also in the amplifier core, that is (Fig. 7.2.3):

$$k_{BC} = \frac{1 + |S_{BB}S_{CC} - S_{CB}S_{BC}|^2 - |S_{BB}|^2 - |S_{CC}|^2}{2 \cdot |S_{CB}| |S_{BC}|} > 1 \qquad (7.2.6)$$

as if the amplifier core is stable, it will turn out to be even more so once it has been matched in input and output.

More details are reported in many scientific texts and documents, including [1] and [2].

7.2.3 Gain

Gain is another key feature of a good amplifier. In the case of microwave amplifiers, it is important to have good gain characteristics in the band defined by the design specifications. The maximum gain of an amplifier like the one shown in Fig. 7.2.3 is defined as:

$$G_{ma} = \left| \frac{S_{21}}{S_{12}} \right| \left[k - \left(k^2 - 1 \right)^{1/2} \right] \tag{7.2.7}$$

and is related to the Rollet factor and therefore to the stability of the circuit.

From the relation (7.2.7) it can be seen that for $k > 1$, the gain tends to decrease. In the design phase, therefore, it must be taken into account that in order to have a stable circuit it is necessary to lose some gain compared to the potential gain. If more amplification is needed, it is possible to use multi-stage amplifiers, the most common of which exploit the technique of replicated and cascaded amplifiers, or other techniques such as the one called *cascode*.

7.2.4 Input and output impedance matching

Impedance matching networks must provide adequate load to the device. It can be easily seen that part of the contribution given to the noise figure depends on the input load; this means that the input matching network must be designed in such a way as to minimize the noise figure, while the output matching network can be designed to have maximum gain. The effect of the input load on the noise figure is described by the following relationship:

$$NF = NF_{min} + 4 \cdot \frac{R_s}{Z_0} \cdot \left(\frac{|\Gamma_S - \Gamma_N|^2}{\left(1 - |\Gamma_S|^2 \right) \cdot |1 - \Gamma_N|^2} \right) \tag{7.2.8}$$

The noise figure has its minimum value NF_{min} when the input load Γ_S is equal to Γ_N, which is the input load that minimizes the noise added by the amplifier. R_s is the noise resistance value that determines what the increase in the noise figure is. Z_0 is the characteristic impedance of the reflection coefficient and is typically 50 Ohm. The three parameters NF_{min}, Γ_N, and R_s depend on the frequency and bias current, and are generally provided by the device supplier for several frequency values with the optimum bias current; they can be interpolated for other frequencies with the same bias current. In the design phase, it is necessary to choose between an input load capable of providing the minimum noise figure and an input load capable of providing the maximum gain, or a trade-off between the two. An input load that not give the maximum gain does not give a perfect match. Therefore, an amplifier with minimum noise figure usually has a bad input match and a non-optimum gain. Once the input load has been choosen, the output matching network is designed for perfect output match. The gain obtained with a minimum noise figure and a perfect output match is called associated
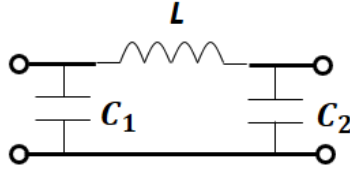
Figure 7.2.4: Generic structure of an impedance matching network (single cell).

gain G_A, also usually given by the supplier in the data sheet of the active device. The structure of a generic impedance matching network is shown in Fig. 7.2.4.

In the design of single frequency microwave amplifiers, for the input and output loads, single matching cells are usually used (one in input and one in output) with suitable values of L, C_1 and C_2. In the event that an amplification on a more or less wide band of frequencies is required, the cascading of more cells would allow for an impedance matching on more frequencies and therefore to satisfy the specifications [1], [2].

7.3   Microwave transistor

The choice of the transistor in the design of microwave amplifiers is a very delicate phase and to which a lot of attention must be paid because, depending on the transistor chosen, the project specifications can be met or not. For a LNA, the choice must obviously fall on those active devices capable of providing a value of NF_{min} as low as possible in the frequency range of interest. In Table 7.1, the families of transistors used for microwave applications related to the semiconductor of which they are composed are shown.

In order to have a reference term with which to be able to compare the various families of transistors with each other, figures of merit are defined, which set the limits in frequency and power of these active devices. In particular, there are limitations to the maximum speed that carriers can reach in a semiconductor, to the maximum electric field that can exist in the semiconductor before the breakdown and to the maximum current that a transistor can pass through. Starting from these assumptions, it has been shown that the relationship is valid [3]:

$$P_m f_T^2 = \frac{1}{X_c} \left(\frac{E_m v_{tm}}{2\pi} \right)^2 \tag{7.3.1}$$

206

	Si	SiGe	GaAs	InP	GaN
BJT	X				
HBT		X	X	X	
MOSFET	X				
HEMT			X	X	X
MESFET			X*		

Bipolar transistor family
Field Effect transistor family
Disused

Table 7.1: Microwave transistors families.

	v_{tm} [cm/s]	E_G [eV]
Si	$1,0 \cdot 10^7$	1,12
Ge	$0,6 \cdot 10^7$	0,66
GaAs	$2,0 \cdot 10^7$	1,43
2-DEG*	$5,5 \cdot 10^7$	-----
AlGaAs	-----	1,65

*: 2-DEG: two dimensional electron gas.

Table 7.2: Typical values of v_{tm} and E_G for different types of semiconductors.

where P_m is the maximum power that can be delivered by the transistor, $f_T = 1/(2\pi\tau) = v_{tm}/(2\pi L)$ is the cut-off frequency of the device linked to the inverse of the transit time of the carriers through the active region with length L traveled at the speed v_{tm}, E_m is the maximum electric field applicable before the breakdown, v_{tm} is the maximum carrier drag speed, and $X_c = 1/(2\pi f_T C_c)$ is the reactance associated with the junction where the breakdown occurs.

From (7.3.1) it can be deduced that, for a given X_c and for a given device $(E_m v_{tm})$, the delivered power decreases if the cut-off frequency increases. Furthermore, the power can be increased by increasing the section of the device and therefore decreasing X_c.

Typical values of v_{tm} for electrons, for the breakdown electric field E_G, related to the width of the band gap, are reported in Table 7.2.

From these considerations emerges the superiority of gallium arsenide and heterostructure devices over traditional silicon and germanium devices.

In conclusion, in microwave applications the bipolar transistor (BJT) is

Figure 7.4.1: Pinout of the transistor Infineon BFP720: B = base, C = collector, E = emitter.

the most widely used device in the S band up to about 4 GHz, while MESFET dominates between 4 and 20 GHz. For applications at higher frequencies, heterostructure devices are becoming more and more widespread (HEMT).

Useful figures of merit for comparing different transistors are the cutoff frequency f_T and the minimum noise figure NF_{min}.

More detailed information on the various types of transistors, such as methods of operation, equivalent circuits for small signals, noise characteristics and manufacturing techniques are given in [2].

7.4   5 GHz switchable Low Noise Amplifier

The design specifications for this low noise amplifier included an operating frequency on the 5 GHz carrier of Wi-Fi (Wi-Fi5) systems, an amplification of at least 10 dB in single stage, good input and output matching, and minimum noise figure $\leqslant$ 1dB. In order to build the amplifier core, it was decided to use an Infineon BFP720 transistor [4], which is a wideband SiGe C (Silicon-Germanium Carbon) bipolar NPN heterojunction transistor (HBT). This device has the following features:

- $NF_{min} = 0.7$ dB at 5.5 GHz, with 3 V, 5 mA bias voltage/current;

- high gain $G_{ma} = 19.5$ dB at 5.5 GHz, with 3 V, 13 mA bias voltage/current;

- third order interception point: $OIP_3 = 23$ dBm at 5.5 GHz, with 3 V, 13 mA bias voltage/current.

The pinout of the transistor is shown in Fig. 7.4.1. In Fig. 7.1.2 the trends for the noise figure and gain as the collector bias current vary are reported.

In order to have good performance, 2 V as bias voltage for the transistor and 10 mA as collector current were chosen, at which the transistor (alone) would be able to provide a gain greater than 20 dB, and a noise figure less than 0.8 dB.

All the various design phases were carried out using the AWR Microwave Office software [5], in which the following transistor models were imported:

- non-linear model (SPICE model), to be able to carry out the biasing in the correct way and to verify the "big signal" behavior of the amplifier, including the switching technique;

- linear model (S parameters), in order to carry out the analysis on the stability, on the minimum noise figure and on the input and output impedance matching of the LNA ("small signal" analysis).

Both models are available on the online AWR software's library.

7.4.1   Transistor bias

The first design phase concerns the choice of the most suitable bias configuration for the transistor. Looking at the BFP720 data sheet, $V_{CE} = 2$ V and $I_C = 10$ mA have been chosen. Given the combination of these two values, by plotting in AWR the graph in which the collector current is used as a function of the collector-emitter voltage, it is possible to extrapolate the correct value that must be present in the base to have the correct biasing. The base current value $I_B \cong 0.045$ mA.

To obtain these values, in the design of the core it was decided to supply the 2 V on the collector in a non-direct way by exploiting potential drops, starting from an external power supply of 3 V. As can be seen from Fig. 7.4.3, the application of a 27 Ohm resistor and a 71.5 Ohm resistor on the collector branch was sufficient to bring the necessary 2 V and 10 mA to the transistor; on the base branch, on the other hand, it was necessary to place a 49.3 kOhm resistor in order to obtain a base current of approximately 0.045 mA. From the same figure it can also be seen how the external power supplies (both 3 V) have been provided separate in order to completely eliminate the probability of the occurrence of oscillations due to the presence of loops in the circuit. Two cooling capacitances are provided on the base and collector branches (C_2 and C_3), in order to eliminate or reduce any unwanted effects due to the radio-frequency component present in the circuit. Instead, blocking capacitors (C_1 and C_4), have been used on input and output branches of the amplifier, in order to eliminate the presence of any spurious continuous or low frequency components. The inductors L_1, L_2 and L_3 must be determined by small signal analysis.
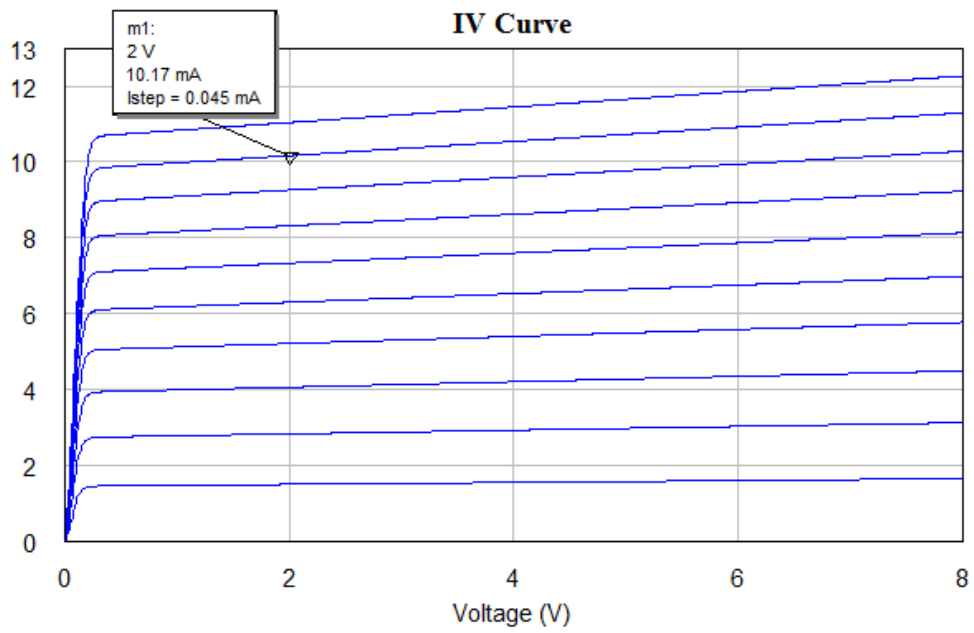
Figure 7.4.2: I_C [mA] vs. V_{CE} [V] curves.
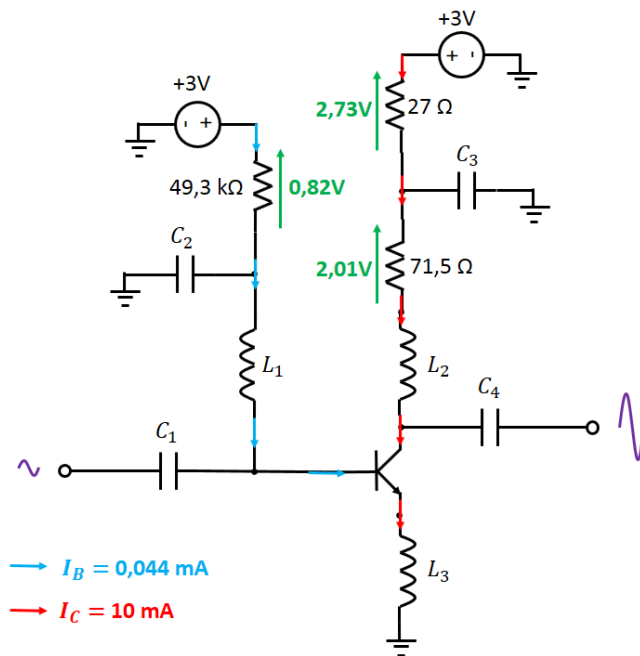
Figure 7.4.3: Core of the 5 GHz LNA (ideal circuit).

210
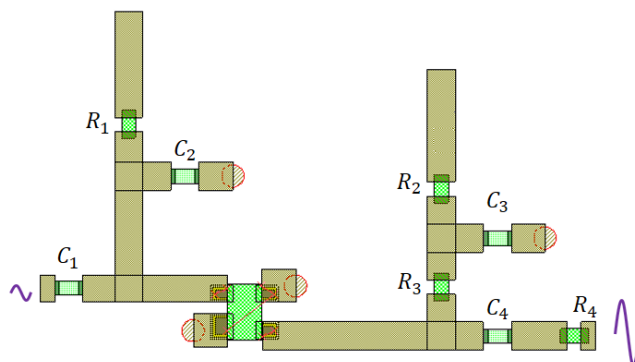
Figure 7.4.4: Final layout of the core of the proposed 5 GHz LNA.

7.4.2 Microwave design

The next step in LNA design is to optimize the other core components of the device. The LNA was designed on a Rogers RO4003C substrate [6] having a thickness of 0.81 mm, with 0.035 mm thick copper and with the following dielectric design characteristics: $\varepsilon_r = 3.6$, $\tan\delta = 0.0024$. This information is important because thanks to it, it was possible to extrapolate the correct dimensions of the microstrips and the optimal values for L_1, L_2, L_3, C_1, C_2, C_3 and C_4. First of all, the connections between the components shown in Fig. 7.4.3 have been replaced by pieces of microstrip line having starting dimensions equal to 1x1 mm^2. Subsequently, for the inductors and for the capacitors, ranges of values within which the optimizer should have sought the optimum values were set in the ideal models present in AWR. The optimization process was carried out using the *Simplex Optimizer* and the *Random Local* alternately, in order to avoid encountering possible local minima of the optimal solution. The goals of the LNA core optimization were to have a $NF_{min} \leqslant 0.9$, $G_{ma} \geqslant 12$ dB in the 4.7 GHz - 5.3 GHz band, and a Rollet factor $k > 1$ over the entire available band (0 GHz - 12 GHz). In order to reach the pre-established goals, the dimensions of each section of microstrip were also made to vary, taking into account the fact of not exceeding too much in the final dimensions of the layout. Once the goals were achieved, the S-parameter models of capacitors and inductors were introduced into the circuit, in order to faithfully simulate the real behavior of these devices in the LNA core. The S-parameter models were supplied by various manufacturers of electronic components for microwave and radio-frequency devices.

Fig. 7.4.4 shows the final layout of the LNA core at 5 GHz, while Table 7.3 shows the list of components necessary for its realization.

Label	Value	Description	Part Number	Producer
C_1	0,7 pF	0402'' SMD Capacitor	GJM1555C1HR70BB01	muRata
C_2	820 pF	0402'' SMD Capacitor	GRM1555C1H821GA01	muRata
C_3, C_4	0,2 pF	0402'' SMD Capacitor	GJM1555C1HR20BB01	muRata
R_1	49,3 kΩ	0402'' SMD Resistor	-------------	generic
R_2	27 Ω	0402'' SMD Resistor	-------------	generic
R_3	71,5 Ω	0402'' SMD Resistor	-------------	generic
R_4	5 Ω	0402'' SMD Resistor	-------------	generic

Table 7.3: List of the passive electronic components of the core of the 5 GHz LNA.

Capacitors C_1, C_3 and C_4 have been replaced by high Q chip multi-layer ceramic capacitors of the GJM series produced by muRata [7], while to replace C_2 a chip multilayer ceramic capacitor for general purposes of the GRM series also produced by muRata was used [8]. In the final layout of the LNA core the inductors on the base and collector branches have disappeared: this choice was due to the fact that the optimal values obtained for the ideal inductor models were very small (in the order of tenths of nH), and for this reason it was decided to replace the effect of those inductances by the microstrip lines with appropriate length arranged in those positions in the circuit. This design choice has led to benefits in terms of noise figure especially if we consider the inductor on the base branch: in fact an inductor has its own internal resistance, and as mentioned above, can contribute to having a noise that is subsequently amplified by the transistor. All the via holes in the circuit were considered to be made in copper material with 0.8 mm diameter, of which an internal thickness of 0.1 mm was considered.

The stability factor k of the LNA core is shown in Fig. 7.4.5. As it is possible to see, in the whole band for which the S parameters of the transistor are available we have $k \geqslant 1.2$. For the minimum noise figure, a $NF_{min} < 0.93$ dB at 5 GHz was obtained. As can be seen from the curves shown in Fig. 7.4.6, the application of copper transmission lines and all other components (resistors and capacitors) led to an increase in the minimum noise figure of 0.17 dB at 5 GHz. The LNA's core has a gain of 13 dB at 5 GHz, and from Fig. 7.4.7 it can be seen how the gain is significantly decreased (about 7 dB) compared to the gain it could provide on its own. As mentioned this is the
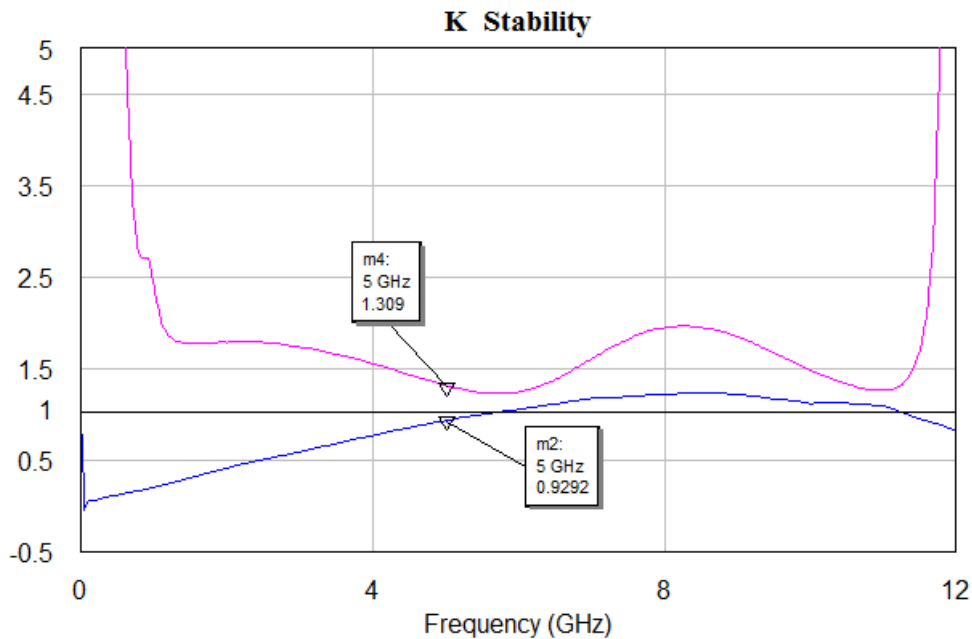
Figure 7.4.5: Stability factor of the LNA core: in blue BFP720 Rollet Factor, in pink LNA core Rollet Factor.

price to pay for having a stable and non-oscillating circuit. In Fig. 7.4.8, instead, the S parameters relative to the LNA core are shown: as can be seen from the trends of the transmission and reflection coefficients on the two ports, the circuit is mismatched in impedance and therefore both the signal arriving in input to the amplifier, and the amplified output one, risk being dissipated and attenuated due to the lack of the condition of maximum power transfer. To do this, it is necessary to affix networks in input and output such as to be able to return complex impedances which are conjugated to those present at the ports of the LNA core (as seen in Fig. 7.2.3).

To be able to carry out the impedance matching on the input and output ports to 50 Ohm, we used two networks such as those shown in Fig. 7.2.4. With the aid of AWR we went to verify the type of impedance present in the input and output of the LNA core. In Fig. 7.4.9 it can be seen that at the input there is an inductive impedance, since, in the band chosen for the analysis (4.7 GHz - 5.3 GHz) the representative curve is found in the upper half of the Smith chart. The situation is different for the output impedance which has capacitive characteristics (lower half of the Smith chart). From the analysis of Fig. 7.4.9, it is therefore clear that the input network must have a representative impedance of the capacitive type, so as to bring it back to the 50 Ohm foreseen for the input, while, for the output network, the
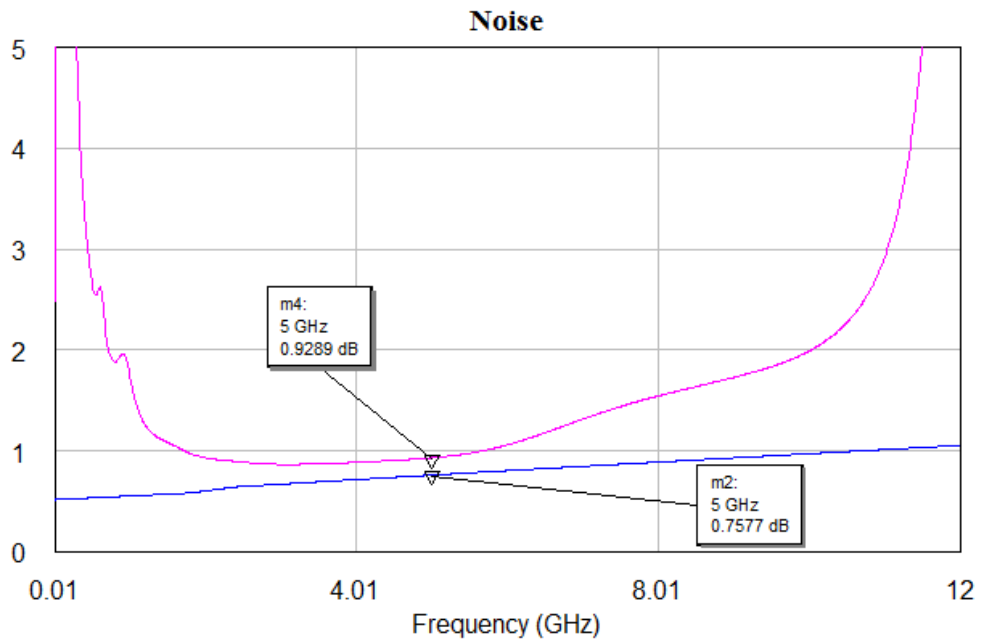
Figure 7.4.6: Minimum noise figure in dB of the LNA core: in blue BFP720 NF_{min}, in pink LNA core NF_{min}.
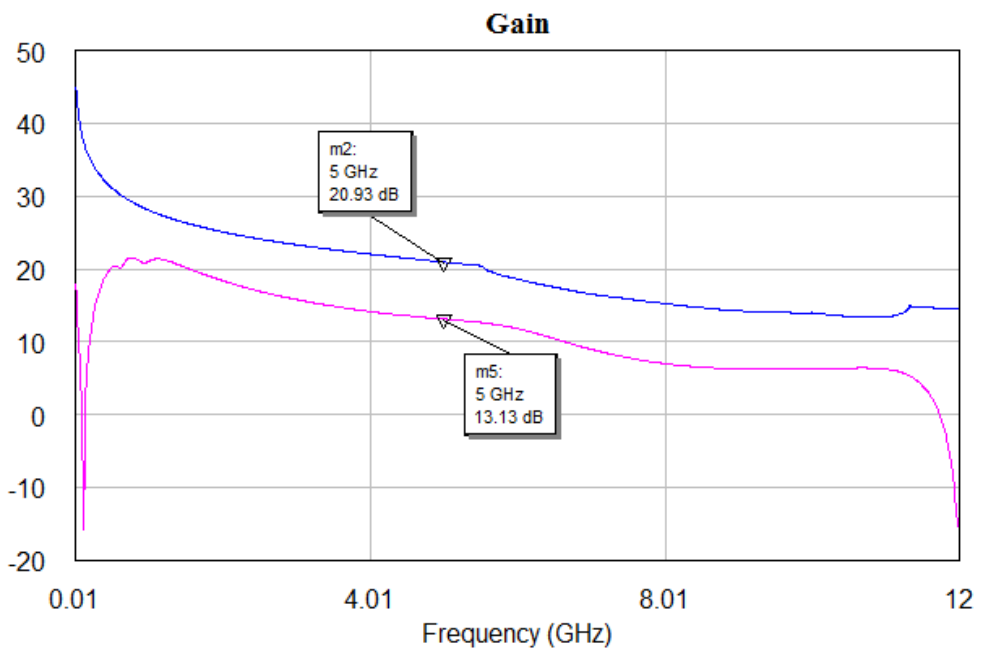
Figure 7.4.7: Maximum gain in dB of the LNA core: in blue BFP720 G_{ma}, in pink LNA core G_{ma}.
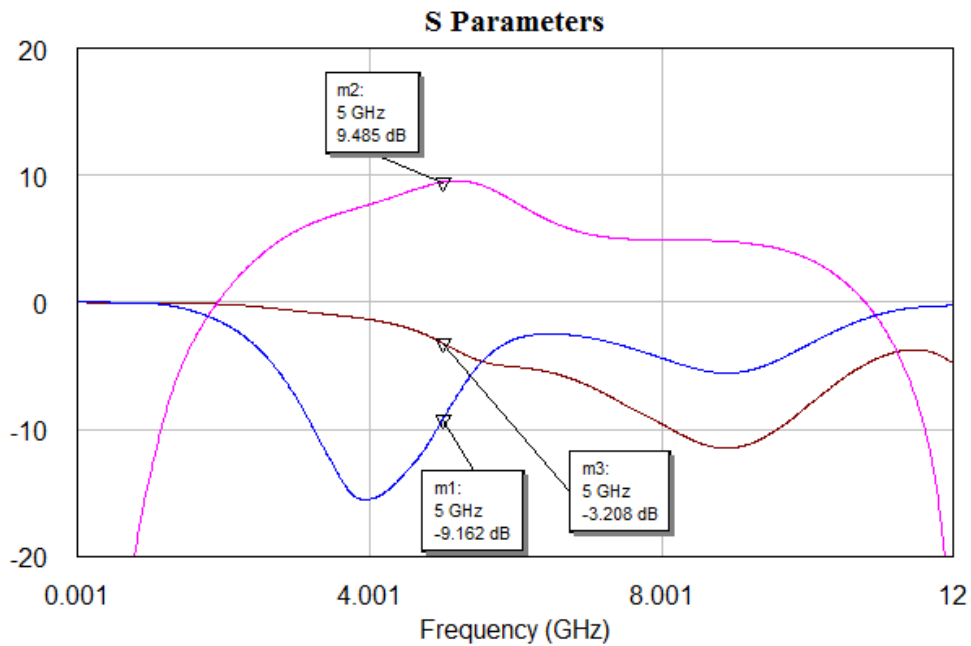
Figure 7.4.8: LNA's core S parameters: s_{11} [dB] (blue), s_{21} [dB] (pink), and s_{22} [dB] (brown).

Label	Value	Description	Part Number	Producer
L_1	5,6 nH	0402″ SMD Inductor	LQG15HN5N6S02	muRata
L_2	4,3 nH	0402″ SMD Inductor	LQG15HN4N3S02	muRata

Table 7.4: List of the inductors [9] used for the input and output matching networks of the 5 GHz LNA.

network must have inductive characteristics.

Fig. 7.4.10 shows the layouts of the input and output matching networks for the LNA obtained with the same optimization method used for the core. Since the optimization was done for a 600 MHz band, it was necessary to add two matching cells in the output network. As it is possible to see from the layouts, open stubs have been used to replace the capacitances towards ground, while the stubs closed towards ground replace inductances towards ground. Table 7.4 shows the characteristics of the inductors used in the matching networks.

Fig. 7.4.11 shows the effects introduced by the matching networks on the final circuit, the layout of which is shown in Fig. 7.4.12.
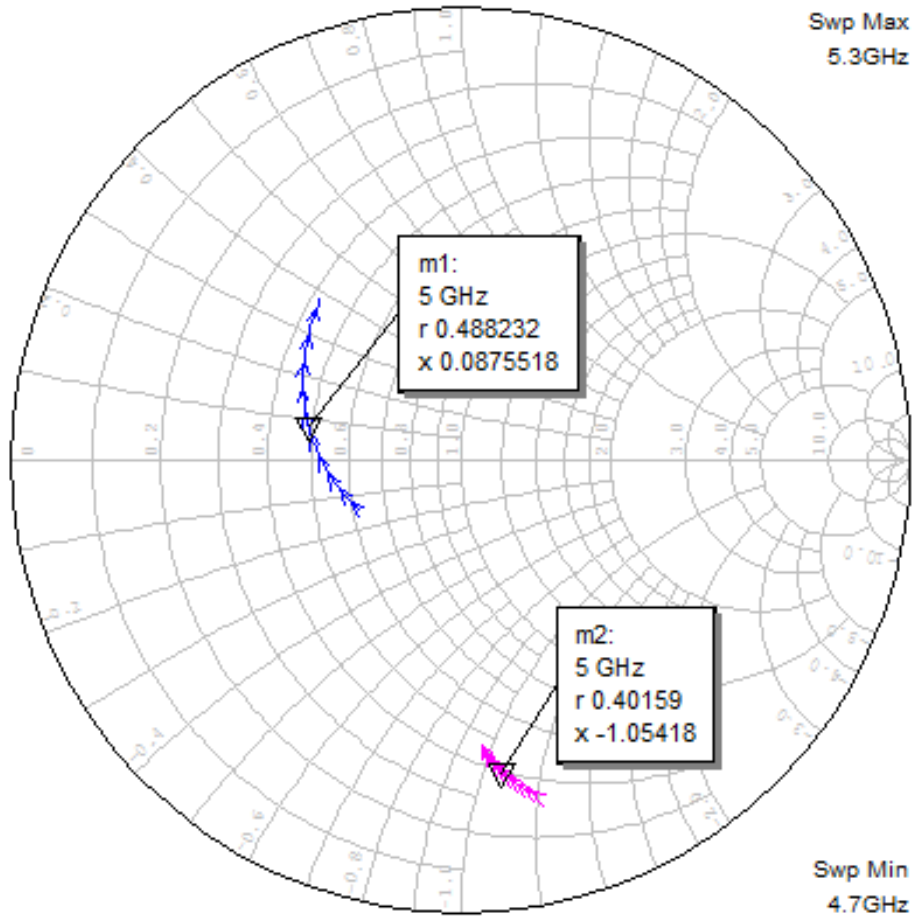
Figure 7.4.9: LNA core input (blue) and output (pink) impedance.
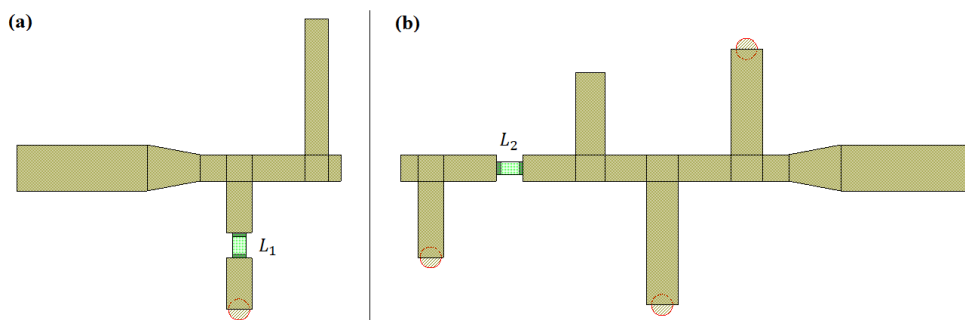
Figure 7.4.10: Final designs of input (a) and output (b) matching networks.
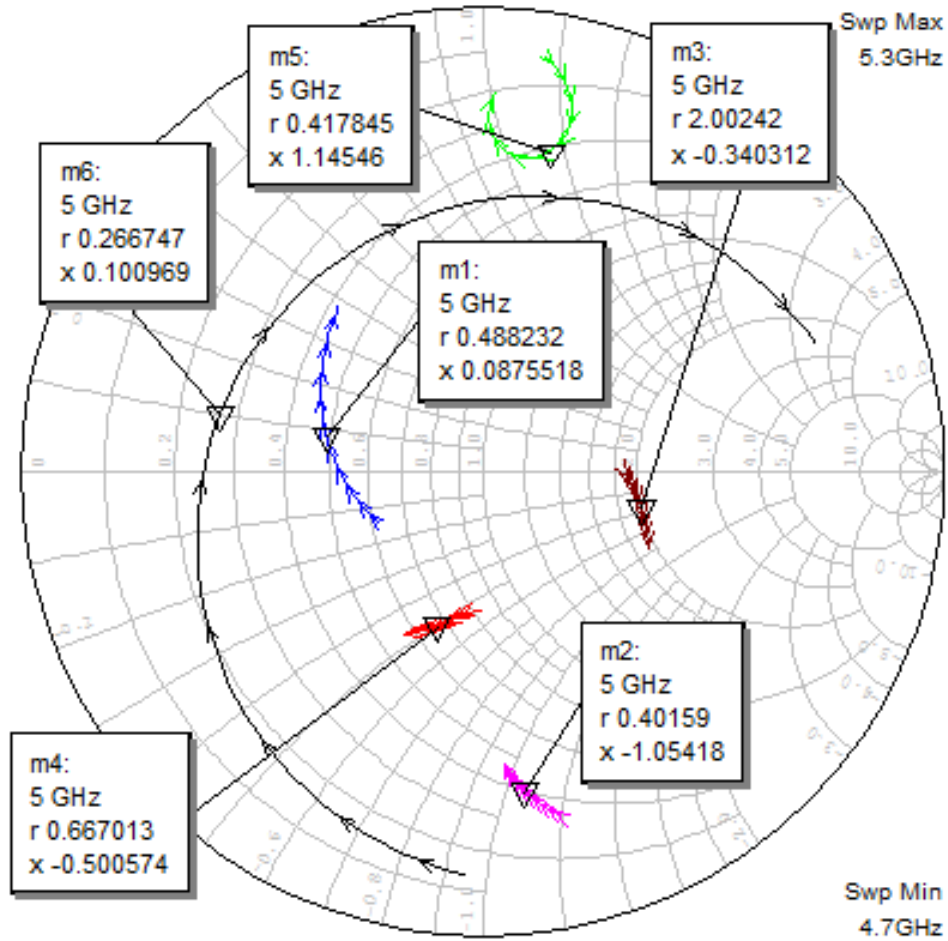
Figure 7.4.11: LNA core input (blue) and output (pink) impedance. Capacitive output impedance (red) of the input matching network and inductive input impedance (green) of the output matching network. LNA with matching network input (brown) and output (black) impedance. Observation band: 4.7 GHz - 5.3 GHz.
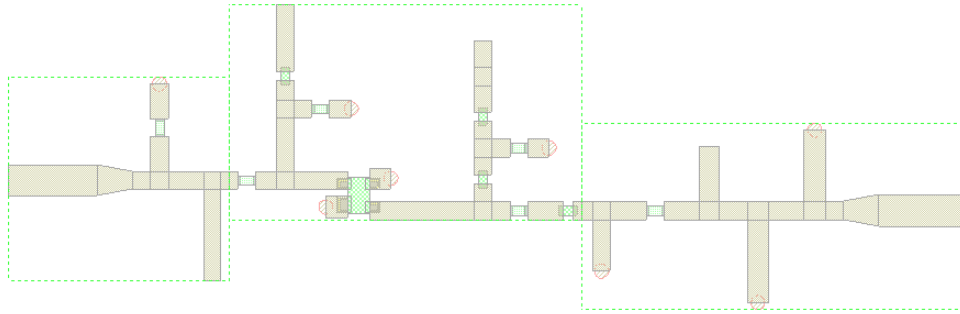
Figure 7.4.12: 5 GHz LNA with matching network layout.

The final size of the LNA is $56 \times 19 \times 0.81$ mm^3. The inclusion of the matching networks in the circuit has greatly improved stability, allowing the k factor to be much higher than 1 in the 0 GHz - 12 GHz band. NF_{min} also stands at acceptable values around 1 dB, while $G_{ma} = 12.58$ dB at 5 GHz. The results obtained from the final circuit of the LNA are shown in Fig. 7.4.13 - Fig. 7.4.16, where the results provided by the electromagnetic simulations of the circuit carried out thanks to the AXIEM simulator [10]. AXIEM allows to make a planar 3-D electromagnetic analysis of the circuit through the Method of Moments (MoM) and its use is necessary as it allows to take into account electromagnetic phenomena that the AWR simulator cannot consider (for example coupling between lines neighbors, etc.), and should give a more precise indication of what should then be the reality found in the measurement phase.

For completeness, the input and output stability circles of the LNA core and of the LNA with matching networks simulated in AWR and AXIEM are also reported. From the graphs it can be seen how the use of the matching networks has favored the extension of the stability region, especially at the output port, passing from the area contained in the blue circle (LNA core), to the area present outside the pink and brown circles (LNA with matching networks). In fact, in AWR if the dashed circle is contained within the continuous one, the stable region is that which is outside the continuous circle (stability factor = 1), while if the continuous circle is contained within the dashed one, the stable region is the one that is inside the circle with a continuous line (stability factor = -1).

7.4.3 LNA nonlinear analysis

In this phase we describe the non-linear analysis carried out thanks to the harmonic balance and the nonlinear model of the BFP720 transistor. In par-
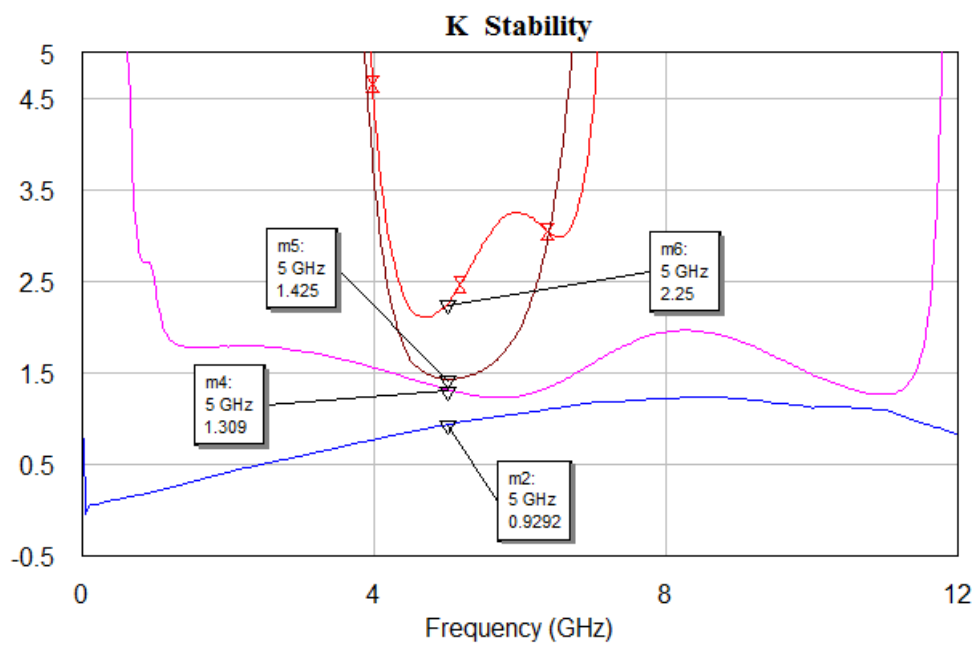
Figure 7.4.13: Stability factor of the LNA core: BFP720 Rollet Factor (blue), LNA core Rollet Factor (pink), LNA with matching networks Rollet factor (brown), LNA with matching network Rollet factor - AXIEM (red).
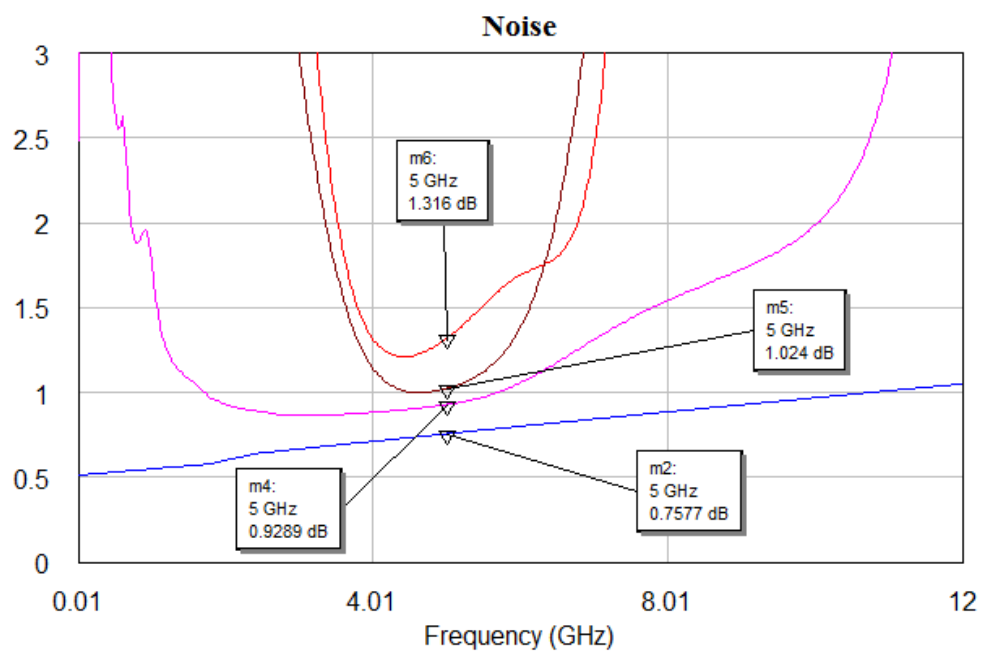
Figure 7.4.14: Minimum noise figure in dB of the LNA core: BFP720 NF_{min} (blue), LNA core NF_{min} (pink), LNA with matching network NF_{min} (brown), LNA with matching network - AXIEM NF_{min} (red).
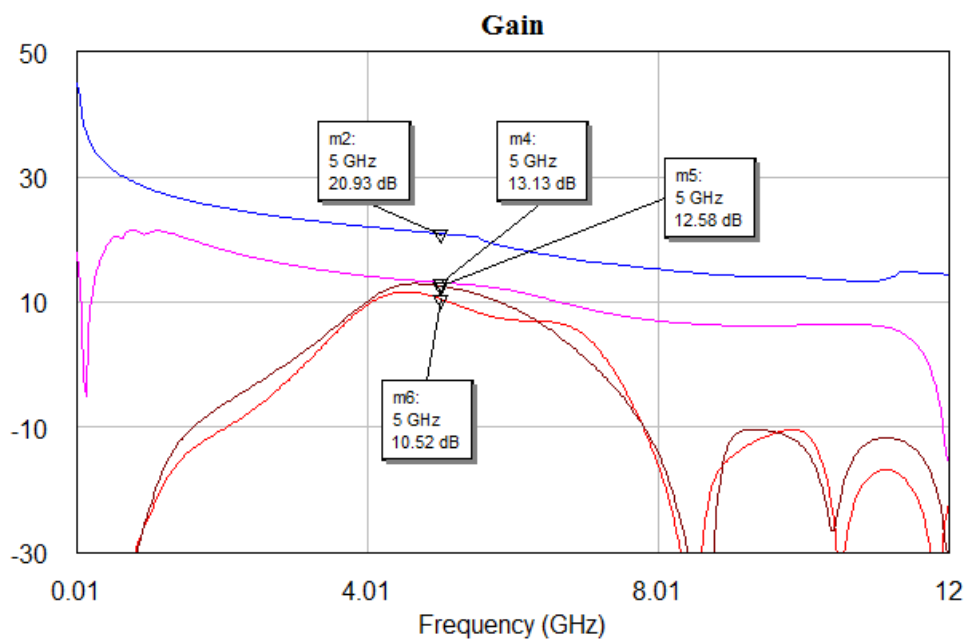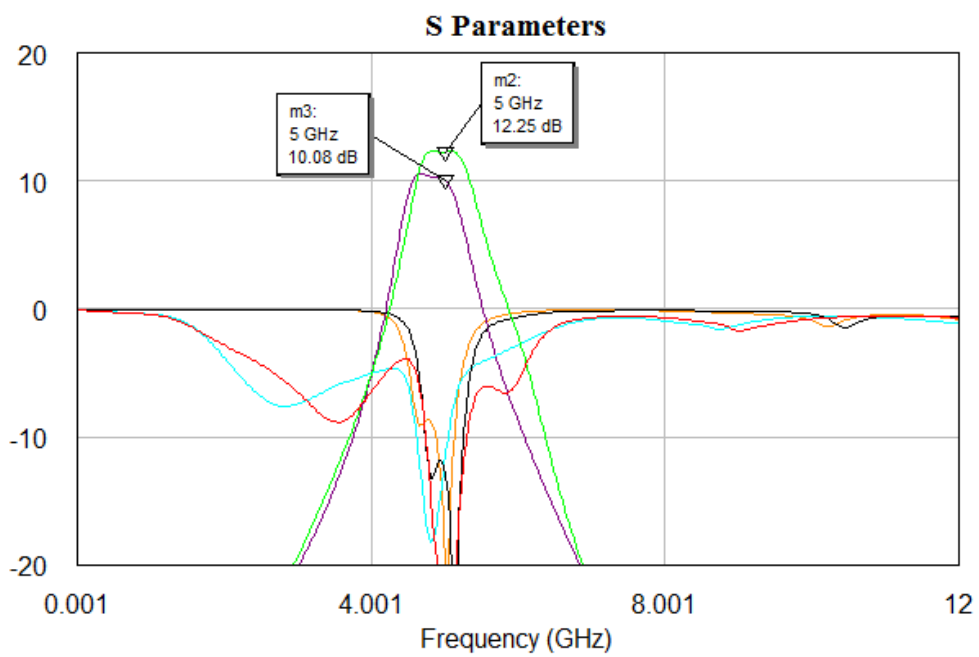
Figure 7.4.15: Maximum gain in dB of the LNA core: BFP720 G_{ma} (blue), LNA core G_{ma} (pink), LNA with matching networks G_{ma} (brown), LNA with matching networks - AXIEM G_{ma} (red).

Figure 7.4.16: LNA with matching network S parameters (s_{11} = red, s_{21} = green, and s_{22} = black), LNA with matching network - AXIEM S parameters (s_{11} = cian, s_{21} = violet, and s_{22} = orange).
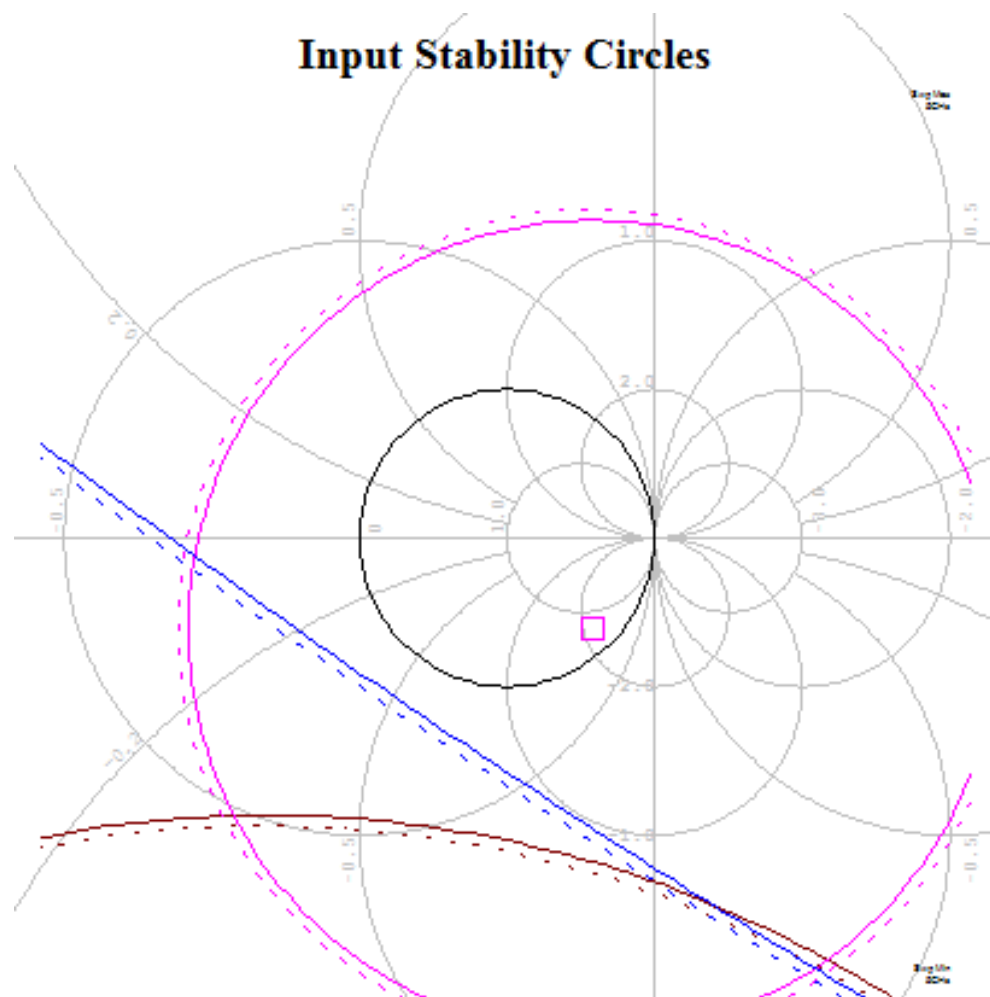
Figure 7.4.17: Input Stability Circles: LNA core (blue), LNA with matching networks (pink), LNA with matching networks - AXIEM (brown).
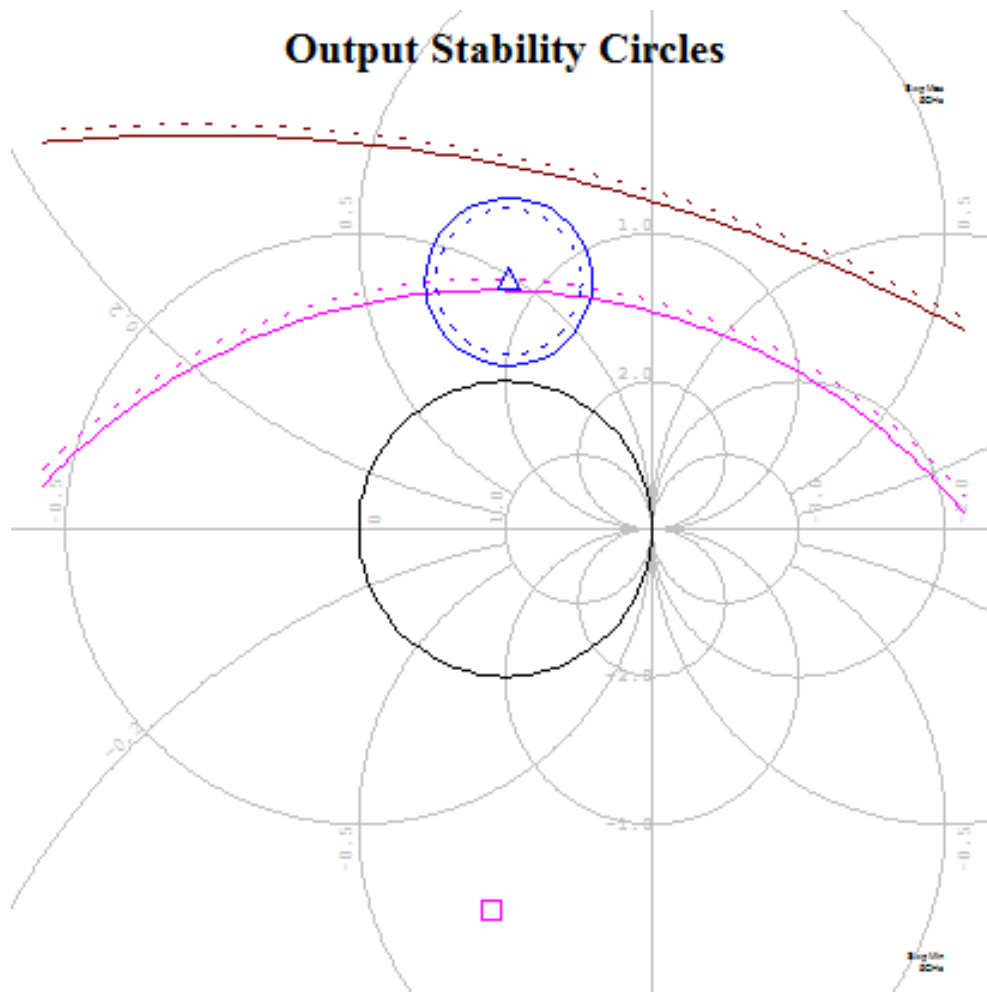
Figure 7.4.18: Output Stability Circles: LNA core (blue), LNA with matching networks (pink), LNA with matching networks - AXIEM (brown).
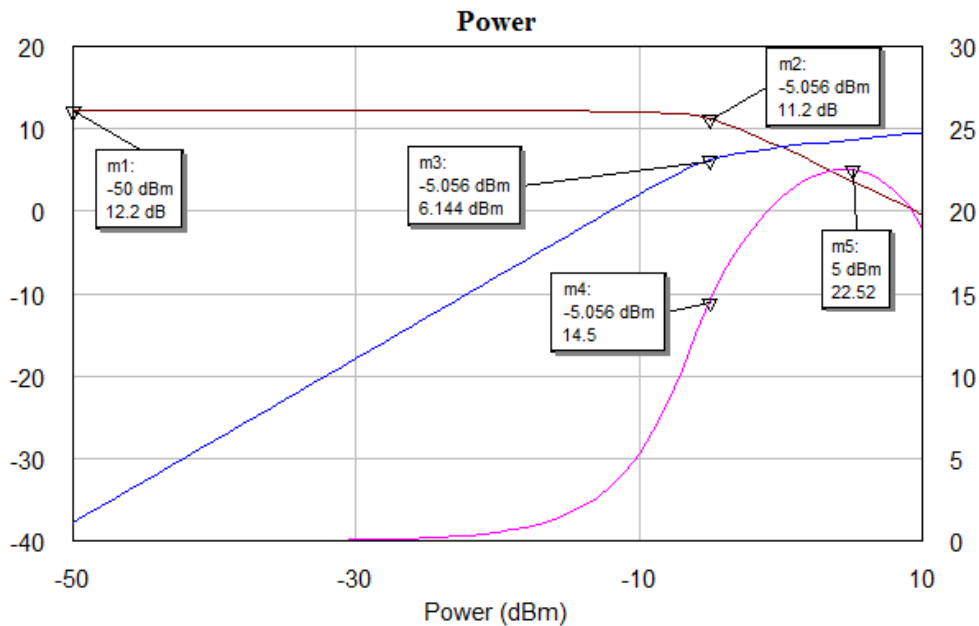
Figure 7.4.19: LNA's nonolinear characteristics: P_o/P_i (blue), efficiency (pink), power gain (brown).

ticular we want to see the typical characteristics of the amplifier, such as the compression point at 1 dB, the efficiency and the ratio between output power and input power (P_o/P_i). Fig. 7.4.19 shows the quantities just mentioned when the amplifier works at 5 GHz. The compression point at 1 dB is for an input power equal to -5.056 dBm. Such low values are admissible as we are analyzing an LNA that usually receives signals with very low power levels in input. At the 1 dB compression point, there is an efficiency of 14.5%, even if its maximum efficiency is equal to 22.5%, where however the gain, in that region, has a sharp drop.

7.4.4 Switching capability

The switching capability is implemented by applying an ON/OFF voltage to the collector, which turns the transistor ON and OFF as needed and based on the context in which the LNA is used. Through the nonlinear analysis it was possible to verify this type of operation by applying a 5 GHz signal with power equal to -10 dBm to the LNA input, and on the collector an alternating voltage with 0 V - 3 V amplitude, 50 MHz period and duty cycle at 50%. The effect of the action of the alternating voltage on the collector has made it possible to obtain the same ON/OFF effect at the output of the
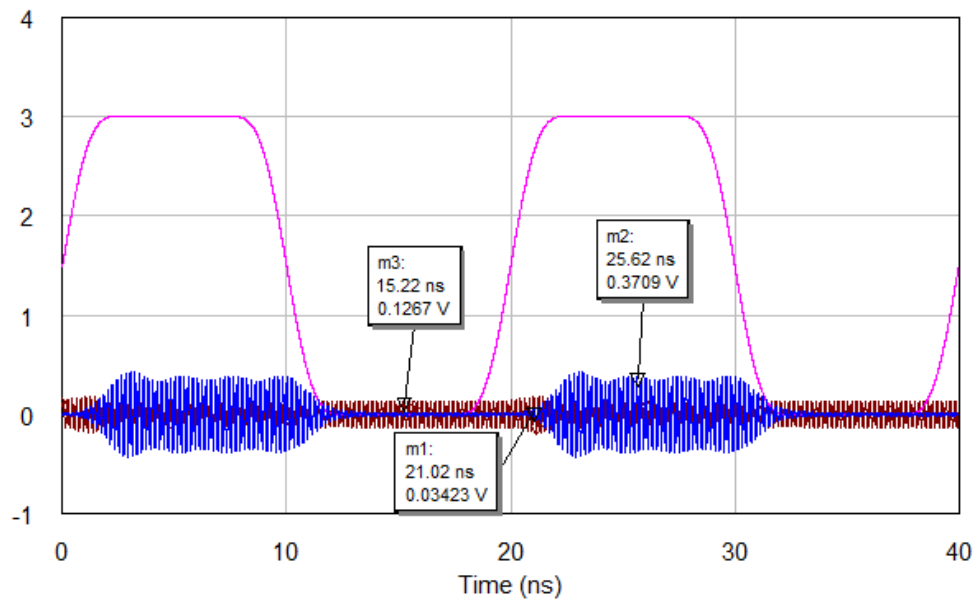
Figure 7.4.20: Switching effect on the LNA output signal: 50MHz driving collector voltage (pink), LNA input signal (brown), LNA output signal (blue).

LNA, as can be seen in Fig. 7.4.20.

The passive component that greatly affects the switching ability and above all the duration and shape of the LNA output signal is the cooling capacitor placed on the collector branch (C_3 in Fig. 7.4.4). In fact, the capacitor combined with the bias resistors R_2 and R_3, and the collector/emitter capacitance of the BFP720 transistor provide, in addition to the stability of the LNA, a very good low pass characteristic. To understand what happened if the value of the capacitor C_3 was changed, the equivalent wiring diagram of the collector branch was implemented in the MULTISIM environment [11], shown in Fig. 7.4.21. As can be seen from the green trend shown on the oscilloscope, if a 0.2 pF cooling capacitor were used (as obtained from the optimization in AWR), there is no distorting effect due to the low pass filtering action of the collector branch. On the other hand, if a capacitor with a larger capacitance, for example 0.2 nF (200 pF), was inserted, the effect of the capacitor would be greater, as it would be of far greater value than the collector/emitter capacitance. Fig. 7.4.22 shows the output of the simulated circuit in MULTISIM, and the result obtained by simulating the switching ability of the LNA implemented in AWR with $C_3 = 0.2$ nF. As it is possible to see, a too large capacitance can lead not only to an attenuation of the output signal (compared to the case $C_3 = 0.2$ pF), but also to an asynchronism

226

between the 50 MHz driving signal and the output signal of the LNA.

7.4.5 Measurement results

The prototype of the LNA circuit was made using a CNC milling machine. A picture of the realized circuit is shown in Fig. 7.4.23. The measurements of the transmission, and input and output reflection coefficients have been performed with Anritsu MS46122B vector network analyzer. Measurement results are reported in Fig. 7.4.24.

As it possible to see, the electromagnetic simulation performed with AX-IEM turned out to be much more reliable than the simulation in AWR which, all in all, does not differ greatly from the results obtained in measurement. The transmission coefficient in fact, has a peak at 5 GHz of 11 dB, while it has values higher than 10 dB in the band ranging from 4.53 GHz to 5.14 GHz. In input, the LNA has a good impedance matching in the 4.5 GHz - 5.1 GHz band (-10 dB is taken as a reference), while at the output there is a very reduced impedance matching compared to that obtained by the two different types of simulation, in the 4.98 GHz - 5.103 GHz band. This mismatch, and in general the differences respect to the simulation in AXIEM may be due to the welds applied manually to fix all the components of the circuit and to fix all the via holes.

From the S parameters through (7.2.4), (7.2.5), and (7.2.7) it was possible to have a comparison also between simulated and measured Rollet factors, and between simulated and measured gains (Fig. 7.4.25).

Rollet factor k is much greater than 1 over the entire useful band. The gain also shows a very similar trend to what was obtained in the two different simulations, and at 5 GHz its value is equal to 11.84 dB.

In order to provide the LNA's switching capability, it was decided to integrate it with a control unit. Fig. 7.4.26 shows the conceptual scheme of the switching LNA. The integrative part relating to the collector voltage control is composed of a clock generator and an operational amplifier in a buffer configuration (with unity gain) used to supply the LNA with the correct current value necessary to its operation ($I_c = 10$ mA in ON state).

To generate the control voltage we used the Si5351A component which is an I^{2}C programmable CMOS clock generator from Silicon Labs [12]. The pinout of the device is shown in Fig. 7.4.27.

As shown in Fig. 7.4.26, between the clock generator and the LNA an amplifier has been placed in a unit gain buffer configuration. The aim of this device was to introduce an impedance reduction such as to provide the necessary 10 mA on the collector. The operational amplifier (op-amp) chosen for this purpose is the THS3491 from Texas Instruments [13]. Its pinout is
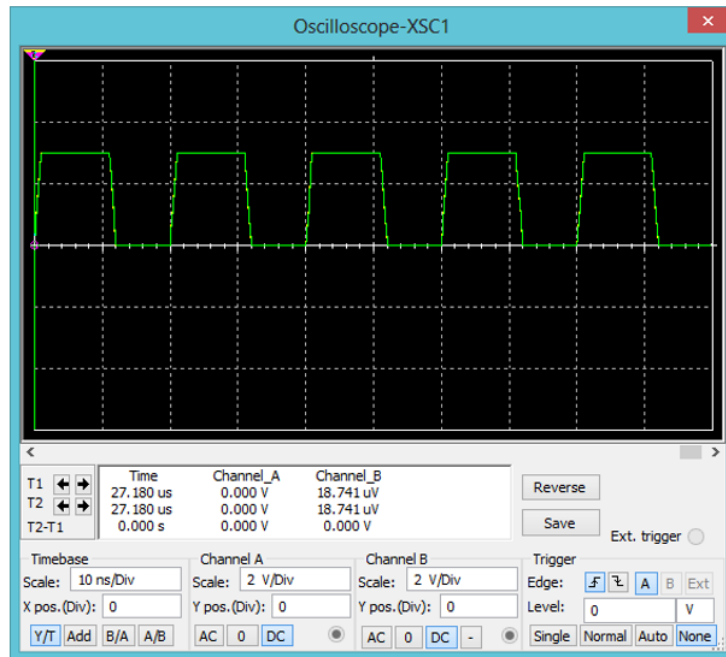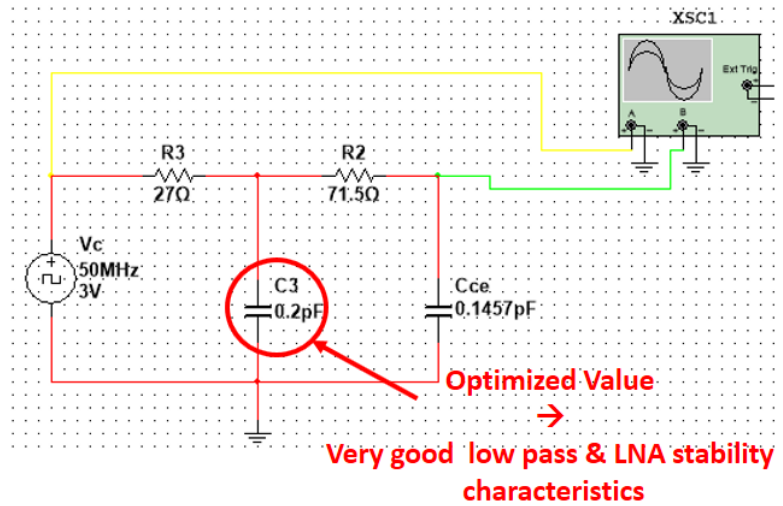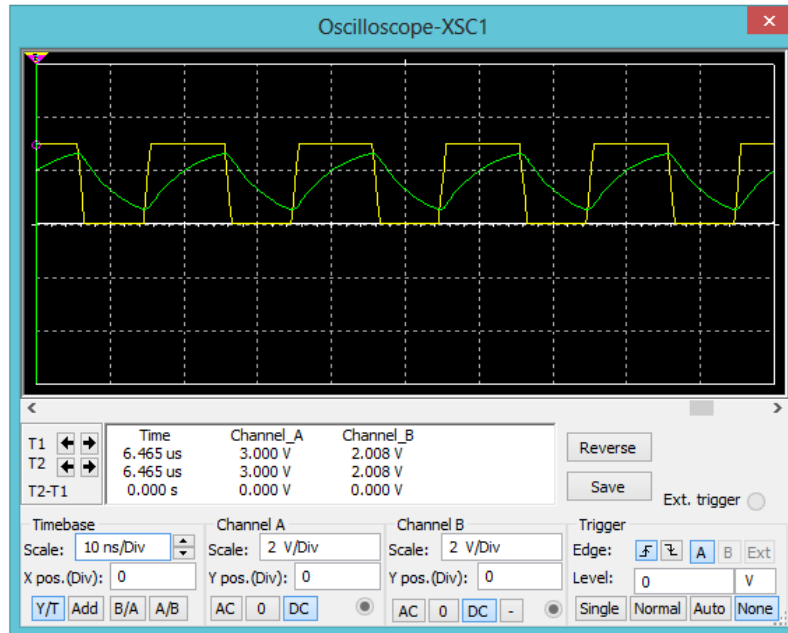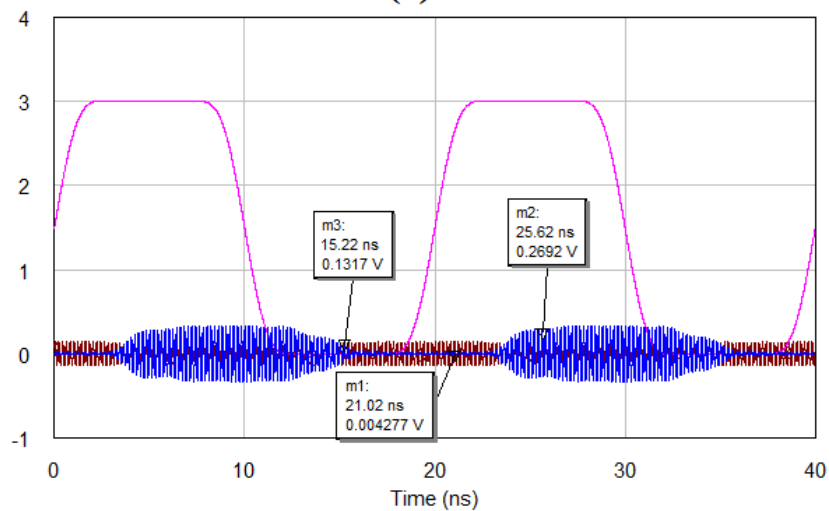
Figure 7.4.21: Collector branch analysis with C_3 optimum value.

(a)

(b)

Figure 7.4.22: Collector branch analysis: (a) Capacitor effect on the collector pin of BFP720 (green), (b) switchable capability of the LNA with $C_3 = 0.2$ nF.
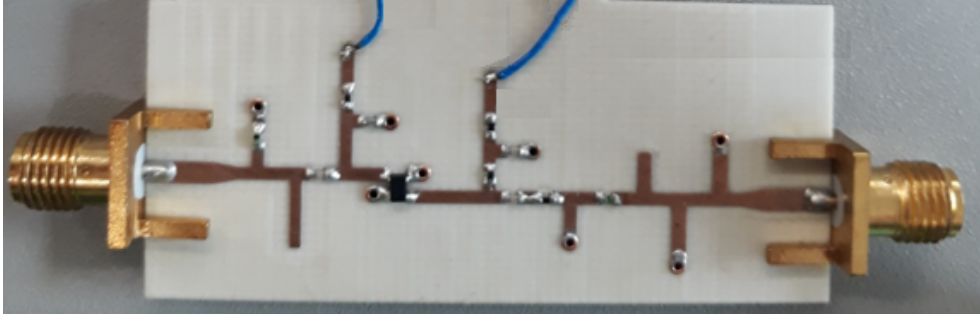
Figure 7.4.23: Realized 5 GHz Low Noise Amplifier on Rogers RO4003C substrate.
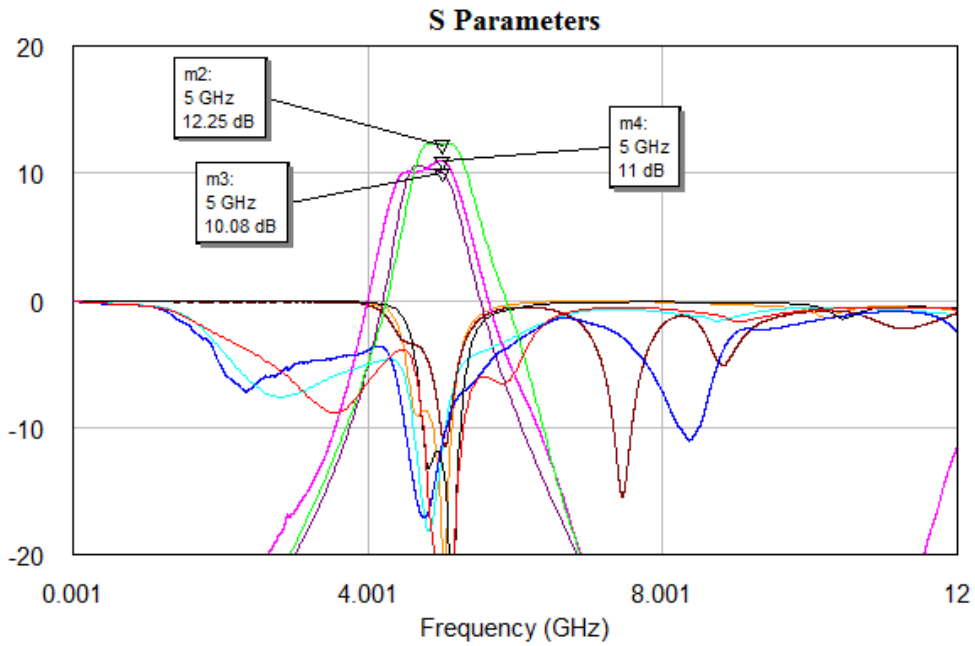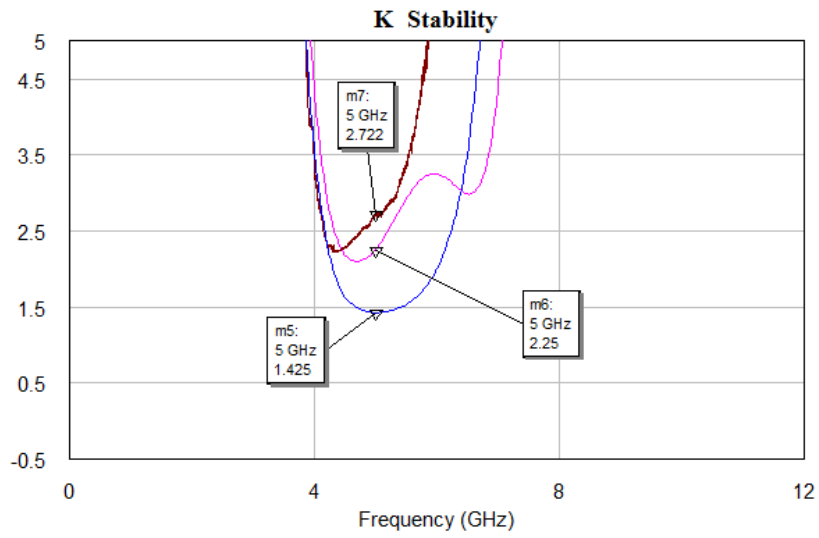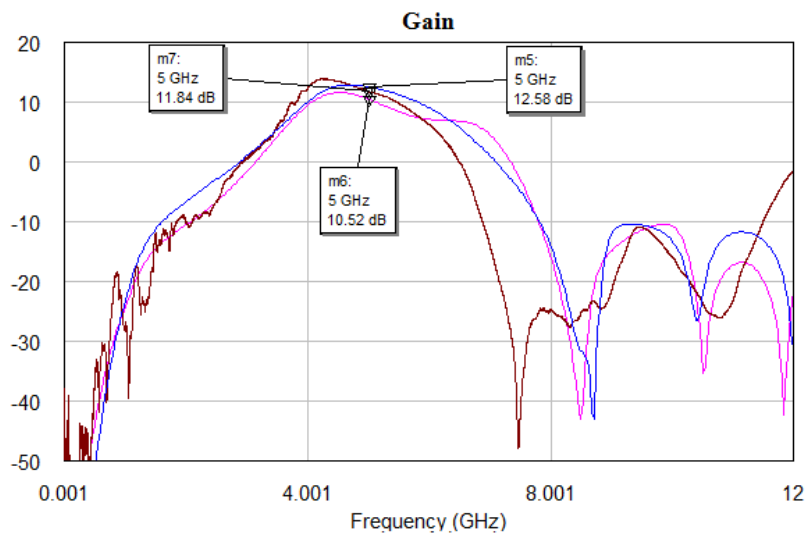

Figure 7.4.24: LNA's S parameters AWR simulation (s_{11} = red, s_{21} = green, s_{22} = black), LNA's S parameters AXIEM simulation (s_{11} = cian, s_{21} = violet, s_{22} = orange), LNA's S parameters measurement (s_{11} = blue, s_{21} = pink, s_{22} = brown).

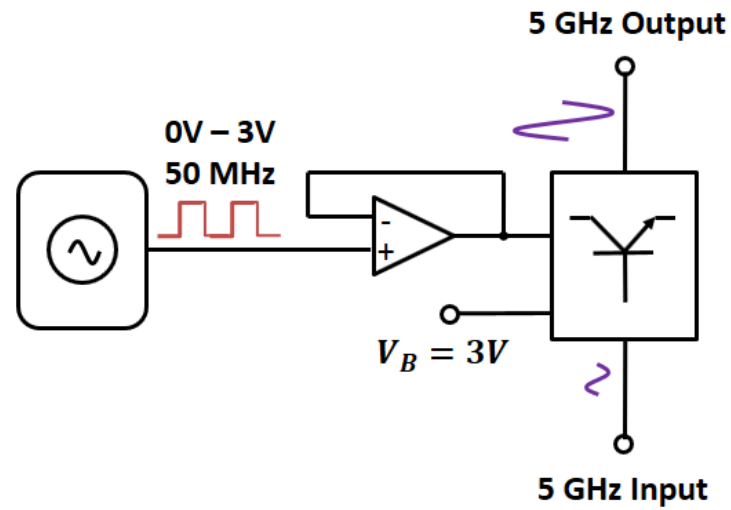Figure 7.4.25: Measured Rollet factor (a), and measured Gain (b).

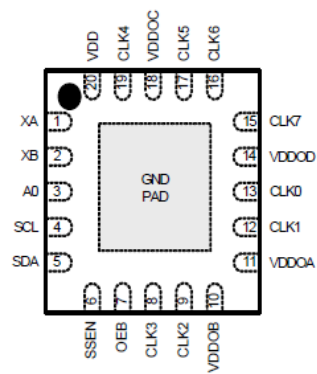Figure 7.4.26: Switchable LNA chain.

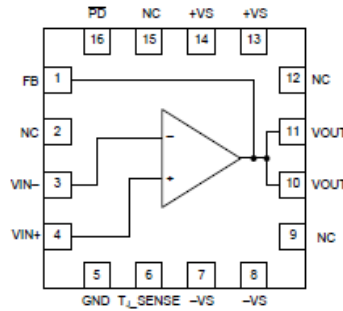Figure 7.4.27: Si5351A 20-QFN package pinout top view.

Figure 7.4.28: THS3491 16-QFN package pinout top view.

Label	Value	Description	Part Number	Producer
C_1, C_2	0,1 pF	0402'' SMD Capacitor	GJM1555C1H1R0BB01	muRata
R_1, R_2	1 kΩ	0402'' SMD Resistor	-------------	generic
$XTAL$	--------	Crystal 27.0000 MHz 10 pF	7M-27.000MEEQ-T	TXC Corporation
$CLKG$	--------	IC CLK Generator 200 MHz	Si5351A-B-GM	Silicon Labs
OA	--------	IC OPAMP	THS3491IRGTR	Texas Instruments

Table 7.5: List of components related to the control circuit.

shown in Fig. 7.4.28. This device was chose for its excellent performances in terms of operating bandwidth (900 MHz) and slew rate (800 V/μs), so as not to have distortions of the control voltage sent by the clock generator on its output.

The final layout of the switchable LNA is shown in Fig. 7.4.29. The list of components used for the control part of the switchable LNA is reported in Table 7.5.

As can be seen, in the circuit all those components necessary for the functioning of the clock generator (capacitors, crystal, etc.) have been inserted. As regards the op-amp, in addition to having inserted two cooling capacitors on the power supply branches (13.6 μF), a 2.7 kOhm resistor has been inserted between the feedback pin (pin 1 in Fig. 7.4.28) and the inverting pin of the amplifier (pin 3 in Fig. 7.4.28). This operation led to solving the stability problems encountered in the case of feedback made with the direct connection of pin 1 and pin 3 of the op-amp. Fig. 7.4.30 shows the final circuit of the 5 GHz switchable LNA made on Rogers RO4003C substrate. The
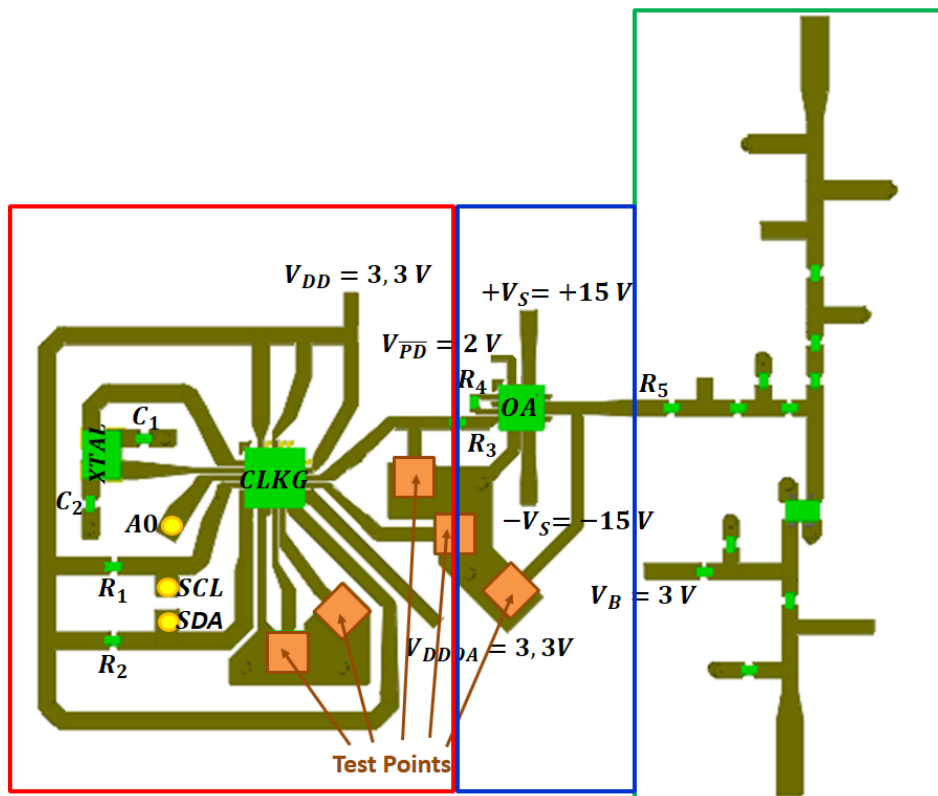
Figure 7.4.29: Switchable LNA final layout: clock generator circuitry (red), buffer amplifier (blue), and 5 GHz low noise amplifier (green).
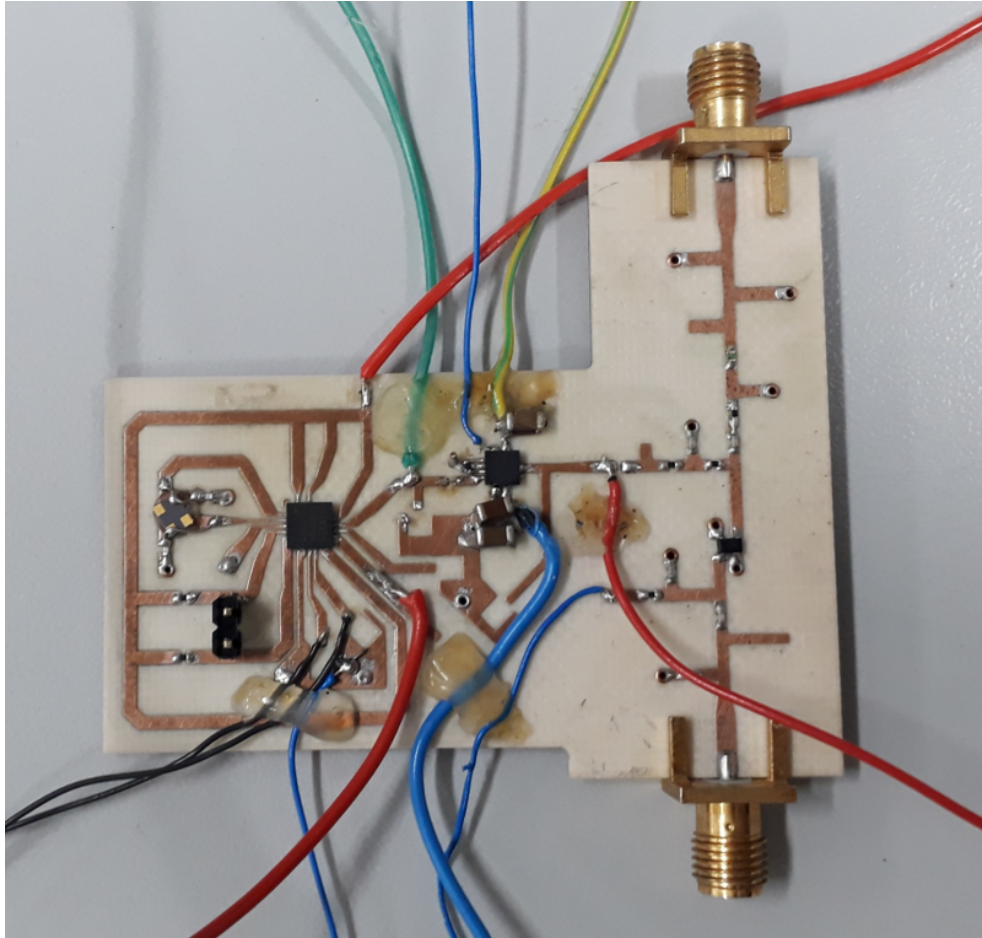
Figure 7.4.30: Realized 5 GHz switchable low noise amplifier.

clock generator programming was performed on the **SCL** and **SDA** ports, through I²C programming, thanks to the help of the ATmega328P microcontroller of an Arduino UNO Rev3 board [14]; pin **A0**, on the other hand, was connected to the ground.

The switching capability was tested by sending a 5 GHz sinusoidal signal with -10 dBm power input via a signal generator. The output of the amplifier was connected to a LeCroy WaveMaster 8600A oscilloscope in order to view the trend of the output signal. Fig. 7.4.31 shows the switching control signal (yellow) and the LNA output signal (pink), which reflect the simulated trends reported in Fig. 7.4.20.
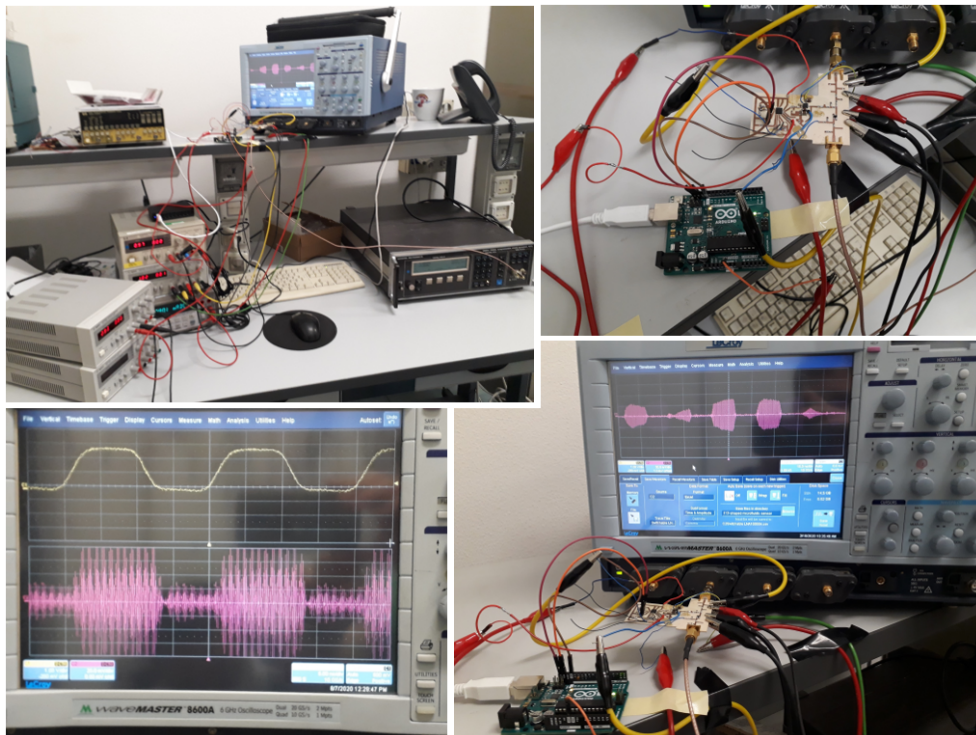
Figure 7.4.31: Measurement of the switchable capability of the 5 GHz switchable low noise amplifier.
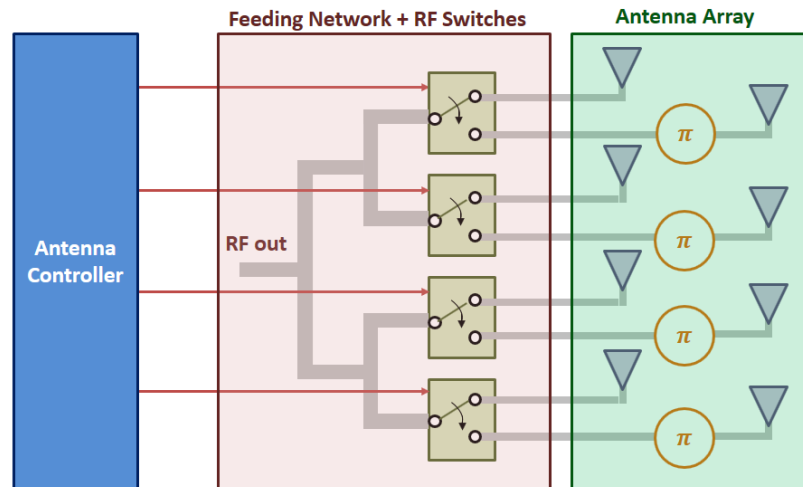
Figure 7.5.1: Classical schematic of a time-modulated receiver.

7.5 Application

Thanks to its particular ability, the switchable LNA can be used in an intelligent receiving system like the one shown in Fig. 7.5.1.

The system was proposed in [15]-[16], which defines the potential of the time-modulated antenna array (TMAA) receiving system that can be used in wireless broadband system. The authors have set the goal of implementing a controllable system with which to obtain a bandwidth of the used channels above 50 MHz, using ultrafast microwave switches, digital delay lines with a defined number of steps, and fast control circuitry. The proposed switchable LNA would replace the microwave switches, as it can be controlled by the same control circuitry.

The idea of introducing the switchable LNA in this receiving system is leading to collaboration with the authors of the articles concerning the TMAA and a joint work should be published shortly.

7.6 Conclusions

In this chapter a new functionality method for microwave low noise amplifiers was described. In order to improve the performances of the receiving equipment in terms of noise figure, it was decided to apply a driven voltage to the LNA that was able to switch it ON and OFF on command in order to isolate the receiving part of the system from the transmitting one. This technique, in fact, would make it possible to eliminate devices such as
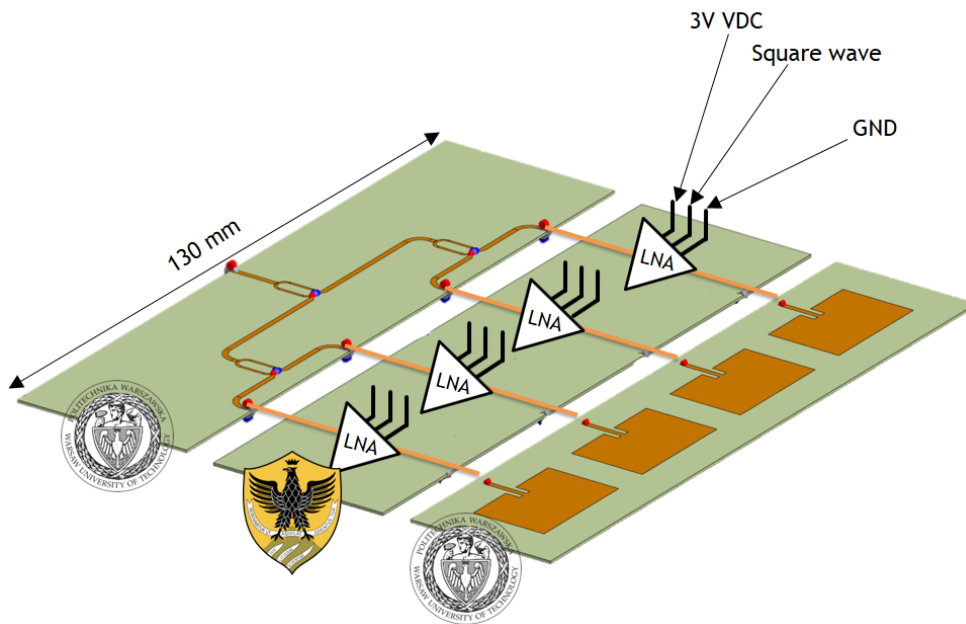
Figure 7.5.2: New time-modulated antenna array design concept.

microwave switches and circulators that introduce background noise, thus improving performance also from the point of view of the overall dimensions of the entire system. An LNA with this capability could also be used in phased array receiving systems: it would in fact be possible to drive some of the branches making up the multi-antenna structure in order to obtain particular beam-forming. Given the operational frequency chosen, the LNA could be used in applications and systems that use the second Wi-Fi carrier (Wi-Fi5).

Bibliography

[1]   G. D. Vendelin, A. M. Pavio, and U. L. Rohde. *Microwave Circuit Design Using Linear and Nonlinear Techniques*, Second Edition, John Wiley & Sons, Inc., Jan. 2005.

[2]   S. D'Agostino, S. Pisa, and P. Marietti. *Sistemi elettronici per le microonde*, CEA, Elettronica applicata, Jan. 1996.

[3]   E. O. Johnson. RCA rev., Vol. 26, 6, 167-177, 1995.

[4]   infineon.com/cms/en/product/rf-wireless-control/rf-transistor/ultra-low-noise-sigec-transistors-for-use-up-to-12-ghz/bfp720/

[5]   awr.com/awr-software/products/microwave-office

[6]   rogerscorp.com/-/media/project/rogerscorp/documents/advanced-connectivity-solutions/english/data-sheets/ro4000-laminates-ro4003c-and-ro4350bdasta-sheet.pdf

[7]   murata.com/en-eu/products/capacitor/mlcc/smd/gjm

[8]   murata.com/en-eu/products/capacitor/mlcc/smd/grm

[9]   murata.com/en-eu/products/inductor/chip/rf2

[10]   awr.com/awr-software/products/axiem

[11]   ni.com/it-it/support/downloads/software-products/download.multisim.html#312060

[12]   silabs.com/documents/public/data-sheets/Si5351-B.pdf

[13]   ti.com/lit/ds/symlink/ths3491.pdf

[14]   store.arduino.cc/arduino-uno-rev3

[15]   G. Bogdan, K. Godziszewski, Y. Yashchyshyn, C. H. Kim, and S. -B. Hyun. *Time-Modulated Antenna Array for Real-Time Adaptation in Wideband Wireless Systems - Part I: Design and Characterization*, IEEE Transactions on Antennas and Propagation, Vol. 68, No. 10, pp. 6964-6972, Oct. 2020.

[16]   G. Bogdan, K. Godziszewski, and Y. Yashchyshyn. *Time-Modulated Antenna Array for Real-Time Adaptation in Wideband Wireless Systems - Part II: Adaptation Study*, IEEE Transactions on Antennas and Propagation, Vol. 68, No. 10, pp. 6973-6981, Oct. 2020.

Capitolo 8

General Conclusions

In order to satisfy the initial objectives, the research activities have spanned many of the fronts concerning aspects related to wireless sensor networks and the IoT. The research was focused on the development of mathematical and electromagnetic models which allowed to obtain interesting and innovative results. From these models it has been possible to design and build extremely functional devices that can be used in various and different contexts of short-range networks. In particular two types of UWB wearable all-textile antenna able to be reconfigured between a monopole and a microstrip-like antenna have been proposed and discussed. These devices are based on a circular radiating disk that works as a monopole when placed orthogonal to a ground plane and as a microstrip patch when it is lying parallel to two different types of matching surfaces: a modified ground plane in the first antenna, and FSS in the second. Thanks to these innovative techniques, numerical analysis shows that both topologies have satisfactory UWB characteristic with bandwidth compliant with FCC regulation and a fair system fidelity factor that allows the antenna as air interface for wearable sensors and short range communication devices. To improve the performance from the point of view of measurements, the use of more accurate tools, like cutting plotter, could be a very good solution for the realization of the conductive parts of the antenna made on conductive fabrics. The antenna connectorization phase remains critical, as tin soldering on conductive fabrics, or the use of conductive glues, often do not provide optimal performance.

Given the good results obtained in the design of wearable devices, the research work also involved the field of passive microwave sensors. The choice of designing completely passive devices is combined with the philosophy of strong pervasiveness, low energy consumption and low production costs, typical of the concept of the Internet of Things. A sensor operating in the microwave frequency band, which exploits the principle of harmonic RADAR

thanks to the detector properties of a zero bias Schottky diode has been designed. From the theory of transmission lines, the design phase of the device involved the study and application of a completely passive network which had the purpose of balancing the capacitive reactance of the diode, in order to obtain an impedance match with 50 Ohms. The sensor was made and applied to an enlarged version of the metamaterial-based wearable UWB antenna, in order to be used in a detection scenario based on the harmonic RADAR. From the measurements carried out in the laboratory, it was clear the sensor's ability to provide a second harmonic response to the transceiver system that interrogates it, even for low power values of the continuous wave interrogating signal (-10 dBm). The goodness of the results obtained from the measures, comparable with those that were the data estimated in the design phase, suggests that the system may be suitable for use in emergency situations where it is necessary to try to identify and save people in post-disaster scenarios.

The challenge related to the choice of low environmental impact materials usable in microwave design has also been accepted and successfully overcome. In fact a new way of measuring dielectric materials having dielectric constants between 1 and 10, and thicknesses between 0 mm and 5 mm has been described. A strenght of this measurement technique lies in the fact that it has a real instrument that allows to not to "waste" every time a piece of sample on which it would have been necessary to make the measurer in order to identify its dielectric properties. Three pairs of algorithms were presented in order to derive the relative dielectric constant and loss tangent values. Several simulations tests were carried out and then the measurement phase. As it is possible to see from various results tables, the combination of the *electromagnetic map extraction method* and the *Svačina and Schneider mixed method* manages to return values of relative dielectric constant and loss tangent close to what they should be. The *conformal mapping method*, combined with *Schneider's method*, and the *updated variational method* also manage to give an idea of what the real relative permittivity and loss tangent values could be. The *upgrated variational method*, however, even if it returns values slightly closer to *electromagnetic map extraction method* for intermediate permittivities ($\varepsilon_r = 3 \div 5$), can provide dielectric constant values too low and close to 1 in cases where a low relative dielectric constant material is being measured ($\varepsilon_r = 1.2 \div 1.6$). The processing times are also very high compared to all other methods, which makes it "inconvenient" for carrying out preliminary analyzes. To reduce the analysis times it may be better to use the *conformal mapping method* (in the case of relative dielectric constant values $\leqslant 5$), and then move on to the use of the *electromagnetic map extraction method*. As regards the extrapolation of the loss tangent

value, the *Svačina and Schneider mixed method* is the one that among the analyzed methods, is closest to the real values. Thanks these studies it has been possible to use materials such as felt, denim, polylactic acid (PLA), and cardboard in the design of microwave antennas and sensors.

Remaining in the context of the characterization of dielectrics it was decided to design a microfluidic sensor based on microstrip T-resonator. The sensor has been realized using a 3D printing technique, it has a compact and thin structure allowing a useful channel of about 12 μl. Numerical and experimental results show a very large variation of the resonant frequency passing from low permittivity low loss liquids to water based liquids. Given the goodness of the results obtained, we wanted to use the sensor to identify the percentages of a known solute dissolved in an acqueous solution. Considering the poor resistance properties of PLA to the presence of water and humidity, it was decided to create a new low-cost sensor in cardboard, with a microfluidic channel made with a small tube used in chemical laboratories. Through the results obtained during the simulation phase, then confirmed by the measurements, the ability of the instrument to be able to detect small variations in the concentration of dissolved solute in an acqueous solution was evident. The structure of the sensor permits to include multiple microfluidic channels allowing the simultaneous analysis at different frequencies and/or different analytes.

Remaining in the field of laboratory sensors, a new method for the design of a completely passive RFId tag for breaking test of materials has been described. Starting form the mathematical formulation that makes the behavior of a generic 2-port device representable, the goal was to synthesize the tag through the matrix representation of its intrinsic impedances. Thanks to this method it was possible to represent and interpret the phase and amplitude response (in terms of gain) of the 2-port device, allowing stronger control in the design phase of the tag/device. The resulting $\widetilde{\tau}_n - \varphi_n$ nomogram is the map through which it was possible to synthesize the couplet composed of two dipoles with T-match circuits, which together with the chosen RFId chip, led to the realization of the basic structure of the proposed passive tag. Through the study of the possible behaviors carried out on the $\widetilde{\tau}_n - \varphi_n$ nomogram it was decided to use the tag as a sensor for the breaking test of materials. In particular, by analyzing the behavior of the impedance of the port left free, a pair of copper-based filiform conductors were finally applied in order to detect the impedance variations obtained as a result of the spreading apart of the two terminals themselves. The spreading would emulate the behavior that would occur following a breakage of the material under test. The prototype was interrogated with a reader placed 50 cm from the sensor in the laboratory. The measurements confirmed what was achieved in the study

analysis phases carried out during the simulation phase.

In the field of active radio-frequency electronics a new functionality method for microwave low noise amplifiers was investigated. In order to improve the performances of a receiving equipment in terms of noise figure, it was decided to apply a driven voltage to the LNA with the ability to switch it ON and OFF on command in order to isolate the receiving part of the system from the transmitting one. This technique, in fact, would make it possible to eliminate devices such as microwave switches and circulators that introduce background noise, thus improving performance also from the point of view of the overall dimensions of the entire system. An LNA with this capability could also be used in phased array receiving systems: it would in fact be possible to drive some of the branches making up the multi-antenna structure in order to obtain particular beam-forming. Given the operational frequency chosen (5 GHz), the LNA could be used in applications and systems that use the second Wi-Fi carrier (Wi-Fi5).